UNIVERSITY OF OKLAHOMA

GRADUATE COLLEGE

SEARCHING FOR NEW PHYSICS THROUGH GRAVITATIONAL WAVES

A DISSERTATION

SUBMITTED TO THE GRADUATE FACULTY

in partial fulfillment of the requirements for the

Degree of

DOCTOR OF PHILOSOPHY

By

DANIEL VAGIE
Norman, Oklahoma
2021

SEARCHING FOR NEW PHYSICS THROUGH GRAVITATIONAL WAVES

A DISSERTATION APPROVED FOR THE
HOMER L. DODGE DEPARTMENT OF PHYSICS AND ASTRONOMY

BY THE COMMITTEE CONSISTING OF

Dr. Kuver Sinha, Chair

Dr. Howard Baer

Dr. John Stupak, III

Dr. Bruno Uchoa

Dr. Christian Remling

This dissertation is dedicated to my family and most importantly, my loving and supportive wife who has been there for me every step of the way.

Acknowledgements

I would first like to express my sincere appreciation and gratitude to my dissertation advisor, Professor Kuver Sinha, whose advice and expertise has led me on a successful path to completing my studies. Thank you for being an amazing mentor and having faith in me while I learned to become a better researcher. I would not be where I am today without your guidance. I would like thank my two collaborators and friends, Huaike Guo and Graham White, who I worked closely with on many projects. I am thankful for having the opportunity to work side by side with you and learning everything I could from you. I appreciate your trust and support during our endeavors. I would also like to thank Professor Howard Baer, Professor John Stupak, Professor Bruno Uchoa, and Professor Christian Remling for being great committee members and providing helpful feedback. I would also like to thank my collaborators Chen Sun, Joshua Swaim, Alexandre Alves, Tathagata Ghosh, Lauren Pearce, and Alex Kusenko for being apart of my journey and providing me with the opportunity to learn from each one of you.

Table of Contents

List of Tables

List of Figures

Abstract

Stochastic gravitational waves are features of many new physics models that introduce additional interactions to the Standard Model of Particle Physics. These interactions typically occur in the very early universe which poses a challenge for current detectors. The detection of gravitational waves at ground based or future space based detectors will offer a unique insight into the early universe and allow for a complementarity with particle physics detectors to discover new interactions. Gravitational waves can be generated from several sources such as the merging of Bose-Einstein Condensates, phase transitions, and inflation while providing a unique test for baryogenesis mechanisms. In this work we show that accurately predicting the gravitational wave signals and placing precise constraints on parameter spaces of particle physics models is essential for discovering new physics and mapping out the cosmological history of the early universe.

Chapter 1

Introduction

Since the first direct detection of gravitational waves (GWs) by the LIGO and Virgo collaborations [18], a new interface has arrived in particle physics – its intersection with GW astronomy. While ground based GW detectors have their best sensitivity at frequencies $\sim \mathcal{O}(100)$ Hertz and their main targets are black hole and neutron star binaries, there is now growing interest in building space-based interferometer detectors for milli-Hertz or deci-Hertz frequencies. Many detectors have been proposed, such as the Laser Interferometer Space Antenna (LISA) [19], the Big Bang Observer (BBO), the DECi-hertz Interferometer Gravitational wave Observatory (DECIGO) [20], Taiji [21] and Tianqin [22]. The physical sources of GWs in this frequency band include supermassive black hole binaries [23], extreme mass ratio inspirals [24] and the stochastic background of primordial GWs produced during first order cosmological phase transitions [25].

This offers tremendous opportunities for theorists, as a new window to the early Universe opens up. Aspects of dark sector physics and baryon asymmetry can now be framed fruitfully in a language that lends itself to data from the GW frontier. The key connection is *phase transitions*, which on the one hand are a primary target of future GW experiments, and on the other are important features of scalar potentials and hence have historically been the target of collider physics.

Primordial stochastic gravitational waves from first order cosmological phase transitions have become a new cosmic frontier to probe particle physics beyond

the standard model [25, 26, 27, 28, 10, 29]. Alongside extensive studies on the theory side, direct searches for stochastic gravitational waves at LIGO and Virgo have also been performed using their O1 and O2 data sets [30, 31]. They will come online within the next decade or so and can probe lower frequencies coming from an electroweak scale phase transition [32, 33, 34, 35, 36, 37, 38, 39, 40, 41, 42, 43, 44, 45, 46, 47].[1] Precise calculations of the gravitational wave power spectrum are required to have any hope of inferring parameters of the underlying particle physics model. There have been significant advances in this direction in recent years. In particular, it is now generally accepted that the dominant source for gravitational wave production in a thermal plasma is the sound waves [67], although a more precise understanding of the onset of the turbulence is still needed to settle this issue. For the acoustic production of gravitational waves, many large scale numerical simulations have been performed [68, 69], with the result that standard spectral formulae are now available for general use. These results have also been understood reasonably well for relatively weak transitions, through the theoretical modeling of the hydrodynamics [70] and with the recently proposed sound shell model [71, 3].

Even the very early Universe is transparent to gravitational waves, making searches for the gravitational wave background of the Universe a unique probe of the cosmos before big bang nucleosynthesis. Ubiquitous in the literature is the generation of a gravitational wave background from an inhomogeneous transition

[1] Note that they are also poised to probe hidden sector transitions [48, 49, 50, 51, 52, 53, 54, 55, 56, 57, 58, 59, 60, 61, 62] and transitions from multi-step GUT breaking [63, 64, 65, 66]

of the ground state (for a review see [26, 27, 10]). In the standard model of particle physics, there is no mechanism for such a gravitational wave background to be produced. Specifically, both the QCD and electroweak transitions are predicted to be smooth [72, 73, 74, 75, 76, 77]. This implies that any gravitational wave background resulting from a strong first order phase transition is proof that the standard model is incomplete.

The electroweak transition can be made strongly first order through the introduction of new states at around the electroweak scale [78, 32, 37, 79, 80, 81, 82, 83, 84, 85, 33, 86, 34, 87, 88, 89, 90, 38, 41, 91, 35, 92, 93, 94, 39, 95, 96, 97, 98, 99, 100, 101, 102, 103]. The QCD transition can be catalyzed by changing the number of light fermions [104] or having a very large lepton asymmetry [105, 106, 107]. Additionally there are strong motivations to believe that the standard model is incomplete and additions to the standard model can also leave cosmic fingerprints. For instance, baryonic matter can only explain a fraction of the matter observed and the missing dark matter can be a part of a hidden sector that undergoes a phase transition [48, 52, 55, 59, 108, 109, 110, 111, 57, 112, 113, 60, 114, 115, 116, 117, 118, 119]. Second, the near unification of gauge coupling constants along with conspiracy of gauge anomaly cancellation motivates grand unification which can sequentially break into the standard model gauge group and leave a gravitational wave background [120, 63, 121, 64, 66, 122, 65]. Finally, the generation of neutrino masses can arise through a $B - L$ breaking transition [123, 42, 121, 61, 124, 125]. In each case, an observed signal not only sheds light on our cosmic history, but on a range of energy scales spanning from sub-GeV to

the PeV scale [126] (even higher scales have been proposed, though technology needs to improve to make the sensitivity cosmologically relevant [127] with the possible exception of NEMO [128]).

In the last few years, there has been increasing interest in ultra-light bosonic dark matter (DM) candidates such as the axion. While the QCD axion was originally motivated by the strong CP problem [129, 130], string theory predicts a vast landscape of axion-like particles (ALPs) [131, 132, 133, 134] with masses across several orders of magnitude and a rich phenomenology. Studies of sub-eV (pseudo-) scalars as DM candidates have yielded interesting signals and novel proposals for direct detection experiments [135, 136, 137, 138, 139], to name a few.

In particular, due to its bosonic nature, ultra-light bosonic DM can exhibit collective behaviors at the macroscopic level that are not obvious at the Lagrangian level. It has been observed and well understood in condensed matter physics that for bosons there exists a unique phase, the Bose-Einstein Condensate (BEC) phase, once the ensemble is cooled down below the critical temperature. Given the abundance of the DM population, this translates the requirement of the occupancy number $n > (mv)^3$ to an upper bound of the scalar mass, $m <$ eV [140]. The maximal mass of the BEC object can be crudely estimated as $M \lesssim M_{Pl}^2/m$ [141]. This singles out two scales of particular interest to the community: galactic scale BEC with $m \sim 10^{-22}$ eV, and stellar scale BEC with $m \sim 10^{-10}$ eV.

On galactic scales, condensates of ultralight bosons have been shown to produce core like halos by quantum pressure [142, 143, 144, 145, 146, 147], with various

studies on its constraints [148, 149, 150, 151, 6]. A good understanding of the theoretical mass profile of such a BEC system not only provides insights on the particle nature of DM, but could also have implications for quasar lensing time delay and the recent Hubble tension [152]. On smaller scales, such BEC systems can form stellar scale structures dubbed boson stars [153, 154], with scalars free from interaction [155], with attractive ϕ^4 interaction [156, 157, 158, 159, 160, 161, 162, 163, 164], repulsive ϕ^4 interaction [141, 165, 166], and repulsive $\cos(\phi/f)$ potential [140, 167]. A few variations such as multistate boson stars from generic scalars have also been explored, in an attempt to reproduce realistic models of DM halos [168]. BEC states with angular momentum is studied in a recent work [169]. New ways of probing BEC systems at different scales include using Big Bang Nucleosynthesis (BBN) [170], galaxy rotation curves [171, 151], gravitational wave (GW) from binary boson star mergers [172, 167], GW from BEC collisions [173], speed of GWs passing through BEC [174], electromagnetic emission [175, 176, 177], GW from extreme mass ratio inspiral systems [178], and optical lensing [179].

The slight asymmetry between matter and anti-matter is one of the cornerstone puzzles of modern particle cosmology, as the Standard Model fails to provide an explanation [180, 181, 182]. An elegant paradigm for explaining the slight asymmetry is the Affleck-Dine mechanism [183, 184, 182, 185]. Supersymmetric theories generically have flat directions [186, 184], which have non-zero baryon or lepton number. During inflation, a scalar condensate generically develops in these directions, whose non-zero vacuum expectation value (VEV) spontaneously breaks C and CP. At the end of inflation, a baryon and/or lepton asymmetry is generated

as the VEV coherently evolves and the condensate fragments [187]. These resulting clumps may be long-lived non-topological solitons (Q-balls) [188, 189, 190, 191], carrying either lepton or baryon number [192]. This global charge is transferred to Standard Model particles when the Q-balls decay.

However, the Affleck-Dine mechanism is generically a high-scale phenomenon, making it difficult to confirm observationally. In this paper, we argue that a broad class of Affleck-Dine models significantly enhance the primordial gravitational wave power spectrum. This provides a novel mechanism to test or constrain these models.

The following chapters are organized as follows. Chapter 3 provides an introduction to gravitational waves in the context of Electroweak Phase Transitions originating in the Higg's sector where a complementarity with collider experiments is studied in the Singlet Extended Standard Model (xSM). Phase transitions may occur at any scale, not neccessarily at the electroweak scale, and thus a proper treatment of the scale factor at the time of the phase transition is important for estimating the size of the peak spectrum observed today. In chapter 4, we study phase transitions in an expanding universe and derive a suppression factor of the spectrum which is the result of the finite lifetime of the source inducing the gravitational waves. We continue the discussion of gravitational waves in an expanding universe in chapter 5 while looking at three common models and compare the different levels of diligence used in the literature to understand the impact precision has on estimating the graviational wave spectrum. We change direction in chapter 6 to study the mass and compactness profiles of BEC

systems composed of two ultralight scalars on both stellar and galactic scales with implications of gravitational wave signals at LIGO for binary mergers of two boson stars. In chapter 7, we show that the sudden decay of Q-balls into fermions can result in a rapid transition from matter to radiation domination which enhances the primordial gravitational wave signal. This signal is detectable by future space based detectors, providing a mechanism to test Affleck-Dine baryogenesis.

Chapter 2

Phase Transition in the Standard Model

Gravitational waves produced by phase transitions in the early universe are predicted by many theories beyond the Standard Model and allow for an out of equilibrium environment which is essential for theories like electroweak baryogenesis. This out of equilibrium environment, along with the gravitational wave generation, is only achievable with a first order phase transition. The Standard Model has the ability to produce a first order phase transition through the Higgs mechanism and the evolution of the electroweak vacuum but the experimental value of the Higgs mass forces the phase transition to be a smooth cross over transition [73]. The following sections will introduce the Standard Model, its cross over transition, and how we can deform the Higgs sector effective potential with new interactions to allow for a first order phase transition.

2.1 Standard Model

A potential of a scalar field ϕ with spin zero has the form

$$V(\phi) = \mu^2 \phi^\dagger \phi + \lambda \left(\phi^\dagger \phi\right)^2, \tag{2.1}$$

which takes on a "Mexican hat" shape when $\mu^2 < 0$ and $\lambda > 0$. The minimum of the potential can be found to be located at $\frac{\partial V(\phi)}{\partial \phi} = v = \frac{|\mu|}{\sqrt{\lambda}}$. In the Standard Model, the scalar field can be regarded as the Higgs field which is a weak isospin

doublet of 4 components

$$\phi = \frac{1}{\sqrt{2}} \begin{pmatrix} \phi_1 + i\phi_2 \\ \\ \phi_3 + i\phi_4 \end{pmatrix}. \tag{2.2}$$

The Higgs potential is symmetric in rotations in ϕ space but if we choose a direction of fluctuation,

$$\phi_0 = \frac{1}{\sqrt{2}} \begin{pmatrix} 0 \\ \\ v \end{pmatrix}, \tag{2.3}$$

we spontaneously break the symmetry. A fluctuation of the field around the minimum, $\phi \to \phi_0 + h$, will result in

$$\phi = \frac{1}{\sqrt{2}} \begin{pmatrix} 0 \\ \\ v + h \end{pmatrix}, \tag{2.4}$$

where we associate h with the Standard Model Higgs Boson. The minimum v has been experimentally measured to be $v = 246$ GeV.

In addition to the scalar Higgs Boson, the Standard Model contains six spin 1/2 quarks (up, down, charm, strange, top, and bottom), six spin 1/2 leptons (electron, muon, tau electron, neutrino, muon neutrino, and tau neutrino), and four spin 1 vector bosons (gluon, photon, Z, W). The fermions such as the quarks and leptons couple to the Higgs field through interactions like

$$-y_f \left(\bar{f}_L \phi f_R + \bar{f}_R \phi f_R \right), \tag{2.5}$$

where f is the (left, right) fermion field and y_f is the coupling to the Higgs field. The spontaneous symmetry breaking of Higgs results in the generation of the masses for the fermions

$$m_f = \frac{y_f v}{\sqrt{2}}. \tag{2.6}$$

The interaction term of the vector bosons to the Higgs is

$$g^2 \phi^\dagger V_\mu V^\mu \phi, \tag{2.7}$$

where V is a vector boson and g is the gauge charge of the vector boson in the covariant derivative. This term will generate a mass for the vector bosons after symmetry breaking as well. The masses of the W and Z bosons are

$$M_W = \frac{vg}{2}, \quad M_Z = \frac{v\sqrt{g^2 + g'^2}}{2}. \tag{2.8}$$

The mass terms for the fermions and vector bosons are not explicitly allowed because of chiral symmetry and gauge invariance respectively. These terms only arise due to the field dependence of the scalar field in the interaction terms and the spontaneous symmetry braking by expanding about fluctuations near the minimum of the Higgs potential.

2.2 Phase Transition

The theory of phase transitions can be understood from the thermodynamic properties of a free gas consiting of bosonic and fermionic fields. A simple effective potential can be derived to trace the phase structure at finite temperature and analyze the dynamics of the phase transition such as in Sec. 4.3. The effective potential was originally used as a high temperature approximation for the standard model (see, e.g., Ref. [17]). In the Standard Model, the origin of the electroweak symmetry breaking is predicted to be that of a second order phase transition. When the universe was very hot, symmetry was restored and the expectation

value of the Higgs sat at origin where $< \phi >= 0$. As the universe began to cool, the universe smoothly transitioned from $< \phi(T) >= 0$ to $< \phi(0) >= v = 246$ GeV. This smooth cross over transition is not an out of equilibrium process and thus will not produce gravitational waves or baryeogensis. If the transition was first order, where at some critical temperature a new minimum at $< \phi(T_c) >= 0$ became degenerate with $< \phi(T_c) >= v(T_c)$ seperated by a potential barrier, the universe can tunnel from the symmetric phase to the broken phase providing the out of equilibrium environment and generate gravitational waves through bubble nucleation of the new phase. This out of equilibrium environment can prevent the baryon asymmetry from being washed out depending on the strength of the transition. This section is devoted to deriving the effective potential at finite temperature and discuss the phase transition structure of the Standard Model.

The free energy density of a gas at temperature T in a volume $\mathcal{V}$ is given by

$$f_B = V_{0,B} + T \int \frac{d^3k}{(2\pi)^3} \ln\left(1 - \exp^{-\beta\omega_{\vec{k}}}\right), \tag{2.9}$$

where $V_{0,B}$ is a constant representing the zero-temperature ground state, and $\beta = 1/T$ and $\omega_{\vec{k}}$ is the angular frequency for each momentum mode $|\vec{k}|$. The free energy density can be derived from the partition function of a bosonic harmonic oscillator. Similarly, the free energy density for a fermionic field is

$$f_F = -V_{0,F} - T \int \frac{d^3k}{(2\pi)^3} \ln\left(1 + \exp^{-\beta\omega_{\vec{k}}}\right). \tag{2.10}$$

The free energy densities can be written as

$$f_{B,F} = T^4 J_{B,F}\left(\frac{m}{T}\right), \tag{2.11}$$

where T is the temeperature that sets the dimensions of the free energy and $J_{B,F}$ is a dimensionless function. The free energy density is purely a function of mass and temperature.

The free energy density of the Standard Model Higgs boson can be written as the combination of tree level potential defined in Eq. 2.1 and the free energy density in Eq. 2.11:

$$f(\phi, T) = V_0\phi + T^4 \left(\sum_B J_B \left(\frac{M_B}{T} \right) + \sum_F \left(\frac{M_F}{T} \right) \right), \tag{2.12}$$

where we sum over all the bosons and fermions at temperature T. At finite temperature, the vacuum expectation value of the Higgs boson becomes temperature dependent and we aim to minimize $f(\phi, T)$. The masses of the fermions and bosons are no longer constant but now depend on the temperature dependent vacuum expectation value. The masses of particles will evolve as

$$M_{B,F}(\phi) = c_{B,F}\phi, \tag{2.13}$$

where B, F runs over the bosons and fermions of the theory and c is a constant that depends on the coupling in the interaction term. Calculating the integral in Eq. 2.11 is numerically expensive but we can expand the integral using the large temperature approximation to yield

$$\begin{aligned} f = &- g_{\text{eff}} \frac{\pi^2}{90} T^4 + V_0(\phi) \\ &+ \frac{T^2}{24} \left(\sum_S M_S^2(\phi) + 3 \sum_V M_V^2(\phi) + 2 \sum_F M_F^2(\phi) \right) \\ &- \frac{T}{2\pi} \left(\left(M_S^2(\phi) \right)^{3/2} + \sum_V \left(M_V^2 \right)^{3/2} \right), \end{aligned} \tag{2.14}$$

where we sum over the scalars, vectors bosons, and fermions of the theory. The constants in front of the summations are the degrees of freedom. The effective number of relativistic degrees of freedom g_{eff} is

$$g_{\text{eff}} = \frac{7}{8} 4N_F + 3N_V + 2N_V 0 + N_S, \tag{2.15}$$

where N_F is the number of fermions, N_S is the number of scalar bosons, and N_V and N_{V_0} are the number of massive and massless vector bosons respectively. The effective degrees of freedom is temperature dependent and can be assumed to be 106.75 for the Standard Model at large temperatures $T \gtrsim 100$ GeV. Above this temperature, all Standard Model particles are assumed to be relativistic and coupled to the plasma. The field dependent effective potential of the full free energy density in Eq. 2.14 in the high temperature expansion can be generically written as

$$V_T(\phi) = D\left(T^2 - T_0^2\right)\phi^2 - ET\phi^3 + \frac{\lambda_T}{4}\phi^4, \tag{2.16}$$

where in the Standard Model, the parameters E, D, λ_T, and T_0 will depend on masses and couplings in Eq. 2.13. Here $D > 0$, $E > 0$, $\lambda > 0$ and λ has a weak dependence on T. The first term has a positive coefficient when $T > T_0$ to restore the symmetry. The third, the cubic term, when is sufficiently smaller, helps create a barrier together with the first term, and creates another minimum. In the Standard Model, the main contributions to Eq. 2.16 are the mass of the Higgs M_H, mass of W boson M_W, the mass of the Z boson m_Z, and the mass of the

top quark M_T which give

$$E = \frac{1}{4\pi v^3}\left(2M_W^3 + M_Z^3\right) \tag{2.17}$$

$$D = \frac{1}{8v^2}\left(2M_W^2 + M_Z^2 + 2M_t^2\right) \tag{2.18}$$

$$\lambda_T = \lambda + \ ... \tag{2.19}$$

$$T_0 = \sqrt{\frac{1}{4D}} M_H^2 + \ ... \tag{2.20}$$

$$\tag{2.21}$$

where $M_H = 126$ GeV, $v = 246$ GeV, $M_W = 80.38$ GeV, $M_Z = 91.19$ GeV, and $M_t = 172.76$ GeV. We note that the temperature dependent potential should depend on all of the Standard Model particles that acquire mass at finite temperature. However, we only keep the heavier particles as they are the dominate species in Eq.2.21. For simplicity, we drop the one-loop order terms that are proportional to $\phi^4 \ln(\phi/v^2)$ and $m^4 \ln(m^2/T)$.

In Fig. 2.1, we plot the phase structure of the generic effective potential in Eq. 2.16 for two sets of benchmark points in (E, D, λ_T, T_0). The left panel represents a second order phase transition while the right panel shows a first order phase transition. Both panels show the evolution of the effective potential as the minimum of ϕ varies with temperature. At large T, both figures have symmetry restored and the minimum sits at the origin. As the universe begins to cool, the left panel shows that the minimum smoothly crosses over to a non-zero value and evolves to the zero temperature minimum. The right panel shows that a new minimum begins to form as the universe cools and eventually become degenerate with the symmetric minimum at some critical temperature. Below

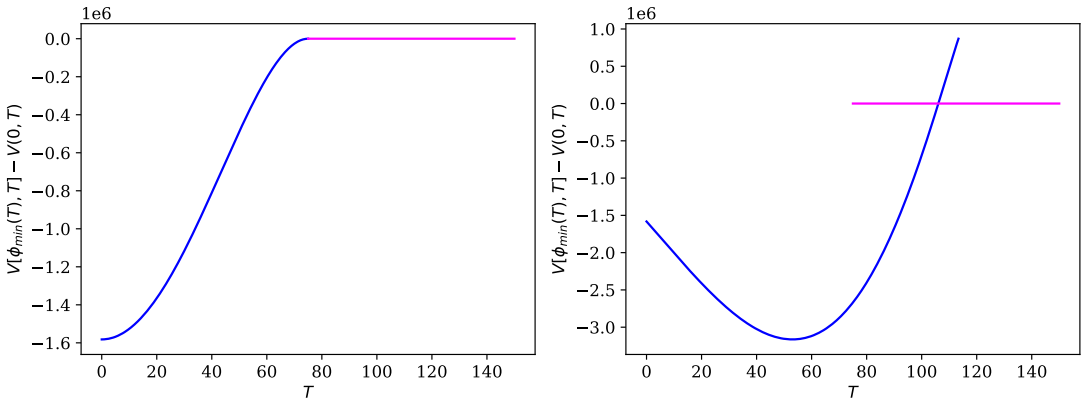

Figure 2.1: Left panel: the temperature dependent effective potential as a function of the minimum of ϕ for a second order phase transition. Right panel: the temperature dependent effective potential as a function of the minimum of ϕ for a first order phase transition.

the critical temperature, the new phase becomes more energetically favorable and the universe tunnels to the new phase and breaks the symmetry. Both panels have $D = 0.1, \lambda_T = 0.2$, and $T_0 = 75$. In the left panel, we set $E = 0$ to eliminate the barrier. We choose $E = 0.1$ in the right panel to introduce a barrier. The benchmarks in Fig. 2.1 were choosen at random but by varying the barrier term in the effective potential, we were able drastically change the behavior of the phase transition. In the Standard Model, the Higgs mass is too large to allow for a first order phase transition. A first order phase transition can occur, however, if we deform the Higgs potential with new interactions through the introduction of new particles which can modify the parameters (E, D, λ_T, T_0). This can lead to a symmetry breaking pattern such as the right panel of Fig. 2.1 or if there are additional scalars, there can be more complicated phase structures with multi-step

transitions.

Chapter 3

Electroweak Phase Transitions

3.1 Introduction

The purpose of our work is to *explore the complementarity of future GW detectors and future particle colliders in probing phase transitions in the early Universe* – in the simplest particle physics setting possible, but also with great attention to detail within such a setting. The natural choice is the electroweak phase transition (EWPT) [32] with the simplest extension of the Higgs sector: the singlet scalar augmented Standard Model or the xSM[1]. This model is capable of providing a strongly first order EWPT through a tree level barrier and is the simplest model in Class IIA of the tree level renormalizable operators described in [198] (see Ref. [199, 63, 200, 201, 202, 203, 54, 204, 205, 206, 207, 208, 209, 210, 120, 211, 90, 212, 213, 214, 36, 215, 216, 123, 217, 218] for related studies). It has been extensively investigated in phenomenological studies [219, 84, 220, 221], studies of EWPT [84, 219, 222, 223, 224] and di-Higgs analyses [225] guided by the requirements of EWPT [220], and electroweak baryogenesis (EWBG).

We perform a detailed scan of this model, shedding light on the following issues: (*i*) the EWPT patterns admitted by the model, and the proportion of parameter space for each pattern; (*ii*) the regions of parameter space that give detectable GWs at future space-based detectors; (*iii*) the current and future

[1]Hidden sector phase transitions are also being actively investigated [48, 193, 112, 194, 195], and exploring complementarity in such settings is an interesting future direction. We refer to Ref. [25, 196, 26, 197, 27] for recent work on these topics.

collider measurements of di-Higgs production, as well as searches for a heavy weak diboson resonance, and how these searches interplay with regions of parameter space that exhibit strong GW signals; and (*iv*) the complementarity of collider and GW searches in probing this model.

We first carefully work out and incorporate all phenomenological constraints: boundedness of the Higgs potential from below, electroweak vacuum stability at zero temperature, perturbativity, perturbative unitarity, Higgs signal strength measurements and electroweak precision observables. Then, we identify the regions of parameter space which give large signal-to-noise-ratio (SNR) at LISA. We carefully address subtle issues pertaining to the bubble wall velocity v_w, making a distinction between v_w, which enters GW calculations, and the velocity v_+ that is used in EWBG calculations. The relation between these two velocities is determined from a hydrodynamic analysis by solving the velocity profile surrounding the bubble wall. We provide a description of different fluid velocity profiles and investigate the behavior of the normalized energy released during the phase transition, α, which primarily determines the SNR, as a function of the model parameters. On the collider side, we identify the subset of points with large SNR at LISA that are most promising in terms of di-Higgs and weak diboson production studies, setting the stage for future benchmark points.

Much remains to be understood about the Higgs sector. On the collider side, measuring the Higgs cubic and quartic couplings through double or triple Higgs production, both non-resonant as well as resonant, is an extremely difficult but central goal of future experiments (see e.g., [226, 227, 1, 228, 229, 230, 2]). While

any deviation of the shape of the Higgs potential from what is expected within the Standard Model (SM) would hint to new physics, the sensitivities of such collider studies are found to be rather low. The detection of GWs from EWPT in future experiments can offer a complementary method of probing the currently largely unknown Higgs potential. Our work is a step in that direction.

The paper is structured as follows. In Sec. 3.2, we define the Higgs potential and set the notations. The standard phenomenological analysis is discussed in the following Sec. 3.3. The next Sec. 3.4 discuss the details of the EWPT and GW calculations, after which the results and discussions from the full scan is presented in Sec. 3.5 and we summarize in Sec. 3.6.

3.2 The Model

In this section, we fix our notation by defining the potential for the gauge singlet extended SM, known as the"xSM". This model is defined with the following potential setup [219, 84, 220]:

$$\begin{aligned} V(H,S) &= -\mu^2 H^\dagger H + \lambda (H^\dagger H)^2 + \frac{a_1}{2} H^\dagger H S \\ &\quad + \frac{a_2}{2} H^\dagger H S^2 + \frac{b_2}{2} S^2 + \frac{b_3}{3} S^3 + \frac{b_4}{4} S^4, \end{aligned} \tag{3.1}$$

where $H^{\mathrm{T}} = (G^+, (v_{\mathrm{EW}} + h + iG^0)/\sqrt{2})$ is the SM Higgs doublet and $S = v_s + s$ the real scalar gauge singlet. All the model parameters in the above equation are real. The parameters μ and b_2 can be solved from the two minimization conditions

around the EW vacuum($\equiv (v_{\rm EW}, v_s)$),

$$\mu^2 = \lambda v_{\rm EW}^2 + \frac{1}{2} v_s (a_1 + a_2 v_s),$$
$$b_2 = -\frac{1}{4v_s}[v_{\rm EW}^2 (a_1 + 2a_2 v_s) + 4v_s^2 (b_3 + b_4 v_s)], \tag{3.2}$$

and λ, a_1, a_2 can be replaced by physical parameters θ, m_{h_1} and m_{h_2} from the mass matrix diagonalization [2]:

$$\lambda = \frac{m_{h_1}^2 c_\theta^2 + m_{h_2}^2 s_\theta^2}{2v_{\rm EW}^2},$$
$$a_1 = \frac{2v_s}{v_{\rm EW}^2}[2v_s^2 (2b_4 + \widetilde{b}_3) - m_{h_1}^2 - m_{h_2}^2 + c_{2\theta}(m_{h_1}^2 - m_{h_2}^2)],$$
$$a_2 = \frac{-1}{2v_{\rm EW}^2 v_s}[-2v_s (m_{h_1}^2 + m_{h_2}^2 - 4b_4 v_s^2)$$
$$+ (m_{h_1}^2 - m_{h_2}^2)(2c_{2\theta} v_s - v_{\rm EW} s_{2\theta}) + 4\widetilde{b}_3 v_s^3], \tag{3.3}$$

where $\widetilde{b}_3 \equiv b_3/v_s$ and we have defined the physical fields h_1 and h_2 as

$$h_1 = c_\theta h + s_\theta s, \qquad h_2 = -s_\theta h + c_\theta s, \tag{3.4}$$

with a mixing angle θ. We note that h_1 is identified as the SM Higgs while h_2 is a heavier scalar. The coupling of h_1 with the SM particles is reduced by a factor of c_θ while the coupling of h_2 with SM particles is $(-s_\theta)$ times the corresponding SM couplings and vanishes in the case of zero mixing angle.

With choices of parameter transformations described above, the potential is fully specified by the following five parameters:

$$v_s, \qquad m_{h_2}, \qquad \theta, \qquad b_3, \qquad b_4. \tag{3.5}$$

The model defined here has several variants in the literature. For example, since the potential can be defined with a translation in the S direction $S \to S' = S - v_s$,

[2] Here $s_\theta \equiv \sin\theta$ and $c_\theta \equiv \cos\theta$.

such that $\langle S \rangle = 0$, the resulting potential will take the same form as Eq. 3.1 but with the addition of a non-zero tadpole term $b_1 S$ [225]. The potential and physics remain the same but the parameters in the potential will transform accordingly. The transformation rules to and from this basis are given in Appendix F. There is also a variant where there is a spontaneously broken Z_2 symmetry $S \to -S$; this corresponds to a subset of the parameter space here where $a_1 = b_3 = 0$.

We further note that we do not include CP-violation in this study since the magnitude of the CP-violation is typically very constrained by current electric dipole moment searches (e.g., [231, 232, 90] or the included CP-violation may be large but has little effect on EWPT [233].

3.3 Phenomenological Constraints

In this section, we briefly discuss the phenomenological constraints used in our analysis, following the standard treatments given in Refs. [234, 221, 225]. The phenomenological discussion includes boundedness of the Higgs potential from below, EW vacuum stability at zero temperature, perturbativity, perturbative unitarity, Higgs signal strength measurements and electroweak precision observables.

First, the potential needs to be bounded from below. Requiring this for arbitrary field directions gives us the condition [225],

$$\lambda > 0, \quad b_4 > 0, \quad a_2 \geqslant -2\sqrt{\lambda b_4}. \tag{3.6}$$

Next, the EW vaccum also needs to be stable at zero temperature. Using physical parameters as input will automatically guarantee that the EW vacuum is a

minimum. To ensure that the above EW vacuum is stable, one should require that no deeper minimum exists in the potential. In our analysis, we find all the minima by firstly solving $\partial V/\partial\phi_i = 0(\phi_1 \equiv h,\ \phi_2 \equiv s)$ and subsequently calculating eigenvalues of the Hessian matrix $\{\partial^2 V/\partial\phi_i\partial\phi_j\}$ to determine the nature of the extrema for each set of parameter input.

Next, Higgs signal strength measurements in various channels require the couplings of h_1 to be not far from the SM Higgs couplings. In the xSM, the couplings of h_1 to SM particles are reduced by a factor of $\cos\theta$, therefore the Higgs signal strength is given by $\mu_H = \cos^2\theta$. Experimentally, the most recent ATLAS and CMS combined fit of this value is $\mu_H = 1.09^{+0.11}_{-0.10}$ [235] and a χ^2 analysis shows that $|\sin\theta| > 0.33$ are excluded at 95% CL [236].

Moreover, unitarity puts constraints on the high energy behavior of particle scatterings. Requiring further the perturbativity of these scatterings at high energy will lead to constraints on the model. This tree level perturbativity requirement is quantified as the condition that the partial wave amplitude $a_l(s)$ for all $2 \to 2$ processes satisfies $|\mathrm{Re}\, a_l(s)| \lesssim 1/2$ for $\sqrt{s} \to \infty$. We consider all channels of scalar/vector boson $2 \to 2$ scatterings at the leading order in the high energy expansion, with details of the S-matrix given in Appendix. E.

Electroweak precision measurements, which mainly include the W boson mass measurement [237] and the oblique EW corrections [238, 239], put further constraints on the model. The W boson mass m_W can be calculated given experimentally measured values of G_F, m_Z and the fine structure constant at zero momentum transfer $\alpha(0)$ [237]. The function relating m_W and these three

parameters depends on the loop corrections of the vector boson self-energies. Comparing this calculated m_W with the experimental measurement $m_W^{\rm exp} = 80.385 \pm 0.015$GeV [240, 241, 242] highly constrains the modification of the loop corrections by new physics effects. In this model, the modified loop corrections result from reduced Higgs couplings and from the presence of the heavier scalar h_2 and are only dependent on (θ, m_{h_2}) at one-loop level. The same parameter dependence enters the oblique S, T, U parameters and it turns out that the W-mass constraint is much more stringent than that from the oblique corrections [237, 221].

To give the reader a flavor of the above phenomenological constraints, we fix $m_{h_2} = 300\,\text{GeV}$, $\theta = 0.2$, $b_4 = 4$ and show the various bounds on the remaining two parameters $(v_s/v_{\rm EW}, b_3/v_{\rm EW})$ in Fig. 3.1. This choice of m_{h_2} and θ evades the constraints from the W-mass as well as the oblique EW corrections and regions outside the color-shaded regions are excluded by the remaining constraints. It can be seen from this figure that the least constraining condition comes from the perturbative unitarity requirement for this parameter choice. The bounded-from-below condition is more restrictive and also separates the plane into two disconnected regions while the stability of the EW vacuum at zero temperature shrinks the allowed parameter space even more. We also overlaid on this plot the points which pass the various EWPT requirements and give GW signals with varying SNR. More details are given in the caption and in the following section.

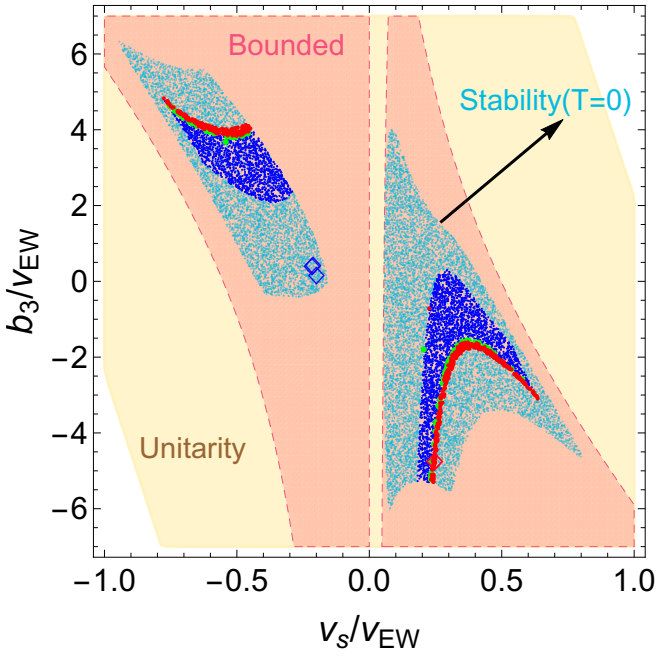

Figure 3.1: An illustrative plot showing various phenomenological constraints. The shaded regions are allowed by requirements of unitarity, boundedness of the potential from below, and stability of EW vacuum at zero temperature. Points are also overlapped on this plot where various EWPT criteria are fulfilled and with SNR > 50 (red), $50 >$ SNR > 10 (green) and SNR < 10 (blue). The diamond-shaped points give two-step EWPT.

3.4 EWPT and Gravitational Waves

3.4.1 Effective Potential

EWPT is an essential step in generating the observed baryon asymmetry in the universe by providing an out-of-equilibrium environment, one of the three Sakharov conditions [180], in the framework of electroweak baryogenesis (see [243] for a recent review). Augmented with the rapid baryon number violating Sphaleron

process outside the electroweak bubbles and the CP-violating particle scatterings on the bubble walls, a net baryon number can be produced inside the bubbles. Aside from the particle interactions, which are used in EWBG calculations, the cosmological context that characterizes the dynamics of the EWPT can be calculated from the finite temperature effective potential. The standard procedure of calculating it includes adding the tree level effective potential, the Coleman-Weinberg term [244] and its finite temperature counterpart [245] as well as the daisy resummation [246, 247]. Since the EWPT in this model is mainly driven by the cubic terms in the potential and out of concern of a gauge parameter dependence [248] of the effective potential calculated in the above standard procedure, we take here the high temperature expansion approximation, which is gauge invariant, in line with previous analyses of this model [219, 84, 222, 220, 249]. This effective potential is then given by [3]

$$\begin{aligned} V(h,s,T) = &-\frac{1}{2}[\mu^2 - \Pi_h(T)]h^2 - \frac{1}{2}[-b_2 - \Pi_s(T)]s^2 \\ &+\frac{1}{4}\lambda h^4 + \frac{1}{4}a_1 h^2 s + \frac{1}{4}a_2 h^2 s^2 + \frac{b_3}{3}s^3 + \frac{b_4}{4}s^4, \end{aligned} \tag{3.7}$$

where $\Pi_h(T)$ and Π_s are the thermal masses of the fields,

$$\begin{aligned} \Pi_h(T) &= \left(\frac{2m_W^2 + m_Z^2 + 2m_t^2}{4v^2} + \frac{\lambda}{2} + \frac{a_2}{24}\right)T^2, \\ \Pi_s(T) &= \left(\frac{a_2}{6} + \frac{b_4}{4}\right)T^2, \end{aligned} \tag{3.8}$$

[3] We also note that we have neglected a tadpole term proportional to $T^2 s$, which originates from the a_1 and b_3 terms in the potential in Eq. 3.1, since it comes with a factor $v_s/v_{\rm EW}$ and is suppressed for most of the parameter space giving detectable GWs, to be presented in later sections. Indeed its effect has been found to be numerically negligible from previous studies [219, 84].

where the gauge and Yukawa couplings have been written in terms of the physical masses of W, Z and the t-quark. With this effective potential, the thermal history of the EW symmetry breaking can be analyzed. It depends mainly on the following key parameters:

$$T_c, \quad T_n, \quad \alpha, \quad \beta, \quad v_w. \tag{3.9}$$

Here T_c is the critical temperature at which the metastable vacuum and the stable one are degenerate. Below T_c, the phase at the origin in the field space becomes metastable and the new phase becomes energetically preferable. The rate at which the tunneling happens is given by [250]

$$\Gamma \sim \mathcal{A}(T) e^{-S_3/T}, \tag{3.10}$$

where S_3 is the 3-dimensional Euclidean action of the critical bubble, which minimizes the action

$$S_3(\vec{\phi}, T) = 4\pi \int r^2 dr \left[\frac{1}{2} \left(\frac{d\vec{\phi}(r)}{dr} \right)^2 + V(\vec{\phi}, T) \right], \tag{3.11}$$

and satisfies the bounce boundary conditions

$$\frac{d\vec{\phi}(r)}{dr}\Big|_{r=0} = 0, \qquad \vec{\phi}(r=\infty) = \vec{\phi}_{\rm out}. \tag{3.12}$$

Here $\vec{\phi}_{\rm out}$ denotes the two components vev of the fields outside the bubble, which is not necessarily the origin for two-step EWPT. The prefactor $\mathcal{A}(T) \propto T^4$ on dimensional grounds. Its precise determination needs integrating out fluctuations around the above static bounce solution (see e.g., [251, 252] for detailed calculations or [253] for a pedagogical introduction). For the EWPT to complete, a sufficiently large bubble nucleation rate is required to overcome the expansion rate. This is

quantified as the condition that the probability for a single bubble to be nucleated within one horizon volume is $\mathcal{O}(1)$ at a certain temperature [52]:

$$\int_0^{t_n} \Gamma V_H(t) dt = \int_{T_n}^{\infty} \frac{dT}{T} \left(\frac{2\zeta M_{\rm Pl}}{T} \right)^4 e^{-S_3/T} = \mathcal{O}(1), \tag{3.13}$$

where $V_H(t)$ is the Horizon volume, $M_{\rm Pl}$ is the Planck mass and $\zeta \sim 3 \times 10^{-2}$. From this equation, it follows that $S_3(T)/T \approx 140$ [254] and the temperature thus solved is defined as the nucleation temperature T_n. Expanding the rate at T_n, one can define the duration of the EWPT in terms of the inverse of the third parameter β [254]:

$$\beta \equiv H_n T_n \left. \frac{d(S_3/T)}{dT} \right|_{T_n} , \tag{3.14}$$

where H_n is the Hubble rate at T_n.

Next, α is the vacuum energy released from the EWPT normalized by the total radiation energy density ($\equiv \rho_R$) at T_n [255]:

$$\alpha = \frac{\Delta\rho}{\rho_R} = \frac{1}{\rho_R} \left[-V(\vec{\phi}_b, T) + T \frac{\partial V(\vec{\phi}_b, T)}{\partial T} \right] \Bigg|_{T=T_n} , \tag{3.15}$$

where $\rho_R = g_* \pi^2 T_n^4/30$ with $g_* \approx 100$ and $\vec{\phi}_b$ denotes the two components vev of the broken phase. In this expression, the first term is the free energy from the effective potential and the second term denotes the entropy production. Finally, v_w is the bubble wall velocity.

Given that a first order EWPT can proceed and complete, the baryon asymmetry is generated outside the bubbles and then captured by the expanding bubble walls. When the EWPT finishes, the universe would be in the EW broken phase with non-zero baryon asymmetry. To ensure that these baryons would not

be washed out, the Sphaleron rate needs to be sufficiently quenched inside the bubbles. This condition is known as the strongly first order EWPT (SFOEWPT) criterion [256, 243]:

$$\frac{v_H(T)}{T}\Big|_{T=T_n} \gtrsim 1. \tag{3.16}$$

The conventional choice of the temperature at which the above condition is evaluated is T_c, but a more precise timing is the nucleation temperature T_n, which we use here. Since generally $T_n < T_c$ and $v_h(T_n) > v_h(T_c)$, it might seem at first glance that the above condition is weaker when implemented at T_n than at T_c. However the implicit assumption associated with the former requires the capability of the EWPT to successfully nucleate, i.e., the condition Eq. 3.13 should be satisfied in the first place, which is typically a more stringent requirement of the potential.

The presence of two scalar fields gives a richer pattern of EWPT and makes it possible to complete the EWPT with more than one step [257, 258, 52]. One can immediately imagine mainly the following EWPT types:

(A): $(0,0) \to (v_H \neq 0, v_S \neq 0)$

(B): $(0,0) \to (v_H = 0, v_S \neq 0) \to (v_H \neq 0, v_S \neq 0)$

(C): $(0,0) \to (v_H \neq 0, v_S = 0) \to (v_H \neq 0, v_S \neq 0)$

where the last vacuum configuration $(v_H \neq 0, v_S \neq 0)$ in each case would eventually evolve to the EW vacuum at $T = 0$ [4]. Here pattern (A) is a one step EWPT from the origin in field space to the EW symmetry breaking vacuum directly,

[4] More exotic patterns might appear but should be of negligible phase space.

due mainly to the negative cubic term in the effective potential. This one step phase transition results in a typical GW spectrum as shown in the left panel of Fig. 3.3. Quite differently, patterns (B) and (C) are two-step EWPT, which differ only in how the vacuum transits for these two steps. For example, in case (B), the universe first goes to a vacuum which has non-zero vev for the singlet field and then transits to the would-be EW vacuum at high temperature. Case (C) is different in that it breaks the EW vacuum first and then further goes to the would-be vacuum in a subsequent step of phase transition. For each transit of the vacuum, it can be either first or second order, depending on whether there is a barrier separating the two vacua. We note that for case (C), baryon production generally needs to occur in the first step, otherwise, the exponentially reduced Sphaleron rate would greatly suppress the baryon number violating process in the second step as the EW symmetry is already broken outside the bubbles. Therefore the SFOEWPT criterion is imposed in the first step for this case.

We note that with the aid of the analytical methods presented in Ref. [223, 52], it is possible to locate the region of the parameter space that gives exactly one specific type of EWPT by imposing various conditions on the input parameters. However, our task here is to reveal the overall behavior of the parameter space concerning EWPT and GW. Therefore we adopt here a scan-based analysis which covers the entire parameter space and for each scanned parameter space point, we determine its pattern of EWPT and calculate GW properties. This way, we can determine the most probable pattern of EWPT admitted by this model.

3.4.2 Hydrodynamics

Successful EWBG usually requires a subsonic v_w to give sufficient time for chiral asymmetry propagation ahead of the wall and for conversion to baryon asymmetry through the Sphaleron process. On the other hand, a larger v_w is better for GW production. Therefore a tension may arise between successful EWBG and a loud GW signal production. This problem can potentially be solved when the hydrodynamic properties of the fluid are taken into account [259]. This is because the expanding wall stirs the fluid surrounding the bubble wall and a non-zero velocity profile exists for the plasma ahead of the wall (see Ref. [70] for a recent combined analysis). In the bubble wall frame, this means the plasma outside the bubble will head towards the bubble wall with a velocity ($\equiv v_+$) that can be different from v_w. Therefore it is v_+ rather than v_w that should be used in EWBG calculations. While the above argument still needs to be scrutinized taking into account the particle transport behavior around the bubble wall in the process of EWBG, we assume tentatively that this is true in this work.

This hydrodynamic treatment hinges on solving the fluid velocity profile $v(r,t)$ around the bubble wall given inputs of (α, v_w), where r is the distance from the bubble center and t is counted from the onset of the EWPT. Due to the properties of the problem here, v is a function solely of $r/t \equiv \xi$. The differential equation governing the velocity profile is derived from the conservation of the energy momentum tensor describing the fluid and scalar field [70]:

$$2\frac{v}{\xi} = \frac{1-v\xi}{1-v^2}\left[\frac{\mu^2}{c_s^2} - 1\right]\partial_\xi v, \tag{3.17}$$

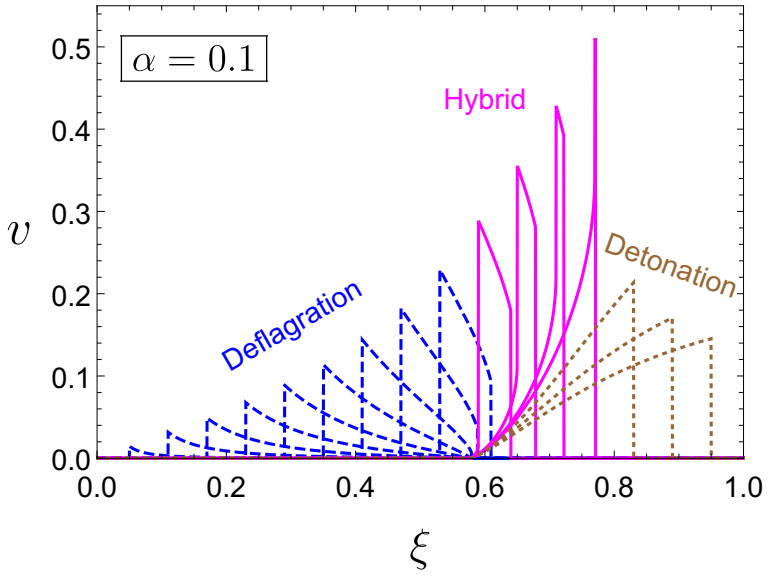

Figure 3.2: A set of fluid velocity profiles obtained when v_w is increased from small to large values(from left to right), for $\alpha = 0.1$. Three modes of profiles are obtained, deflagration (blue dashed), supersonic deflagration (aka hybrid, magenta solid) and detonation (brown dotted).

where $c_s = 1/\sqrt{3}$ is the speed of sound in the plasma and $\mu(\xi, v) = (\xi - v)/(1 - \xi v)$ is a Lorentz boost transformation. Far outside the bubble and deep inside the bubble, the plasma will not be stirred, that is $v \to 0$ serves as the boundary condition. At the phase boundary, the velocity of the plasma inside and outside the bubble wall are denoted as v_- and v_+ in the bubble wall frame, both heading towards the bubble center. The same energy momentum conservation, when applied across the bubble wall, gives a continuity equation connecting v_- with v_+. Therefore the whole fluid velocity profile can be solved from the center of the bubble to far outside the bubble where the plasma is unstirred.

The solutions of the fluid profiles can be classified into three modes depending

on the value of v_w. A set of profiles $v(\xi)$ are shown in Fig. 3.2 for $\alpha = 0.1$. For $v_w < c_s$, a deflagration mode is obtained, in which case, the plasma ahead of the bubble wall flows outward while it remains static inside the bubble, corresponding to the profiles with blue-dashed lines. It can also be seen from this figure that as v_w increases in this mode, a discontinuity in $v(\xi)$ appears outside the bubble and $v(\xi)$ jumps to zero. This is the location of the shock front, and beyond this point the solution of Eq. 3.17 is invalid and a shock front develops such that $v(\xi)$ goes to zero consistently. When v_w surpasses c_s but is less than a certain threshold $\xi_J(\alpha)$, a supersonic deflagration mode [260] appears (magenta solid profiles) where the plasma inside the bubble has a non-zero profile, while still taking the form of deflagration outside the bubble. Here $\xi_J(\alpha)$, as a function of α, corresponds to the Jouguet detonation [261], used in earlier studies. It is also evident that in this mode, as v_w increases, the shock front becomes closer to the bubble wall until it coincides with the bubble wall, where $v_w = \xi_J(\alpha)$ and the fluid enters the third, detonation mode (brown dotted profiles). In this mode, the plasma outside the bubble has zero velocity and therefore $v_+ = v_w$. If a subsonic velocity is required in EWBG, we conclude that the deflagration mode will not work for EWBG. On the contrary, $v_+ < v_w$ in the deflagration and supersonic deflagration modes and a solution for the tension between EWBG and GW might be achieved.

Therefore, instead of treating v_w as a free parameter in the GW calculations, we require, given a certain input of α, the corresponding v_+ to have subsonic value, taken to be 0.05 here, a choice usually used in EWBG calculations [262, 263, 264, 265, 233]). The procedure of achieving the above goal is as follows: for

each given α we iterate over v_w and solve the whole fluid profile until $v_+ = 0.05$ is reached. The resulting v_w is used in GW calculations [5].

With $v(\xi)$ obtained, one can also calculate the bulk kinetic energy normalized by the vacuum energy released during the EWPT [70]:

$$\kappa_v = \frac{3}{\Delta\rho\ v_w^3} \int \omega(\xi) \frac{v^2}{1-v^2} \xi^2 d\xi, \tag{3.18}$$

where $\omega(\xi)$ is the enthalpy density, varying as function of ξ, and can be solved once $v(\xi)$ is found. The remaining part $1 - \kappa_v \equiv \kappa_T$ gives the fraction of the vacuum energy going to heat the plasma. Therefore a reheating temperature can be defined as

$$T_* = T_n (1 + \kappa_T \alpha)^{1/4}. \tag{3.19}$$

This leads to an increase in entropy density and thus a dilution of the generated baryon asymmetry [257]. Typically in EWBG calculations, the wall curvature is neglected and the transport equations depend on a single coordinate $\bar{z}$ in the bubble wall rest frame, where $\bar{z} > 0$ (< 0) corresponds to broken (unbroken) phase. The solved baryon asymmetry density n_B is a constant inside the bubbles(see, e.g., [266]):

$$n_B = \frac{3\Gamma_{\rm ws}}{D_q \lambda_+} \int_0^{-\infty} n_L(\bar{z}) e^{-\lambda_- \bar{z}} d\bar{z} \quad , \tag{3.20}$$

where $s(T) = 2g_*\pi^2 T^3/45$ is the entropy density, $\Gamma_{\rm ws} \approx 120 \alpha_w^5 T$ is the weak Sphaleron rate in the EW symmetric phase [267], $\lambda_\pm = (v_+ \pm \sqrt{v_+^2 + 15\Gamma_{\rm ws} D_q})/(2D_q)$ with D_q the diffusion constant for quarks [267] and n_L is the chiral asymmetry

[5] For two-step EWPT, a small v_+ is not necessarily required for both steps of EWPT. However since v_w is otherwise an almost free parameter, we stick to the choice $v_+ = 0.05$ for both steps.

of left-handed doublet fields which serves as a source term in baryon asymmetry generation. The determination of n_L is a key part in EWBG calculations and is decoupled from the analysis of EWPT dynamics here. In above expression, we have replaced v_w by v_+, to take into account the distinction between these two velocities. If the temperature at which n_B is calculated is T_n, then after the bubbles have collided, the temperature of the plasma is given, to a good approximation, by T_* rather than T_n or T_c, which are conventionally used. The diluted baryon asymmetry is then given by

$$\frac{n_B}{s}|_{T=T_*} = \xi_D \frac{n_B}{s}|_{T=T_n}, \tag{3.21}$$

where $\xi_D \equiv (1+\kappa_T\alpha)^{-3/4}$ captures the dilution effect of the generated baryon asymmetry by reheating of the plasma. We then need to make sure that ξ_D does not become too small, since otherwise a stronger CP-violation will be needed, which might be excluded by the stringent limits from electric dipole moment searches [268, 269].

3.4.3 Stochastic Gravitational Waves

During the EWPT, bubbles of EW broken phase expand and collide with each other, which destroys the spherical symmetry of a single bubble, thus leading to the emission of gravitational waves [255]. Due to the nature of this process and according to the central limit theorem, the generated gravitational wave amplitude is a random variable which is isotropic, unpolarized and follows a Gaussian distribution. This therefore allows the description of gravitational wave

amplitude using its two-point correlation function and is parametrized by the gravitational wave energy density spectrum $\Omega_{\rm GW}(f)$, as a function of frequency f. A natural consequence is that the GWs produced during the EWPT, when redshifted to the present, give a peak frequency at around the mili-Hertz range [32], falling right within the band of future space-based gravitational wave detectors.

It is now well known that there are mainly three sources of gravitational wave production in this process: bubble wall collisions [270, 271, 272, 273, 274, 275], sound waves in the plasma [67, 68] and magneto-hydrodynamic turbulence (MHD) [67, 68]. The total energy density spectrum can be obtained approximately by adding these contributions:

$$\Omega_{\rm GW}h^2 \simeq \Omega_{\rm col}h^2 + \Omega_{\rm sw}h^2 + \Omega_{\rm turb}h^2. \tag{3.22}$$

Recent studies suggest that the energy deposited in the bubble walls is negligible, despite the possibility that the bubble walls can run away in some circumstances [276]. Therefore while a bubble wall can reach relativistic speed, its contribution to gravitational waves can generally be neglected [277]. We thus include only the contribution of sound waves and turbulence in the gravitational wave spectrum calculations.

The dominant contribution comes from sound waves. By evolving the scalar-field and fluid model on 3-dimensional lattice, the gravitational wave energy density spectrum can be extracted, with an analytical fit formula available [68]:

$$\begin{aligned}\Omega_{\rm sw}h^2 = 2.65\times10^{-6}\left(\frac{H_*}{\beta}\right)\left(\frac{\kappa_v\alpha}{1+\alpha}\right)^2\left(\frac{100}{g_*}\right)^{1/3}\\ \times v_w\left(\frac{f}{f_{\rm sw}}\right)^3\left(\frac{7}{4+3(f/f_{\rm sw})^2}\right)^{7/2}.\end{aligned} \tag{3.23}$$

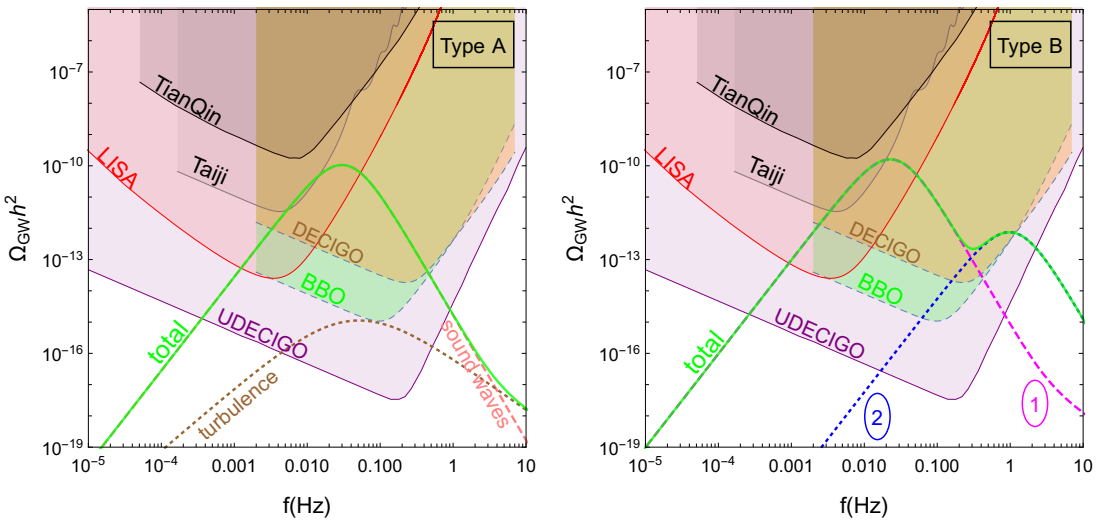

Figure 3.3: Examples showing GW energy density spectra from one step (left) and two-step (right) EWPT. For the left panel, the individual contributions from sound waves and magnetohydrodynamic turbulence are shown with their sum denoted by the green solid line. For the right panel, the total contributions from both the first step and second step are shown and with their sum denoted by the green solid line.

Here H_* is the Hubble parameter at T_* when the phase transition has completed. It has a value close to that evaluated at the nucleation temperature T_n for sufficiently short EWPT [25]. We take T_* to be the reheating temperature, defined earlier in Eq. 3.19. Moreover, $f_{\rm sw}$ is the present peak frequency which is the redshifted value of the peak frequency at the time of EWPT ($= 2\beta/(\sqrt{3}v_w)$):

$$f_{\rm sw} = 1.9 \times 10^{-5} \frac{1}{v_w} \left(\frac{\beta}{H_*}\right) \left(\frac{T_*}{100\text{GeV}}\right) \left(\frac{g_*}{100}\right)^{1/6} \text{Hz}, \tag{3.24}$$

where κ_v is defined in Eq. 3.18 and can be calculated as a function of (α, v_w) by solving the velocity profiles described in Sec. 3.4 [70]. It should be noted that a more recent numerical simulation by the same group [69, 71] shows a slightly

enhanced $\Omega_{\rm sw}h^2$ and reduced peak frequency $f_{\rm sw}$. We also note that the results from these simulations are currently limited to regions of small v_w and α and therefore their validity for ultra-relativistic v_w and large α (say $\alpha \gtrsim 1$) remains unknown. In the absence of numerical simulations for these choices of parameters at present, we assume that the results shown here apply for these cases and remind the reader to keep the above caveats in mind.

The fully ionized plasma at the time of EWPT can result in the formation of MHD turbulence, which gives another source of gravitational waves. The resulting contribution can also be modelled similarly with a fit formula [278, 279],

$$\begin{aligned}\Omega_{\rm turb}h^2 = 3.35\times10^{-4}\left(\frac{H_*}{\beta}\right)\left(\frac{\kappa_{\rm turb}\alpha}{1+\alpha}\right)^{3/2}\left(\frac{100}{g_*}\right)^{1/3}\\ \times v_w\frac{(f/f_{\rm turb})^3}{[1+(f/f_{\rm turb})]^{11/3}(1+8\pi f/h_*)},\end{aligned} \tag{3.25}$$

where $f_{\rm turb}$ is the peak frequency and is given by,

$$f_{\rm turb} = 2.7\times10^{-5}\frac{1}{v_w}\left(\frac{\beta}{H_*}\right)\left(\frac{T_*}{100{\rm GeV}}\right)\left(\frac{g_*}{100}\right)^{1/6}{\rm Hz}. \tag{3.26}$$

Here the factor $\kappa_{\rm turb}$ describes the fraction of energy transferred to the MHD turbulence and is given roughly by $\kappa_{\rm turb}\approx\epsilon\kappa_v$ with $\epsilon\approx 5\sim10\%$ [68]. We take $\epsilon = 0.1$ in this study.

In both Eq. 3.23 and 3.25, the value of v_w is found by requiring that $v_+ = 0.05$ by solving the velocity profiles, as discussed in the previous section. For the two-step EWPT, as discussed in last section, if both steps in case (B) and (C) are first order, then there would be two subsequent GW generation at generally different peak frequencies and amplitudes, corresponding to the example shown in the right panel of Fig. 3.3.

The detectability of the GWs is quantified by the signal-to-noise ratio (SNR), whose definition is given in Ref. [25]:

$$\mathrm{SNR} = \sqrt{\delta \times \mathcal{T} \int_{f_{\min}}^{f_{\max}} df \left[\frac{h^2 \Omega_{\mathrm{GW}}(f)}{h^2 \Omega_{\mathrm{exp}}(f)} \right]^2}. \tag{3.27}$$

Here $h^2\Omega_{\mathrm{exp}}(f)$ is the experimental sensitivity and corresponds to the lower boundaries of the color-shaded regions in Fig. 3.3 for the shown detectors [6]. $\mathcal{T}$ is the mission duration in years for each experiment, assumed to be 5 here. The factor δ comes from the number of independent channels for cross-correlated detectors, which equals 2 for BBO as well as UDECIGO and 1 for the others [280]. In our numerical analysis, we stick to the most mature LISA detector with the C1 configuration, defined in Ref. [25]. To qualify for detection, the SNR needs to be larger than a threshold value, which depends on the details of the detector configuration. For example, for a four-link LISA configuration, the suggested value is 50 while for a six-link configuration, this value can be much lower (SNR = 10), since in this case a special noise reduction technique is available based on the correlations of outputs from the independent sets of interferometers of one detector [25].

As an example, we scan over the EW vacuum stability regions in the plane $(v_s/v_{\mathrm{EW}}, b_3/v_{\mathrm{EW}})$ of Fig. 3.1 and found the regions which can give successful bubble nucleations, satisfy the SFOEWPT criterion and generate GWs. These regions are plotted with blue (SNR < 10), green ($50 >$ SNR > 10) and red (SNR > 50). Here most of the points give type (A) EWPT with only several points for type

[6] There are possible astrophysical foregrounds coming from, e.g., the superposition of unresolved (i.e., low SNR) gravitational wave signals of the white dwarf binaries in our Galaxy [23]. Including these will slightly reduce the SNR calculated here.

(B) or (C), denoted by diamond shapes.

3.5 Results and Discussions

In this section, we perform a full scan of the parameter space to address the following questions:

(a) What kind of EWPT patterns can this model admit and in what proportion of the parameter space for each pattern?

(b) What is the region of parameter space that can give strong detectable gravitational waves at future space-based gravitational wave detectors?

(c) Do current collider measurements of double Higgs production and searches for a heavy resonance decaying to weak boson pairs exclude the points that give strong gravitational waves and could future high luminosity LHC (HL-LHC) at 3ab^{-1} probe the parameter space giving strong gravitational waves?

(d) How will a future space-based gravitational wave experiment complement current and future searches for a heavy scalar resonance?

The full scan is performed using the input of the tadpole basis parameters with the following ranges for parameters:

$$\begin{aligned} &b_4 \in [0.001, 5], \qquad b_3/v_{\text{EW}} \in [-10, 10], \\ &a_2 \in [-2\sqrt{\lambda b_4}, 25], \quad \theta \in [-0.35, 0.35], \\ &m_{h_2} \in [260, 1000], \end{aligned} \tag{3.28}$$

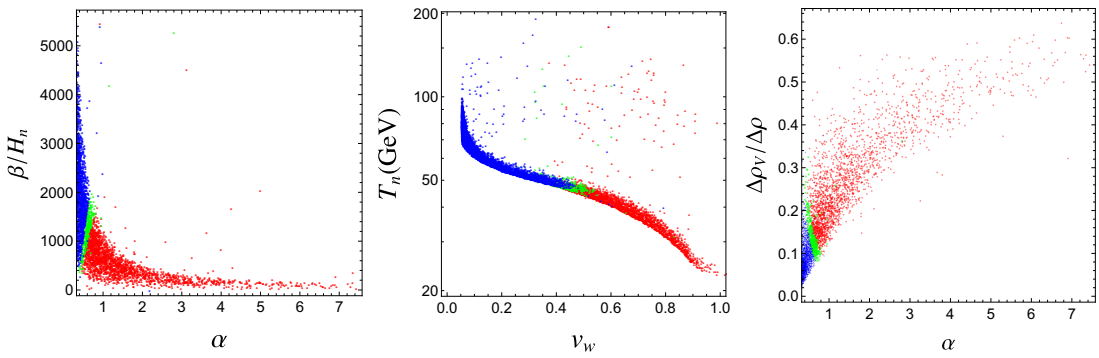

Figure 3.4: The physical parameters characterizing the dynamics of the EWPT: in the plane of $(\alpha, \beta/H_n)$ (left), (v_w, T_n) (middle) and $(\alpha, \Delta\rho_V/\Delta\rho)$ (right). In all these plots, the colors denote SNR > 50 (red), $50 >$ SNR > 10 and SNR < 10 (blue). Points depicted here pass all phenomenological constraints and give successful bubble necleations.

where the lower range of a_2 is determined by the requirement that the potential is bounded from below. The scan takes into account the previously discussed theoretical and phenomenological requirements. Points which pass these selection criteria are fed into `CosmoTransitions` [281] for calculating the thermal history and the parameters relevant for EWPT. Those which can give a successful EWPT by meeting the bubble nucleation criteria are further scrutinized for the EWPT type and SFOEWPT conditions. The final remaining points are used to calculate the gravitational wave spectra, the SNR and collider observables.

3.5.1 EWPT and GW

We first give the answer to question (a): *what kind of EWPT patterns can this model admit and in what proportion of the parameter space for each pattern ?*

We find, of the xSM parameter space where a successful EWPT can be

obtained, about 99% gives type (A) EWPT and the remaining slightly less than 1% can give type (B) EWPT. We do not observe type (C) EWPT. For type (A), 22% (19%) gives SNR larger than 10 (50). So there is a sufficiently large parameter space which can give detectable GW production.

The strength of the stochastic GW background is mainly governed by the two parameters α and β/H_n, where a larger α and a smaller β/H_n gives stronger GW SNR, as shown in the left panel of Fig. 3.4, where the colors denote SNR < 10 (blue), $50 >$ SNR > 10 (green) and SNR > 50 (red). We observe that the points which give detectable GWs lie in the bottom right region of the population.

Physically, α quantifies the amount of energy released during the EWPT and therefore a larger α gives stronger GW signals. In addition, for fixed v_w, a larger α leads to a larger fraction of energy transformed into the plasma kinetic energy, quantified by κ_v, and therefore a further gain in GW production. A further enhancement for larger α comes from the fact that since we fixed $v_+ = 0.05$, increasing α also increases v_w. It should be noted, even without an explicit calculation, that for each fixed value of α, the allowed values of v_w are limited to a certain range (see e.g., Fig. 1 in Ref. [249]). This comes from two considerations: (1) admitting consistent hydrodynamic solutions of the plasma imposes a lower limit on v_w; (2) v_w larger than $\xi_J(\alpha)$ gives a detonation mode of the velocity profile, in which case $v_w = v_+ > c_s$ and therefore v_+ is too large for EWBG to work. We further note that for $\alpha \gtrsim 1$ and $v_w \sim 1$, the calculations of the GW spectra may become unreliable for the following reasons: (i) While the study of Ref. [277] suggests that the energy stored in the scalar field kinetic energy is

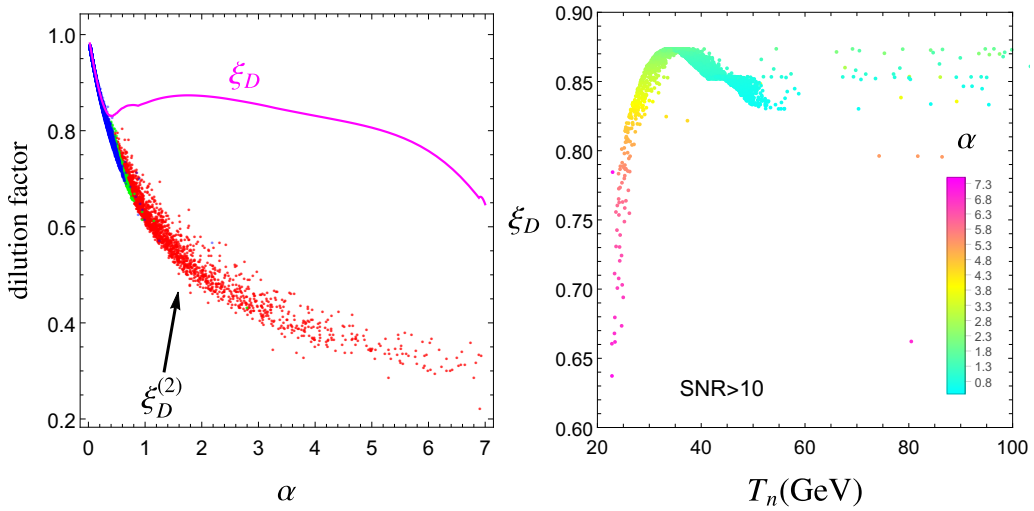

Figure 3.5: Figures showing the dilution effect of the baryon asymmetry. The left panel shows two different definitions of the dilution factor and the right panel shows the dilution factor ξ_D defined in Eq. 3.21 versus T_n.

negligible, a very large α might lead to a non-negligible contribution from the bubble collisions. Therefore a better understanding of the energy budget for this region is needed; (*ii*) the numerical simulations are all performed for relatively small α as well as v_w and thus the use of these results for large α and v_w may not be applicable; (*iii*) The universe is no longer radiation dominated at the EWPT but rather vacuum energy dominated. This has the consequence that bubbles might never meet to finish the EWPT and the universe would be trapped in the metastable phase (see Ref. [282] for a recent analysis). Despite these issues, we find 49% of points with SNR > 10 have $\alpha < 1$ and removing the points with $\alpha > 1$ does not change the main findings of our work.

We now turn to the parameter β/H_n, which roughly characterizes the inverse

time duration of the EWPT. A smaller β/H_n or equivalently a longer EWPT generates stronger GW signals. This is due to the particular feature of the GWs coming from the sound waves in the plasma. As was found in the original papers on the importance of sound waves in generating the GWs [67, 68], one enhancement comes from $1/(\beta/H_n)$ compared with the conventional bubble collision contribution. As long as the mean square fluid velocity of the plasma is non-negligible, GWs will continue being generated and the energy density of the GW is thus proportional to the duration fo the EWPT. It should be noted that β/H_n also determines the peak frequency of the GW spectra.

The bubble wall velocity v_w also plays an important role here and the dependence of the SNR on v_w is shown in the middle panel of Fig. 3.4, where the vertical axis is chosen to be T_n. It is clear that points with larger SNR have larger v_w since, for fixed v_+, a larger α implies a larger v_w. It can also be seen from this plot that the SNR increases as T_n decreases. This is easily understood, since a smaller T_n typically implies a larger amount of supercooling and therefore a larger α. The supercooling can be quantified by the fraction of the first term($\equiv \Delta\rho_V$) of Eq. 3.15 in the total released vacuum energy, which we plot in the right panel. We can see from this figure that larger SNR indeed implies larger amount of supercooling. However the amount of supercooling as quantified by $\Delta\rho_V/\Delta\rho$ is less than 0.6 for most of the parameter space. The remaining part comes from the second term of the definition of α.

The entropy production, if sizeable, can pose a problem for baryon asymmetry generation, as it will effectively dilute the baryon asymmetry n_B/s by increasing

s. In Sec. 3.4.2, we encode this effect in a dilution factor ξ_D. Here since κ_T is a function of v_w and α while v_w is also a function of α when v_+ is fixed, we find ξ_D is solely a function of α. This functional relation is shown as the magenta line in the left panel of Fig. 3.5 and all points from the scan fall on this line. The message from this figure is that most of the points have $\xi_D \gtrsim 0.65$ and those with a smaller α have a dilution factor closer to 1. In particular, the points with $\alpha \lesssim 1$ for which GW can be reliably calculated, the dilution effect is rather small as $\xi_D \gtrsim 0.8$. Given the current relatively large uncertainties in the EWBG calculations, the dilution effect poses no real problem for the baryon asymmetry generation. Note that previous studies [257] used a different quantification of the dilution factor, with the definition:

$$\xi_D^{(2)} = \frac{s}{s + \Delta s}, \tag{3.29}$$

where s is the entropy density at T_n and Δs is calculated from the second term in the definition of α in Eq. 3.15. To compare with the factor ξ_D, what we use here, we show values of this factor in the same plot of ξ_D for every point that gives detectable GWs. It is evident from this figure that these two factors are roughly the same and both decrease linearly for $\alpha \lesssim 0.4$. For $\alpha \gtrsim 0.4$, $\xi_D^{(2)}$ gives an overestimation of the dilution effect while ξ_D firstly increases a little bit before slowly dropping. Since the dilution factor we use here is based on a faithful hydrodynamic analysis, it gives a more precise description of the dilution effect. We also show ξ_D calculated for all the points versus T_n as a scatter plot in the right panel of Fig. 3.5, from which we find a larger dilution effect appears for

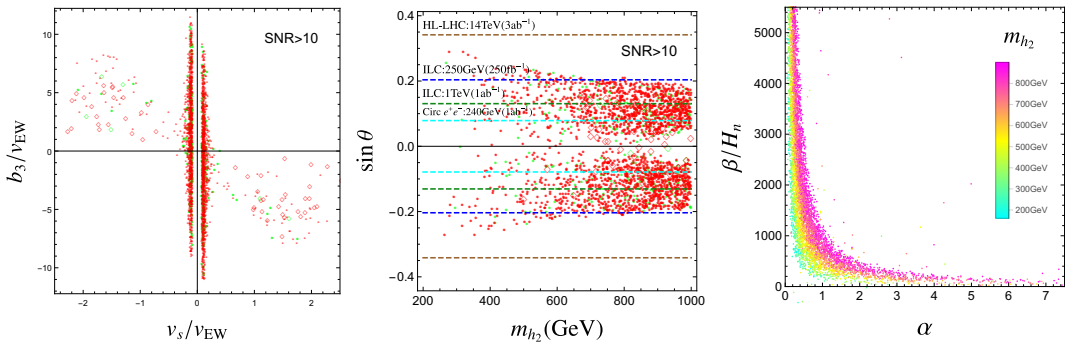

Figure 3.6: Points depicted here pass all phenomenological constraints and give successful bubble nucleations, along with detectable GWs at LISA (SNR $>$ 10). We show them in the planes of the input parameters: in plane $(b_3, v_s)/v_{\rm EW}$ (left) and $(\sin\theta, m_{h_2})$ (middle). We distinguish those points which give SNR $>$ 50 (red) with those of $50 >$ SNR > 10 (green) in these two plots. The right panel shows all the points in the plane $(\alpha, \beta/H_n)$ with the colors denoting the values of m_{h_2}, as shown in the legend.

typically smaller T_n and those with $\alpha \lesssim 1$ fall in the high T_n region.

The two-step EWPT, for which type (B) is the only observed here, constitutes about one percent of all the surviving parameter space. Of this tiny parameter space, more than half the points give detectable GWs.

3.5.2 Parameter Space Giving Detectable GWs

With a summary of the points described in previous section, we give in this section the answer to question (b), which, we recall, was: *What is the region of parameter space that can give strong detectable gravitational waves at future space-based gravitational wave detectors?*

The results are shown in terms of the three plots in Fig. 3.6. As was discussed in the previous section, a large α and small β/H_n leads to loud GW signals. Even though the relation between $(\alpha, \beta/H_n)$ and the physical input parameters is not transparent as many numerical details are involved, it can still be revealed by the plots in Fig. 3.6. From the left panel in Fig. 3.6, we can see that the majority of the points are concentrated in two regions of parameter space where v_s is rather small. In particular, we find $20\,\text{GeV} \lesssim |v_s| \lesssim 50\,\text{GeV}$ for most points, with a peak distribution at around 20 GeV. The appearance of two regions comes from the bounded-from-below requirement of the potential, similar to Fig.1. While phenomenological constraints have the effect of shrinking both the regions, the appearance of points far outside the two regions indeed shows that the main cause of the narrow regions comes from the requirements of EWPT and GWs. Therefore it is fair to say that the region that gives detectable GWs from a type (A) EWPT mainly comes from the parameter space with smaller v_s. On the other hand, the regions which provide type (B) EWPT are dramatically different from these regions, since most of the diamonds lie beyond the two narrow regions, as can be seen from the figure.

The middle figure shows these regions in the $(m_{h_2}, \sin\theta)$ plane. It is clear that the points are concentrated around the region with larger m_{h_2}. For smaller m_{h_2}, the density of points becomes much smaller. To have a better understanding of the role of m_{h_2} in GW production, we show in the right panel its role in determining $(\alpha, \beta/H_n)$, denoted by the colors. In this figure, the points are separated into different bands characterized by the value of m_{h_2}. For fixed β/H_n, a larger m_{h_2}

gives a larger α, thus larger SNR. This explains the concentration of the points in the m_{h_2} direction in the middle figure. In the $\sin\theta$ direction, the value of θ is more constrained for larger m_{h_2}. The outer boundary comes mainly from the W-mass constraint. The requirements from EWPT and larger GW signals also show their effects in this plot. For example, very small values of θ give rarer points. We also overlaid on this plot the various sensitivity projections from colliders in probing the value of θ, which includes HL-LHC, ILC with two configurations (ILC-1: 250GeV, 250fb^{-1}, ILC-3: 1TeV,1ab^{-1}) and future circular e^+e^- colliders (240GeV, 1ab^{-1}), all taken from Ref. [84]. We see that HL-LHC can barely probe any points; ILC-1 can probe a fraction of the small m_{h_2} points as well as a few large m_{h_2} points; ILC-3 can probe about a half of both light and heavy h_2 points; the future circular colliders can probe even more of the parameter space. We also can see that most of the points coming from the two-step EWPT lie at the very small θ region, even though a few do have larger θ. Therefore GW detections serve as a complementary probe of this region. We also note that for very small values of θ and m_{h_2}, the search for long lived particles can be used to probe this region (eg., the MATHUSLA detector) [283].

3.5.3 Correlation with Double Higgs Production Searches

Exploring possible deviations from the expected SM value of the cubic Higgs coupling through di-Higgs production is an important target of the HL-LHC. New physics scenarios, especially those designed for providing a SFOEWPT for baryon asymmetry generation, typically modify this coupling. Therefore di-Higgs

production is correlated with EWPT and thus GW production. Future GW and collider experiments can then operate in a way that complement each other in exploring new physics scenarios. With the parameter space giving detectable GW identified in the previous section, we can find the correlation by calculating the corresponding di-Higgs cross sections and compare it with present di-Higgs measurements and with future projections.

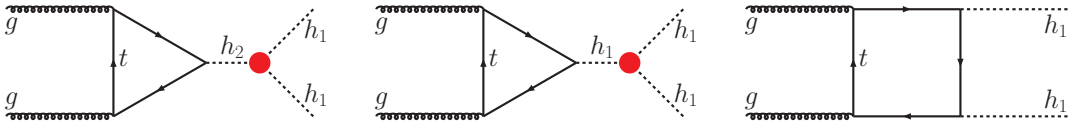

Figure 3.7: Representative resonant (left) and non-resonant (middle and right) Feynman diagrams contributing to di-Higgs production.

The leading order Feynman diagrams for double Higgs production occur at one-loop and consist of both the resonant and non-resonant channels, as shown in Fig. 3.7. The non-resonant channel includes the box diagrams and a triangle diagram involving the vertex $h_1h_1h_1$. The resonant channel is the production of a on-shell h_2 which subsequently decays into two Higgs, thus including the $h_2h_1h_1$ vertex. The amplitude at leading order was given in the early papers [284, 285] with the result expressed in terms of Passarino-Veltman scalar integrals. This result has also been implemented into `MadGraph` [286] taking into account the presence of a heavier SM-like scalar [7], which we use for calculating the corresponding cross sections for each point shown here. This takes as input the modified Higgs top Yukawa coupling, the Higgs trilinear coupling, the heavy scalar top coupling, the

[7] https://cp3.irmp.ucl.ac.be/projects/madgraph/wiki/HiggsPairProduction

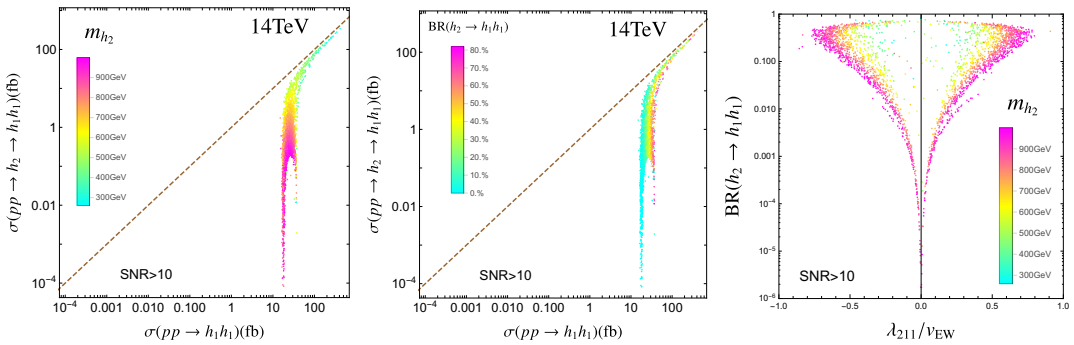

Figure 3.8: Resonant contribution to the cross section for di-Higgs production, versus the total cross-section. The left plot shows the correlation of the two cross sections, with the colors denoting values of m_{h_2}. The middle plot has the colors switched to the branching ratio of $h_2 \to h_1 h_1$. The right plot shows this branching ratio versus the trilinear coupling $h_2 h_1 h_1$, where the color denotes m_{h_2}. In the left two plots, the dashed line denotes the place where these two cross sections are the same.

$h_2 h_1 h_1$ coupling and the mass as well as the decay width of h_2. Since h_2 decays into SM particles with reduced coupling $(-\sin\theta)$ as compared with the SM Higgs and also decays to a pair of h_1, the total width is simply given by:

$$\Gamma_{h_2} = \sin^2\theta\, \Gamma_{\rm SM}(h_2 \to X_{SM}) + \Gamma(h_2 \to h_1 h_1), \tag{3.30}$$

where $\Gamma_{\rm SM}(h_2 \to X_{SM})$ denotes an exact SM Higgs-like h_2 decaying into the SM particles.

For the di-Higgs production, if the resonant production of $h_1 h_1$ via the h_2 resonance dominates the cross section, then the cross section can be written in the narrow width approximation as

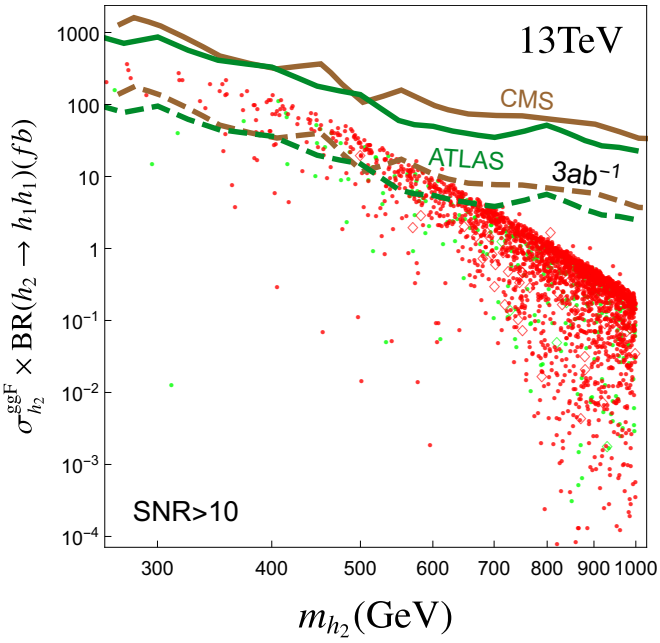

Figure 3.9: The upper limits on di-Higgs resonant production cross section from ATLAS and CMS combined searches, shown as solid green and brown lines for ATLAS and CMS, respectively. The dashed lines denote the corresponding future projections for 3ab^{-1} of data at the HL-LHC (13TeV). As in the other plots, we distinguish those points which give SNR $>$ 50 (red) and those of 50 $>$ SNR $>$ 10 (green).

$$\sigma(pp \to h_1 h_1) = \sigma(pp \to h_2)\mathrm{BR}(h_2 \to h_1 h_1). \tag{3.31}$$

In reality, interference effects between the resonant and non-resonant diagrams may be important and lead to constructive or destructive effect on the final full cross section [236]. We thus compare, for each scanned point, the obtained cross section for both the full calculation and the above approximation from the purely resonant production. This is shown in the left and middle plots of Fig. 3.8 for $\sigma(pp \to h_1 h_1)$ versus $\sigma(pp \to h_2 \to h_1 h_1)$ for all the points which give

detectable GW signals, that is, those with SNR > 10. These cross sections are both calculated at leading order but we have added a common K-factor of 2.27 to take into account of higher order corrections. The colors in the left panel denote the values of m_{h_2} and those in the middle denote BR($h_2 \to h_1 h_1$). It is clear from these figures that the resonant cross section is always less than the full one-loop result and drops sharply as m_{h_2} is increased (left panel). Since, as we have seen in previous sections, the points with large SNR are concentrated around the region with larger m_{h_2}, most of the points with detectable GWs turn out to give small di-Higgs production and even negligible resonant production. The colors in the left panels make it clear that most of the points which have larger m_{h_2} (and larger SNR) tend to give very small di-Higgs production, with a cross section of $\mathcal{O}(10)$fb, while smaller m_{h_2} gives $\mathcal{O}(100)$fb. Moreover, there is a sharp drop of the resonant production cross section. From the middle panel, we can see that the color of decreasing branching ratio $h_2 \to h_1 h_1$ coincides partly with increasing m_{h_2} for the very large m_{h_2} points. The small branching ratio is found for a majority of points and is due to the smallness of λ_{211}. This can be seen from the right panel, where this correlation is shown with the color denoting m_{h_2}. It is found that a majority of points which have large m_{h_2} give small branching ratio. This can partly explain the cause of the drop of the resonant production.

On the experimental side, both the ATLAS and CMS collaborations have recently published their search results for non-resonant and resonant di-Higgs productions using the data collected in 2016 at 13 TeV, with nearly the same integrated luminosity. The CMS search result is based on the 35.9fb^{-1} data,

in the di-Higgs decay channels $b\bar{b}\gamma\gamma$ [287], $b\bar{b}\tau^+\tau^-$ [288], $b\bar{b}b\bar{b}$ [289, 290, 291, 292] and $b\bar{b}WW/ZZ$ [293], with a recent combination given in [294]. ATLAS used 36.1fb^{-1} data and searched in channels $\gamma\gamma b\bar{b}$ [295], $b\bar{b}\tau^+\tau^-$ [296], $b\bar{b}b\bar{b}$ [297], $WW^{(*)}WW^{(*)}$ [298] and $b\bar{b}WW^*$ [299], with also a combination of the first three channels [300]. We use the ATLAS and CMS combined limits in the resonant production channels and show them with green and brown solid lines respectively in Fig. 3.9. For the points giving detectable GWs, we calculate the resonant cross sections from gluon fusion at NNLO+NNLL using the available result in Ref. [301]. We can see that none of the points with detectable GW gives cross section above this limit. With the anticipation of HL-LHC at a luminosity of 3ab^{-1} (13TeV), we can get the future projections of this limit by a simple rescaling and obtain the two dashed lines. For this projection, the region with lower $m_{h_2} \lesssim 550$GeV can be partly explored by CMS and a little bit higher for ATLAS, while the high mass region remains out of reach for di-Higgs searches. Yet, Some points of the scanned parameters space with observable SNR show a promising di-Higgs production cross section of 50 fb or more at the LHC which, in principle, can be probed with 3 ab^{-1}. Therefore GW measurements can complement collider searches by revealing the high m_{h_2} region of the xSM model.

3.5.4 Higgs Cubic and Quartic Couplings

Future precise measurements of the Higgs cubic and quartic self-couplings can be used to reconstruct the Higgs potential to confirm ultimately the mechanism

of EW symmetry breaking [8] and shed light on the nature of the EWPT. The measurements of above double Higgs production can be used to determine the cubic coupling and there have been extensive studies on this topic [1]. The best sensitivities obtained for these future colliders is typically at $\mathcal{O}(1)$. Despite the more formidable challenges with the quartic coupling measurement, there is now growing interest in it. Several different methods have been proposed and studied: through triple Higgs production measurement [228], through double Higgs production at hadron colliders where the quartic coupling enters $gg \to hh$ at two-loop [230] or renormalizes the cubic coupling, and at lepton colliders(via Z-associated production $e^+e^- \to Zhh$ and VBF production $e^+e^- \to \nu\nu hh$), where the quartic coupling is involved in the $VVhh$ coupling at one loop [2]. For example, Ref. [2] found a precision of measurement of $\sim \pm 25$ for $(500\text{GeV}, 4\text{ab}^{-1} + 1\text{ TeV}, 2.5\text{ab}^{-1})$ and $\sim \pm 20$ for $(500\text{GeV}, 4\text{ab}^{-1} + 1\text{ TeV}, 8\text{ab}^{-1})$ at 1σC.L., when the cubic coupling is marginalized in their χ^2 analysis.

In the xSM, both the Higgs cubic and quartic couplings are modified compared with their SM counterparts:

$$\begin{aligned} i\lambda_{h_1h_1h_1} = 6\Big[&\lambda v c_\theta^3 + \frac{1}{4}c_\theta^2 s_\theta \left(2a_2 v_s + a_1\right) + \frac{1}{2}a_2 v c_\theta s_\theta^2 \\ &+ \frac{1}{3}s_\theta^3 \left(3b_4 v_s + b_3\right)\Big], \end{aligned} \tag{3.32}$$

$$i\lambda_{h_1h_1h_1h_1} = 6(\lambda c_\theta^4 + a_2 s_\theta^2 c_\theta^2 + b_4 s_\theta^4). \tag{3.33}$$

In the absence of mixing of the scalars($\theta = 0$), these couplings reduce to the corresponding SM values $i\lambda_{h_1h_1h_1} = 3m_{h_1}^2/v$ and $i\lambda_{h_1h_1h_1h_1} = 3m_{h_1}^2/v^2$. When

[8] The Lorentz structure of hWW coupling already gave us some insight about the nature of EW symmetry breaking at the leading order.

$\theta \neq 0$, we parametrize the deviations of these couplings from the SM values as:

$$\Delta\mathcal{L} = -\frac{1}{2}\frac{m_{h_1}^2}{v}(1+\delta\kappa_3)h_1^3 - \frac{1}{8}\frac{m_{h_1}^2}{v^2}(1+\delta\kappa_4)h_1^4, \tag{3.34}$$

and show in Fig. 3.10 these values for the points that give detectable GWs. The features that we can read from this figure are:(1) both $\delta\kappa_3$ and $\delta\kappa_4$ are positive; (2) both variations are $\mathcal{O}(1)$ as $\delta\kappa_3 \in (0,1)$ and $\delta\kappa_4 \in (0,4)$. (3) a correlation exists $\delta\kappa_4 \equiv \eta\delta\kappa_3$, with $\eta \approx 2.8$ for $\delta\kappa_3 \lesssim 0.4$ and most points fall within $\eta \in (2,4)$. To understand these, we note, since phenomenological constraints requires a small θ, we expect the second feature to follow naturally. The other features can be understood by Taylor expanding the couplings for small θ and we find:

$$\begin{aligned}
\delta\kappa_3 &= \theta^2\left[-\frac{3}{2} + \frac{2m_{h_2}^2 - 2b_3v_s - 4b_4v_s^2}{m_{h_1}^2}\right] + \mathcal{O}(\theta^3), \\
\delta\kappa_4 &= \theta^2\left[-3 + \frac{5m_{h_2}^2 - 4b_3v_s - 8b_4v_s^2}{m_{h_1}^2}\right] + \mathcal{O}(\theta^3).
\end{aligned} \tag{3.35}$$

In the above square brackets, the terms proportional to $m_{h_2}^2/m_{h_1}^2$ dominate for the majority of the points since v_s is concentrated at small values; b_3 is at most $\sim 10v_{\rm EW}$, $b_4 \lesssim 5$ from the scan and $m_{h_2} \gtrsim 500$GeV generally holds. Then the above approximations show positive $\delta\kappa_3$ and $\delta\kappa_4$ and give $\delta\kappa_4/\delta\kappa_3 \approx 2.5$, which is fairly close to $\eta = 2.8$. For relatively large θ, high order corrections need to be taken into account and above linear correlation would be changed.

To compare with the direct measurements of these couplings at future e^+e^- colliders and the HL-LHC, we added in Fig. 3.10 the precisions of these measurements from studies in the literature. The two elliptical 68%CL closed contours are taken from Ref. [2] which focuses on the quartic coupling, for two possible

scenarios of the ILC. The bars are the precisions that can be reached from various considerations of future colliders, labelled on the right of the figure, taken from Ref. [1](for other studies, see e.g. [302, 230, 303, 304, 302, 305]). Here the inner and outer bar regions denote the 68%CL and 95%CL results. We can see, it is generically very hard for colliders to probe the cubic coupling at a precision that can reveal the points giving detectable GWs with high confidence level(say 95%) [9]. The most precise comes from the ILC when all possible runs at different luminosities are combined and with the data of HL-ILC included, which gives $0.4 \sim 0.5$ uncertainty on the measurement of $\delta\kappa_3$ at 95%CL. While the analysis in Ref. [1] does not include the quartic coupling, the contours from Ref. [2] do give a hint on its measurement and show that it is infeasible for the colliders to probe the parameter space giving detectable GWs. For the trilinear and quartic coupling deviations that we found, the impact on the triple Higgs cross section is mild for hadron colliders even for a future pp collider at 100 TeV [228, 229], however, resonant contributions in xSM might enhance the cross section up to a factor of $\mathcal{O}(10)$ [306].

Therefore we expect future GW measurements can make a valuable complementary role in determining the Higgs self-couplings, especially the quartic coupling. While we do not have a statistical analysis here, Fig. 3.10 does tell us

[9]It should be noted that both studies used some versions of the effective field theory approach to quantify the modification of the SM couplings due to possible new physics effects. Therefore the precisions overlaid in Fig. 3.10 might not be what the colliders can achieve if the xSM model was used in their studies. However we expect the two contours, taken from Ref. [2], to be largely unaffected since the heavier scalar contribution in their framework is suppressed by extra powers of s_θ. We also expect that the bar regions, taken from Ref. [1], would get tighter since the set of parameters used in their study are highly correlated here.

that $\delta\kappa_4$ is equally important as $\delta\kappa_3$ on GW signal generation since η is at most 4. Thus we expect a full statistical analysis would yield roughly the same precision on the determination of $\delta\kappa_3$ and $\delta\kappa_4$, which is well improved compared with the situation at colliders.

3.5.5 Diboson Resonance Search Limits at Colliders

The WW and ZZ branching ratios become sizeable in parts of the parameter space where the trilinear coupling λ_{211} is relatively small, as one can see from the rightmost panel of Fig. 3.8. In Fig. 3.11, we show the branching ratios of the $h_2 \to WW, ZZ$ and $h_2 \to h_1 h_1$ channels. We see that the WW, ZZ channels can be as big as 90% for a large range of h_2 masses which could show up at searches for weak diboson resonances. Combined, WW, ZZ and $h_1 h_1$ correspond to nearly all the decays of h_2, which make them the best search channels for h_2 resonances at colliders.

Besides the di-Higgs production measurements, which can be used to extract the Higgs cubic and quartic couplings, there also exist generic scalar resonance searches at the LHC. In particular, ATLAS and CMS have performed extensive analyses in the searches for a heavier SM-like scalar resonance in VV and VH decay channels of the heavy scalar ($V = W/Z$). ATLAS gives a recent combination of all previous analyses in bosonic and leptonic final states at $\sqrt{s} = 13\text{TeV}$ with 36fb^{-1} data collected in 2015 and 2016 [307]. The limits are drawn for h_2 production cross section in gluon fusion and vector boson fusion production channels. These two limits are shown in the left and right panels, respectively, in Fig. 3.12 with green

solid lines, together with the detectable GW points. For cross section calculations, we use the set of result calculated to NNLO precision for VBF and for gluon fusion, we use NNLO+NNLL, as also used before in Fig. 3.9.

It is evident that the current limits from diboson searches are rather loose as most points fall under this line, with gluon fusion limit being able to touch a fraction of the lighter h_2 point. For the HL-LHC with $\sim 3\text{ab}^{-1}$, we obtain estimates of future projections by a simple scaling factor and obtain the dashed lines for $\sim 3\text{ab}^{-1}$ at 13TeV (while HL-LHC would probably run at 14TeV). We can see in all cases that the HL-LHC will probe a larger fraction of the parameter space for both ggH and VBF channels. For ggH, this region covers a range from low to high masses. For VBF, it can cover a region of relatively heavy h_2. Both channels are sensitive to h_1h_1 cross section times branching ratio down to ~ 1 fb in some favorable points of the parameters space. The points that can be probed by HL-LHC serve as promising targets for both colliders and GW detectors but a majority of the parameter space will probably be left to GW detectors.

3.6 Summary

In this paper, we embarked on a study of the singlet-extended SM Higgs sector. A detailed scan of the parameter space of this model was performed, incorporating all relevant phenomenological constraints, and regions with large SNR at LISA were identified. Subtle issues pertaining to the bubble wall velocity were discussed, and a range of velocity profiles described.

Our main findings are the following. For the parameter space that satisfies all phenomenological constraints, gives successful EWPT and generates GWs, 99% leads to a one-step EWPT with the remaining to two-step EWPT and 22% generates detectable GWs(SNR > 10) at LISA. The main features of the parameter space that gives detectable GWs is: $20\text{GeV} \lesssim |v_s| \lesssim 50\text{GeV}$, where v_s is the vev of the singlet field; it is more concentrated in the large m_{h_2} region, where m_{h_2} is the mass of the heavier scalar h_2; $\theta \lesssim 0.2$ for the majority of the space. Di-Higgs searches at both ATLAS and CMS are currently unable to probe this parameter space, but HL-LHC will be able to probe the lighter h_2 region while the heavier h_2 region will remain elusive. Weak diboson resonance searches cannot constrain xSM much either but the HL-LHC will be able to probe a large fraction of its parameters space in this channel. The Higgs cubic and quartic couplings are at $\mathcal{O}(1)$ deviations from the SM values and obey a relation $\delta\kappa_4 \approx (2-4)\delta\kappa_3$, where $\delta\kappa_4$ and $\delta\kappa_3$ are the relative deviations of the quartic and cubic couplings from their SM counterparts respectively.

Our results broadly indicate that high energy colliders and GW detectors are going to play complementary roles in probing the parameter space of scalar sectors. Several future directions can be contemplated. It would be interesting to understand how this complementarity plays out in two Higgs doublet models, as well as other scalar sector extensions classified in [198]. It would also be interesting to investigate the complementarity of GW and collider probes for phase transitions in the dark sector. We leave these questions for future study.

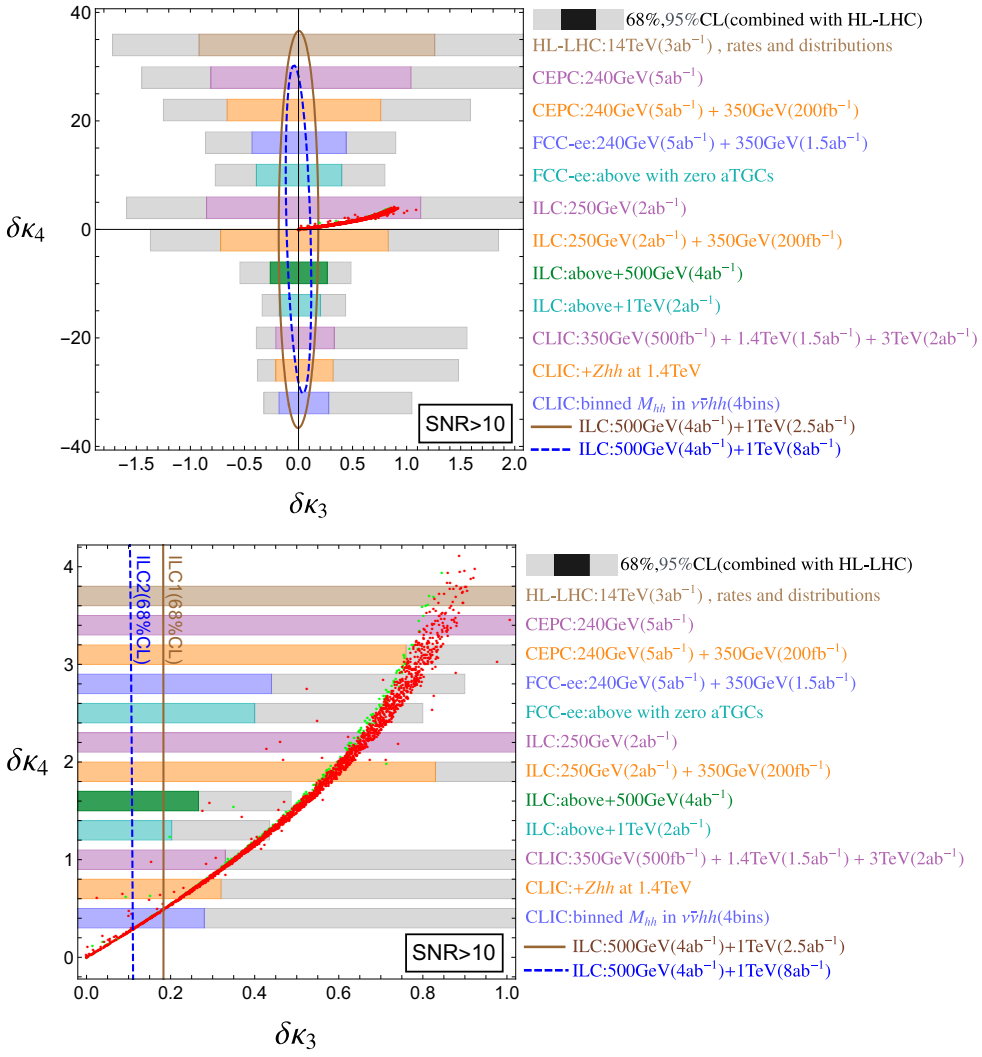

Figure 3.10: The Higgs cubic and quartic couplings $(\Delta\kappa_3, \Delta\kappa_4)$ for parameter space points giving detectable GW. Here the green points give SNR > 10 and the red gives SNR > 50. The bars denote the sensitivity of $\Delta\kappa_3$ from a global analysis of future colliders in Ref. [1], for various detector scenarios shown on the right side of the figures. The brown solid and blue dashed lines are the 1σ contours for two different ILC scenarios taken from Ref. [2]. The bottom panel is a zoomed-in version of the top one.

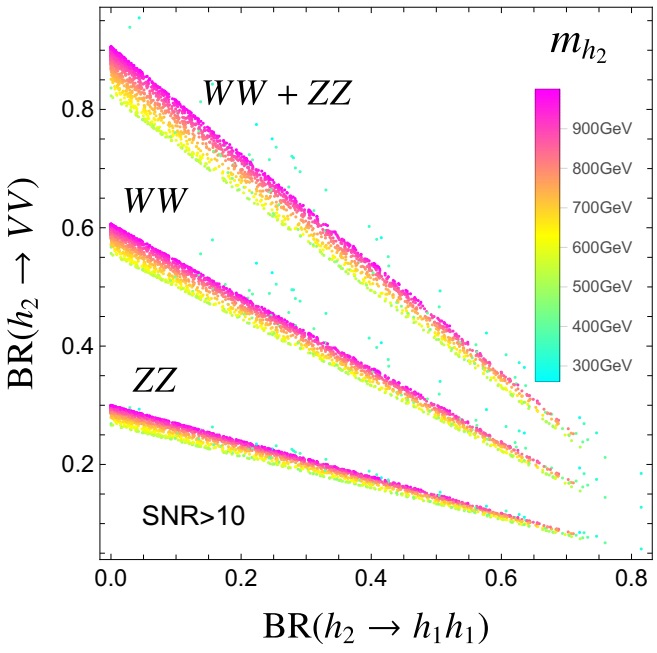

Figure 3.11: The branching ratios of h_2 in $h_1 h_1$ and VV final states, where $VV = WW, ZZ, WW + ZZ$, with the color denoting the value of m_{h_2}.

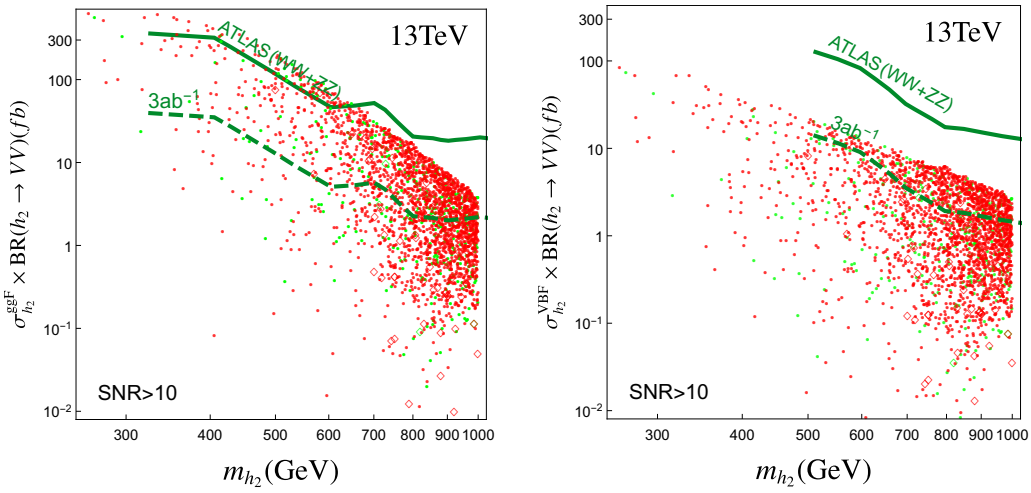

Figure 3.12: Combined limits from ATLAS (solid line) and future HL-LHC projections (dashed line) for searches of a heavy SM-like resonance in the WW/ZZ channel from gluon fusion (left) and vector boson fusion production (right). As in the other plots, we distinguish those points which give SNR $>$ 50(red) and those of 50 $>$ SNR $>$ 10(green).

Chapter 4

Phase Transitions in an Expanding Universe

4.1 Introduction

The first major goal of this paper is to undertake a careful analysis of the gravitational wave power spectrum in a generic expanding universe. This is necessary, since the standard result for the spectrum is obtained in Minkowski spacetime where the effect of the expansion of the universe is neglected. In the Minkowski spacetime, the spectrum is proportional to $H_*\tau_{\rm sw}$ as derived in Ref. [68], where the generalization to the expanding universe with radiation domination was also carried out based on rescaling properties of the fluid. It was concluded that the effective lifetime of the sound waves is a Hubble time when comparing this spectrum with that derived in the Minkowski spacetime. The reason that this conclusion was reached is due to the absence of the term $H_*\tau_{\rm sw}$ in the spectrum for radiation dominated universe and the otherwise very similar form as in Minkowski spacetime (see Appendix B for a re-derivation of this result). Later studies suggest that the lifetime generally is smaller than a Hubble time such that $H_*\tau_{\rm sw} < 1$ [42, 282, 308, 10]. This, when combined with the Minkowski result that the spectrum is proportional to $H_*\tau_{\rm sw}$, leads to the conclusion that there is a suppression of the spectrum when compared with the case when $H_*\tau_{\rm sw} = 1$ is used. We note in retrospect that the spectrum found in above radiation dominated universe is obtained assuming actually an infinite lifetime of the source, i.e.,

$\tau_{\rm sw} \to \infty$ and the correct dependence on $\tau_{\rm sw}$ is a different one. It is the purpose of this paper to provide an accurate $\tau_{\rm sw}$ dependence for the spectrum and show its implications. Moreover the role of the expansion in the process of the phase transition and in the calculation of the spectrum has not been fully revealed. We thus present a comprehensive and very careful analysis of the spectrum, clarifying subtle issues when the calculation is generalized from Minkowski spacetime to an expanding universe, and ultimately providing an accurate spectrum in a standard radiation dominated universe and in other expansion scenarios. We also perform a detailed calculation of the nucleation and growth of bubbles in an expanding background, including tracking the shrinking volume available for new bubbles to nucleate in as well as the total area of uncollided walls. Both are needed for an accurate understanding of how the volume fraction and mean bubble separation evolve throughout the phase transition. We then derive and solve the equations governing the evolution of the fluid velocity field in an expanding Universe and then proceed to a derivation of the spectrum for different expansion scenarios.

The second major goal of this paper is encapsulated in the title: after having calculated the gravitational wave spectrum in an expanding universe, we want to explore the extent to which the phase transition can distinguish between *different expansion histories*. In other words, we would like to interrogate how well a phase transition can serve as a *cosmic witness*. This is important, since growing evidence suggests that the standard assumption of radiation domination prior to Big Bang Nucleosynthesis may be too naive [309, 310]. An early matter dominated era, for example, is motivated by the cosmological moduli problem [311, 312, 313, 314],

hints from dark matter searches [315, 316, 317, 318, 319, 320, 321, 322, 323], and perhaps even baryogenesis [324]. Another possibility of a non-standard expansion history is kination, which we do not cover in this paper but can be explored by our methods [325, 326, 327, 328, 329, 330, 331, 332, 333, 334]. We note that gravitational waves have been previously employed to investigate early universe cosmology [335, 336, 197, 337, 338, 339].

Our goal is to provide a general theoretical framework to calculate the gravitational wave spectrum in different cosmic expansion histories. This includes scrutiny for changes in different aspects. The dynamics of the phase transition in an expanding universe is studied in Sec. 4.3, the velocity field power spectrum is calculated in Sec. 4.4 and the gravitational wave spectrum in Sec. 4.5. The main findings of the first two aspects are as follows.

1. The mean bubble separation R_* is related to β through a generalized relation for the exponential nucleation (Eq. 4.77):

$$R_*(t) = \frac{a(t)}{a(t_f)}(8\pi)^{1/3}\frac{v_w}{\beta(v_w)}, \tag{4.1}$$

   where t_f is the time when the false vacuum fraction is $1/e$, at which $\beta(v_w)$ is evaluated, and $\beta(v_w)$ can vary by $\sim 20\%$ for different v_w. This relation is also confirmed by numerical calculations and is accurate up to an uncertainty of 2%. If one uses the conformal version of R_* and β, then they satisfy the same relation as in Minkowski spacetime (see Eq. 4.73).

2. We derived the bubble lifetime distribution in a generic expanding universe in Eq. 4.56, and the conformal lifetime $\eta_{\rm lt}$ rather than ordinary lifetime $t_{\rm lt}$

should be used. It coincides with the distribution $e^{-\widetilde{T}}$ found in Minkowski spacetime [3] for exponential nucleation.

3. We derived the full set of differential equations in an expanding universe for the fluid and order parameter field model as used in numerical simulations. We find that in the bubble expansion phase the full field equations do not admit rescalings of the quantities that would reduce the expressions to their counterparts in Minkowski spacetime; this rescaling does, however, work in the bag equation of state model. This implies the velocity profile maintains the same form when appropriate rescalings and variable substitutions are used.

4. We generalized the sound shell model to an expanding universe and calculated the velocity field power spectrum [71, 3].

For the gravitational wave energy density spectrum, the main results are:

1. The peak amplitude of the gravitational wave spectrum visible today has the form (see Eq. 4.172)

$$h^2\Omega_{\rm GW} = 8.5\times10^{-6}\left(\frac{100}{g_s(T_e)}\right)^{1/3}\Gamma^2\bar{U}_f^4\left[\frac{H_s}{\beta(v_w)}\right]v_w\times\Upsilon. \tag{4.2}$$

Here $\Gamma\sim 4/3$ is the adiabatic index, $g_s(T_e)$ is the relativistic degrees of freedom for entropy at T_e when the gravitational wave production ends, $\bar{U}_f$ is the root mean square fluid velocity (see Fig. 4.18), v_w is the wall velocity, H_s is the Hubble rate when the source becomes active, and Υ is the suppression factor arising from the finite lifetime, $\tau_{\rm sw}$, of the sound waves.

For radiation domination, it is given by

$$\Upsilon = 1 - \frac{1}{\sqrt{1 + 2\tau_{\rm sw} H_s}}, \tag{4.3}$$

where the standard spectrum generally used corresponds to the asymptotic value $\Upsilon = 1$ when $\tau_{\rm sw} H_s \to \infty$. However the onset of non-linear shocks and turbulence which can disrupt the sound wave source occurs at around $\tau_{\rm sw} H_s \sim H_s R_* / \bar{U}_f$. This means the asymptotic value will not be reached and there is a suppression to the standard spectrum. In Fig. 4.1 we compare our result with the suppression factor recently proposed in [42] (see also [282, 308]). Similarly, the spectrum for matter domination has also been derived in our work and a similar suppression factor Υ is observed, which has an asymptotic value of 2/3.

2. We find a change to the spectral form, depending upon whether the phase transition occurs during a period of matter or radiation domination. The change in the form is not leading order, due to the fact that the velocity profiles remain largely unchanged and that the autocorrelation time of the source is much smaller than the duration of the transition. This is in contrast to gravitational waves generated from cosmic strings [339]. Even then, the modification of the spectrum presents an enticing possibility that the gravitational waves formed during a phase transition can bear witness to an early matter dominated era. We leave a further detailed exploration of the change of the spectral form for future work.

The remainder of this paper is organized as follows. We firstly lay out the

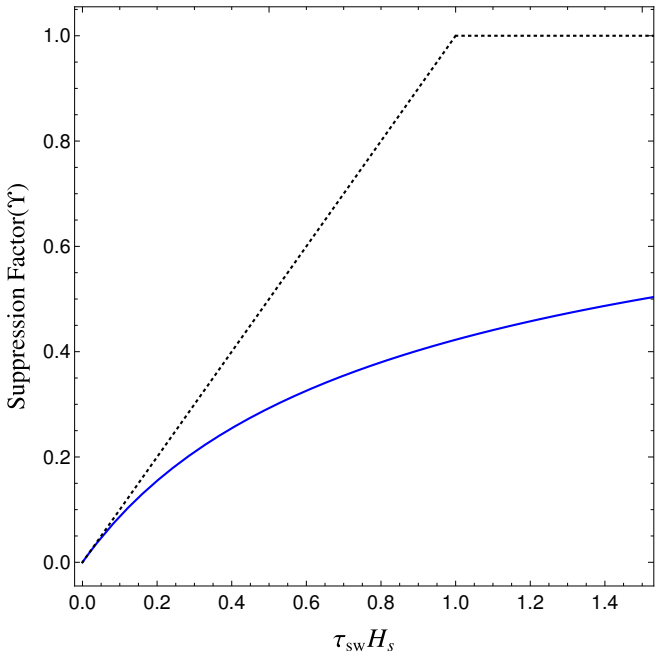

Figure 4.1: The suppression factor (blue solid line) as a function of the lifetime of the dominant source, the sound waves, in unit of the Hubble time at t_s, the time when the source becomes active. The black dashed line denotes $\mathrm{Min}(\tau_{\rm sw}H_s, 1)$.

theoretical framework for the stochastic gravitational wave calculation in the next Sec. 4.2 and study the details of the phase transition dynamics in an expanding universe in Sec. 4.3. After that, we summarize the full set of fluid equations applicable in an expanding universe and study the velocity profile as well as the velocity power spectrum using the sound shell model in Sec. 4.4. We then analytically calculate the gravitational waves from sound waves in both radiation dominated and matter dominated scenarios in Sec. 4.5. We summarize our results in Sec. 4.6.

4.2 Theoretical Framework

In this section, we set up the framework for calculating the stochastic gravitational waves in the presence of a source, which also serves to define our notation. The power spectrum of the gravitational waves, as will be discussed, depends on the unequal time correlator of the source. Therefore this correlator is of central importance in this work and is discussed in the second subsection.

4.2.1 Gravitational Waves

The gravitational wave is the transverse traceless part of the perturbed metric. Neglecting the non-relevant scalar and vector perturbations, the metric is defined in the FLRW universe as:

$$ds^2 = -dt^2 + a(t)^2(\delta_{ij} + h_{ij}(\mathbf{x}))d\mathbf{x}^2, \tag{4.4}$$

where h_{ij} is only the transverse traceless part of the perturbed 3×3 metric matrix (see, e.g., [340] for a detailed discussion). It is convenient, most often, to work in Fourier space, with the following convention:

$$h_{ij}(t, \mathbf{x}) = \int \frac{d^3q}{(2\pi)^3} e^{i\mathbf{q}\cdot\mathbf{x}} h_{ij}(t, \mathbf{q}), \tag{4.5}$$

where $\mathbf{q}$ is the comoving wavenumber, in accordance with the comoving coordinate $\mathbf{x}$. The physical coordinate is $a\mathbf{x}$ and the physical wavenumber is $\mathbf{q}/a$. The Fourier component $h_{ij}(t, \mathbf{q})$ is thus of dimension -3.

Gravitational waves are sourced by the similarly defined transverse traceless part of the perturbed energy momentum tensor of the matter content, defined by [340]

$$T_{ij} = a^2 \pi_{ij}^T + \cdots , \tag{4.6}$$

where "$\cdots$" denotes the neglected non-relevant parts. Its Fourier transform is defined by

$$\pi_{ij}^T(t, \mathbf{x}) = \int \frac{d^3q}{(2\pi)^3} q e^{i\mathbf{q}\cdot\mathbf{x}} \pi_{ij}^T(t, \mathbf{q}). \tag{4.7}$$

Since π_{ij}^T is of dimension 4, the dimension of its Fourier component $\pi_{ij}^T(t, \mathbf{q})$ is 1. The Einstein equation leads to a master equation governing the time evolution of each Fourier component of the gravitational waves, which is decoupled from the scalar and vector perturbations,

$$h_{ij}''(t, \mathbf{q}) + 2\frac{a'}{a} h_{ij}'(t, \mathbf{q}) + q^2 h_{ij}(t, \mathbf{q}) = 16\pi G a^2 \pi_{ij}^T(t, \mathbf{q}) \ . \tag{4.8}$$

Here $' \equiv \partial/\partial\eta$, with η being the conformal time. Derivatives with respect to the coordinate time will be denoted by a dot. The gravitational wave energy density,

as denoted by $\rho_{\rm GW}$ here, is defined as

$$\rho_{\rm GW}(t) = \frac{1}{32\pi G}\langle \dot{h}_{ij}(t,\mathbf{x})\dot{h}_{ij}(t,\mathbf{x})\rangle, \tag{4.9}$$

with the angle brackets, $\langle\cdots\rangle$, denoting both the spatial and ensemble average. Due to the overall spatial homogeneity of the universe, we can define the power spectrum of the derivative of the gravitational wave amplitude as:

$$\langle \dot{h}_{ij}(t,\mathbf{q}_1)\dot{h}_{ij}(t,\mathbf{q}_2)\rangle = (2\pi)^3\delta^3(\mathbf{q}_1+\mathbf{q}_2)P_{\dot{h}}(q_1,t). \tag{4.10}$$

Then the gravitational wave energy density follows

$$\rho_{\rm GW}(t) = \frac{1}{32\pi G}\frac{1}{2\pi^2}\int dq\ q^2 P_{\dot{h}}(t,q), \tag{4.11}$$

and the gravitational wave energy density spectrum:

$$\frac{d\rho_{\rm GW}(t)}{d\ln q} = \frac{1}{64\pi^3 G}q^3 P_{\dot{h}}(t,q). \tag{4.12}$$

It is conventional to use the dimensionless energy density fraction of the gravitational waves $\Omega_{\rm GW}(t) = \rho_{\rm GW}(t)/\rho_c(t)$ where ρ_c is the critical energy density at time t. The corresponding dimensionless version of the spectrum is [1]

$$\mathcal{P}_{\rm GW}(t,q) \equiv \frac{d\Omega_{\rm GW}(t)}{d\ln q} = \frac{1}{24\pi^2 H^2}q^3 P_{\dot{h}}(t,q) = \frac{1}{24\pi^2 H^2 a^2}q^3 P_{h'}(t,q), \tag{4.13}$$

where in the last step $P_{h'}(t,q)$ is defined by replacing $\dot{h}$ with h' in Eq. 4.10.

We thus need to solve for $h_{ij}(\eta,\mathbf{q})$ by solving Eq. 4.8 together with equations governing the evolution of the source. We will follow the conventional approach by neglecting the back-reaction of the metric on the source and calculate the stress

[1] $\mathcal{P}_{\rm GW}$ is also denoted as $\Omega_{\rm GW}(t,q)$.

tensor with a modelling of the phase transition process. Once $\pi_{ij}^T(t, \mathbf{q})$ is provided in this way, then $h_{ij}(t, \mathbf{q})$ can be solved from Eq. 4.8 with Green's function and with the following boundary conditions

$$G(\widetilde{\eta} \leqslant \widetilde{\eta}_0) = 0, \qquad \frac{\partial G(\widetilde{\eta}, \widetilde{\eta}_0)}{\partial \widetilde{\eta}}|_{\widetilde{\eta}=\widetilde{\eta}_0^+} = 1, \tag{4.14}$$

where $\widetilde{\eta} = q\eta$, which is a dimensionless quantity and $\widetilde{\eta}_0$ is the time when the phase transition starts. With the Green's function, the solution of the inhomogeneous Eq. 4.8 is given by

$$h_{ij}(t, \mathbf{q}) = 16\pi G \int_{\widetilde{\eta}_0}^{\widetilde{\eta}} d\widetilde{\eta}' G(\widetilde{\eta}, \widetilde{\eta}') \frac{a^2(\eta')\pi_{ij}^T(\eta', \mathbf{q})}{q^2}, \tag{4.15}$$

and its derivative with respect to the conformal time follows simply:

$$h'_{ij}(\eta, \mathbf{q}) = 16\pi G \int_{\widetilde{\eta}_0}^{\widetilde{\eta}} d\widetilde{\eta}' \frac{\partial G(\widetilde{\eta}, \widetilde{\eta}')}{\partial \widetilde{\eta}} \frac{a^2(\eta')\pi_{ij}^T(\eta', \mathbf{q})}{q}. \tag{4.16}$$

Then we can calculate the 2-point correlation function:

$$\begin{aligned}\langle h'_{ij}(\eta, \mathbf{q}_1) h'_{ij}(\eta, \mathbf{q}_2)\rangle = (16\pi G)^2 \int_{\widetilde{\eta}_0}^{\widetilde{\eta}} d\widetilde{\eta}_1 \int_{\widetilde{\eta}_0}^{\widetilde{\eta}} d\widetilde{\eta}_2 \frac{\partial G(\widetilde{\eta}, \widetilde{\eta}_1)}{\partial \widetilde{\eta}} \frac{\partial G(\widetilde{\eta}, \widetilde{\eta}_2)}{\partial \widetilde{\eta}} \\ \times \frac{a^2(\eta_1)a^2(\eta_2)}{q^2} \langle \pi_{ij}^T(\eta_1, \mathbf{q}_1)\pi_{ij}^T(\eta_2, \mathbf{q}_2)\rangle.\end{aligned} \tag{4.17}$$

Supposing that the gravitational wave generation finishes at $\widetilde{\eta}_f$, the upper limits for the integrals in the expression above will be $\widetilde{\eta}_f$. Subsequently, the energy density of the gravitational waves for modes inside the horizon will be simply diluted as $1/a^4$. We thus see that at the core of the gravitational wave energy density spectrum calculation is the unequal time correlator (UETC) of π_{ij}^T. It can be parametrized in the following way due to the overall spatial homogeneity of the universe [68]

$$\langle \pi_{ij}^T(\eta_1, \mathbf{q}_1)\pi_{ij}^T(\eta_2, \mathbf{q}_2)\rangle = \Pi^2(q_1, \eta_1, \eta_2)(2\pi)^3\delta^3(\mathbf{q}_1 + \mathbf{q}_2). \tag{4.18}$$

It is obvious that the dimension of $\Pi^2(k,\eta_1,\eta_2)$ is 5.

4.2.2 Unequal Time Correlator of the Fluid Stress Energy Tensor

Let us first write down the energy momentum tensor of the matter content in the universe. Here we keep the dominant contribution from the fluid and assume the fluid velocities are non-relativistic following Ref. [3], then

$$\begin{aligned} T_{ij} &= a^2\left[p\delta_{ij} + (p+e)\gamma^2 v^i v^j\right], \\ T_{i0} &= a\left[-(p+e)\gamma^2 v^i\right], \\ T_{00} &= \gamma^2(e+pv^2), \end{aligned} \tag{4.19}$$

where e is the energy density, p is the pressure and the velocity is defined w.r.t the conformal time $v^i = dx^i/d\eta$. Then, comparing with Eq. 4.6 and neglecting the non-relevant parts, we have

$$\pi_{ij} = (p+e)\gamma^2 v^i v^j, \tag{4.20}$$

Here the scale factor dependent $(p+e)$, takes its homogeneous value (defined with a bar) to leading order $\bar{e}+\bar{p} \equiv \bar{\omega}$ which scales as $1/a^4$, and γ is the Lorentz factor. The calculation of the correlator of π_{ij}^T parallels that in Minkowski spacetime:

$$\begin{aligned} & \langle \pi_{ij}^T(\eta_1,\mathbf{k})\pi_{ij}^T(\eta_2,\mathbf{q})\rangle \\ = \;& \Lambda_{ij,kl}(\hat{\mathbf{k}})\frac{1}{(2\pi)^6}\int d^3\mathbf{x}\int d^3\mathbf{y} e^{-i\mathbf{k}\cdot\mathbf{x}} e^{-i\mathbf{q}\cdot\mathbf{y}}\langle \pi_{kl}^T(\eta_1,\mathbf{x})\pi_{ij}^T(\eta_2,\mathbf{y})\rangle, \\ = \;& \Lambda_{ij,kl}(\hat{\mathbf{k}})\bar{\omega}^2\frac{1}{(2\pi)^6}\int d^3\mathbf{x}\int d^3\mathbf{y} e^{-i\mathbf{k}\cdot\mathbf{x}} e^{-i\mathbf{q}\cdot\mathbf{y}}\langle v^k(\eta_1,\mathbf{x})v^l(\eta_1,\mathbf{x})v^i(\eta_2,\mathbf{y})v^j(\eta_2,\mathbf{y})\rangle, \\ = \;& \bar{\omega}^2\Lambda_{ij,kl}(\hat{\mathbf{k}})\frac{1}{(2\pi)^{12}}\int d^3\mathbf{q}_1\int d^3\mathbf{q}_3 \underbrace{\langle \widetilde{v}^k_{\mathbf{q}_1}(\eta_1)\widetilde{v}^{l*}_{\mathbf{q}_1-\mathbf{k}}(\eta_1)\widetilde{v}^i_{\mathbf{q}_3}(\eta_2)\widetilde{v}^{j*}_{\mathbf{q}_3-\mathbf{q}}(\eta_2)\rangle}_{\equiv X^{klij}}. \end{aligned} \tag{4.21}$$

Here $\Lambda_{ij,kl}$ is the standard projection operator and $\Lambda_{ij,kl}(\hat{k}) = P_{ik}(\hat{k})P_{jl}(\hat{k}) - \frac{1}{2}P_{ij}(\hat{k})P_{kl}(\hat{k})$ with $P_{ij}(\hat{k}) = \delta_{ij} - \hat{k}^k\hat{k}^j$. $\widetilde{v}^i_{\mathbf{q}}$ is the Fourier transform of the velocity field $v^i(\mathbf{x})$. Due to the nature of the first order phase transition process and according to the central limit theorem, $\widetilde{v}^i_{\mathbf{q}}(\eta)$ follows the Gaussian distribution to a good approximation. Also as in Ref. [3], we neglect the rotational component, then the two point correlator can be defined in the following way:

$$\langle \widetilde{v}^i_{\mathbf{q}}(\eta_1)\widetilde{v}^{j*}_{\mathbf{k}}(\eta_2)\rangle = \delta^3(\mathbf{q}-\mathbf{k})\hat{q}^i\hat{k}^j G(q,\eta_1,\eta_2), \tag{4.22}$$

and higher order correlators can be reduced to the two point correlator. Defining $\widetilde{\mathbf{q}}_1 \equiv \mathbf{q}_1 - \mathbf{k}$ and $\widetilde{\mathbf{q}}_3 \equiv \mathbf{q}_3 - \mathbf{q}$, then

$$\begin{aligned} X^{klij} &= \langle \widetilde{v}^k_{\mathbf{q}_1}(\eta_1)\widetilde{v}^{l*}_{\widetilde{\mathbf{q}}_1}(\eta_1)\rangle\langle \widetilde{v}^i_{\mathbf{q}_3}(\eta_2)\widetilde{v}^{j*}_{\widetilde{\mathbf{q}}_3}(\eta_2)\rangle + \langle \widetilde{v}^k_{\mathbf{q}_1}(\eta_1)\widetilde{v}^{i}_{\mathbf{q}_3}(\eta_2)\rangle\langle \widetilde{v}^{l*}_{\widetilde{\mathbf{q}}_1}(\eta_1)\widetilde{v}^{j*}_{\widetilde{\mathbf{q}}_3}(\eta_2)\rangle \\ &\quad + \langle \widetilde{v}^k_{\mathbf{q}_1}(\eta_1)\widetilde{v}^{j*}_{\widetilde{\mathbf{q}}_3}(\eta_2)\rangle\langle \widetilde{v}^{l*}_{\widetilde{\mathbf{q}}_1}(\eta_1)\widetilde{v}^{i}_{\mathbf{q}_3}(\eta_2)\rangle. \end{aligned} \tag{4.23}$$

The first term contributes trivially to $\mathbf{k} = 0$ and, collecting all other contributions, we have

$$\langle \pi^T_{ij}(\eta_1,\mathbf{k})\pi^T_{ij}(\eta_2,\mathbf{q})\rangle = \delta^3(\mathbf{k}+\mathbf{q})\bar{\omega}^2\frac{1}{(2\pi)^6}\int d^3\mathbf{q}_1 G(q_1,\eta_1,\eta_2)G(\widetilde{q}_1,\eta_1,\eta_2)(1-\mu^2)^2\frac{q_1^2}{\widetilde{q}_1^2}. \tag{4.24}$$

Comparing with Eq. 4.18, it follows that

$$\Pi^2(k,\eta_1-\eta_2) = \bar{\omega}^2\int\frac{d^3q}{(2\pi)^3}G(q,\eta_1,\eta_2)G(\widetilde{q},\eta_1,\eta_2)\frac{q^2}{\widetilde{q}^2}(1-\mu^2)^2, \tag{4.25}$$

where $\widetilde{q} = |\mathbf{q}-\mathbf{k}|$ and $\mu = \hat{\mathbf{q}}\cdot\hat{\mathbf{k}}$. Here Π^2 depends on $\eta_1 - \eta_2$ rather than on η_1 and η_2 separately. This is because the source is largely stationary.

We will later see that the fluid equations maintain the same form as in the Minkowski spacetime once properly rescaled quantities and previously defined $v^i(\mathbf{x})$ are used (see also Ref. [68]). In particular it means that we can define a rescaled stress energy tensor ($\widetilde{\pi}^T_{ij}$) for the fluid:

$$\pi^T_{ij}(\mathbf{q},\eta) = \frac{a_s^4}{a^4(\eta)}\widetilde{\pi}^T_{ij}(\mathbf{q},\eta), \tag{4.26}$$

where a_s is a reference scale factor when the source becomes active. Similarly we can define a rescaled and dimensionless two point correlator $\widetilde{\Pi}$ following Ref. [68] by

$$\Pi^2(q,t_1,t_2) \equiv \frac{a_s^8}{a^4(\eta_1)a^4(\eta_2)}\left[\left(\bar{\widetilde{e}}+\bar{\widetilde{p}}\right)\bar{U}_f^2\right]^2 L_f^3\widetilde{\Pi}^2(qL_f, q\eta_1, k\eta_2), \tag{4.27}$$

where $\bar{\widetilde{e}}$ and $\bar{\widetilde{p}}$ are the rescaled average energy density and pressure, which correspond to the quantities measured at t_s. The quantity $\bar{U}_f$ describes the magnitude of the fluid velocity and is dimensionless. The correlator, Π^2, on the left hand side of the equation has dimension 5. Therefore, the additional length factor L_f^3 is inserted here to make $\widetilde{\Pi}$ dimensionless. Since this length scale is free from the effect of the expanding universe, it is a comoving length scale. It is found from numerical simulations [68, 69] that the typical scale in the gravitational wave production is the (comoving) mean bubble separation R_{*c}. So we will choose $L_f = R_{*c}$.

The calculation of the UETC requires us to scrutinize the entire process of the phase transition and the gravitational wave production. This task can be separated into two parts. The first part is a study of the bulk parameters characterizing the process of the phase transition, which we will perform in the

next section. The second part is understanding the evolution of the source, which we go on to perform in Sec. 4.4.

4.3 Dynamics of the Phase Transition

In this section, we study the changes to the dynamics of the phase transition in an expanding universe. This includes parameters characterizing the behavior of the bubble formation, expansion and percolation: the bubble nucleation rate, the fraction of the false vacuum, the unbroken area of the walls at a certain time, etc. These will eventually be incorporated in the calculation of the velocity power spectrum in the sound shell model. Another set of important quantities characterize the statistics of the bubbles ever formed: the bubble lifetime distribution, as well as the bubble number density. These are also needed in the velocity power spectrum calculation. Moreover, the timing of some important steps in the phase transition are also included, like the nucleation temperature and the percolation temperature. Other changes to the parameters entering the gravitational wave power spectrum calculation are also included, with β/H a representative example. We now proceed to a detailed discussion of these quantities.

4.3.1 Bubble Nucleation Rate

The first and most basic ingredient in the analysis of a first order cosmological phase transition is the nucleation rate of the bubbles in the meta-stable vacuum at finite temperature [341, 342]. The number of bubbles nucleated per time per

physical volume is given by the following formula:

$$p = p_0 \exp\left[-\frac{S_{3,b}(T)}{T}\right]. \tag{4.28}$$

Here S_3 is the Euclidean action of the underlying scalar field $\vec{\phi}$ that minimizes the solution

$$S_3(\vec{\phi}, T) = 4\pi \int dr r^2 \left[\frac{1}{2}\left(\frac{d\vec{\phi}(r)}{dr}\right)^2 + V(\vec{\phi}, T)\right], \tag{4.29}$$

with the following bounce boundary conditions:

$$\frac{d\vec{\phi}(r)}{dr}\Big|_{r=0} = 0, \qquad \vec{\phi}(r=\infty) = \vec{\phi}_{\text{out}}, \tag{4.30}$$

where $\vec{\phi}_{\text{out}}$ are the components of the vacuum expectation value for the scalar field outside the bubble. For the pre-factor, we see that $p_0 \propto T^4$ on dimensional grounds, while its precise determination requires integrating out fluctuations around the bounce solution (see e.g., [251, 252] for detailed calculations or [253] for a pedagogical introduction).

The function $S_3(T)/T$ generally starts from infinity at T_c and drops sharply as temperature decreases, with a typical profile shown in Fig. 4.2. Bubbles will be nucleated within a short range of time, say at t_*, when this rate changes slowly, which admits the following Taylor expansion:

$$p(t) = p_0 \exp\left[-S_* + \beta(t - t_*)\right], \tag{4.31}$$

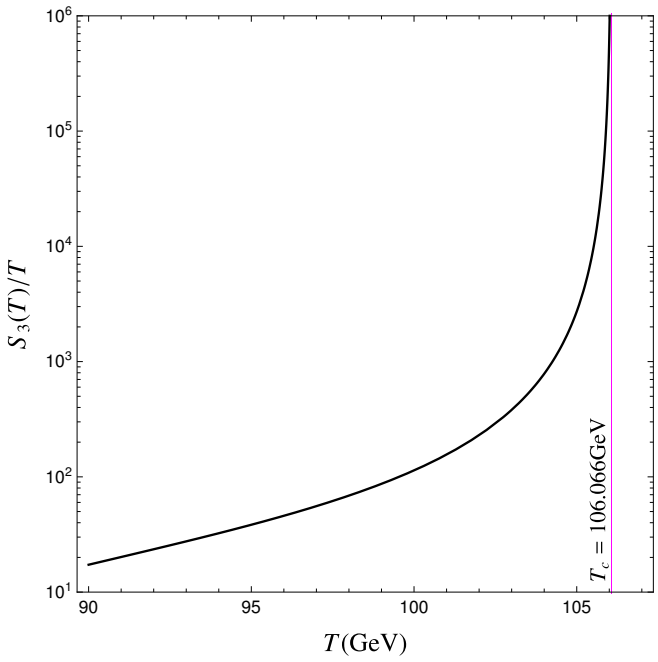

Figure 4.2: The representative profile of $S_3(T)/T$ for the example used in Sec. 4.3. See Appendix. A for details on how to reproduce this.

where $S_* \equiv S_3(T_*)/T_*$ and $\beta \equiv d\ln p(t)/dt|_{t=t_*}$ [2]. More explicitly, we have

$$\frac{S_3}{T} = \frac{S_3}{T}\bigg|_{t_*} + \underbrace{\frac{d(S_3/T)}{dT}\frac{dT}{dt}\bigg|_{t=t_*}}_{\equiv -\beta}(t-t_*), \tag{4.33}$$

and thus

$$\frac{\beta}{H_*} = -\frac{1}{H_*}\frac{dT}{dt}\,\frac{d(S_3/T)}{dT}\bigg|_{t=t_*}. \tag{4.34}$$

We will later see how t_* should be chosen. For now, we provide a generic expression for β during an expanding universe, which needs the relation between t

[2] If there exists a barrier at zero temperature, then $S_3(T)/T$ will reach a minimum, say at t_*. The rate can be expanded around the minimum:

$$p(t) = p_0 \exp\left[-S_* - \frac{1}{2}\beta_2^2(t-t_*)^2\right], \tag{4.32}$$

with $\beta_2 \equiv S''(t_*)$ and the first derivative vanishing. The bubble nucleation will happen mostly around t_*, making it look like an instantaneous nucleation [71].

and T. Suppose the universe is expanding as $a = c_a t^n$ and the radiation sector is expanding adiabatically such that entropy s_R is conserved per comoving volume for the radiation sector:

$$s_R(T)a^3 = \text{const.} \tag{4.35}$$

Here $s_R \propto T^3$, giving then $T \propto 1/a \propto t^{-n}$. This is the case for a radiation dominated universe, and for a matter dominated universe where the non-relativistic matter does not inject entropy to the radiation sector. However when the matter decays into radiation, entropy injection into the radiation sector gives a different dependence $T \propto a^{-3/8}$ [343]. Generically, we can assume [3]

$$T \propto a^{-\gamma} \ , \tag{4.36}$$

which then leads to $T = c_T t^{-n\gamma}$, with c_T being another constant. We thus have

$$\frac{dT}{dt} = -c_T n\gamma \ t^{-n\gamma-1}. \tag{4.37}$$

Moreover $H = \dot{a}/a = n/t$. Then

$$\frac{1}{H}\frac{dT}{dt} = -c_T\gamma \ t^{-n\gamma} = -\gamma \ T. \tag{4.38}$$

Therefore β/H_* reduces to the following form

$$\frac{\beta}{H_*} = \gamma \ T \frac{d(S_3/T)}{dT}\bigg|_{t=t_*}. \tag{4.39}$$

It is obvious from this result that β/H_* does not depend on n, i.e., it does not depend on how the scale factor evolves with time but rather on how T decreases

[3] Not to be confused with the Lorentz factor.

with the scale factor through γ. For both the standard radiation dominated universe and an early matter dominated universe wherein the matter is decoupled from the radiation, $\gamma = 1$. For the matter dominated universe wherein the matter decays into radiation, $\gamma = 3/8$, which gives a smaller β/H_* [335].

4.3.2 False Vacuum Fraction

The false vacuum fraction $g(t_c, t)$ at $t > t_c$ can be obtained following the derivation in Ref. [344]

$$g(t_c, t) = \exp\left[-\frac{4\pi}{3}\int_{t_c}^{t} dt' p(t') a^3(t') r(t', t)^3\right] \equiv \exp[-I(t)]. \tag{4.40}$$

Here $I(t)$ corresponds to the volume of nucleated bubbles per comoving volume, double counting the overlapped space between bubbles and virtual bubbles within others. $r(t', t)$ is the comoving radius of the bubble nucleated at t' and measured at t,

$$r(t', t) = \int_{t'}^{t} dt'' \frac{v_w}{a(t'')}. \tag{4.41}$$

For Minkowski spacetime, $r(t', t) = v_w(t - t')$. For a FLRW spacetime $r(t', t) = v_w(\eta' - \eta)$, which takes the same form as the Minkowski spacetime, irrespective of the detailed expansion behavior, when conformal time is used. In obtaining the above results, a constant bubble wall velocity v_w has been assumed and the initial size of the bubble has been neglected. This is justified as the initial size is very small.

Eq. 4.40 can be recast in a form that is convenient for calculations, in terms of the temperature. Suppose that the scale factor at the time of the critical

temperature is a_c and that the scale factor at a later time is related to it by

$$\frac{a}{a_c} \equiv \left(\frac{T_c}{T}\right)^{1/\gamma}. \tag{4.42}$$

The comoving bubble radius can be conveniently expressed with an integral over temperature:

$$r(T', T) = \frac{v_w}{a_c} \int_T^{T'} \frac{dT''}{T''} \frac{1}{\gamma H(T'')} \left(\frac{T_c}{T''}\right)^{-1/\gamma}. \tag{4.43}$$

Accordingly $I(T)$ can be written as

$$I(T) = \frac{4\pi}{3} \int_T^{T_c} \frac{dT'}{T'} \frac{1}{\gamma H(T')} \bar{p}_0 T'^4 \exp\left[-\frac{S_3(T')}{T'}\right] \left(\frac{T_c}{T'}\right)^{3/\gamma} [a_c r(T', T)]^3. \tag{4.44}$$

Here the factor $\bar{p}_0$ is defined by $p_0 = \bar{p}_0 T^4$ and we choose $\bar{p}_0 = 1$ in the examples of analysis as is usually done in the literature. A different choice of $\bar{p}_0$ would, of course, affect the resulting false vacuum fraction and thus the relevant temperatures defined [345]. Since the focus here is on the changes due to different expansion histories, a fixed choice of $\bar{p}_0$ serves our purpose well. For the Hubble rate, we need to be more precise with regard to the matter content. We consider a universe consisting of both radiation and non-relativistic matter and define κ_M to be the fraction of the total energy density at T_c that is non-relativistic matter:

$$\kappa_M = \left.\frac{\rho_{\text{Matter}}}{\rho_{\text{Total}}}\right|_{T=T_c}. \tag{4.45}$$

We also neglect the vacuum energy for these examples, though it certainly exists during a phase transition.

$$H = H(T_c)\sqrt{\frac{\kappa_M}{y^3} + \frac{1-\kappa_M}{y^4}}, \tag{4.46}$$

where $y = a/a(T_c)$. We show in Fig. 4.3 the false vacuum fraction during the phase transition, for a purely radiation dominated universe with $\kappa_M = 0$ and a matter dominated one with $\kappa_M = 0.9$, and for three choices of bubble wall velocities $v_w = 0.3, 0.7, 0.9$. For both choices of κ_M, it is clear from these FiguresPT that increasing v_w speeds up the process of phase transition. From $\kappa_M = 0$ to $\kappa_M = 0.9$, a larger energy density and thus a larger Hubble rate is obtained, which decreases the function $r(T', T)$ and $I(I)$ and thus slows down the drop of $g(T_c, T)$.

One often encounters the percolation temperature, which is defined such that the fraction in true vacuum is about 30% of the total volume [282], i.e., when

$$g(T_c, T_p) \approx 0.7, \quad \text{or} \quad I(T_p) \approx 0.34, \tag{4.47}$$

and corresponds to the intersection points of the horizontal line with the curves in Fig. 4.3. Since different choices of v_w and κ_M lead to different $g(T_c, T)$, the corresponding values of T_p are also different.

4.3.3 Unbroken Bubble Wall Area

With the false vacuum fraction in Eq. 4.40, the unbroken bubble wall area during the phase transition can be derived [3] and will be used in the derivation of the bubble lifetime distribution. Consider a comoving volume of size V_c and a sub-volume occupied by false vacuum $V_{c,\text{False}}$. Then the comoving unbroken bubble wall area $\mathcal{A}_c(t)$ at t satisfies the following relation:

$$dg(t_0, t) = \frac{dV_{c,\text{False}}}{V_c} = -\mathcal{A}_c(t)\frac{v_w dt}{a(t)} = -\mathcal{A}_c(t) v_w d\eta. \tag{4.48}$$

Then $\mathcal{A}_c$ is given by

$$\mathcal{A}_c(t) = -\frac{1}{v_w}\frac{dg(t_0,t)}{d\eta} = a(\eta)\frac{H(T)\gamma T}{v_w}\frac{dg(T_c,T)}{dT}. \tag{4.49}$$

One can also define the proper area per proper volume

$$\mathcal{A} = \frac{\text{Proper Area}}{\text{Proper Volume}} = \frac{a^2 \times \text{Comoving Area}}{a^3 \times \text{Comoving Volume}} = \frac{1}{a}\mathcal{A}_c. \tag{4.50}$$

Since $\mathcal{A}_c(t)$ and $\mathcal{A}$ are the area per volume, they are of dimension 1, and can be presented in units of m^{-1} or GeV. A more meaningful representation can be obtained by comparing it with the typical scale at the corresponding temperature. One such quantity is β_c, to be defined later, which is the comoving version of the β parameter and is related to the mean bubble separation (also to be defined later). We show $\mathcal{A}_c/\beta_c$ in Fig. 4.4 for different choices κ_M and v_w, similar to what are used in Fig. 4.3. We can see the area first increases as more bubbles are formed and expanding. It decreases as bubbles collide with each other and the remaining false vacuum volume is shrinking to zero. The different behaviors when changing v_w and the amount of non-relativistic matter contents coincide with what we observe in Fig. 4.3.

4.3.4 Bubble Lifetime Distribution

The bubble lifetime distribution describes the distribution of bubble lifetime for all the bubbles ever formed and destroyed during the entire process of the phase transition. This can be obtained with the help of the unbroken bubble wall area derived earlier, by generalizing the result derived in Ref. [3] to the expanding universe. We start by considering the number of bubbles that are created at t'

and are destroyed with comoving radius r. Here a bubble is defined as destroyed when approximately half of its volume is occupied by the expanding true vacuum space. These bubbles are therefore at a comoving distance of r at t' from the part of the unbroken bubble wall, assuming constant and universal bubble wall velocity v_w. The time t when this set of bubbles is destroyed is connected with t' and r by

$$r = \int_{t'}^{t} \frac{v_w dt''}{a(t'')}. \tag{4.51}$$

Since only two quantities out of (r, t', t) are independent, we denote $\mathcal{A}_c(t(t', r))$ as $\mathcal{A}_c(t', r)$ and define the number of bubbles per comoving volume as $n_{b,c}$. We then have (see an illustration and more details in Fig. 4.5):

$$d^2 n_{b,c} = p(t') \left[a^3(t')\mathcal{A}_c(t', r)dr\right] dt'. \tag{4.52}$$

This implies that:

$$d\left(\frac{dn_{b,c}}{dr}\right) \equiv dn_{b,c}(r) = p(t') \left[a^3(t')\mathcal{A}_c(t', r)\right] dt'. \tag{4.53}$$

Now, for fixed r, we consider all the bubbles ever formed before a time t_f:

$$n_{b,c}(r)|_{t_c}^{t_f} = \int_{t_c}^{t_f} dt' p(t') \left[a^3(t')\mathcal{A}_c(t', r)\right], \tag{4.54}$$

and $n_{b,c}(r) = 0$ at t_c for all r. Consider a time when all bubbles have disappeared, when t_f is large enough. Now $n_{b,c}(r)|_{t_f}$ becomes a constant $\widetilde{n}_{b,c}(r)$. We can then relate r with the lifetime of the bubbles. For the bubble nucleated at t' and destroyed at t, we have

$$r = \int_{t'}^{t} dt'' \frac{v_w dt''}{a(t'')} = v_w \eta_{\rm lt}, \tag{4.55}$$

where $\eta_{\rm lt}$ is the conformal lifetime of the bubble. Thus, r has the same relation with the conformal lifetime as its relation with $t_{\rm lt}$ in Minkowski spacetime. We can therefore proceed to derive a conformal lifetime distribution for all bubbles ever formed and destroyed:

$$\widetilde{n}_{b,c}(\eta_{\rm lt}) \equiv \frac{dn_{b,c}}{d\eta_{\rm lt}} = v_w \widetilde{n}_{b,c}(r) = v_w \int_{t_c}^{t_f} dt' p(t') a^3(t') \mathcal{A}_c(t', v_w \eta_{\rm lt}). \tag{4.56}$$

Remember $\mathcal{A}_c(t', v_w\eta_{\rm lt}) = \mathcal{A}_c(t(t', v_w\eta_{\rm lt}))$ and it is evaluated at t, which should be determined through Eq. 4.55 given t' and $\eta_{\rm lt}$. To present a numerically convenient representation of the above result, we convert coordinate time t to conformal time η and then to temperature. For the bubble formed at t', the corresponding conformal time is related to temperature by

$$\eta' - \eta_c = \int_{t_c}^{t'} \frac{dt''}{a(t'')} = \frac{1}{a_c} \int_{T'}^{T_c} \frac{dT''}{T''} \frac{1}{\gamma H(T'')} \left(\frac{T_c}{T''}\right)^{-1/\gamma} \equiv \Delta\eta(T', T_c). \tag{4.57}$$

Then for the bubble with conformal lifetime $\eta_{\rm lt}$, the conformal time for its destruction is given by $\eta_{\rm lt} + (\eta' - \eta_c)$, with the corresponding temperature T determined through

$$\eta_{\rm lt} + (\eta' - \eta_c) = \Delta\eta(T, T_c). \tag{4.58}$$

This temperature, or time, is what should be used in $\mathcal{A}_c$, rather than T'. With the relation between T and T' found, it is then straightforward to do the integral in Eq. 4.56, which requires only converting t' to temperature.

4.3.5 Bubble Number Density

The evolution of the bubble number density per proper volume $n_b = N_b/V$ is governed by the following equation

$$\frac{d[n_b a^3(t)]}{dt} = p(t)g(t_c, t)a^3(t), \tag{4.59}$$

which can be integrated to give (noting that $n_b(t_c) = 0$):

$$n_b(t) = \frac{1}{a^3(t)} \int_{t_c}^{t} dt' p(t')g(t_c, t')a^3(t'). \tag{4.60}$$

This does not include the decrease of bubble number due to collisions and n_b thus includes all the bubbles ever formed. The result for $n_b(t)$ can be similarly transformed into a function of temperature.

$$n_b(T) = \left(\frac{T}{T_c}\right)^{3/\gamma} \int_{T}^{T_c} \frac{dT'}{T'} \frac{1}{\gamma H(T')} \bar{p}_0 T'^4 \exp\left[-\frac{S_3(T')}{T'}\right] g(T_c, T') \left(\frac{T_c}{T'}\right)^{3/\gamma}. \tag{4.61}$$

We show n_b in units of m^{-3} in the left panel of Fig. 4.6 and the total bubble number per Hubble volume $n_b/H^3(T)$ in the right panel. We can see that the bubble number density increases for a delayed false vacuum fraction, which is consistent with physical intuition. From n_b, we can define the mean bubble separation, R_*, as

$$R_*(t) = \left[\frac{V(t)}{N_b(t)}\right]^{1/3} = \left[\frac{1}{n_b(t)}\right]^{1/3}. \tag{4.62}$$

This is shown in Fig. 4.7. For both n_b and R_*, it appears they both reach an asymptotic value after the bubbles have disappeared when the curves in these FiguresPT become flat. This is misleading as after the time the bubbles have disappeared, n_b will be diluted as $1/a^3$ and accordingly R_* increases as a. The flat

curves in the FiguresPT are simply due to the very tiny change of temperature plotted. From numerical simulations [69, 68], it is found that the peak frequency of the gravitational wave spectrum is related to R_*. Therefore any change on R_* will translate into a shift of the peak frequency of the gravitational waves. Since R_* is of particular importance, it is convenient to use the comoving version of it $R_{*c} = (V_c/N_b)^{1/3}$, which will reach an asymptotic value after the bubble disappearance.

From the right panel of Fig. 4.6, we can easily read off the nucleation temperature T_n, which is defined such that at this temperature there is about one bubble within a Hubble volume [254]. Note T_n obtained this way differs slightly from the usually used, and a bit crude, criterion:

$$\int_{t_c}^{t_n} dt \frac{p(t)}{H(t)^3} = 1, \tag{4.63}$$

which for radiation dominated universe where $H^2 = 8\pi G\rho/3$ and $\rho = \frac{\pi^2}{30} g_*(T) T^4$ translates into the condition:

$$\int_{T_n}^{T_c} \frac{dT}{T} \left(\frac{90}{8\pi^3 g_*}\right)^2 \left(\frac{m_{\rm Pl}}{T}\right)^4 \exp\left[-\frac{S_3(T)}{T}\right] = 1. \tag{4.64}$$

Here $m_{\rm Pl}$ is the Planck mass. A further simplification says that T_n is determined by $S_3(T_n)/T_n = 140$ [254]. These determined T_n differs slightly from the more accurate result obtained by solving directly for n_b with Eq. 4.59.

4.3.6 Relation between β and Mean Bubble Separation (R_*)

It was found from numerical simulations that the peak of the gravitational wave power spectrum is located at $kR_* \sim 10$ [69], where R_* is the mean bubble

separation defined earlier. However the standard spectrum people generally use is expressed in terms of β (see, e.g., [25, 26]). So the relation between β and R_* is needed. It can be derived analytically under reasonable assumptions as was shown in Ref. [3], which says

$$R_* = \frac{(8\pi)^{1/3}}{\beta(v_w)} v_w. \tag{4.65}$$

Here we emphasize that β varies when v_w is changed. The question is then will this relation still hold in an expanding universe. We will answer this question by giving a detailed derivation here, which parallels and generalizes the derivation in Ref. [3].

We rewrite Eq. 4.59 in terms of the conformal time (we still use the same function labels though t is replaced by η)

$$\frac{d(n_{b,c})}{d\eta} = p(\eta) g(\eta_c, \eta) a^4(\eta), \tag{4.66}$$

where $n_{b,c} = n_b a^3$ and is the comoving bubble number density. Here the false vacuum fraction g decreases sharply when its exponent $I(T)$ becomes of order 1. Since $p(\eta)$ increases exponentially, there is a peak for the r.h.s in above equation, at which time the bubbles are mostly nucleated. As g decreases much more sharply than p increases, the rate p only increases slowly during this time duration and it can be Taylor expanded at around this time. This time can be conveniently chosen to be η_0 which satisfies $I(\eta_0) = 1$. Then similarly to Eq. 4.31, we define a Taylor expansion but w.r.t the conformal time:

$$p(\eta) = p_0(\eta_0) \exp[-S_0 + \beta_c(\eta - \eta_0)], \tag{4.67}$$

where we have neglected the very slow change of $p_0(\eta)$ and defined a comoving version of η:

$$\beta_c = \left.\frac{d\ln p}{d\eta}\right|_{\eta=\eta_0}. \tag{4.68}$$

Now lets see how $n_{b,c}$ in Eq. 4.66 can be solved in terms of β_c. To do it, lets firstly see how g or its exponent I can be expressed in terms of β_c. From Eq. 4.40, we can write I in the following way:

$$\begin{aligned} I(\eta) &= \frac{4\pi}{3}\int_{\eta_c}^{\eta} d\eta' a^4(\eta')p(\eta')r(\eta',\eta)^3 \\ &= \frac{4\pi}{3}v_w^3\int_{\eta_c}^{\eta} d\eta' p_0(\eta_0)e^{-S_0+\beta_c(\eta'-\eta_0)}(\eta-\eta')^3 \\ &= 8\pi\frac{v_w^3}{\beta_c^4}p_0(\eta_0)e^{-S_0+\beta_c(\eta-\eta_0)}. \end{aligned} \tag{4.69}$$

Now define a time η_f such that

$$I(\eta_f) = 1, \tag{4.70}$$

then at a later time much simpler expressions can be obtained:

$$I(\eta) = e^{\beta_c(\eta-\eta_f)}, \qquad g(\eta_c,\eta) = e^{-I(\eta)}. \tag{4.71}$$

As $I(\eta)$ depends on the bubble wall velocity v_w, the resulting t_f and more importantly β_c is a function of v_w. Plugging above expressions of $g(\eta_c,\eta)$, $p(\eta)$ into Eq. 4.66, and integrating over η, we have

$$n_{b,c} = \frac{1}{\beta_c}p_0(\eta_0)e^{-S_0+\beta_c(\eta_f-\eta_0)} = \frac{\beta_c^3(v_w)}{8\pi v_w^3}. \tag{4.72}$$

Here the second equality comes from the relation in Eq. 4.70. As noted in Ref. [3], the best choice of t_0 is t_f so that the Taylor expansion of $p(\eta)$ converges

more quickly. This result gives the relation between the comoving mean bubble separation R_{*c} and η_c:

$$R_{*c} = (8\pi)^{1/3} \frac{v_w}{\beta_c(v_w)}. \tag{4.73}$$

We can also write all results in terms of physical quantities. From Eq. 4.68 and enforcing $t_0 = t_f$, we have

$$\beta_c = a(\eta_f)\beta = a(\eta_f) \left[\gamma H(T) T \frac{d(S_3/T)}{dT} \right] \Bigg|_{T=T_f}, \tag{4.74}$$

and thus

$$n_{b,c} = a^3(\eta_f) \frac{\beta^3}{8\pi v_w^3}. \tag{4.75}$$

Note $n_{b,c}$ becomes a constant number as N_b reaches its maximum and the comoving volume is fixed. The physical number density after all the bubbles have vanished will be diluted by the expansion. Suppose we consider the physical number density n_b at time η, then

$$n_b(\eta) = \left(\frac{a(\eta_f)}{a(\eta)} \right)^3 \frac{\beta^3}{8\pi v_w^3}. \tag{4.76}$$

The corresponding physical mean bubble separation would be

$$R_*(\eta) = \frac{a(\eta)}{a(\eta_f)} (8\pi)^{1/3} \frac{v_w}{\beta(v_w)}. \tag{4.77}$$

Therefore the relation between R_* and β is similar to that derived in Minkowski spacetime and needs only additional attention on the scale factors. If one uses R_{*c} and β_c, then the relation is exactly the same as in Minkowski spacetime. We emphasize again that β and β_c are functions of v_w. To see this, we plot R_* at a

time immediately after all the bubbles have disappeared, as a function of v_w, in the left panel of Fig. 4.8. For each v_w, we find the corresponding $\beta(v_w)$ as implied in above equation and compare with $\beta(v_w)$ directly calculated using Eq. 4.74. This comparison is shown in the right panel and the two different determinations differ by at most 2%, where the uncertainty can be attributed to the approximations made.

4.4 Fluid Velocity Field and Power Spectrum

The dominant source of gravitational wave production is the sound waves in a perturbed plasma due to the advancing bubble walls and their interaction with the surrounding fluid. In the sound shell model [71, 3], the total velocity field is modelled as a linear superposition of the individual contribution from each bubble. The first step is then to understand the velocity profile of the fluid around a single bubble. This topic has been extensively studied several decades ago and is reviewed with a complete treatment in Ref. [70]. However the analysis is set in Minkowski spacetime and it is not clear whether it needs changes in an expanding universe. Ref. [346] studied the velocity profile in an expanding universe and found that there is a significant change to the velocity profile and a reduction of energy fraction going into the kinetic energy of the sound waves. But we will see in this section the velocity profile actually remains unchanged. We first review the full set of fluid and field equations and then analyze the fluid velocity profile around a single bubble. Armed with this information, we then find the total

velocity field from a population of bubbles in the sound shell model and calculate the velocity field power spectrum.

4.4.1 Fluid and Field Equations

Numerical simulations that are performed to provide the widely adopted gravitational wave formulae are based on the fluid-order parameter field model [68, 347, 348] in Minkowski spacetime. Here we generalize the full set of equations used in the simulations to the FLRW universe. Our purpose is to understand whether simulations can be done in Minkowski spacetime and then generalized to an expanding universe by simple rescalings of the physical quantities. This is an important question as it is computationally very expensive to do a numerical simulation.

The universe consists of: (1) the underlying scalar field(s) responsible for the phase transition; (2) the relativistic plasma whose constituent particles can interact with the scalar field(s); (3) magnetic field produced from the phase transition; (4) other sectors which do not directly interact with either the scalar field, the plasma or the magnetic field, though they do interact gravitationally. We will neglect (3) by focusing on the dominant source for gravitational wave production, and only consider (4) through its effect on the expansion. Given our cosmological context, the total energy momentum tensor for (1) and (2) is given by [68]

$$T^{\mu\nu} = \partial^\mu\phi\partial^\nu\phi - \frac{1}{2}g^{\mu\nu}\partial_\mu\phi\partial^\mu\phi + (e+p)U^\mu U^\nu + g^{\mu\nu}p, \tag{4.78}$$

where $U^\mu = \gamma(1, \mathbf{v}/a)$ with $\gamma = 1/\sqrt{1-v^2}$ and $\mathbf{v} = d\mathbf{x}/d\eta$. The energy and momentum densities are given by

$$\begin{aligned} e &= a_B T^4 + V(\phi, T) - T\frac{\partial V}{\partial T}, \\ p &= \frac{1}{3} a_B T^4 - V(\phi, T), \end{aligned} \tag{4.79}$$

where $a_B = g_* \pi^2/30$ and g_* is the relativistic degrees of freedom. It is certainly conserved, i.e., $T^{\mu\nu}{}_{;\mu} = 0$ [4], and it is usually split into two parts by adding and subtracting a friction term δ^ν [347]:

$$\begin{aligned} T^{\mu\nu}{}_{;\mu}|_{\text{field}} &= (\partial^2\phi)\partial^\nu\phi + \frac{1}{\sqrt{g}}(\partial_\mu\sqrt{g})(\partial^\mu\phi)(\partial^\nu\phi) - \frac{\partial V}{\partial\phi}\partial^\nu\phi = \delta^\nu, \\ T^{\mu\nu}{}_{;\mu}|_{\text{fluid}} &= \partial_\mu\left[(e+p)U^\mu U^\nu\right] + \left[\frac{1}{\sqrt{g}}(\partial_\mu\sqrt{g})g^\nu_\lambda + \Gamma^\nu_{\mu\lambda}\right](e+p)U^\mu U^\lambda + g^{\mu\nu}\partial_\mu p + \frac{\partial V}{\partial\phi}\partial^\nu\phi = -\delta^\nu \end{aligned} \tag{4.80}$$

Note here the appearance of $\partial_\mu g$ and $\Gamma^\nu_{\mu\lambda}$ as we are using a generic metric. The friction term δ^ν is modelled by $\delta^\nu = \eta U^\mu \partial_\mu\phi\partial^\nu\phi$. For high temperatures it can be chosen as $\eta = \widetilde{\eta}\phi^2/T$ [69], which works well in that case [349] but may lead to numerical singularities for small temperature. The numerical simulations on sound waves adopted a constant value for the lower temperature case [5]. Note the exact set of equations can also be derived from field theory [345, 350].

In an FLRW universe, the field energy momentum conservation leads to a scalar equation:

$$-\ddot{\phi} + \frac{1}{a^2}\nabla^2\phi - \frac{\partial V}{\partial\phi} - 3\frac{\dot{a}}{a}\dot{\phi} = \eta\gamma(\dot{\phi} + \frac{1}{a}\mathbf{v}\cdot\nabla\phi), \tag{4.81}$$

[4] The subscript ";" denotes covariant derivative.

which is just the Klein-Gordon equation for the scalar field when the friction term is absent, i.e., when $\eta = 0$. The vector part of the fluid energy-momentum conservation gives:

$$\dot{Z}^i + \frac{1}{a}\nabla\cdot(\mathbf{v}Z^i) + 5\frac{\dot{a}}{a}Z^i + \frac{1}{a^2}\partial_i p + \frac{1}{a^2}\frac{\partial V}{\partial\phi}\partial_i\phi = -\frac{1}{a^2}\eta\gamma(\dot{\phi} + \frac{1}{a}\mathbf{v}\cdot\nabla\phi)\partial_i\phi, \quad (4.82)$$

where $Z^i \equiv \gamma(e+p)U^i = \gamma^2(e+p)v^i/a$. The parallel projection along U_ν for the fluid gives another scalar equation:

$$\dot{E} + p[\dot{\gamma} + \frac{1}{a}\nabla\cdot(\gamma\mathbf{v})] + \frac{1}{a}\nabla\cdot(E\mathbf{v}) - \gamma\frac{\partial V}{\partial\phi}(\dot{\phi} + \frac{1}{a}\mathbf{v}\cdot\nabla\phi) + 3\frac{\dot{a}}{a}\gamma(e+p) = \eta\gamma^2(\dot{\phi} + \frac{1}{a}\mathbf{v}\cdot\nabla\phi)^2, \quad (4.83)$$

where $E \equiv e\gamma$. While the above equations form a complete set, the velocity profile is usually derived from a different scalar equation, the perpendicular projection for the fluid along the direction $\bar{U}_\nu$, which is defined by

$$\bar{U}^\mu U_\mu = 0, \qquad \bar{U}^\mu\bar{U}_\mu = 1, \quad (4.84)$$

and takes the explicit form $\bar{U}^\mu = \gamma(v, \hat{v}^i/a)$. This gives

$$\left[\frac{\dot{a}}{a}v + \gamma^2\left(\dot{v} + \frac{1}{2a}\hat{\mathbf{v}}\cdot\nabla v^2\right)\right](e+p) + v\dot{p} + \frac{1}{a}\hat{\mathbf{v}}\cdot\nabla p + \frac{\partial V}{\partial\phi}(v\dot{\phi} + \frac{1}{a}\hat{\mathbf{v}}\cdot\nabla\phi) = -\eta\gamma(v\dot{\phi} + \frac{1}{a}\hat{\mathbf{v}}\cdot\nabla\phi)(\dot{\phi} + \frac{1}{a}\mathbf{v}\cdot\nabla\phi). \quad (4.85)$$

These equations are direct generalizations of those in Ref. [68] to an FLRW universe. It is not possible, however, to express the above equations in a form used in Minkowski spacetime and the problem lies with the scalar field. Despite this, the effect on the bubble and fluid motions should be minor, since the bubble collision process is fast compared with the long duration of the ensuing sound waves.

The process of the phase transition can thus be divided into two stages. The first stage is the bubble collision and disappearance of the symmetric phase, and the second is the propagation of sound waves. The difference between them is that the first stage takes a much shorter time, while the second is long-lasting. This is indeed what is observed from numerical simulations and should well justify simply neglecting the change of the scale factor during the first stage [68]. In this sense, the numerical simulations as performed in Ref. [68, 69] still give a faithful account of the first step for an expanding universe. However we will see in the next subsection that the analytical modelling of this first stage still admits simple rescaling properties and takes the same form as its Minkowski counterpart.

During the second stage gravitational waves are dominantly produced due to the long-lasting sound waves. Therefore the change of the scale factor can not be ignored. The question is: can we still solely perform numerical simulations in Minkowski spacetime. Fortunately, during this stage, the scalar field plays no dynamical role and we can consider only the fluid. The corresponding equations can indeed be reduced to the Minkowski form. This is achieved by using the conformal time, neglecting the scalar field as well as the friction terms and using $p = e/3$ for the plasma. Then Eq. 4.82, Eq. 4.83 and Eq. 4.85 reduce to (again, $\prime \equiv \partial/\partial\eta$):

$$
\begin{aligned}
&(a^4 S^i)' + \nabla \cdot (a^4 S^i \mathbf{v}) + \partial_i (a^4 p) = 0, \\
&(a^4 e\gamma)' + [\gamma' + \nabla \cdot (\gamma \mathbf{v})](a^4 p) + \nabla \cdot (a^4 e \gamma \mathbf{v}) = 0, \\
&\gamma^2 (v' + \frac{1}{2}\hat{\mathbf{v}} \cdot \nabla v^2)[a^4(e+p)] + v(a^4 p)' + \hat{\mathbf{v}} \cdot \nabla (a^4 p) = 0,
\end{aligned}
\tag{4.86}
$$

where $S^i = aZ^i = \gamma^2(e+p)v^i$. The Minkowski counterpart of these equations can be obtained by setting $a = 1$. This suggests that we can define rescaled quantities $\widetilde{e} = a^4 e/a_s^4$ and $\widetilde{p} = a^4 p/a_s^4$, where a_s is the scale factor when the source becomes active. They are free from the dilution due to the expansion, and that the equations governing $\widetilde{e}$, $\widetilde{p}$ and v take exactly the same form as their Minkowski counterparts, as long as the time t is interpreted as the conformal time η. We will see how these rescaled quantities can be used to derive the modified gravitational wave spectrum in later sections.

We note here that these equations were derived earlier in Ref. [351, 352] when also considering electromagnetism and it was shown that the above rescaling works not only for the purely fluid system but also for a system containing both fluid and electromagnetism. Including electromagnetism will add additional terms to the right hand side of the above equations.

4.4.2 Velocity Profile around a Single Bubble

Solving the velocity profile for a single expanding bubble depends on analyzing the behavior of the system consisting of both the fluid and the scalar field. This is usually done in the so called bag equation of state model, as summarized in Ref. [70]. The energy momentum tensor for the fluid plus scalar field system is assumed to take the following form ("+" for outside the bubble and "−" for inside):

$$T_{\pm}^{\mu\nu} = p_{\pm} g^{\mu\nu} + (p_{\pm} + \rho_{\pm}) U^{\mu} U^{\nu}, \tag{4.87}$$

with the bag equation of state:

$$p_+ = \frac{1}{3}a_+ T_+^4 - \epsilon, \quad e_+ = a_+ T_+^4 + \epsilon,$$
$$p_- = \frac{1}{3}a_- T_-^4, \qquad e_- = a_- T_-^4, \tag{4.88}$$

where ϵ is the vacuum energy difference between the false and true vacua. One can also find the enthalpy $\omega = e + p$. Here v, T and thus e, p, ω all vary from the bubble center to the region far outside the bubble where there is no perturbation. The task is to solve for these fields at regions both inside and outside the bubbles and smoothly match these two sets of solutions through the junction conditions across the bubble wall.

Inside the bubble, we drop all terms related to ϕ including the vacuum energy from ϵ, and we also apply the relation $p = e/3$ [5]. The resulting equations are already given in Eq. 4.86 and the equations are exactly the same as the Minkowski counterpart when the rescaled quantities are used. Now, assuming a spherically symmetric profile and denoting the comoving bubble radius with r and the conformal time elapsed since its nucleation as $\Delta\eta$, the solution should be a self-similar one which depends solely on the ratio $\xi \equiv r/\Delta\eta$. Then we can obtain the same equations as in Minkowski spacetime:

$$\begin{aligned}(\xi - v)\partial_\xi \widetilde{e} &= \widetilde{w}\left[2\frac{v}{\xi} + \gamma^2(1 - \xi v)\partial_\xi v\right], \\ (1 - v\xi)\partial_\xi \widetilde{p} &= \widetilde{w}\gamma^2(\xi - v)\partial_\xi v,\end{aligned} \tag{4.89}$$

[5] Of course, we are assuming a constant value of the speed of sound, i.e., $c_s = 1/\sqrt{3}$. Without doing so, the equations cannot be put into the form in Eq. 4.86. We also dropped any spatial variation of the scalar field and its time variation following the conventional analysis, which amounts to assuming a thin wall.

which can then be combined to give an equation for the velocity field:

$$2\frac{v}{\xi} = \gamma^2(1 - v\xi)\left[\frac{\mu^2}{c_s^2} - 1\right]\partial_\xi v. \tag{4.90}$$

Here $\mu(\xi, v) = (\xi - v)/(1 - \xi v)$, which is the Lorentz boost transformation. This equation can be directly solved given a boundary condition at the wall, to be specified later.

Outside the bubble, the presence of the constant vacuum energy term ϵ seemingly does not allow us to reach Eq. 4.86 for two possible reasons: (1) we can not apply $p = e/3$ since $p = -e$ for vacuum energy; (2) ϵ does not scale like radiation with the behavior $1/a^4$ and the rescaled quantity $a^4 e$ still contains the expansion effect. Let us look more closely at the equations. The parallel projection in Eq. 4.83, when the friction and scalar gradient terms are neglected, becomes

$$\left[(\gamma e)' + 3\frac{a'}{a}\gamma(e + p)\right] + p[\gamma' + \nabla \cdot (\gamma \mathbf{v})] + \nabla \cdot (\gamma e \mathbf{v}) = 0. \tag{4.91}$$

Correspondingly, the perpendicular projection in Eq. 4.85 reduces to

$$\left[\frac{a'}{a}v(e + p) + vp'\right] + \gamma^2(v' + \frac{1}{2}\hat{\mathbf{v}} \cdot \nabla v^2)(e + p) + \hat{\mathbf{v}} \cdot \nabla p = 0. \tag{4.92}$$

In the absence of the vacuum energy inside e and p, both of above equations can be put into the form in Eq. 4.86, by combining the terms in $[\cdots]$ and using $e = 3p$. The resulting equations for the rescaled quantities are the same as in Minkowski spacetime. The presence of ϵ makes this impossible. In Ref. [346], the self-similar velocity profile is assumed anyway. But the existence of an explicit time dependence from a' makes it impossible to solve, except in corners of the

parameter space where it vanishes numerically. It is also in doubt if there exists a self-similar solution at all for these equations and we refrain from going in that direction.

Despite this dilemma, we can still cast above equations in the form 4.86 under the assumption that ϵ is a constant of time during this very short period of time. Then the first equation can be reorganized in the following way:

$$\left[\gamma' + \nabla \cdot (\gamma \mathbf{v}) + 3\frac{a'}{a}\gamma\right](e+p) + \gamma e' + \gamma \mathbf{v} \cdot \nabla e = 0. \tag{4.93}$$

Then ϵ cancels out in $(e+p)$ and drops out in e', and of course also in ∇e. So above e and p can include only the fluid part. Then one can put it back into the previous form 4.91 and define the rescaled quantities: $\widetilde{e}$, $\widetilde{p}$, which obey exactly the same equation as in the Minkowski spacetime. Therefore we obtain the second equation in Eq. 4.86 and the first in Eq. 4.89. Similarly for Eq. 4.92, ϵ drops out in all terms and one can safely define the rescaled quantities, and obtain the third equation in Eq. 4.86 and the second in Eq. 4.89. Combining these two equations again gives the same Eq. 4.90 for the velocity field.

The equation 4.90 for both regions needs the junction conditions at the wall to connect them. They are derived by integrating the conservation of energy momentum tensor across the bubble wall, which gives in the wall frame (note $+, -$ denote quantities at positions immediately outside and inside the wall) [6]

$$T_+^{r\eta} = T_-^{r\eta}, \tag{4.94}$$

$$T_+^{rr} = T_-^{rr}, \tag{4.95}$$

[6]Also we follow the conventional procedure by neglecting the time dependence of the various quantities.

where v_- and v_+ are both at wall frame. These two equations imply

$$(e_+ + p_+)v_+\gamma_+^2 = (e_- + p_-)v_-\gamma_-^2, \tag{4.96}$$

$$(e_+ + p_+)v_+^2\gamma_+^2 + p_+ = (e_- + p_-)v_-^2\gamma_-^2 + p_-. \tag{4.97}$$

Here both $e_\pm$ and $p_\pm$ are the ordinary energy density and pressure and include the vacuum energy ϵ. The reason is while they can be neglected away from the bubble wall due to the vanishing spatial gradient, they jump across the bubble wall and give non-negligible contributions to the above equations. The junction equations can be solved by making the change of variables $v_\pm = \tanh(\vartheta\pm)$ and $\gamma_\pm^2 = \cosh^2(\vartheta\pm)$ which, after simplifying, will yield two linear equations in $\cosh^2(\vartheta+)$ and $\cosh^2(\vartheta-)$. The solution will give

$$\begin{aligned} v_+ &= \sqrt{\frac{(p_- - p_+)(e_- + p_+)}{(e_- - e_+)(e_+ + p_-)}}, \\ v_- &= \sqrt{\frac{(p_+ - p_-)(e_+ + p_-)}{(e_+ - e_-)(e_- + p_+)}}. \end{aligned} \tag{4.98}$$

The product and ratio of v_+ and v_- can further be found,

$$v_+v_- = \frac{p_+ - p_-}{e_+ - e_-}, \quad \frac{v_+}{v_-} = \frac{e_- + p_+}{e_+ + p_-}. \tag{4.99}$$

Plugging $e_\pm, p_\pm$ as specified by the bag equation of state in Eq. 4.88 leads to

$$v_+v_- = \frac{1 - (1 - 3\alpha_+)\sigma}{3 - 3(1 + \alpha_+)\sigma}, \tag{4.100}$$

$$\frac{v_+}{v_-} = \frac{3 + (1 - 3\alpha_+)\sigma}{1 + 3(1 + \alpha_+)\sigma}, \tag{4.101}$$

where α_+ and σ are defined by

$$\alpha_+ = \left.\frac{\epsilon}{a_+T_+^4}\right|_{\text{wall}}, \quad \sigma = \left.\frac{a_+T_+^4}{a_-T_-^4}\right|_{\text{wall}}. \tag{4.102}$$

α_+ characterizes the amount of vacuum energy released from the phase transition normalized by the total radiation energy density immediately outside the bubble (as denoted by the subscript "wall"). It is not the α usually used in phase transition analyses. Rather, its value should be solved from the requirement that far from the bubble where the plasma is not perturbed (denote by ∞), the corresponding α_+ at ∞ matches α. The two equations in Eq. 4.101 can be solved for both r and v_+ to give two branch solutions for the velocity in the symmetric phase,

$$v_+ = \frac{1}{1+\alpha_+}\left[\left(\frac{v_-}{2}+\frac{1}{6v_-}\right) \pm \sqrt{\left(\frac{v_-}{2}+\frac{1}{6v_-}\right)^2 + \alpha_+^2 + \frac{2}{3}\alpha_+ - \frac{1}{3}}\right]. \quad (4.103)$$

Up to this point, the results for the velocity profile are exactly the same as in Minkowski spacetime, but with the understanding that the time t is replaced by the conformal time η, $v = d\mathbf{x}/d\eta$ and (e, p) are replaced by $(\widetilde{e}, \widetilde{p})$. We will not go into the details of the physics of above results but only summarize the main features of the velocity profile relevant for this study and refer the reader to Ref. [70] for a more detailed analysis.

The fluid admits three modes of motion: deflagration, detonation and supersonic deflagration (also called hybrid) [260], with representative velocity profiles shown in Fig. 4.9. For deflagration, the velocity inside the bubble vanishes and is only non-zero outside. Detonation is the opposite, with non-zero velocity inside the bubble. Supersonic deflagration has non-zero velocity both inside and outside the bubble. Therefore for deflagration, $v_- = v_w$ which should be used in Eq. 4.103 to find v_+, choosing a value of α_+. This v_+ is Lorentz transformed to the plasma

static frame to find $v(v_w)$ immediately outside the wall, which is then used as the boundary condition to solve for $v(\xi)$ outside the wall. It might not consistently drop to zero, in which case a shock front is encountered and should be determined. Beyond the shock $v(\xi) = 0$. This gives a complete profile, but not yet the correct one, since a specific value of α_+ is used in above determination of the profile. This value needs to be tuned such that $\alpha_+ = \alpha$ far outside the bubble. For detonation, $v_+ = v_w$ and v_- can be determined from Eq. 4.103 with $\alpha_+ = \alpha$ as outside the bubble the plasma is not perturbed. Then one can Lorentz transform v_- to $v(v_w)$ immediately inside the wall and use it as a boundary condition to determine the full profile. No inconsistency or shock front will be encountered in this case. For supersonic deflagration, the condition $v_- = c_s$ is the boundary condition used. Shock front can exist in this case and should be treated similarly. We refer the reader for more details in Ref. [70].

4.4.3 Velocity Field in the Sound Shell Model

With the velocity profile surrounding a single bubble determined, we can now find the total velocity field, as needed in Eq. 4.22. As we have already seen, in an expanding universe the equations of motion of the fluid are exactly the same as those in non-expanding Minkowski spacetime. This means that the equation of motion for the sound waves remain the same as its Minkowski counterpart, as long as we replace t by η and interpret the velocity as obtained by differentiation with respect to the conformal time. So the procedure parallels that in Ref. [3].

Lets start with the contribution from one bubble. Before it collides with

another bubble at η_{fc} (see Fig. 4.5), the velocity profile is governed by equations given in previous sections. After the collision, the friction vanishes and the velocity field starts freely propagating and becomes sound waves, with the speed of sound c_s. So we need to match the velocity profile surrounding this bubble with the velocity field at the time when the friction vanishes. Before collision, we can Fourier decompose the velocity field as

$$v^i(\eta < \eta_{fc}, \mathbf{x}) = \frac{1}{2}\int \frac{d^3q}{(2\pi)^3}\left[\widetilde{v}^i_{\mathbf{q}}(\eta)e^{i\mathbf{q}\cdot\mathbf{x}} + \widetilde{v}^{i*}_{\mathbf{q}}(\eta)e^{-i\mathbf{q}\cdot\mathbf{x}}\right], \tag{4.104}$$

with $\mathbf{x}$ being the comoving coordinate and $\mathbf{q}$ the comoving wavenumber. After collision, the velocity field freely propagates as sound waves and admits the following decomposition:

$$v^i(\eta, \mathbf{x}) = \int \frac{d^3q}{(2\pi)^3}\left[v^i_{\mathbf{q}}e^{-i\omega\eta+i\mathbf{q}\cdot\mathbf{x}} + v^{i*}_{\mathbf{q}}e^{i\omega\eta-i\mathbf{q}\cdot\mathbf{x}}\right], \tag{4.105}$$

where $\omega = qc_s$. Since the plasma consists of relativistic particles, $c_s = 1/\sqrt{3}$. Here $v^i_{\mathbf{q}}$ is independent of η, different from $\widetilde{v}^i_{\mathbf{q}}(\eta)$.

The task is then to find the contribution to $v^i_{\mathbf{q}}$ from $\widetilde{v}^i_{\mathbf{q}}(\eta)$ at η_{fc}. Since the equation governing the sound waves is of second order, we need the following initial conditions: $\widetilde{v}^i_{\mathbf{q}}(\eta)$ and $\widetilde{v}^{i\prime}_{\mathbf{q}}(\eta)$ at η_{fc}. While one can obtain $\widetilde{v}^i_{\mathbf{q}}(\eta)$ directly from the velocity profile in the previous section, one subtlety appears here for $\widetilde{v}^{i\prime}_{\mathbf{q}}(\eta)$. As demonstrated in Ref. [3], the equation governing $\widetilde{v}^{i\prime}_{\mathbf{q}}(\eta)$ before the collision relies on a force term from the scalar field, which disappears once the collision occurs. So the value $\widetilde{v}^{i\prime}_{\mathbf{q}}(\eta)$ calculated with this force (as was previously used in Ref. [71]) is different from the corresponding value without it. It is the latter one that should enter the initial conditions for the sound waves. In this

case, rather than calculating $\widetilde{v}^{i\prime}_{\mathbf{q}}(\eta)$ from the velocity profile $\widetilde{v}^{i}_{\mathbf{q}}(\eta)$, we need to calculate it directly from the energy fluctuation:

$$\lambda(x) = \frac{\widetilde{e}(x) - \bar{\widetilde{e}}}{\bar{\widetilde{\omega}}}, \tag{4.106}$$

where a bar denotes averaged quantity and tilde denotes rescaled quantity. Similarly its Fourier component $\widetilde{\lambda}_{\mathbf{q}}$ can be defined in analogy to Eq. 4.104. The equations for sound waves then follow:

$$\begin{aligned} \widetilde{\lambda}'_{\mathbf{q}} + iq^j \widetilde{v}^j_{\mathbf{q}} &= 0, \\ \widetilde{v}^{j\prime}_{\mathbf{q}} + c_s^2 iq^j \widetilde{\lambda}_{\mathbf{q}} &= 0. \end{aligned} \tag{4.107}$$

Therefore $\widetilde{v}^{j\prime}_{\mathbf{q}} = -c_s^2 iq^j \widetilde{\lambda}_{\mathbf{q}}$, and one needs to calculate $v^i(\eta, \mathbf{x})$ and $\lambda(\eta, \mathbf{x})$ from the self-similar velocity profile for one bubble. In coordinate space, the velocity profile for the n-th bubble can be written as

$$\mathbf{v}^{(n)}(\eta, \mathbf{x}) = \hat{\mathbf{R}}(\mathbf{x}) v(\xi), \tag{4.108}$$

where $\mathbf{R}(\mathbf{x}) \equiv \mathbf{x} - \mathbf{x}^{(n)}$, $\xi \equiv |\mathbf{R}^{(n)}|/T^{(n)}$ and $T^{(n)}(\eta) \equiv \eta - \eta^{(n)}$, with $\mathbf{x}^{(n)}$ and $\eta^{(n)}$ the coordinate of the bubble center and the conformal time when the bubble is nucleated. Similarly for λ, as it is a scalar field, we can define $\lambda(\eta, \mathbf{x}) \equiv \lambda(\xi)$. With the profile specified in coordinate space, the corresponding Fourier coefficients can be obtained straightforwardly

$$\begin{aligned} \widetilde{v}^{j(n)}_{\mathbf{q}}(\eta_{fc}) &= e^{-i\mathbf{q}\cdot\mathbf{x}^{(n)}} (T^{(n)})^3 i\hat{z}^j f'(z)|_{\eta=\eta_{fc}}, \\ \widetilde{\lambda}^{(n)}_{\mathbf{q}}(\eta_{fc}) &= e^{-i\mathbf{q}\cdot\mathbf{x}^{(n)}} (T^{(n)})^3 l(z)|_{\eta=\eta_{fc}}, \end{aligned} \tag{4.109}$$

with $\mathbf{z} \equiv \mathbf{q}T^{(n)}$ and the two functions $f(z)$ and $l(z)$ given by

$$\begin{aligned} f(z) &= \frac{4\pi}{z}\int_0^\infty d\xi\ v(\xi)\ \sin(z\xi), \\ l(z) &= \frac{4\pi}{z}\int_0^\infty d\xi\ \xi\ \lambda(\xi)\sin(z\xi). \end{aligned} \tag{4.110}$$

Then the n-th bubble's contribution to the Fourier coefficient of the sound waves is

$$v_{\mathbf{q}}^{j(n)} = \frac{1}{2}\left[\widetilde{v}_{\mathbf{q}}^{j(n)}(\eta_{fc}) + c_s\hat{q}^j\widetilde{\lambda}_{\mathbf{q}}^{(n)}(\eta_{fc})\right]e^{i\omega\eta_{fc}}, \tag{4.111}$$

and after using the explicit expression of the bubble profile,

$$v_{\mathbf{q}}^{j(n)} = i\hat{z}^j(T_{fc}^{(n)})^3 e^{i\omega\eta_{fc} - i\mathbf{q}\cdot\mathbf{x}^{(n)}}A(z_{fc}), \tag{4.112}$$

where $A(z_{fc}) = [f'(z_{fc}) - ic_s l(z_{fc})]/2$, with an example shown in Fig. 4.10. Thus we have calculated the contribution to $v_{\mathbf{q}}^i$ from one bubble that is nucleated randomly. The randomness of this bubble is reflected in its formation time, location, collision time and its radius. Since the radius at collision is fixed once its formation and collision times are given, there are three independent random variables.

The velocity field after all bubbles have disappeared, can be assumed to be the linear addition of the contributions from all bubbles, which is the essence of the sound shell model [71, 3]. Suppose the total number of bubbles nucleated within a Hubble volume with comoving size V_c is N_b. Then the velocity field can be assumed, according to the sound shell model, to be given by

$$v_{\mathbf{q}}^i = \sum_{n=1}^{N_b} v_{\mathbf{q}}^{i(n)}. \tag{4.113}$$

4.4.4 Velocity Power Spectrum

As these N_b bubbles are just one realization of the phase transition, the resulting $v^i_{\mathbf{q}}$ has a random nature with it and follows a Gaussian distribution to a good approximation according to the central limit theorem [7]. Randomness of this kind can be removed by doing an ensemble average of the product: $\langle v^i_{\mathbf{q}} v^{j*}_{\mathbf{q}} \rangle$, which is all needed for a Gaussian distribution. Now let us see how this is achieved.

The N_b bubbles can be separated into groups with the bubbles within each group sharing a common formation and collision time. Then the only variable that is random across the bubbles of one group, e.g., group g with N_g bubbles, is the spatial locations of the bubbles when they form. Now consider group g. Its contribution to the correlator is

$$\langle v^i_{\mathbf{q_1}} v^{j*}_{\mathbf{q_2}} \rangle_g = \hat{q}^i_1 \hat{q}^j_2 [T^{(g)}_{fc}]^6 A(z^{(n)}_{fc}) A(z^{(m)}_{fc})^* e^{i(\omega_1-\omega_2)\eta^{(g)}_{fc}} \langle \sum_{m,n=1}^{N_g} e^{i\mathbf{q_2}\cdot\mathbf{x^{(m)}} - i\mathbf{q_1}\cdot\mathbf{x^{(n)}}} \rangle \quad (4.114)$$

Here the order of the ensemble average and the summation can be switched. Since the ensemble average of each of these N_g terms gives the same result and oscillatory cross terms vanish, we have

$$\begin{aligned} \langle \sum_{m,n=1}^{N_g} e^{i\mathbf{q_2}\cdot\mathbf{x^{(m)}} - i\mathbf{q_1}\cdot\mathbf{x^{(n)}}} \rangle &= N_g \delta_{mn} \langle e^{i\mathbf{q_2}\cdot\mathbf{x^{(m)}} - i\mathbf{q_1}\cdot\mathbf{x^{(n)}}} \rangle \\ &= N_g \frac{1}{V_c} \int d^3\mathbf{x}^{(*)}\ e^{i(\mathbf{q_2}-\mathbf{q_1})\cdot\mathbf{x}^{(*)}} \\ &= N_g \frac{1}{V_c} (2\pi)^3 \delta^3(\mathbf{q_1}-\mathbf{q_2}). \end{aligned} \quad (4.115)$$

The constraint $\mathbf{q_1} = \mathbf{q_2}$ removes the $\eta^{(g)}_{fc}$ dependence, leading to a result solely dependent on the conformal lifetime of the bubble $T^{(g)}_{fc} \equiv \eta_{\rm lt}$ but not their absolute

[7] If there is a sufficiently large population of bubbles within this single volume, the summation of these contributions can also remove the randomness, equivalent to an ensemble average.

formation or destruction time:

$$\langle v^i_{\mathbf{q_1}} v^{j*}_{\mathbf{q_2}} \rangle_g = \hat{q}^i_1 \hat{q}^j_2 \eta^6_{\rm lt} |A(q\eta_{\rm lt})|^2 \frac{N_g}{V_c} (2\pi)^3 \delta^3(\mathbf{q_1} - \mathbf{q_2}). \tag{4.116}$$

This result means that we can combine groups with the same $\eta_{\rm lt}$, and of course, different formation time, by solely enlarging the value of N_g. In the following we will simply stick to the group label "g", though its definition is changed and now includes all bubbles with the same $\eta_{\rm lt}$. Restricting to a sufficiently small region centered at $\eta_{\rm lt}$, the number N_g is an still an infinitesimally small fraction of N_b and can be written as

$$N_g = N_b P(\eta_{\rm lt}) d\eta_{\rm lt}, \tag{4.117}$$

where $P(\eta_{\rm lt})$ is the probability density for bubbles to have conformal lifetime in the range $(\eta_{\rm lt}, \eta_{\rm lt} + d\eta_{\rm lt})$, thus with dimension 1 and normalized by

$$\int d\eta_{\rm lt} P(\eta_{\rm lt}) = 1. \tag{4.118}$$

Adding the contributions from all the groups and noting that cross terms vanish due to the oscillatory behavior, we have

$$\langle v^i_{\mathbf{q_1}} v^{j*}_{\mathbf{q_2}} \rangle = \hat{q}^i_1 \hat{q}^j_2 (2\pi)^3 \delta^3(\mathbf{q}_1 - \mathbf{q}_2) \int d\eta_{\rm lt} \left[P(\eta_{\rm lt}) \frac{N_b}{V_c} \right] \eta^6_{\rm lt} |A(q\eta_{\rm lt})|^2. \tag{4.119}$$

One can now identify the quantity in the square bracket as the conformal lifetime distribution defined in Eq. 4.56:

$$P(\eta_{\rm lt}) \frac{N_b}{V_c} = \widetilde{n}_{b,c}(\eta_{\rm lt}). \tag{4.120}$$

Since $P(\eta_{\rm lt})$ is of dimension 1, it is convenient to define a dimensionless version of it: ν, with

$$P(\eta_{\rm lt}) \equiv \beta_c \nu(\beta_c \eta_{\rm lt}), \tag{4.121}$$

and thus

$$\widetilde{n}_{b,c}(\eta_{\rm lt}) = \frac{\beta_c}{R_{*c}^3}\nu(\beta_c\eta_{\rm lt}), \tag{4.122}$$

where R_{*c} is the asymptotic comoving mean bubble separation. Then we have

$$\langle v^i_{\mathbf{q_1}} v^{j*}_{\mathbf{q_2}}\rangle = \hat{q}^i_1\hat{q}^j_2(2\pi)^3\delta^3(\mathbf{q}_1-\mathbf{q}_2)\underbrace{\frac{1}{R_{*c}^3\beta_c^6}\int d\widetilde{T}\widetilde{T}^6\nu(\widetilde{T})|A(\frac{q\widetilde{T}}{\beta_c})|^2}_{\equiv P_v(q)}, \tag{4.123}$$

with here $\widetilde{T} = \beta_c\eta_{\rm lt}$, and we have defined the spectral density $P_v(q)$ for the plane wave amplitude $v^i_{\mathbf{q}}$. Lets write down the explicit expression for $\nu(\widetilde{T})$. From Eq. 4.122 and 4.56, we have

$$\nu(\widetilde{T}) \;=\; v_w R_{*c}^3\int_{t_c}^{t_f} dt' p(t') a^3(t')\frac{\mathcal{A}_c(t', v_w\widetilde{T}/\beta_c)}{\beta_c}, \tag{4.124}$$

which can be directly used for numerical calculations once t' is transformed to T' as demonstrated in previous sections. The numerically calculated distribution for the examples we have been using is shown in Fig. 4.11. For all choices of κ, v_w, the distributions are almost indistinguishable, shown as the blue curve, and it coincides with the gray dashed curve which denotes the distribution $e^{-\widetilde{T}}$, derived analytically in Ref. [3]. With $\nu(\widetilde{T})$ obtained, the spectral density $P_v(\widetilde{T})$ can be calculated straightforwardly from its definition in Eq. 4.123.

To calculate the velocity power spectrum, we need to evaluate the correlator

$$\langle\widetilde{v}^i_{\mathbf{q}}(\eta_1)\widetilde{v}^{j*}_{\mathbf{k}}(\eta_2)\rangle| = \delta^3(\mathbf{q}-\mathbf{k})\hat{q}^i\hat{k}^j G(q,\eta_1,\eta_2), \tag{4.125}$$

and it can be shown that

$$G(q,\eta_1,\eta_2) = 2P_v(q)\cos[\omega(\eta_1-\eta_2)]. \tag{4.126}$$

Plugging it into Eq. 4.24 or 4.25 gives the stress energy correlator. Also the velocity field power spectrum $\mathcal{P}_v$ follows naturally,

$$\begin{aligned}\mathcal{P}_v &= \frac{q^3}{2\pi^2}[2P_v(q)] \\ &= \frac{1}{64\pi^4 v_w^6}(qR_{*c})^3 \int d\widetilde{T}\widetilde{T}^6\nu(\widetilde{T})\left|A\left(\frac{(qR_{*c})\widetilde{T}}{(8\pi)^{1/3}v_w}\right)\right|^2, \end{aligned} \tag{4.127}$$

and we have used $\beta_c R_{*c} = (8\pi)^{1/3}v_w$. It is obvious to see that $\mathcal{P}_v$ is dimensionless, as it is constructed with purely dimensionless quantities. A representative profile for the velocity power spectrum is shown in Fig. 4.12 assuming an exponential bubble nucleation rate, and more details about its properties can be found in Ref. [71].

4.5 Gravitational Wave Power Spectrum

We can now go back to Eq. 4.17 and collect all the pieces to calculate the gravitational power spectrum. It only remains to calculate the Green's function, and it requires to specify an expansion scenario. We will as usual focus on the RD and MD scenarios as examples, but the method here is applicable to any expansion history.

4.5.1 Solutions in Radiation and Matter Domination

First, we choose a parameter to measure the time of the cosmic history. It can either be the actual time t, the conformal time η, the redshift z or the scale factor a. To present a result independent of the origin of the time coordinate, we choose the dimensionless scale factor ratio $y \equiv a/a_s$, giving then $d/dt = \dot{a}/a_s d/dy$. Here

a_s is the time when the source, the sound waves, becomes active, so that y starts from 1. The Friedmann equation gives the relation between y and the conformal time

$$y = \frac{\kappa_M}{4}(a_s H_s)^2(\eta - \eta_s)^2 + a_s H_s(\eta - \eta_s) + 1. \tag{4.128}$$

It is obvious that when $\eta = \eta_s$, we have $y = 1$. Also it does not matter how the origin of the conformal time is chosen as it only depends on $\Delta\eta \equiv \eta - \eta_s$. For RD, where $\kappa_M \sim 0$, we have $y = a_s H_s(\eta - \eta_s) + 1$. For MD, $\kappa_M \approx 1$ and $y = [\frac{1}{2}a_s H_s(\eta - \eta_s) + 1]^2$. In the literature, it is usually approximated that $a \propto \eta$ deep inside the radiation era or $a \propto \eta^2$ deep inside the matter era. However we remain agnostic about when the phase transition happens and do not require it to start deep inside the radiation or matter era. Also the duration of the phase transition is very small compared with the conformal time, which makes such approximation quite crude. But our choice using y is free from above limitations and offers a more accurate description of phase transition process.

With y, the Hubble rate, when assuming the existence of both matter and radiation components, takes the following form

$$H = H_s\sqrt{\frac{\kappa_M}{y^3} + \frac{1 - \kappa_M}{y^4}}, \tag{4.129}$$

where κ_M is the matter fraction of the total energy density at t_s. Note this κ_M is defined differently from that in Eq. 4.46, which is defined at T_c. If the lifetime of the sound waves is sufficiently long, we can neglect this difference.

Switching from the conformal time η to y in Eq. 4.8, the Einstein equation

becomes [8]:

$$(\kappa_M y + 1 - \kappa_M)\frac{d^2 h_q}{dy^2} + \left[\frac{5}{2}\kappa_M + \frac{2(1-\kappa_M)}{y}\right]\frac{dh_q}{dy} + \widetilde{\widetilde{q}}^2 h_q = \frac{16\pi G a(y)^2 \pi_q^T(y)}{(a_s H_s)^2} \quad (4.130)$$

Here $\widetilde{\widetilde{q}} \equiv q/(a_s H_s)$, and characterizes the number of wavelengths contained within a Hubble radius at t_s. The Green's function can be found by solving the homogeneous version of this equation, together with a slightly modified boundary conditions compared with Eq. 4.14:

$$G(y \leqslant y_0) = 0, \qquad \frac{\partial G(y, y_0)}{\partial y}|_{\widetilde{\eta}=\widetilde{y}_0^+} = \frac{1}{\kappa_M y_0 + 1 - \kappa_M}. \quad (4.131)$$

The solution to the homogeneous equation is a linear combination of the hypergeometric function and Bessel functions. For the case of radiation domination $\kappa_M \ll 1$ and matter domination $\kappa_M \approx 1$, the solutions take simpler forms that can be expressed in terms of elementary functions. For RD, the equation becomes simpler when expressed using the parameter $\widetilde{y}$, defined by

$$\widetilde{y} = y\widetilde{\widetilde{q}} = q(\eta - \eta_s) + \widetilde{\widetilde{q}} = \Delta\widetilde{\eta} + \widetilde{\widetilde{q}}. \quad (4.132)$$

Then the Einstein equation becomes

$$\frac{d^2 h_q}{d\widetilde{y}^2} + \frac{2}{\widetilde{y}}\frac{dh_q}{d\widetilde{y}} + h_q = \frac{16\pi G a(y)^2 \pi_q^T(y)}{q^2}. \quad (4.133)$$

The corresponding Green's function can be easily solved:

$$G(\widetilde{y}, \widetilde{y}_0) = \frac{\widetilde{y}_0 \sin(\widetilde{y} - \widetilde{y}_0)}{\widetilde{y}}. \quad (4.134)$$

For MD, the wave equation can be similarly simplified with

$$\widetilde{y} = y\widetilde{\widetilde{q}}^2 = \left[\frac{1}{2}\Delta\widetilde{\eta} + \widetilde{\widetilde{q}}\right]^2. \quad (4.135)$$

[8] We are using a simplified notation for h and π^T

Note this definition is different from that in the radiation dominated case. Then the Einstein equation becomes

$$\widetilde{y}\frac{d^2h_q}{d\widetilde{y}^2}+\frac{5}{2}\frac{dh_q}{d\widetilde{y}}+h_q=\frac{16\pi Ga(\widetilde{y})^2\pi_q^T(\widetilde{y})}{q^2}. \tag{4.136}$$

The homogeneous equation for h_q can be transformed into the Bessel equation for a different variable $Z(\lambda)$ defined by $h_q=(\lambda/2)^{-3/2}Z(\lambda)$ with $\lambda=2\sqrt{\widetilde{y}}$:

$$\lambda^2Z''(\lambda)+\lambda Z'(\lambda)+\left[\lambda^2-\left(\frac{3}{2}\right)^2\right]Z(\lambda)=0. \tag{4.137}$$

The two independent solutions are the first and second kind Bessel functions both with order 3/2, which can all be expressed in elementary functions. Upon using the boundary conditions, the Green's function is found to be [9] :

$$G(\widetilde{y},\widetilde{y}_0)=\frac{(\lambda\lambda_0+1)\sin(\lambda-\lambda_0)-(\lambda-\lambda_0)\cos(\lambda-\lambda_0)}{\lambda^3/2}. \tag{4.139}$$

Finally in both cases, the gravitational wave amplitude is given by

$$h_{ij}(\widetilde{y},\mathbf{q})=\int_{\widetilde{y}_s}^{\widetilde{y}}d\widetilde{y}'G(\widetilde{y},\widetilde{y}')\frac{16\pi Ga(\widetilde{y}')^2\pi_{ij}^T(\widetilde{y}',\mathbf{q})}{q^2}. \tag{4.140}$$

[9] Alternatively, one can express above Green's functions using the conformal time. The corresponding Green's functions are defined to be zero for $\eta\leqslant\eta_0$ and for $\eta>\eta_0$,

$$G(\widetilde{\eta},\widetilde{\eta}_0)=\begin{cases}\frac{\widetilde{\eta}_0}{\widetilde{\eta}}\sin(\widetilde{\eta}-\widetilde{\eta}_0), & \text{RD}\\ \frac{\widetilde{\eta}_0}{\widetilde{\eta}^3}\left[(\widetilde{\eta}_0-\widetilde{\eta})\cos(\widetilde{\eta}-\widetilde{\eta}_0)+(\widetilde{\eta}_0\widetilde{\eta}+1)\sin(\widetilde{\eta}-\widetilde{\eta}_0)\right]. & \text{MD}\end{cases} \tag{4.138}$$

We note that there is a typo in the Green's function for the matter dominated universe given in Ref. [335], where instead of $(\widetilde{\eta}_0-\widetilde{\eta})\cos(\widetilde{\eta}-\widetilde{\eta}_0)$, they have $-(\widetilde{\eta}_0-\widetilde{\eta})\cos(\widetilde{\eta}-\widetilde{\eta}_0)$.

4.5.2 Gravitational Wave Power Spectrum

The spectral density for h', when using $\widetilde{y}$ and the dimensionless stress energy tensor correlator $\widetilde{\Pi}$ defined in Eq. 4.27, becomes

$$P_{h'} = [16\pi G\left(\bar{\widetilde{\epsilon}}+\bar{\widetilde{p}}\right)\bar{U}_f^2]^2 L_f^3 \int_{\widetilde{y}_s}^{\widetilde{y}} d\widetilde{y}_1 \int_{\widetilde{y}_s}^{\widetilde{y}} d\widetilde{y}_2 \left(\frac{\partial\widetilde{y}}{\partial\widetilde{\eta}}\right)^2 \frac{\partial G(\widetilde{y},\widetilde{y}_1)}{\partial\widetilde{y}} \frac{\partial G(\widetilde{y},\widetilde{y}_2)}{\partial\widetilde{y}} \times \frac{a_s^8}{a^2(\widetilde{y}_1)a^2(\widetilde{y}_2)} \frac{\widetilde{\Pi}^2(kL_f, k\eta_1, k\eta_2)}{k^2}. \quad (4.141)$$

From the explicit form of the Green's functions derived earlier, we can see $P_{h'}$ has the correct behavior $\propto 1/a(\widetilde{y})^2$ for the mode deep inside the horizon [10]. The dimensionless source correlator can be obtained from Eq. 4.25, 4.27, 4.126:

$$\widetilde{\Pi}^2\left(kR_{*c}, \beta_c\left|\eta_1-\eta_2\right|\right) = \frac{\pi}{2}\frac{1}{\bar{U}_f^4}\int d^3\widetilde{q}\mathcal{P}_v(\widetilde{q})\mathcal{P}_v(\widetilde{\bar{q}})\frac{(1-\mu^2)^2}{\widetilde{q}\widetilde{\bar{q}}^5} \times \cos\left[c_s\widetilde{q}\frac{\beta_c(\eta_1-\eta_2)}{\beta_c R_{*c}}\right]\cos\left[c_s\widetilde{\bar{q}}\frac{\beta_c(\eta_1-\eta_2)}{\beta_c R_{*c}}\right] \quad (4.142)$$

Here $\widetilde{q} = qR_{*c}$, a dimensionless quantity, and we use $L_f = R_{*c}$. In Fig. 4.13, we show this auto-correlator of the source as a function of $\beta_c|\eta_1-\eta_2|$. We can see the correlation is quickly lost as $\beta_c|\eta_1-\eta_2|$ becomes larger than $\mathcal{O}(1)$. Since the source correlator depends only on $\eta_1-\eta_2$, we can change the integration variables from $\widetilde{y}_{1,2}$ to a quantity proportional to $(\eta_1-\eta_2)$ and another independent linear combination. For RD and MD, the relation between $(\eta_1-\eta_2)$ and $y_{1,2}$ is given from Eq. 4.132, 4.135:

$$\frac{\beta_c(\eta_1-\eta_2)}{\beta_c R_{*c}} = \frac{1}{R_{*c}a_s H_s}\begin{cases} y_1-y_2 \\ 2(\sqrt{y_1}-\sqrt{y_2}) \end{cases}, \quad (4.143)$$

[10] For modes deep inside the horizon, $\widetilde{y} \gg 1$ and $\widetilde{y}_0 \gg 1$. Then both Green's functions take a universal form $\frac{a_0}{a}\sin(\widetilde{\eta}-\widetilde{\eta}_0)$. This implies that $h' \propto 1/a$, $P_{h'} \propto 1/a^2$ and $\mathcal{P}_{\rm GW} \propto 1/a^4$, behaving like radiation which is true for massless gravitons.

where the upper row applies to RD and lower one to MD. Then for RD, we can make the following change of variables:

$$\begin{cases} y_1 \\ \\ y_2 \end{cases} \quad \Rightarrow \quad \begin{cases} y_1 - y_2 \equiv y_- \ , \\ \\ \frac{y_1+y_2}{2} \equiv y_+ \ . \end{cases} \tag{4.144}$$

The integration range is $1 - \frac{1}{2}y_- \leqslant y_+ \leqslant y + \frac{1}{2}y_-$ when $1 - y \leqslant y_- \leqslant 0$, and $1 + \frac{1}{2}y_- \leqslant y_+ \leqslant y - \frac{1}{2}y_-$ when $0 \leqslant y_- \leqslant y - 1$. Similarly for MD, we can perform the following transformations:

$$\begin{cases} y_1 \\ \\ y_2 \end{cases} \quad \Rightarrow \quad \begin{cases} \lambda_1 - \lambda_2 \equiv y_- \ , \\ \\ \frac{\lambda_1+\lambda_2}{2} \equiv y_+ \ , \end{cases} \tag{4.145}$$

where $\lambda_i = 2\sqrt{y_i}$ and the Jacobian is $\sqrt{y_1 y_2}$. The range of integration is $2 + \frac{1}{2}y_- \leqslant y_+ \leqslant 2\sqrt{y} - \frac{1}{2}y_-$ when $0 \leqslant y_- \leqslant 2(\sqrt{y} - 1)$ and $2 - \frac{1}{2}y_- \leqslant y_+ \leqslant 2\sqrt{y} + \frac{1}{2}y_-$ when $2(1 - \sqrt{y}) \leqslant y_- \leqslant 0$.

It turns out the relation $y_- \ll y_+$ generally holds, barring special parameter space. This can be seen from Eq. 4.143 by noting that $\beta_c R_{*c} = (8\pi)^{1/3} v_w \approx 3v_w < 3$, $R_{*c} a_s H_s \sim \mathcal{O}(10^{-3})$ from Fig. 4.7, and thus $y_- \sim \mathcal{O}(10^{-3})/v_w \times \beta_c(\eta_1 - \eta_2)$. Except for extremely small v_w, which gives highly suppressed gravitational waves, we have $y_- \ll 1$. On the contrary, $y_+ \sim \mathcal{O}(1)$. Then we have $y_- \ll y_+$. This means in the integration over y_+, we can keep the leading order in y_-.

Now lets look in more detail at the integrand. For RD and MD, the factor containing Green's function can be written as

$$\frac{\partial G(\widetilde{y}, \widetilde{y}_1)}{\partial \widetilde{y}} \frac{\partial G(\widetilde{y}, \widetilde{y}_2)}{\partial \widetilde{y}} = \begin{cases} \frac{1}{\widetilde{y}^2} \left[c_0^R \widetilde{y}^0 + c_{-1}^R \frac{1}{\widetilde{y}} + \cdots \right] \\ \\ \frac{1}{\widetilde{y}^3} \left[c_0^M \widetilde{y}^0 + c_{-1}^M \frac{1}{\widetilde{y}} + \cdots \right] \end{cases} \equiv \begin{cases} \frac{1}{\widetilde{y}^2} \\ \\ \frac{1}{\widetilde{y}^3} \end{cases} \times \mathcal{G}_2(\widetilde{y}, \widetilde{y}_1, \widetilde{y}_2) \tag{4.146}$$

Then

$$\mathcal{P}_{\rm GW}(y, kR_{*c}) = \frac{\left[16\pi G\left(\widetilde{\bar{\epsilon}}+\widetilde{\bar{p}}\right)\bar{U}_f^2\right]^2}{24\pi^2 H^2 H_s^2}\frac{1}{y^4}(kR_{*c})^3 \times \int dy_- \widetilde{\Pi}^2\left(kR_{*c}, \beta_c|\eta_1-\eta_2|\right)\left[\int dy_+ \frac{\mathcal{G}_2(\widetilde{y}, \widetilde{y}_1, \widetilde{y}_2)}{\widetilde{\widetilde{k}}^2}\begin{Bmatrix} y_1^{-2}y_2^{-2} \\ y_1^{-3/2}y_2^{-3/2}\end{Bmatrix}\right] \quad (4.147)$$

In the square bracket, $y_{1,2}$ are understood to be functions of $y_\pm$ (note that $\widetilde{y}$ is defined differently for matter and radiation cases). The reason we associate a factor of $\widetilde{\widetilde{k}}^{-2}$ with $\mathcal{G}_2$ is that $\mathcal{G}_2 \propto \widetilde{\widetilde{k}}^2$ to a good approximation. For both RD and MD, the integral over y_+ leads to a result in the following form:

$$\left[\int dy_+ \cdots\right] = \frac{1}{2}\Upsilon(y)\cos\left(\widetilde{\widetilde{k}} y_-\right). \quad (4.148)$$

The profile in a wide range of y is shown in Fig. 4.15. We can see Υ of RD is slightly larger than MD. For both cases, Υ approaches an asymptotic value: 1 for RD and 2/3 for MD, irrespective of how long the source lasts. This is due to the dilution of the source over time, which makes the contribution from later time increasingly suppressed. To have a better understanding of the behavior of $\Upsilon(y)$, lets see how they can be obtained in a simpler analytical way.

First for RD, neglecting terms suppressed by $(R_{*c}a_sH_s)$ or y^{-1}, the dominant contributions to the integrand of the power spectrum are

$$\mathcal{G}_2^{\rm RD} = \frac{1}{2y_+^2}\left\{\cos\left[\widetilde{\widetilde{k}} y_-\right] + \cos\left[2\widetilde{\widetilde{k}}(y-y_+)\right]\right\} + \cdots. \quad (4.149)$$

The second term is y_- independent and is a highly oscillatory function of y_+, which averages to zero during the integration over y_+ (see Fig. 4.14 for the non-oscillatory and oscillatory contributions). On the other hand, the first term, a

function of y_-, when integrated, gives the dominant contribution:

$$\Upsilon_{\rm RD} = 1 - \frac{1}{y}. \tag{4.150}$$

For $y \gg 1$, it approaches an asymptotic value of 1. Since this asymptotic value can only be reached for a long enough source, a realistic phase transition might not satisfy this. We will come to this point later.

Similarly for MD, we can perform analogous manipulations and keep only the leading order and also non-oscillatory term:

$$\mathcal{G}_2^{\rm MD} = \frac{8}{y_+^4} \cos\left[\widetilde{\widetilde{k}} y_-\right] + \cdots . \tag{4.151}$$

Upon integration, it gives the dominant contribution:

$$\Upsilon_{\rm MD} = \frac{2}{3}\left(1 - \frac{1}{y^{3/2}}\right). \tag{4.152}$$

For $y \gg 1$, it approaches the previously observed asymptotic value of 2/3. Thus barring other differences for RD and MD, the different expansion behaviors lead to a suppression of gravitational wave spectrum for MD, when compared with RD.

With $\Upsilon(y)$ obtained, the power spectrum as a function of y can be written in the following form

$$\begin{aligned}\mathcal{P}_{\rm GW}(y, kR_{*c}) = &\frac{[16\pi G\left(\widetilde{\widetilde{\epsilon}} + \widetilde{\widetilde{p}}\right)\bar{U}_f^2]^2}{48\pi^2 H^2 H_s^2} \frac{1}{y^4} (kR_{*c})^3 \\ &\times \left[\int dy_- \cos\left(\widetilde{\widetilde{k}} y_-\right) \widetilde{\Pi}^2\left(kR_{*c}, \beta_c|\eta_1 - \eta_2|\right)\right] \times \Upsilon(y). \end{aligned} \tag{4.153}$$

Here note that using Eq. 4.143, we have $\widetilde{\widetilde{k}} y_- = k(\eta_1 - \eta_2)$. The integral over y_- is obtained by plugging the explicit expression of $\widetilde{\Pi}$, which results in a three-fold

integral. The integration of y_- over the three trigonometric functions result in a δ function, and makes the angle integration of $\widetilde{q}$ in Eq. 4.142 trivial. We are left eventually with a one fold integral over the magnitude of $\widetilde{q}$, and the spectrum can be put in the following standard form:

$$\mathcal{P}_{\rm GW}(y, kR_{*c}) = 3\Gamma^2\ \bar{U}_f^4 \frac{H_{R,s}^4}{H^2 H_s}(a_s R_{*c}) \frac{(kR_{*c})^3}{2\pi^2} \widetilde{P}_{\rm gw}(kR_*) \times \frac{1}{y^4}\Upsilon(y), \quad (4.154)$$

where $\Gamma = \bar{\widetilde{w}}/\bar{\widetilde{e}} \approx 4/3$, $H_{R,s}$ is defined to contain only the radiation energy density at t_s: $H_{R,s} = H_s\sqrt{1-\kappa_M}$, and the integral is hidden inside $\widetilde{P}_{\rm gw}(kR_*)$:

$$\widetilde{P}_{\rm GW}(kR_*) = \frac{1}{4\pi c_s kR_*}\left(\frac{1-c_s^2}{c_s^2}\right)^2 \int_{z_-}^{z_+} \frac{dz}{z} \frac{(z-z_+)^2(z-z_-)^2}{z_+ + z_- - z} \bar{P}_v(z)\bar{P}_v(z_+ + z_- - z). \quad (4.155)$$

Here $z = qR_{*c}$, $z_\pm = \frac{1}{2}\frac{kR_{*c}}{c_s}(1 \pm c_s)$ and $\bar{P}_v(z) = \frac{\pi^2}{\bar{U}_f^2}\frac{\mathcal{P}_v(z)}{z^3}$. Using Eq. 4.127, the explicit expression for $\bar{P}_v$ is

$$\bar{P}_v(z) = \frac{1}{64\pi^2 v_w^6}\frac{1}{\bar{U}_f^2}\int d\widetilde{T}\ \widetilde{T}^6 \nu(\widetilde{T}) \left| A\left(\frac{z\widetilde{T}}{(8\pi)^{1/3}v_w}\right)\right|^2. \quad (4.156)$$

Plugging in the explicit expressions of H and $H_{R,s}$, we have

$$\mathcal{P}_{\rm GW}(y, kR_{*c}) = 3\Gamma^2\ \bar{U}_f^4 (H_s a_s R_{*c}) \frac{(kR_{*c})^3}{2\pi^2} \widetilde{P}_{\rm gw}(kR_*) \times \left\{ \begin{array}{c} 1 \\ \\ \frac{(1-\kappa_M)^2}{\kappa_M y + 1 - \kappa_M} \end{array} \right\} \times \Upsilon(y). \quad (4.157)$$

For both RD and MD, the shape of the spectra are the same to a good approximation, and are the same as that derived in the sound shell model and thus the properties of its shape [3] apply here for both cases. In particular, the peak frequency of the spectrum is located at around $kR_{*c} \approx 10$. This mean a larger or smaller R_* can red or blue shift the spectrum respectively. For example, as shown in Fig. 4.7, increasing v_w reduces R_{*c} and thus blue-shift the spectrum. For MD, it has a larger R_* and thus red-shift the spectrum.

For RD, we recover the result found in Ref. [68], as long as $\Upsilon(y) = 1$, which is only true for $y \gg 1$. The reason only this asymptotic value is obtained in Ref. [68] is due to the over-simplifying assumptions used (see Appendix B), in which case the second terms in both Eq. 4.150 and 4.152 are missing. Whether or not the asymptotic values can be reached depends on how long the source remains active, and we continue in the next section on this question.

4.5.3 Lifetime of the Source

As we saw earlier, the presence of an asymptotic value for Υ for large y in both cases is due to the dilution of the source energy density. This asymptotic value was used in Ref. [68] to reach the conclusion that for RD the effective lifetime of the source is a Hubble time H_s^{-1} for RD, i.e., $\tau_{\rm sw} = 1/H_s$, which as we have seen is only true if $\Upsilon = 1$ for $y \gg 1$. The question is, however, whether this asymptotic value can be reached in a realistic time frame. In Fig. 4.17, we show the time elapsed since the reference time t_s, in unit of the Hubble time H_s^{-1}. For RD,

$$\frac{t - t_s}{1/H_s} = \frac{y^2 - 1}{2}, \tag{4.158}$$

and for MD

$$\frac{t - t_s}{1/H_s} = \frac{2}{3}(y^{3/2} - 1). \tag{4.159}$$

At about a Hubble time, $\Upsilon \approx 0.4$ for both RD and MD, which is less than a half of the asymptotic value for RD and 60% for MD. We need many Hubble times for Υ to approach the asymptotic value. The problem is certain physical processes might prohibit the sound waves from being active for such a long time,

and thus the asymptotic value might never be reached. One such process is the possible formation of shocks and turbulence. Another is the existence of possible dissipative processes, whose presence damps the sound waves. If either of these processes quenches the sound waves, the asymptotic value will not be achieved. In this case, the effective lifetime is shorter than the Hubble time for RD, and the result obtained with an effective lifetime of a Hubble time overestimates the gravitational wave production. The time scale for turbulence is roughly [353, 69]

$$\tau_{\rm sw} \sim \frac{L_f}{\bar{U}_f} \sim \frac{R_*}{\bar{U}_f}. \tag{4.160}$$

Therefore

$$\frac{\tau_{\rm sw}}{1/H_s} \sim \frac{H_s R_*}{\bar{U}_f}. \tag{4.161}$$

As we have seen in Fig. 4.7, $H_s R_s \sim 10^{-3}$ and different expansion histories lead to larger or smaller values. To delay the appearance of turbulence and thus approach the asymptotic value of Υ thus requires smaller fluid velocity $\bar{U}_f$ or larger bubble separation. While $H_s R_*$ depends on specific expansion behavior adopted, the value of $\bar{U}_f$ is more or less universal, and its value is shown in Fig. 4.18 on the plane of (v_w, α). We show here two versions of it obtained using two different methods: one by solving the velocity profile around a single bubble and the other by integrating over the velocity power spectrum (see Ref. [3] for details). Thus whether or not above ratio becomes large enough depends on the details of the phase transition in a given cosmological context. Even in cases where the turbulence is delayed or not present, i.e., for sufficiently strong or weak phase transitions respectively, the damping of the sound waves caused by some weak

processes could still shorten the lifetime in the form of shear viscosity [68]. It seem unlikely for any scenario to be very close to the asymptotic value.

4.5.4 Spectrum Today

We will mainly consider the case of RD as it is the most frequently encountered scenario. Denote the temperature after the gravitational wave production as T_e with the scale factor being a_e. The amount of redshifting is described by the scale factor ratio a_e/a_0. For radiation in thermal equilibrium and in adiabatic expansion, the relation between a_e and a_0 is governed by entropy conservation:

$$g_s(T_e)a_e^3T_e^3 = g_s(T_{\gamma 0})a_0^3T_{\gamma 0}^3, \tag{4.162}$$

where g_s is the relativistic degrees of freedom for entropy; $T_{\gamma 0}$ is the temperature of the CMB photon with $T_{\gamma 0} \approx 2.73K$. At the present time, the relativistic species includes photons and decoupled neutrinos, thus $g_s = 2 + \frac{7}{8} \times 2N_{\text{eff}}(\frac{4}{11})^{3/3} \approx 3.94$ for $N_{\text{eff}} = 3.046$. Using these, the ratio of the scale factor can be put into the following form:

$$\frac{a_e}{a_0} = 1.65 \times 10^{-5} \left(\frac{g_s(T_e)}{100}\right)^{1/6} \left(\frac{T_e}{100\text{GeV}}\right) \left(\frac{1\text{Hz}}{H_e}\right). \tag{4.163}$$

For the peak frequency at $kR_* = z_p$ [11] where $z_p \approx 10$ [69], the frequency at t_e is

$$f_p = \frac{z_p}{2\pi R_*(t_e)}, \tag{4.164}$$

where $R_*(t_e)$ is evaluated at the end of the gravitational wave production and note all previously generated gravitational waves at higer frequencies at $kR_{*c} = z_p$ have

[11] We use a notation where k in kR_* is physical wavenumber, and k in kR_{*c} is a comoving wavenumber.

all redshifted to the frequency produced at t_e. Then the corresponding frequency today is

$$f_{\rm SW} = 2.65 \times 10^{-5}{\rm Hz} \left(\frac{g_s(T_e)}{100}\right)^{1/6} \left(\frac{T_e}{100{\rm GeV}}\right) \left(\frac{z_p}{10}\right) \left(\frac{1}{H_e R_*(t_e)}\right). \quad (4.165)$$

We can express R_* by $\beta(v_w)$ using Eq. 4.77, so that,

$$\frac{1}{H_e R_*(t_e)} = (8\pi)^{-1/3} \frac{a(t_f)}{a(t_e)} \frac{1}{v_w} \frac{\beta(v_w)}{H_e} = (8\pi)^{-1/3} \frac{1}{v_w} \frac{\beta(v_w)}{H_e} \times \frac{1}{y}. \quad (4.166)$$

Here we neglect the very small difference between t_f, the time when all the bubbles have disappeared and t_s, and we have shown explicitly the dependence of β on v_w. Also note β is evaluated at t_f when $I(t_f) = 1$. The factor y^{-1} is significant when the lifetime of the source is long. Then the present peak frequency becomes

$$f_{\rm SW} = 8.97 \times 10^{-6}{\rm Hz} \frac{1}{v_w} \left(\frac{g_s(T_e)}{100}\right)^{1/6} \left(\frac{T_e}{100{\rm GeV}}\right) \left(\frac{z_p}{10}\right) \left[\frac{\beta(v_w)/y}{H_e}\right]. \quad (4.167)$$

For the energy fraction of gravitational waves, the dilution of gravitational waves leads to the following connection:

$$\begin{aligned} h^2\Omega_{\rm GW}(t_0, f) &= h^2 \left(\frac{a_e}{a_0}\right)^4 \left(\frac{H_e}{H_0}\right)^2 \Omega_{\rm GW}(t_e, a_0 f/a_e), \\ &= 1.66 \times 10^{-5} \left(\frac{100}{g_s(T_e)}\right)^{1/3} \Omega_{\rm GW}(t_e, a_0 f/a_e). \end{aligned} \quad (4.168)$$

Here $h \approx 0.673$, the Hubble parameter today in unit of 100km/s/Mpc. Then plugging the explicit expression for $\mathcal{P}_{\rm GW}$ in Eq. 4.157, we have

$$h^2\Omega_{\rm GW}(f) = 4.98 \times 10^{-5} \left(\frac{100}{g_s(T_e)}\right)^{1/3} \Gamma^2 \bar{U}_f^4 \left[H_s R_*(t_s)\right] A\, \mathcal{S}_{\rm SW}(f) \Upsilon(y). \quad (4.169)$$

Here we have defined $A\mathcal{S}_{\rm SW}(f)$ to be $(kR_*)^3 \widetilde{P}_{\rm gw}(kR_*)/(2\pi^2)$ with appropriate redshifting factors included. One can either use the prediction from the sound

shell model to determine $A\mathcal{S}_{\rm SW}(f)$, or use result from numerical simulations [69]. We choose the latter as it should give a more accurate result, in which case $A \approx 0.058$ and [26]

$$\mathcal{S}_{\rm SW}(f) = \left(\frac{f}{f_{\rm SW}}\right)^3 \left[\frac{7}{4+3(f/f_{\rm SW})^2}\right]^{7/2}. \tag{4.170}$$

For the term $H_s R_*(t_s)$, similar to Eq. 4.166, we can write

$$H_s R_*(t_s) = (8\pi)^{1/3} v_w \frac{H_s}{\beta(v_w)}. \tag{4.171}$$

Therefore the final spectrum is [12]

$$h^2\Omega_{\rm GW}(f) = 8.5\times 10^{-6}\left(\frac{100}{g_s(T_e)}\right)^{1/3}\Gamma^2\bar{U}_f^4\left[\frac{H_s}{\beta(v_w)}\right] v_w \mathcal{S}_{\rm SW}(f)\times\Upsilon(y). \tag{4.172}$$

For a long lifetime of the source, the main changes are the suppression factor $\Upsilon(y)$. In Fig. 4.19, we show the spectra for several choices of $H_*\Delta t$, with $z_p = 10$ (see caption for more details).

For MD, apparently the extra dominant matter content will decay to radiation at some time later, which will inject entropy to the standard radiation sector. This can be studied using two methods. In the first method, one can assume a very quick and thus instantaneous decay of the matter, which then allows to use energy conservation to get the new heated radiation temperature. In the second method, a more precise account of the matter decay is provided, with

[12] Note current simulations only probe relatively weak transitions and this spectrum might not be applicable for strong transitions $\alpha \sim 1$. As shown in a recent simulation [5], a deficit in the gravitational wave production has been found for such strong transitions. This reduction is more severe for small v_w, and of course a large α, and would require extremely strong couplings to the plasma which might be a rare case. We also note that a large α, such as the region when $\alpha > 1$ in Fig. 4.18, might leads to a temporary inflationary stage with exponential expansion (see e.g., [282]) and contradicts the assumed radiation domination for this spectrum. In this case, one should use the corresponding Green's function and follow previous steps in deriving this spectrum.

the conclusion that there is no heating up of the radiation but one gets a slower cooling of the radiation, as was firstly pointed out in Ref. [343]. Therefore one needs to follow more closely the entropy evolution by taking into account finite matter decay width, following the procedure of Ref. [343] or a more closely related example studied in Ref. [336]. This however introduces extra model dependent varieties and is beyond the scope of this work.

4.6 Summary

We studied in detail the cosmological first order phase transition and the calculation of resulting stochastic gravitational waves in an expanding universe, with radiation and matter dominated universe as two representative examples. Firstly we studied the changes to process of bubble formation and collision, including important observables such as the mean bubble separation and its relation with β. We also derived the unbroken bubble wall area, the bubble conformal lifetime distribution which are needed for the calculation of the gravitational wave spectrum. We then derived the full set of differential equations as used in numerical simulations in an expanding universe. We found that simple rescalings work such that the equations governing the velocity profile around a single bubble maintains the same form as in Minkowski spacetime in the bag model and that the velocity profile remains the same when appropriate substitution of variables are used. We then generalized the sound shell model to the expanding universe and derived the velocity power spectrum. This result is used to derive analytically the gravitational wave power

spectrum from the sound waves, the dominant source. We found that the standard formula of the spectrum needs to include an additional suppression factor Υ, which is a function of the lifetime of the source. For radiation domination, the asymptotic value of Υ is 1 when the lifetime of the source is very long, and corresponds to the usually adopted spectrum in the literature. This asymptotic value however can not be reached as the onset of shocks and turbulence may disrupt the sound waves and possible dissipative processes may further damp it. Therefore an additional suppression factor needs to be taken into account when using the gravitational wave spectrum from sound waves and we provided simple analytical expression for Υ.

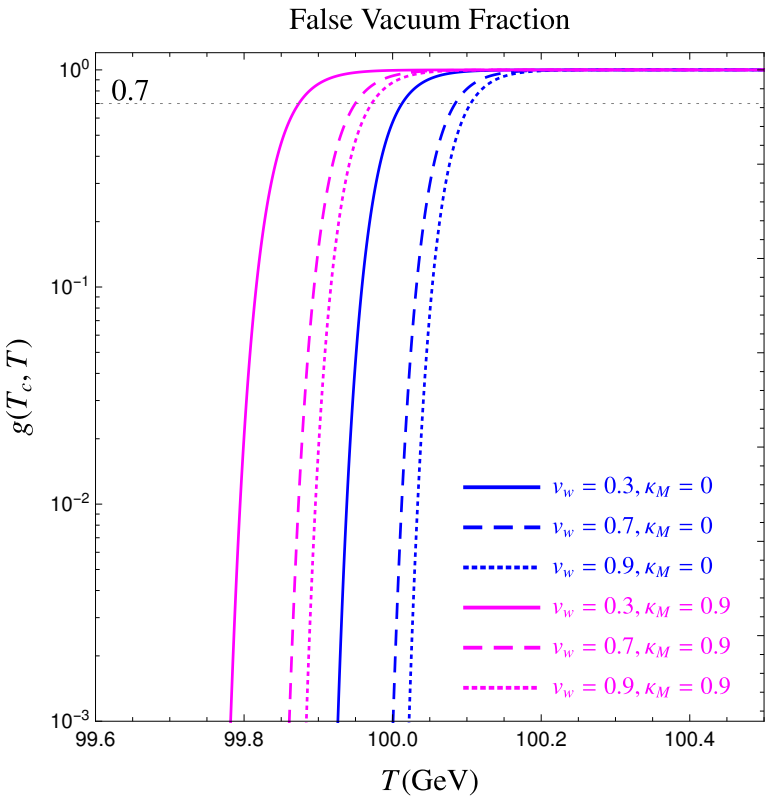

Figure 4.3: The false vacuum fraction as defined Eq. 4.40 for different fractions of matter energy density at T_c ($\kappa_M = 0, 0.9$, defined in Eq. 4.45) and for several bubble wall velocities ($v_w = 0.3, 0.7, 0.9$). The case of $\kappa_M = 0$ corresponds to a radiation dominated universe and $\kappa_M = 0.9$ for matter domination. The horizontal line at $g = 0.7$ is roughly the time when the bubbles percolate.

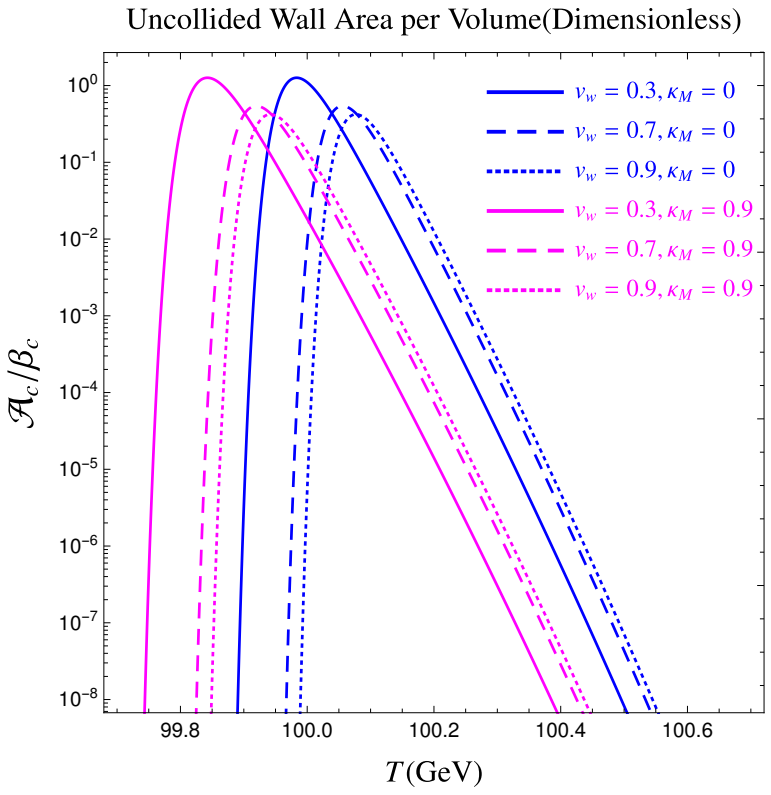

Figure 4.4: The dimensionless comoving uncollided bubble wall area as defined in Eq. 4.49 and Eq. 4.68 for different values of κ_M (defined in Eq. 4.45) and v_w.

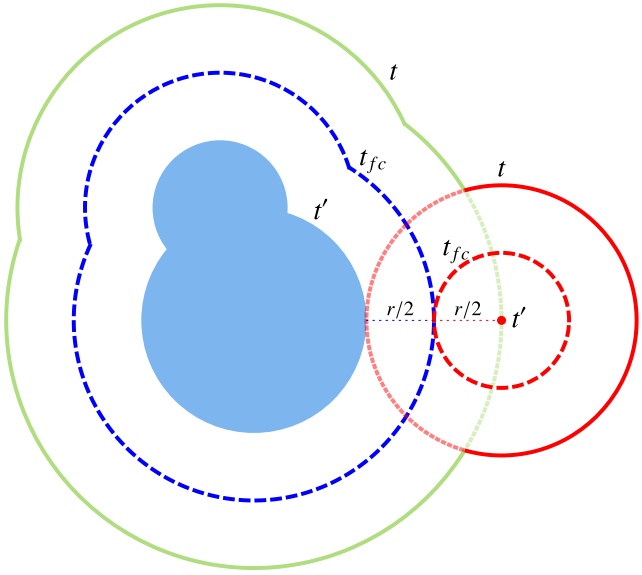

Figure 4.5: Illustration for the calculation of the bubble lifetime distribution. At t', there is a central blue blob composed of two already collided bubbles depicting a region of true vacuum space which is expanding into the surrounding false vacuum space, and also a small red nucleus denoting a bubble starting to form. At this time, the comoving distance between the red dot and the nearest blue boundary is r. At t_{fc}, the walls of the blue blob and the fledged red bubble advance to the place denoted by blue and red dashed circles respectively, where they make the first contact. At t, they reach the place denoted by the solid blue and red circles, where half of the red bubble is devoured by the blue one, and the red bubble is defined to be destroyed with a final radius r.

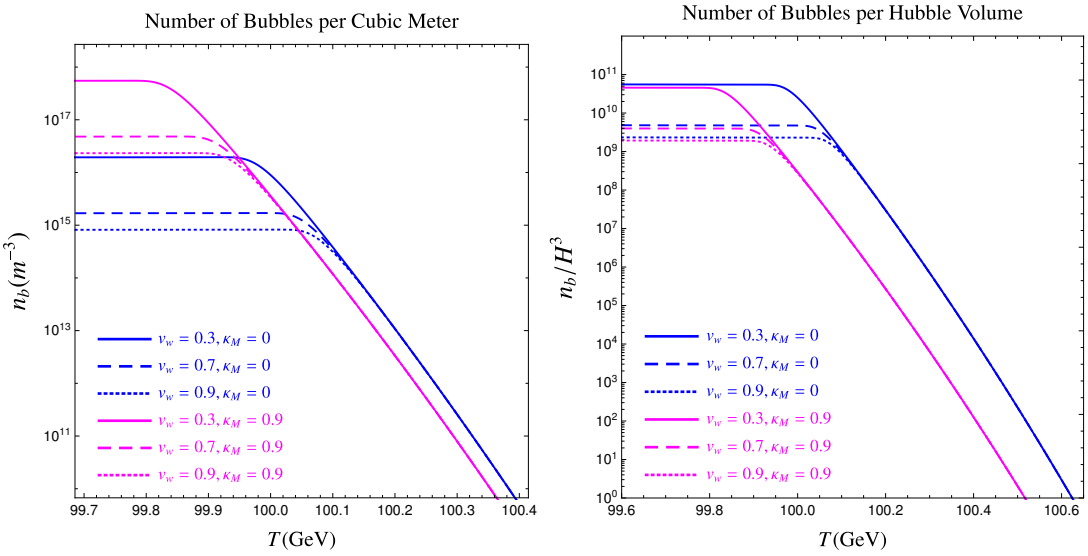

Figure 4.6: The number of bubbles (see Eq. 4.60) per m^3(left) and per Hubble volume(right) as a function of temperature for difference fractions of non-relativistic matter content at the critical temperature κ_M (defined in Eq. 4.45) and for different bubble wall velocities v_w.

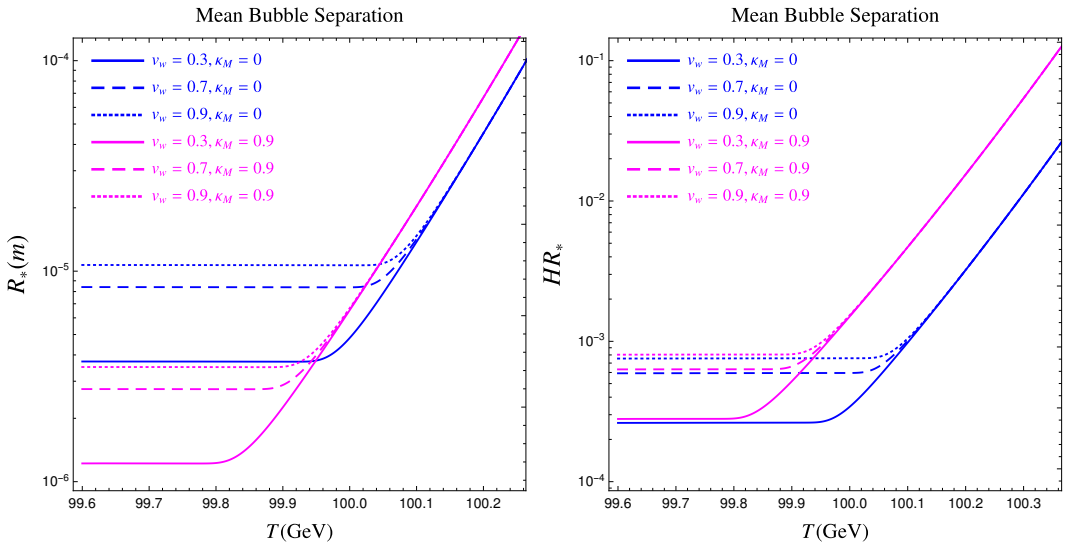

Figure 4.7: Mean bubble separation R_* (defined in Eq. 4.62) for different fractions of the non-relativistic matter content at the critical temperature κ_M and for different bubble wall velocities v_w. The left panel is in unit of meter and the right in unit of Hubble radius.

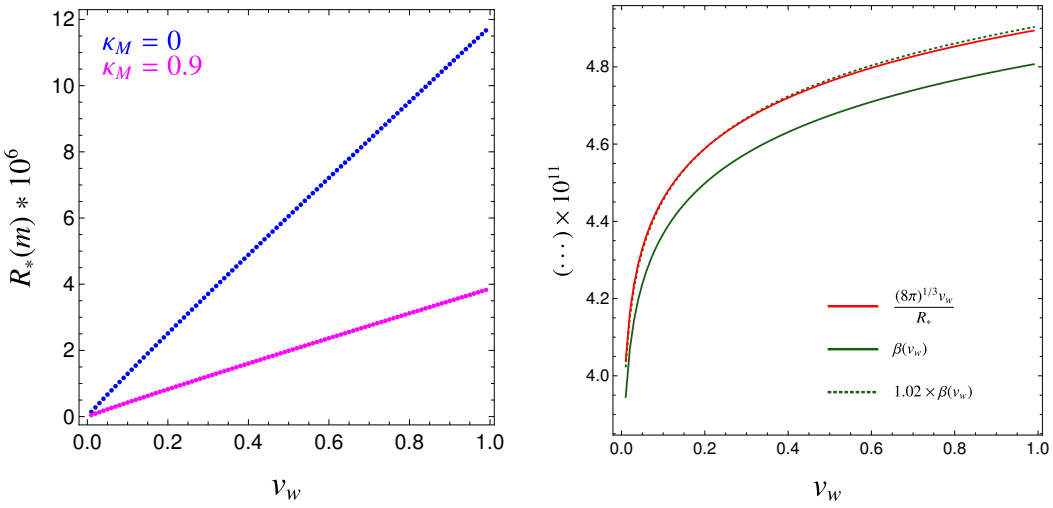

Figure 4.8: The left panel shows the mean bubble separation R_* immediately after all the bubbles have disappeared versus bubble wall velocity v_w for $\kappa_M = 0$ and $\kappa_M = 0.9$. The right panel shows $\beta(v_w)$ calculated using Eq. 4.34 at t_f, as compared with that calculated from R_* using Eq. 4.77 for $\kappa_M = 0$. The dotted line shows these differ by roughly 2%. For $\kappa_M = 0.9$, it shows similar behavior.

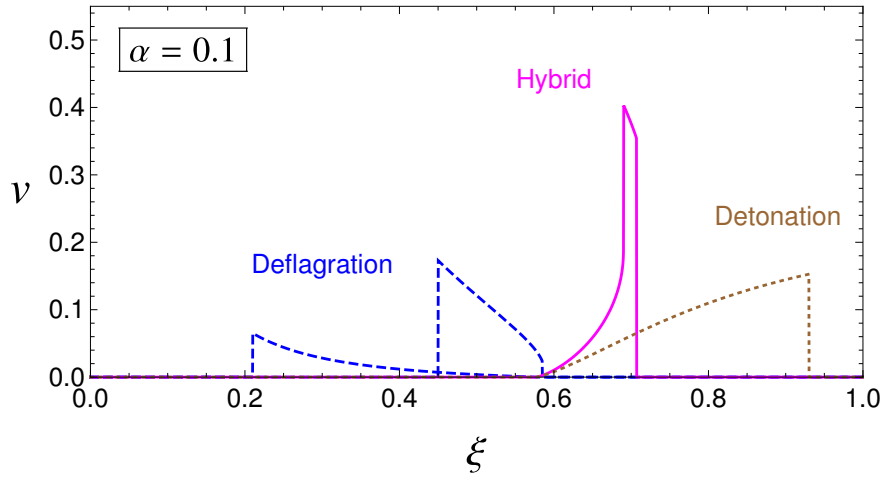

Figure 4.9: Representative velocity profiles surrounding the bubble walls.

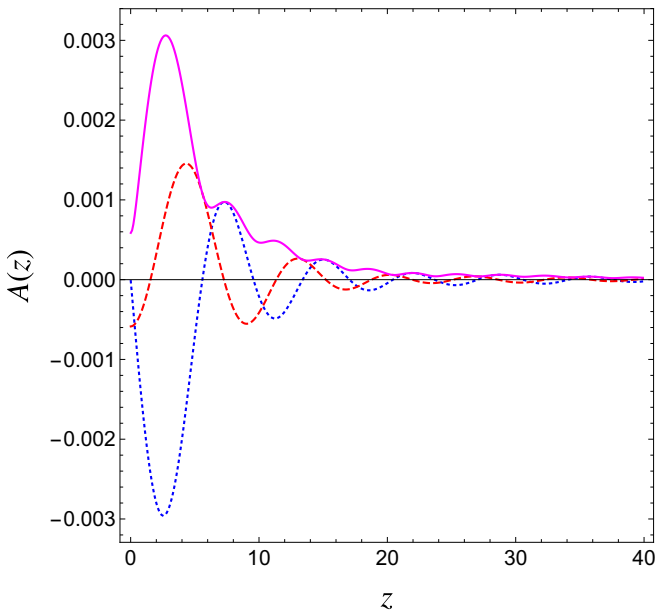

Figure 4.10: The real (blue dotted), imaginary (red dashed) parts and absolute value (magenta solid) of $A(z)$ (defined below Eq. 4.112) for $v_w = 0.92$ and $\alpha = 0.0046$.

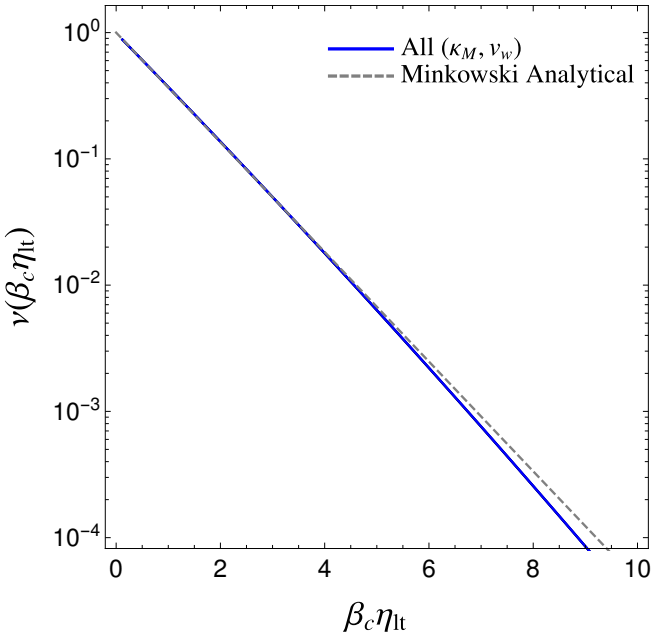

Figure 4.11: The dimensionless bubble lifetime distribution $\nu(\beta_c\eta)$ defined in Eq. 4.122 and more explicitly in Eq. 4.124. All previously used choices of κ, v_w give the same blue line. The gray dashed line is the analytically derived result $e^{-\beta t_{\rm lt}}$ in Ref. [3].

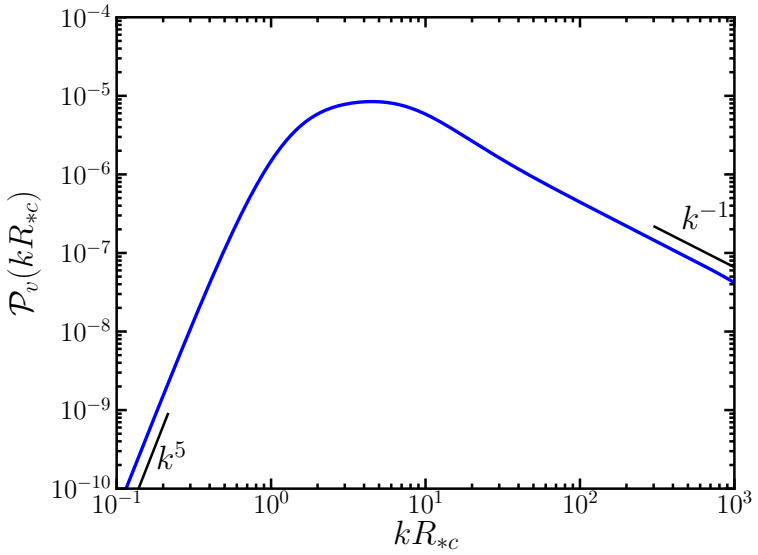

Figure 4.12: Representative velocity power spectrum calculated in the sound shell model for a weak phase transition with $\alpha = 0.0046$ and $v_w = 0.92$. The bubbles are assumed to nucleate exponentially. The low and high frequency regimes follow the k^5 and k^{-1} power law fits respectively (black solid lines). See Ref. [3] for more details of its properties.

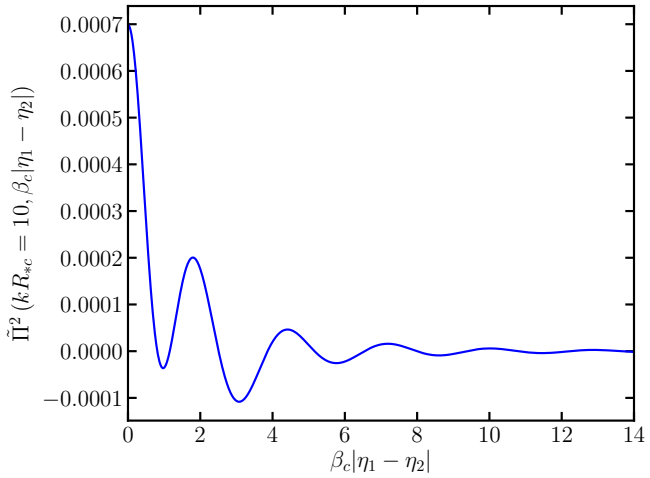

Figure 4.13: Autocorrelation of the source for $kR_{*c} = 10$, calculated with the explicit expression in Eq. 4.142.

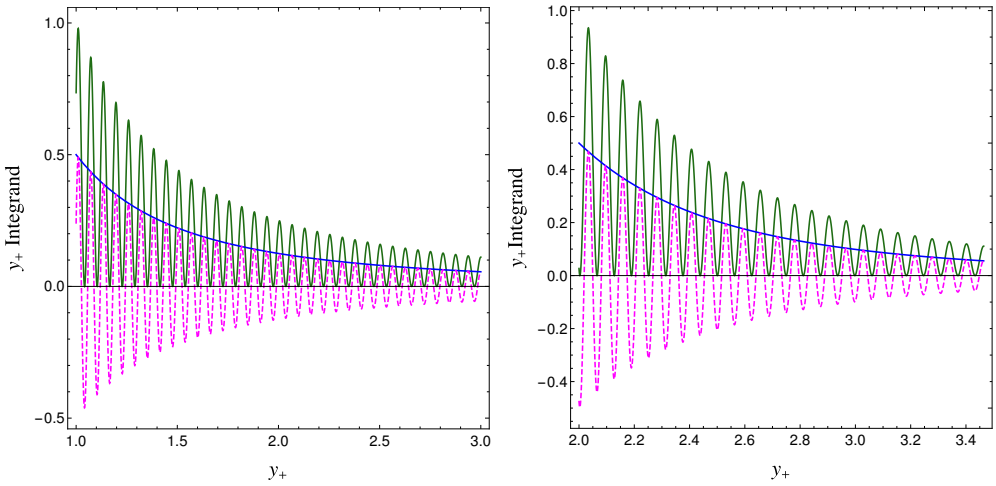

Figure 4.14: The integrand of y_+ integration, with $y = 3$. Left is RD and right is MD. The blue is the dominant non-oscillatory part, the magenta dashed is the oscillatory part(kR_{*c} chosen to be 0.04) and the dark green is the total contribution.

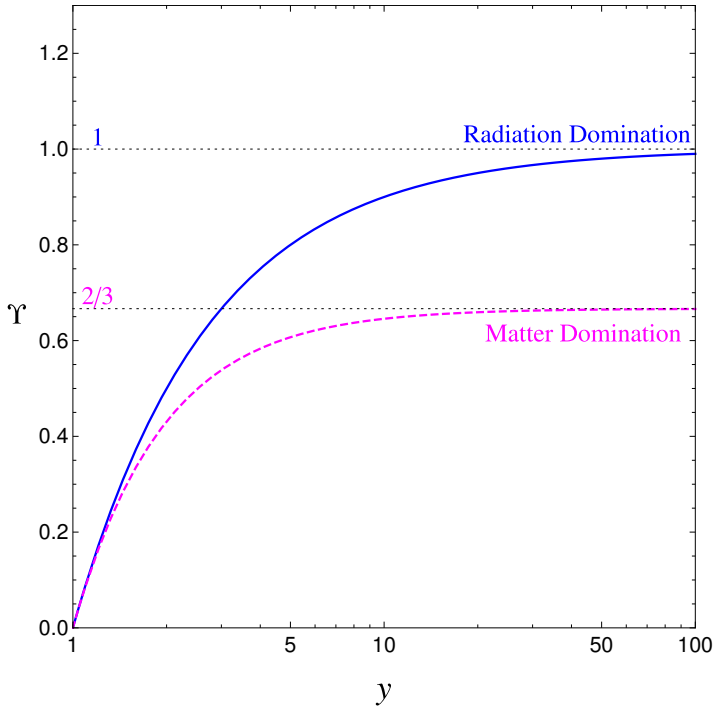

Figure 4.15: The function ϒ for radiation domination(blue solid) and matter domination(magenta dashed).

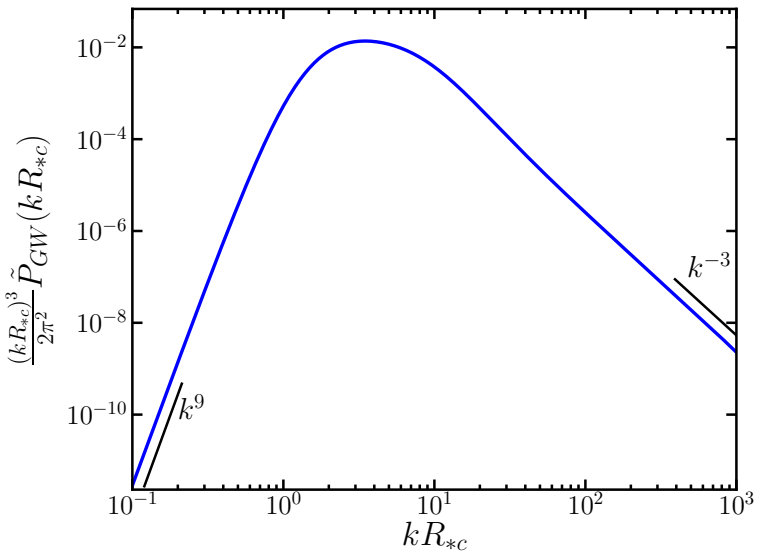

Figure 4.16: The dimensionless gravitational wave power spectrum computed in the sound shell model. The calculation was performed for a weak phase transition with $\alpha = 0.0046$, $v_w = 0.92$, and exponential bubble nucleation. The low and high frequency regimes follow the k^9 and k^{-1} power law fits respectively (black solid lines). See Ref. [3] for more details of its properties.

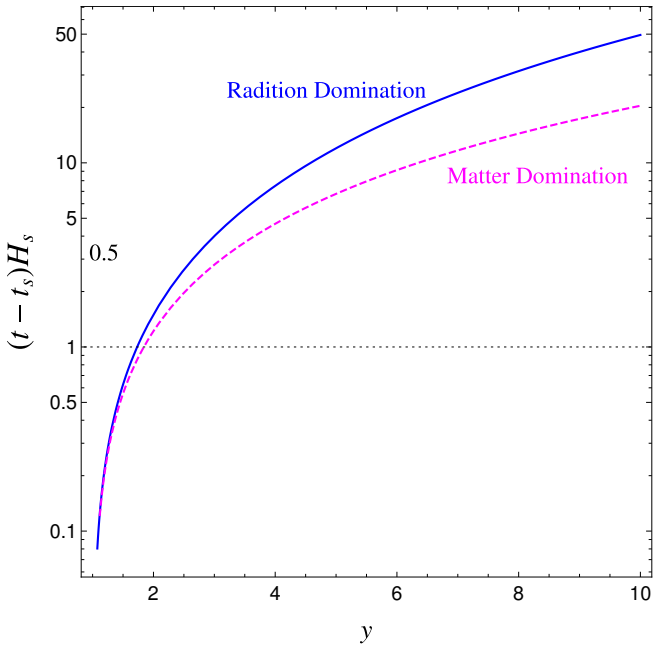

Figure 4.17: Time elapsed since t_s in unit of Hubble time H_s^{-1} at t_*.

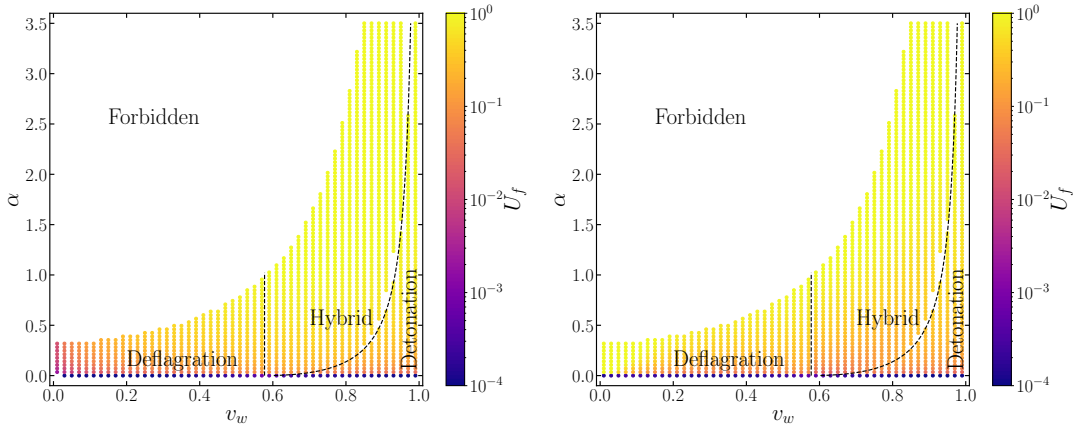

Figure 4.18: $\bar{U}_f$ on the plane of (v_w, α). The left figure is $\bar{U}_f$ of the fluid around a single bubble. The right figure is $\bar{U}_f$ of the fluid calculated from the velocity power spectrum.

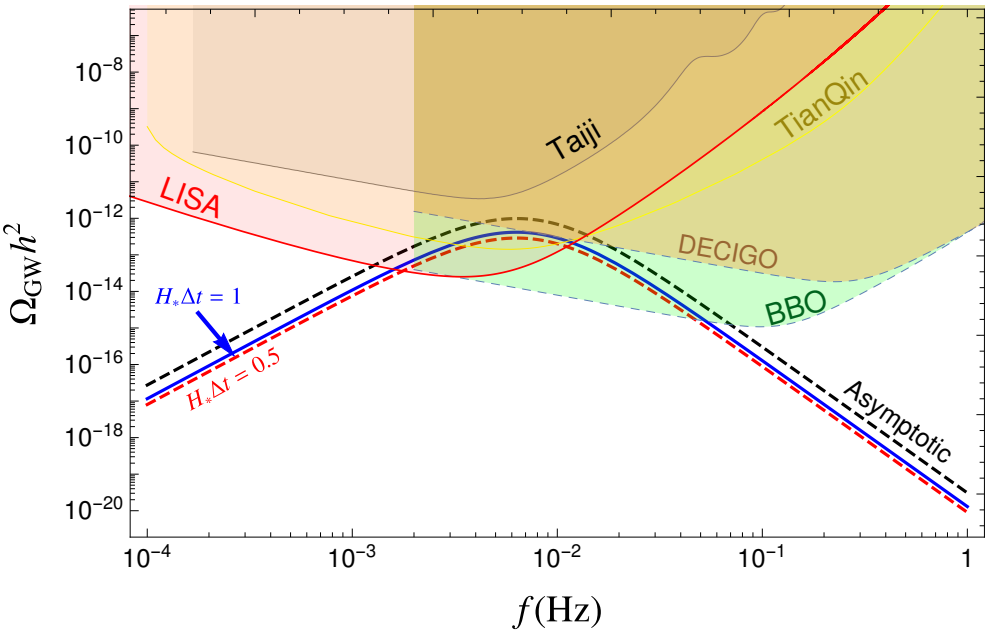

Figure 4.19: The present day gravitational wave energy density spectra for $H_*\Delta t = 0.5, 1$ and for $H_*\Delta t \gg 1$ when it takes the asymptotic form. Here $\Delta t = t - t_s$ and is the time elapsed since t_s, the time when the source becomes active. In all three cases, $v_w = 0.3$, $\alpha = 0.1$, $T_e = 100$GeV and $\beta/(yH_*) = 100$. The shaded regions at the top are experimental sensitive regions for several proposed space-based detectors.

Chapter 5

Benefits of Diligence

5.1 Introduction

Any strong first order transition produces three contributions to a stochastic background [26, 27, 10]. It is generally accepted that the acoustic contribution dominates over bubble collisions and turbulence, therefore this is what we will focus on here [67, 71, 69]. The acoustic contribution has been studied both in simulations and a combination of analytic and numerical techniques and there has been much recent progress.

Given the enormous opportunity to shed light on both cosmology and particle physics, it is worth examining in detail the theoretical underpinnings of any given model in order to enumerate both theoretical uncertainties in basic methods and the degree of benefit in more accurate calculations or, equivalently the cost of various approximations. Approximations can arise in two steps in predicting an observable from a given model as shown in Fig. 5.1. First the calculation of macroscopic thermal parameters, including the latent heat and the time scale of the transition, are often calculated using perturbative techniques which can introduce large errors [354] in particular when long wavelength modes are not resummed carefully enough [355, 356, 4, 357].[1] The second step, which we focus on in this paper, converts macroscopic thermal parameters into a prediction for

[1] Other important problems in common calculations are gauge dependence [248] and the inhomogeneous background [358, 359].

the spectrum - in particular the peak frequency and amplitude. Ultimately, both steps will likely require simulations to truly perform precision cosmology on a future hypothetical observation.[2] However, this is impractical for the analysis of large numbers of parameter sets for large numbers of models. We therefore examine several layers of improvement in the prediction of the peak amplitude that have recently arisen in several models involving physics beyond the standard model

- The finite lifetime of the source first estimated in Ref. [282] and derived in the sound shell model in an expanding background in Ref. [361].
- Going beyond the bag model approximation in solving the hydrodynamic equations [362, 363].
- Calculating the mean bubble separation from the evolution of the bubble number density.
- Calculating the fraction of energy in the fluid from solving the hydrodynamic equations rather than using a fit [5].
- Including fits for the energy lost to vorticity modes [5].

In this paper we will enumerate the error in a number of models in order to get a broad understanding of the numerical importance of diligence. This avoids model-specific effects where accidental cancellations between different

[2]Infrared divergences of the dynamical mode for instance remain even after NLO resummation. As a result perturbation theory even at two loops disagrees substantially with montecarlo simulations very close to the critical temperature [360].

Figure 5.1: The uncertainty in linking a particular model with a set of observables is conceptually presented above. The break down of perturbation theory at finite temperature is the dominant error in the prediction of the evolution of the effective potential and ultimately non-perturbative methods might be required to predict macroscopic thermal parameters. The macroscopic thermal parameters of interest are often taken to be the latent heat, the time scale of the transition (usually approximated), the bubble wall velocity and the temperature of percolation, but if one desires to have an accurate prediction one needs the fluid velocity, the wall velocity, the mean bubble separation, the percolation temperature and the lifetime of the acoustic source (see also Fig. 1 of [4]).

improvements could in principle occur. The models we consider include a toy model introduced for pedagogical purposes, the Standard Model Effective Field Theory (SMEFT), a dark sector Higgs and a real scalar singlet extension (xSM) of the Standard Model. For the benefit of the reader, a demonstration of the importance of diligence is provided at the outset in Fig. 5.2. Here, the relative error in the predicted peak amplitude is shown for SMEFT, the dark sector Higgs model (which we label throughout as "Dark RG") and xSM. Our paper will be devoted to fully explaining Fig. 5.2; for now, we provide a feel for the comparative importance of these errors. For the Dark RG, for example, the relative error is far more manageable than what it is for SMEFT. However, even for that model, the relative error is larger[3] than the error from gauge dependence that is introduced in SMEFT in some commonly used methods. Thus, even this case, which may present an unrealistically optimistic picture, still motivates diligence in the calculation.

The structure of this paper is as follows. In Section 5.2 we outline three methods of various levels of diligence that we find used in the literature, including a level of diligence motivated by its use in the recent review [10]. In Section 5.3 we define the models we will use to demonstrate increasing levels of diligence, and in Section 5.4 we will present our results. We will end with our Conclusion.

[3]up to the caveat that the gauge parameter is varied by an amount allowed by perturbativity considerations.

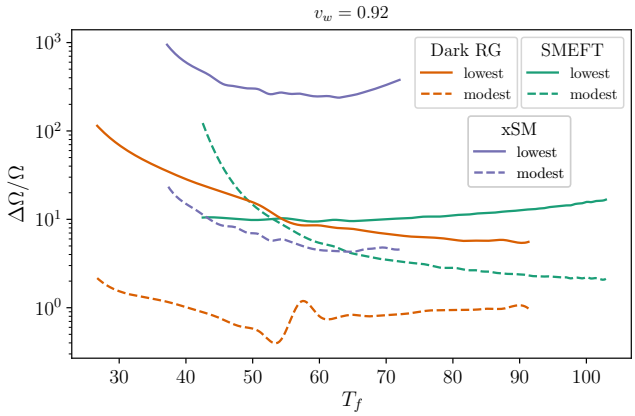

Figure 5.2: The relative error when using the lowest and modest levels of diligence, compared to the highest level of diligence (for which $\Delta\Omega/\Omega = 0$). The vertical axis shows the peak (frequency-independent) gravitational wave energy density for detonation. The precise definition of $\Delta\Omega/\Omega$ is given in Eq. 5.62. The horizontal axis corresponds to the final temperature T_f when the phase transition ends. Three models are shown: SMEFT, a dark sector Higgs model (Dark RG) and the singlet-extended Standard Model (xSM). The figures employ calculations from Eq. (5.7, 5.15, 5.37) and Eq. 5.62. The temperatures are set to T_n (5.4), T_p (5.11), and T_f (4.70) for the lowest, modest, and highest diligence respectively. Both the modest and highest diligence contain suppression factors due to the lifetime of the source. The highest diligence contains the suppression factor due to vorticity effects in the plasma.

5.2 Phase Transition Dynamics

Gravitational waves produced from first order phase transitions is a finite temperature tunneling process, from some false vacuum to the true vacuum. When calculating this transition with perturbation theory, one needs to track the minima of the effective potential from the temperature at which the energy in each vacuum is degenerate - that is the critical temperature. Below the critical temperature, bubbles of the true phase begin to form at some critical radius where the pressure is strong enough to cause expansion. The probability of such bubbles forming increases as the Universe cools, until the nucleation temperature at which there is an average of one bubble per Hubble volume. Slightly below this temperature is the percolation temperature at which bubble collisions are occurring and the final temperature when the phase transition ends. There are simple analytical expressions for these temperature scales which are the result of approximations used in the equations. However, the gravitational wave spectrum is sensitive to the level of diligence that goes into the computations and reducing the error is paramount to probing phase transitions at future gravitational wave detectors. We will now proceed to analyze the different level of diligence used in the literature.

5.2.1 Lowest diligence

Here we will describe the level of lowest diligence in computing the gravitational wave spectrum. At this stage, we will only introduce the various parameter definitions and wait until the highest diligence section for a more in depth look at

the numerical procedure. This level will involve computing all relevant parameters at the nucleation temperature.

The tunneling rate per unit time per unit volume will have the general form

$$p(T) = \bar{p}_0 T^4 e^{-S_3/T}, \tag{5.1}$$

where $\bar{p}_0$ is a dimensionless number that we will assume is $\mathcal{O}(1)$ and S_3 can be found by solving the bounce solutions that minimize the action given by

$$S_3(\vec{\phi}, T) = 4\pi \int dr r^2 \left[\frac{1}{2} \left(\frac{d\vec{\phi}(t)}{dr} \right)^2 + V_{\text{eff}}(\vec{\phi}, T) \right] . \tag{5.2}$$

The nucleation temperature is defined as the temperature at which the probability of a single bubble being nucleated within a Hubble volume is $\mathcal{O}(1)$:

$$\int_0^{t_n} p V_H(t) dt = \int_{T_n}^{\infty} \frac{dT}{T} \left(\frac{2\xi M_{\text{pl}}}{T} \right)^4 \exp^{-S_3/T} \sim \mathcal{O}(1), \tag{5.3}$$

where M_{pl} is the Planck mass, $\xi \sim 3 \times 10^{-2}$, and $V_H(t)$ is the horizon volume. This equation will lead to the simple definition of the nucleation temperature [245, 281, 364, 10]

$$\frac{S_3(T_n)}{T_n} \approx 140. \tag{5.4}$$

It is important to note that the above calculation assumes that the phase transition occurs in a radiation dominated era which is not guaranteed.

The strength of the gravitational wave spectrum will depend on hydrodynamic parameters such as the amount of vacuum energy released during the phase transitions, the inverse time duration of the phase transition, and the fraction of latent heat that goes into the bulk motion of the plasma (referred to as the kinetic efficiency coefficient). We discuss each of these quantities in turn.

The strength of the phase transition is characterized as

$$\alpha(T_n) = \frac{1}{\rho_{\rm rad}} \left(\Delta V_{\rm eff} - \frac{1}{4} \frac{d\Delta V_{\rm eff}}{dT} \right) \Big|_{T_n}, \tag{5.5}$$

where $V_{\rm eff}$ is the finite temperature effective potential and the symbol Δ signifies the difference in the symmetric phase (false vacuum) and the broken phase (true vacuum). The energy density of radiation is given by $\rho_{\rm rad} = \pi^2/30\, g_* T_n^4$ where g_* is the number of effective degrees of freedom at T_n.

The inverse time duration of the phase transition evaluated at the nucleation temperature can be approximated as

$$\beta = H_n T_n \frac{d(S_3/T)}{dT}, \tag{5.6}$$

where $H_n^2 = 8\pi G \rho_{\rm rad}(T_n)/3$ is the Hubble parameter at the nucleation temperature. A smaller β/H and larger α will result in stronger gravitational waves.

The gravitational wave spectrum observed today has a simple broken power law fit [69] in terms of the aforementioned parameters given by

$$h^2 \Omega_{\rm GW}(f) = 8.5 \times 10^{-6} \left(\frac{100}{g_n} \right)^{1/3} \left(\frac{\kappa \alpha}{1+\alpha} \right)^2 \left(\frac{H_n}{\beta} \right) v_w S_{\rm SW}(f), \tag{5.7}$$

where g_n is the number of degrees of freedom at the nucleation temperature and κ is the efficiency coefficient that represents the fraction of the bulk kinetic energy in the plasma relative to the available vacuum energy. The numerical fits for the kinetic efficiency coefficient, κ, were derived in [70] for the different velocity profile types which we give in Appendix C. The spectral shape, $S_{\rm SW}$, and the peak frequency, $f_{\rm SW}$ are given by

$$S_{\rm SW}(f) = \left(\frac{f}{f_{\rm SW}} \right)^3 \left[\frac{7}{4 + 3(f/f_{\rm SW})^2} \right]^{7/2}, \tag{5.8}$$

$$f_{\rm SW} = 1.9 \times 10^{-5} \frac{1}{v_w} \left(\frac{\beta}{H_n}\right) \left(\frac{T_n}{100\,\text{GeV}}\right) \left(\frac{g_n}{100}\right)^{1/6} \text{Hz}. \tag{5.9}$$

The gravitational wave spectrum may be rewritten in terms of the R.M.S velocity, $U_f^2 = \frac{3}{4}\kappa\alpha$, with the replacement

$$\left(\frac{\kappa\alpha}{1+\alpha}\right) \to \Gamma U_f^2, \tag{5.10}$$

where $\Gamma \sim 3/4$ is the adiabatic index which is defined as the ratio of the enthalpy and energy density in the symmetric phase. The term in the denominator on the left hand side, $(1+\alpha)$, is the result of the energy density in the symmetric phase.

5.2.2 Moderate diligence

The level of modest diligence is the approach most frequently used in the recent literature (including the recent LISA review [10]). It closely resembles the lowest diligence with the exception that the thermal parameters are defined at the percolation temperature rather than the nucleation temperature and the finite lifetime of the source is taken into account with an ansatz correction to the peak amplitude. The percolation temperature is here approximated by solving the equation

$$\frac{S_3(T_p)}{T_p} = 131 - \log(A/T^4) - 4\log\left(\frac{T}{100\,\text{GeV}}\right) - 4\log\left(\frac{\beta(T)/H}{100}\right) + 3\log(v_w), \tag{5.11}$$

where $\log(A/T^4) \sim 14$ for an electroweak phase transition. Note that the derivative of the left hand side in Eq. 5.11 appears on the right hand side, as can be seen from Eq. 5.6. The percolation temperature is always below the nucleation temperature

and hence closer to the final temperature when the phase transition ends. This makes using the percolation temperature a better approximation to estimate the thermal parameters. However, if the percolation temperature is significantly far away from the nucleation temperature, one should check if the phase transition can even reach completion at all for cases of strong supercooling, since the universe may become vacuum dominated. The strength of the phase transition and the inverse time duration of the phase transition take on the same form as in Eq 5.5-5.6 but with the replacement $T_n \to T_p$ such that

$$\alpha(T_p) = \frac{1}{\rho_{\rm rad}} \left(\Delta V_{\rm eff} - \frac{1}{4} \frac{d\Delta V_{\rm eff}}{dT} \right) \Big|_{T_p}, \tag{5.12}$$

and

$$\beta = H_p T_p \frac{d(S_3/T)}{dT}, \tag{5.13}$$

where H_p is now the value of the Hubble parameter at the percolation temperature.

The gravitational wave spectrum in Eq. 5.7 assumed that the lifetime of the source is approximately one Hubble time, $H\tau_{sw} = 1$ [365]. It was later pointed out in [42], that a better approximation to the lifetime of the source is

$$t_{\rm sw} = \min \left[\frac{1}{H_p}, \frac{R_*}{U_f} \right], \tag{5.14}$$

where R_* is the mean bubble separation and U_f is the root mean squared velocity defined at $\alpha(T_p)$. The mean bubble separation is related to the inverse time duration using $R_* = (8\pi)^{1/3} v_w/\beta$. We then take into account the finite lifetime of the source in the gravitational wave spectrum through

$$\Omega_{\rm sw} \to \Omega_{\rm sw} t_{\rm sw} H, \tag{5.15}$$

and calculate all temperature dependent quantities at the percolation temperature T_p defined in Eq. 5.11.

5.2.3 High diligence

The highest diligence with which one can calculate the gravitational wave spectrum involves a number of improvements to the predictions of the peak frequency and amplitude:

1 Improving on the bag model approximation for the fluid velocity and fraction of energy that is in gravitational waves;

2 Calculating the fluid velocity and efficiency from solving the hydrodynamic equations rather than using fits (related to the first);

3 Calculating the mean bubble separation from the number density of the bubbles;

4 Taking into account the finite lifetime of the soundwave source, derived in an expanding universe [361];

5 Calculating the suppression due to reheated droplets creating friction that slows collisions.

Note that Ref. [366] used the bag model in their simulations, so we assume that the suppression factor arising from kinetic energy lost in the fluid is independent of the change in the amplitude from improving on the bag model. Also in the last case, and only the last case, we use fits to estimate this degree of suppression

as it relies on a full numerical simulation - methods to approximate this effect we leave to future work. In this section we outline in detail each of the other improvements.

The free energy density f of a model with g_* degrees of freedom consists of a zero temperature scalar potential and a thermal potential that involves the summation over all relativistic species that interact with the scalar ϕ. In the Standard Model, this involves the standard electroweak Higgs field and degrees of freedom $g_{\rm SM} = 106.75$. The free energy density gives

$$f = V_0(\phi) + T^4 \left[\sum_B J_B \left(\frac{M_B}{T} \right) + \sum_F J_F \left(\frac{M_F}{T} \right) \right], \tag{5.16}$$

where the summations run over all relativistic bosons B and fermions F at temperature T. In the high temperature expansion, the free energy density can be written as

$$f = -\frac{1}{3}\frac{\pi^2}{30} g_* T^4 + V_T(\phi), \tag{5.17}$$

where $V_T(\phi)$ is the thermal effective Higgs potential and we explicitly separate out the scalar independent terms that go as T^4. The hydrodynamics of the plasma can be described as a perfect fluid in terms of the energy density e, pressure p, and enthalpy ω. These thermodynamic quantities can be explicitly calculated from the free energy density through the relation $p = -f(\phi, T)$ for the pressure. The energy density and enthalpy are then related to the pressure through

$$e = T\frac{\partial p}{\partial T} - p, \quad \omega = e + p = T\frac{\partial p}{\partial T}. \tag{5.18}$$

These quantities together, along with the velocity of the fluid v, will give the

energy momentum tensor of the plasma

$$T^{\mu\nu} = u^{\mu}u^{\nu}\omega + g^{\mu\nu}p, \tag{5.19}$$

where $g^{\mu\nu}$ is the inverse Minkowski spacetime metric and $u^{\mu}(v)$ is the four velocity of the fluid.

During the period of gravitational wave production, bubbles of the new phase will collide and generate sound waves in the perturbed plasma. The velocity profile around a single bubble is determined by the hydrodynamic quantities and the junction conditions across the bubble wall. We will denote the broken phase inside the bubbles by subscripts "$b, -$" and the symmetric phase outside the bubbles as "$s, +$". The signs "$-, +$" are used to describe quantities behind and in front of the bubble wall. The continuity equations $\partial_{\mu}T^{\mu\nu} = 0$ can be integrated in the wall frame across the bubble wall to give the junction conditions

$$\frac{v_+}{v_-} = \frac{e_b(T_-)+p_s(T_+)}{e_s(T_+)+p_b(T_-)}, \tag{5.20}$$

$$v_+v_- = \frac{p_s(T_+)-p_b(T_-)}{e_s(T_+)-e_b(T_-)}, \tag{5.21}$$

where $v_{\pm}$ and $T_{\pm}$ corresponds to the velocity and temperature of the fluid behind and in front of the bubble wall. We may assume that $T_+ \approx T_-$ and expand the thermodynamic quantities about the symmetric phase so that the ratio of velocities about the junction give

$$\frac{v_+}{v_-} \simeq \frac{\left(v_+v_-/c_{s,b}^2 - 1\right) + 3\alpha_{\bar{\theta}_+}}{\left(v_+v_-/c_{s,b}^2 - 1\right) + 3v_+v_-\alpha_{\bar{\theta}_+}}, \tag{5.22}$$

where $c_{s,b}$ is the speed of sound in the broken phase and $\alpha_{\bar{\theta}_+}$ is the phase transition strength [363]. The speed of sound can be calculated in both the symmetric and

broken phase and is defined in terms of the pressure as

$$c_s^2 = \frac{dp/dT}{de/dT} = \frac{p'(T)}{Tp''(T)}, \tag{5.23}$$

where $(...)'$ denotes derivatives with respect to temperature. In terms of the free energy density, the pressure in the symmetric phase is ϕ independent with $p_s = -f(0,T)$ and the pressure in the broken phase is $p_b = -f(\phi_{\rm min}, T)$ which is evaluated at true vacuum $\phi_{\rm min}$. It is important to keep every term in the free energy density when calculating the speed of sound in order to properly account for the full temperature dependence of the model. This includes keeping all light degrees of freedom that do not acquire field dependent masses that affect the Higgs effective potential. The new phase transition strength parameter $\alpha_{\bar{\theta}_+}$ is dependent on the speed of sound in the broken phase and has a similar form to the bag parameter built up from the trace anomaly,

$$\alpha_{\bar{\theta}_+} = \frac{\bar{\theta}_s(T_+) - \bar{\theta}_b(T_+)}{3\omega_s(T_+)}, \text{ with } \quad \bar{\theta} = \mathrm{e} - \mathrm{p}/\mathrm{c_s^2} \tag{5.24}$$

[363]. Going back to the free energy density, we can define the phase transition strength as a function of temperature

$$\alpha_{\bar{\theta}}(T) = \frac{1}{3\omega_s}\left((1+c_s^{-2})\Delta V_T - T\frac{d\Delta V_T}{dT}\right), \tag{5.25}$$

where V_T is the Higgs effective potential defined in Eq. 5.16-5.17 and Δ denotes the difference between the symmetric and broken phase. The phase transition strength has the same form as the bag model α_θ defined in Eq. 5.5 when $c_s^2 = 1/3$ and $\omega_s = 4/3\rho_{\rm rad}$. The junction conditions to obtain $v_\pm$ will serve as boundary conditions for solving the velocity profile obtained from projecting the continuity

equations into the parallel and perpendicular motions of the fluid flow. The hydrodynamic equations become

$$(\xi - v)\partial_\xi e = \omega \left[2\frac{v}{\xi} + \gamma^2(1 - \xi v)\partial_\xi v \right], \tag{5.26}$$

$$(1 - v\xi)\partial_\xi p = \omega\gamma^2(\xi - v)\partial_\xi v, \tag{5.27}$$

where $\xi = R/t$ is a self similar coordinate defined as the ratio between the distance to the bubble center and the time since nucleation. These hydrodynamic equations may be combined to give the enthalpy profile and the velocity profile:

$$2\frac{v}{\xi} = \gamma^2(1 - v\xi)\left[\frac{\mu^2}{c_s^2} - 1\right]\partial_\xi v, \tag{5.28}$$

$$\partial_\xi \omega = \omega\left(1 + \frac{1}{c_s^2}\right)\gamma^2\mu(\xi, v)\partial_\xi v, \tag{5.29}$$

where $\partial_\xi = \partial_\xi e + \partial_\xi p$ and $c_s^2 = dp/de$ are used to connect the equations. The Lorentz boost transformation used in the equations is defined in terms of the self similar coordinate $\mu(\xi, v) = (\xi - v) / (1 - \xi v)$. In detonations, the fluid velocity ahead of the bubble wall is always zero so that the hydrodynamic profiles are independent of the speed of sound in the symmetric phase. Deflagrations have a non-zero bubble wall velocity ahead of the bubble wall and the equations will then depend on the speed of sound in the symmetric phase. Both profile types will always depend on the speed of sound in the broken phase through the junction conditions. In detonation, it is sufficient to use $\alpha_{\bar{\theta}+} = \alpha_{\bar{\theta}}(T)$ with T usually taken as the nucleation temperature or the percolation temperature. Deflagrations and hybrid modes take $\alpha_{\bar{\theta}}$ as input and require a shooting method by varying $\alpha_{\bar{\theta}}$ until $\alpha_{\bar{\theta}}$ is reached far away from the bubble.

The quantity of interest for the peak gravitational wave energy density is the kinetic energy fraction K which can be solved by the hydrodynamic equations:

$$K = \frac{\rho_{fl}}{e_s}, \tag{5.30}$$

where $\rho_{\text{fl}} = 3/v_w^3 \int d\xi \xi^2 v^2 \gamma^2 \omega$ is the fluid's kinetic energy. We use the publicly available code in [363] to numerically compute the kinetic energy efficiency $\kappa_{\bar{\theta}}$ for a given set of c_s^2 and $\alpha_{\bar{\theta}}$ when comparing to calculations in the bag model. The kinetic energy fraction is related to the efficiency parameter through

$$K = \left(\frac{\bar{\theta}_s - \bar{\theta}_b}{4 e_s} \right) \kappa \left(\alpha_{\bar{\theta}}, c_{s,s}^2, c_{s,b}^2 \right), \tag{5.31}$$

where

$$\kappa = \frac{4 \rho_{\text{fl}}}{3 \alpha_{\bar{\theta}} \omega_s} \tag{5.32}$$

[363]. The quantities $c_{s,s}$, $c_{s,b}$, e_s,ω_s, $\alpha_{\bar{\theta}}$, and κ in determining the kinetic energy fraction K are all calculated at the final temperature T_f when the phase transition ends. The enthalpy-weight root-mean-square fluid velocity around a single bubble may be found from the kinetic energy fraction,

$$\bar{U}_f^2 = \frac{e_s}{\omega_s} K, \tag{5.33}$$

which is evaluated at T_f.

The first numerical simulations of strong first order phase transitions for $\alpha \gtrsim 0.1$ were undertaken in [5] which showed that previous results overestimated the gravitational wave energy density. The rotational component of the fluid velocity, particularly for deflagrations, increases in relative size as the transition strength

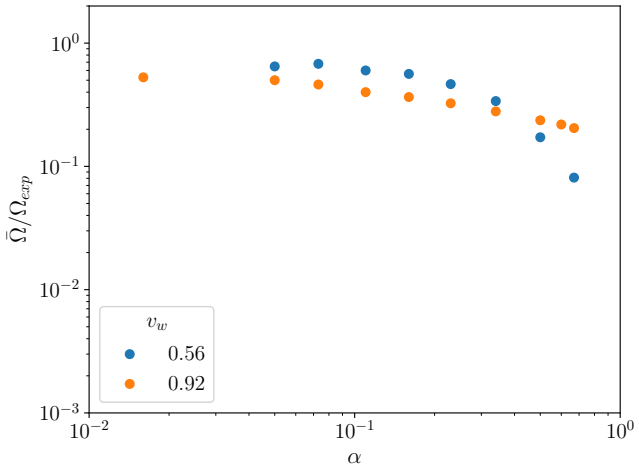

Figure 5.3: Suppression factor with respect to the strength of the phase transition due to vorticity and reheating effects in the plasma. $\bar{\Omega}$ is the reduced peak gravitational wave energy density and Ω_{exp} is the expected peak gravitational wave energy density. The data is taken from [5].

grows. This reduces the amount of available kinetic energy that can be transferred to the fluid. The rotational component for detonations, however, remains small and constant. The probable explanation for this effect is the formation of reheated droplets of the metastable phase that are produced during the collisions of the bubble walls. These droplets can then slow down the bubble walls and reheat the surrounding regions. The simulations considered a simple bag equation of state where the results only depend on input parameters of v_w and α. For a given v_w, we use an interpolation of their results to estimate the corresponding suppression factor to the $\Omega_{\rm GW}h^2$ as a function of α. We show the suppression factor in Fig. 5.3 for two representative bubble wall velocities. We utilize extrapolation for when α is out of range. Although the results were performed using a bag equation of state, we numerically compute α in the beyond the bag model and assume that the suppression from vorticity and reheating derived with a bag model applies without modification. We will test this assumption in future work. Furthermore, the simulations suggest that the RMS fluid velocity $\bar{U}_f$ reaches a maximum that is under-approximated by calculating the expected $\bar{U}_f$ around a single bubble. We use the results of $\bar{U}_{f,\rm max}/\bar{U}_{f,\rm exp}$ to estimate the maximum fluid velocity in the highest diligence after calculating $\bar{U}_f$ in the beyond the bag model.

A careful calculation of the gravitational wave production in an expanding universe will result in a suppression factor of the form

$$\Upsilon_{RD} = 1 - \frac{1}{y}, \tag{5.34}$$

for a radiation dominated era where $y = a/a_s$ is a dimensionless scale factor ratio

normalized by when the source of production becomes active. For a radiation dominated era, the time elapsed since some reference time, t_s, is

$$(t - t_s)H_s = \frac{y^2 - 1}{2}. \tag{5.35}$$

Due to the presence of shocks and turbulence in the plasma, the time elapsed is unlikely to last an arbitrarily long time. The effective lifetime of the source is then given by the timescale of turbulence, $\tau_{\rm sw} = R_*/\bar{U}_f$. This was the basis of the suppression factor used in Eq. 5.14-5.15. We use the estimated maximum of the fluid velocity in the beyond the bag model when calculating the lifetime of the source. The gravitational wave energy density will then be suppressed by

$$\Upsilon = 1 - \frac{1}{\sqrt{1 - 2\tau_{\rm sw}H_s}}, \tag{5.36}$$

which approaches the asymptotic value $\Upsilon = 1$, the lowest diligence, when $\tau_{\rm sw}H_s \to \infty$. When $\tau_{\rm sw}H_s \ll 1$, the suppression factor is approximately $\Upsilon = \tau_{\rm sw}H_s$, the modest diligence.

The peak gravitational wave energy density after taking into consideration the suppressions arising from vorticity and reheating effects in the plasma as well as the lifetime of source becomes

$$h^2\Omega_{\rm GW} = 8.5 \times 10^{-6} \left(\frac{100}{g_*}\right)^{1/3} K^2 \left(\frac{H_*}{\beta}\right) v_w \Upsilon \left(\bar{U}_{f,\rm max}, R_*\right) \left(\frac{\bar{\Omega}(v_w, \alpha)}{\bar{\Omega}_{\rm exp}(v_w, \alpha)}\right), \tag{5.37}$$

where K is calculated in the beyond the bag, β/H_* is calculated from the mean bubble separation, and the last factor arises from the vorticity and reheating effects in the plasma.

5.3 Test models

In this section we examine the numerical difference in predictions arising from different levels of diligence in several models

1 The Standard Model Effective Field Theory (SMEFT), itself close to a toy model when it comes to cosmological phase transitions [97], but which allows for a comparison to the uncertainties arising from gauge dependence and the breakdown of perturbation theory as outlined in [354].

2 Dark Higgs models [55], the simplest phase transition that can occur in a dark sector and has only three free parameters.

3 A real scalar singlet extension to the standard model (xSM) [367]. A model that allows a tree level barrier, like SMEFT, but is on firmer footing as a physical theory.

Using a spectrum of models gives a realistic account of the size of the relative errors for different level of diligence without being overly sensitive to model specific effects. We will also present a toy model in the appendix D, that has the convenient property that much of the analysis can be done analytically.

5.3.1 SMEFT

SMEFT is a model independent method of examining many extensions of the Standard Model by augmenting it with a tower of high dimensional operators, each suppressed by higher and higher powers of the cutoff scale corresponding

to the scale of new physics. Unfortunately, the Standard Model requires such a large change to its potential that the scale of new physics needs to be quite low to augment a strong first order phase transition [97]. In such a case the SMEFT only provides a qualitative description of the UV complete scalar sector, and then only in special circumstances [97]. In the SMEFT the tree level potential is augmented by a single higher dimensional operator

$$V_{\text{tree}} = \mu_h^2 \phi^\dagger \phi + \lambda \left(\phi^\dagger \phi\right)^2 + \frac{1}{M^2}(\phi^\dagger \phi)^3 + \Delta V, \tag{5.38}$$

where M characterizes the cut off scale, ϕ is the SM Higgs doublet and ΔV_h is chosen such that the zero-temperature minimum is shifted to the origin. We will consider the full free energy density at one-loop given by

$$f(\phi, T) = V_{\text{tree}} + V_{\text{CW}} + V_{\text{CT}} + V_T, \tag{5.39}$$

where V_{CW} is the Coleman-Weinberg contribution and V_T is the finite-temperature correction. These are given by

$$V_{\text{CW}}(h, \mu) = \frac{1}{64\pi^2} \sum_\alpha N_\alpha M_\alpha^4(h) \left[\log \frac{M_\alpha^2(h)}{\mu^2} - C_\alpha\right], \tag{5.40}$$

and

$$V_T(h, T) = \frac{T^4}{2\pi^2} \sum_\alpha N_\alpha \int_0^\infty dx\, x^2 \log\left[1 \pm e^{-\sqrt{x^2 + M_\alpha^2(h)/T^2}}\right] \tag{5.41}$$

$$+ \frac{T}{12\pi} \sum_{\text{bosons}\alpha} N_\alpha \left[M_\alpha^3(h) - M_{T,\alpha}^3(h, T)\right], \tag{5.42}$$

where N_α counts the number of degrees of freedom of each particle and C_α is a constant that is 5/6 for gauge bosons and 3/2 for all others. We note that the daisy terms in Eq. 5.42 are the result of a high temperature expansion which

may cause an IR-divergence in the speed of sound for low temperatures [363]. We explicitly check this by including a Boltzmann suppression term when $M_\alpha \lesssim 2.2T$. The sums run over the top quark, W and Z bosons, and the Higgs boson h. The total degrees of freedom in SMEFT is the Standard Model value $g_{\rm SM} = 106.75$. The calculation of the speed of sound requires including all the relativistic particle species in the free energy density. We will account for the remaining light particles that were neglected in V_T by including the term:

$$\delta V_T(h) = -\frac{\pi^2}{90} g'_* T^4, \tag{5.43}$$

to the free energy density where $g'_* = 345/4$. However, in the bag model, the speed of sound is taken to be $c_s^2 = 1/3$ and the light species can be ignored as they do not affect the phase transition dynamics. The last term in V_T corresponds to the resummation of the daisy terms of the scalar bosons. To calculate the effective potential and the counter-terms at zero-temperature, we fix the zero-temperature $\overline{\rm MS}$-parameters by matching the physical observables at the Z boson pole mass m_Z using the full self energies. To go beyond the bag model, we need the absolute pressure in each phase, and not just the relative pressure. We therefore add an overall constant in the potential such that the pressure in the broken phase at zero temperature vanishes at one loop. The scale of the Coleman-Weinberg potential is taken to be at $\mu \sim T$ for the dynamics of the phase transition and we run the parameters to this scale.

5.3.2 Dark Renormalizable Models

Here we will consider a dark Higgs model [48, 117, 55, 116] of the type $SU(N)/SU(N-1)$ with renormalizable operators following the conventions in [55]. The overall scale Λ and the zero temperature vacuum expectation value v are the only inputs of the model. We can then define the zero temperature parameters such as the tachyonic mass and self coupling as

$$-\mu^2(0) = -\frac{\Lambda^4}{v^2}, \tag{5.44}$$

$$\lambda(0) = \frac{\Lambda^4}{v^4}, \tag{5.45}$$

where factors of v/Λ will control the thermal parameters. The tree level potential is then defined as

$$V(H) = \Lambda^4 \left[-\frac{1}{2}\left(\frac{h_D}{v}\right)^2 + \frac{1}{4}\left(\frac{h_D}{v}\right)^4 \right] + \Delta V, \tag{5.46}$$

where h_D is the dark Higgs of the doublet H and ΔV shifts that potential at the minimum to zero. The degrees of freedom of the full dark sector in consideration are

$$n_H = 1,\ n_G = 2N-1,\ n_{GB} = 3\times(2N-1),\ n_f = 2\times N\times N_f, \tag{5.47}$$

where n_G is the number of Goldstone bosons, n_{GB} are the gauge bosons, N_f is the number of fermions,and N is the rank of the group.

The free energy density in consideration is

$$f(h_D, T) = V_{\text{tree}} + V_{\text{CW}} + V_{\text{CT}} + V_T + \delta V_T, \tag{5.48}$$

where V_{CW} and V_T are defined in Eq. (5.40-5.42). Here the summations now only run over the dark sector particles. This requires us to add on the additional

relativistic particles not included in the sum which now include the full degrees of freedom of the Standard Model:

$$\delta V_T = -\frac{\pi^2}{90} g_* T^4, \tag{5.49}$$

where $g_* = 106.75$. We add the term ΔV so that the minimum of the tree-level potential is shifted to zero. We choose the scale of the one-loop potential to be at Λ.

The inclusion of the CW-term will shift the zero-temperature vacuum expectation value away from v. We add the counter-term potential

$$V_{\rm CT}(h_D) = -\frac{\delta\mu^2}{2} h_D^2 + \frac{\delta\lambda}{4} h_D^4 + \delta\Delta V_h, \tag{5.50}$$

where $\delta\mu^2$, $\delta\lambda$, and $\delta\Delta V_h$ are chosen such that

$$\frac{\partial f(h_D, 0)}{\partial h_D}\Big|_v = 0, \tag{5.51}$$

$$\frac{\partial^2 f(h_D, 0)}{\partial h_D^2}\Big|_v = m^2(0) \equiv 2\frac{\Lambda^4}{v^2}, \tag{5.52}$$

$$f(v, 0) = 0, \tag{5.53}$$

to maintain the tree-level structure of the potential. We work in the Landau gauge where the Goldstone bosons have zero mass at the $h_D = v$ which causes an IR-divergence in the one-loop potential. This causes an issue in the evaluation of the counter-terms. One prescription is to remove the Goldstone bosons from the sum in the CW potential. For the purpose of this work, we will follow the procedure in [368] to evaluate the counterterms. This shifts the Goldstone mass by its mass at the one-loop level, i.e

$$m_G(h_D) \to m_G(h_D) + \frac{1}{h_D}\frac{\partial V^{(1)}}{\partial h_D}, \tag{5.54}$$

where

$$m_G(h_D) = \Lambda^4 \left(\frac{h_D^2}{v^4} - \frac{1}{v^2} \right), \tag{5.55}$$

is the field dependent mass of the Goldstone bosons.

5.3.3 xSM

The singlet extended SM, known as "xSM", consists of the standard SM Higgs doublet $H^T = \left(G^+, \left(v_{\rm EW} + h + iG^0\right)/\sqrt{2}\right)$ and a real gauge singlet $S = v_s + s$ where the electroweak vacuum is $(v_{\rm EW}, v_s)$ [369, 219, 98, 40, 41, 249, 370, 371, 372]. The tree level potential in this setup is defined as

$$\begin{aligned} V(H,S) = & -\mu^2 H^\dagger H + \lambda \left(H^\dagger H\right)^2 + \frac{a_1}{2} H^\dagger H S \\ & + \frac{a_2}{2} H^\dagger H S^2 + \frac{b_2}{2} S^2 + \frac{b_3}{3} S^3 + \frac{b_4}{4} S^4 + \Delta V, \end{aligned} \tag{5.56}$$

where ΔV shifts the minimum of the potential to zero. The mass parameters μ^2 and b_2 are related to the other model parameters through the minimization conditions around the electroweak vacuum,

$$\begin{aligned} \mu^2 &= \lambda v_{\rm EW}^2 + \frac{1}{2} v_s \left(a_1 + a_2 v_s\right), \\ b_2 &= \frac{1}{4 v_s} \left[v_{\rm EW}^2 \left(a_1 + 2 a_2 v_s\right) + 4 v_s^2 \left(b_3 + b_4 v_s\right) \right]. \end{aligned} \tag{5.57}$$

The parameters λ, a_1, and a_2 are related to the physical parameters θ, m_{h_1}, and m_{h_2} through the mass matrix diagonalization as

$$\begin{aligned}
\lambda &= \frac{m_{h_1}^2 c_\theta^2 + m_{h_2} s_\theta^2}{2v_{\rm EW}^2}, \\
a_1 &= \frac{2v_s}{v_{\rm EW}^2}\left[2v_s^2\left(2b_4 + \widetilde{b}_3\right) - m_{h_1}^2 - m_{h_2} + c_{2\theta}\left(m_{h_1}^2 - m_{h_2}^2\right)\right], \\
a_2 &= -\frac{1}{2v_{\rm EW}^2 v_s}\left[-2v_s\left(m_{h_1}^2 + m_{h_2}^2 - 4b_4 v_s^2\right) + \left(m_{h_1}^2 - m_{h_2}^2\right)\left(2c_{2\theta}v_s - v_{\rm EW}s_{2\theta} + 4\widetilde{b}_3 v_s^3\right)\right],
\end{aligned} \tag{5.58}$$

where $\widetilde{b}_3 \equiv b_3/v_s$ and θ is the mixing angle of the physical fields h_1 and h_2 defined as

$$h_1 = c_\theta h + s_\theta s, \quad h_2 = -s_\theta h + c_\theta s, \tag{5.59}$$

with $s_\theta \equiv \sin(\theta)$ and $c_\theta \equiv \cos(\theta)$. Here we associate h_1 as the SM Higgs and h_2 is some heavier scalar.

The free energy density we consider in the xSM presented here contains only the high temperature expansion approximation of the full finite temperature one loop effective potential since the phase transition is primarily driven by the cubic terms. The free energy is then

$$\begin{aligned}
f(h,s,T) = &-\frac{1}{2}\left[\mu^2 - \Pi_h(T)\right]h^2 - \frac{1}{2}\left[-b_2 - \Pi_s(T)\right]s^2 \\
&+ \frac{1}{4}\lambda h^4 + \frac{1}{4}a_1 h^2 s + \frac{1}{4}a_2 h^2 s^2 + \frac{b_3}{3}s^3 + \frac{b_4}{4}s^4 \\
&- \frac{1}{3}\frac{\pi^2}{30}g_* T^4,
\end{aligned} \tag{5.60}$$

where we take $g_* = 106.75$. The field dependent thermal mass $\Pi_h(T)$ and $\Pi_s(T)$

are

$$\Pi_h(T) = \left(\frac{2m_w^2 + m_z^2 + 2m_t^2}{4v^2} + \frac{\lambda}{2} + \frac{a_2}{24}\right) T^2,$$
$$\Pi_s(T) = \left(\frac{a_2}{6} + \frac{b_4}{4}\right) T^2, \tag{5.61}$$

where the physical masses of the W, Z, and t-quark are used to define the gauge and Yukawa couplings to h.

5.4 Results

The resulting gravitational wave spectrum is dependent on the level of precision of the thermal parameters. Until recently, the bag model was assumed to compute the phase transition strength and the kinetic energy of the fluid. Going beyond the bag model will require the calculation of the speed of sound in the plasma for both the symmetric and broken phase which should result in a more accurate treatment of the thermal parameters. These quantities are temperature dependent and will change depending on the temperature at which they are computed. Furthermore, the temperature scales of the phase transition such as the nucleation and percolation temperature are also sensitive to level of diligence in the calculations. We use the publicly available codes CosmoTransitions [281] and BubbleProfiler [373] to compute the actions in order to find the relevant transition temperatures.

The lowest diligence level will compute the thermal parameters at the estimated nucleation temperature defined in Eq. 5.4. The strength of the phase transition is calculated using Eq. 5.5, the inverse time duration of the phase transition is calculated using Eq.5.6, and the peak gravitational wave energy density is

calculated using Eq. 5.7.

The modest diligence level will compute the thermal parameters at the estimated percolation temperature in Eq. 5.11. We will use Eq. 5.12, Eq. 5.13, and Eq. 5.15 to estimate the strength of the phase transition, inverse time duration, and peak gravitational wave spectrum respectively. The lifetime of the source is estimated using Eq. 5.14. There is an ambiguity as to which temperature to employ in the calculation of the thermal parameters: the nucleation temperature or the percolation temperature. The true percolation temperature T_p, Eq. 4.47, should lie close to the temperature at which the phase transition ends T_f. The inverse time duration should be computed from the mean bubble separation, Eq. 4.62, which is evaluated at T_f. The highest diligence will evaluate all thermal parameters at T_f to ensure that all quantities are evaluated at the same temperature as the inverse time duration. From here on out, we will associate T_p with Eq. 5.11 when referring to modest diligence. The highest diligence will also utilize the beyond the bag model to calculate the strength of the phase transition Eq. 5.25 and the kinetic energy fraction Eq. 5.31 which requires the numerically calculated speed of sound in Eq. 5.23. The lowest and modest diligence calculations will assume $c_s^2 = 1/3$ as is done in the bag model. The peak gravitational wave spectrum is found from Eq. 5.37 which accounts from the lifetime of the source, Eq. 5.36, as well as vorticity and reheating effects in the plasma. We note that the suppression factor due to the finite lifetime used in Eq. 5.14 is a valid approximation of Eq. 5.36 only when $\tau_{\rm SW} H \ll 1$.

In the following sections, we will compare the different levels of diligence

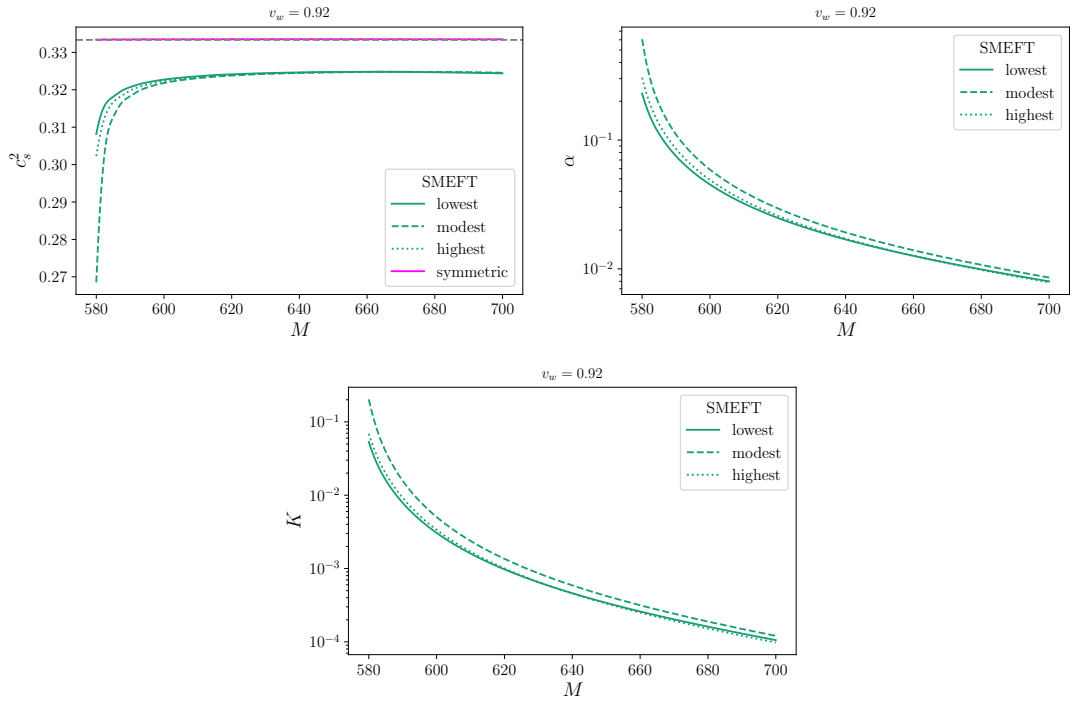

Figure 5.4: **SMEFT**: The top left panel shows the speed of sound calculated in the symmetric and broken phase using Eq. 5.23 at the different levels of diligence. The gray dashed line corresponds to the bag model with $c_s^2 = 1/3$. The symmetric phase (solid magenta) is only shown at highest diligence. The top right panel shows the strength of the phase transition at the different levels of diligence using Eq. (5.5, 5.12, 5.25). The bottom panel shows the kinetic energy fraction at the different levels of diligence where the lowest and modest diligence use fits for κ to get K and the highest diligence uses Eq. 5.31. The temperatures are set to T_n (5.4), T_p (5.11), and T_f (4.70) for the lowest, modest, and highest diligence respectively. The numerical calculation of the speed of sound only enters in the highest diligence of α.

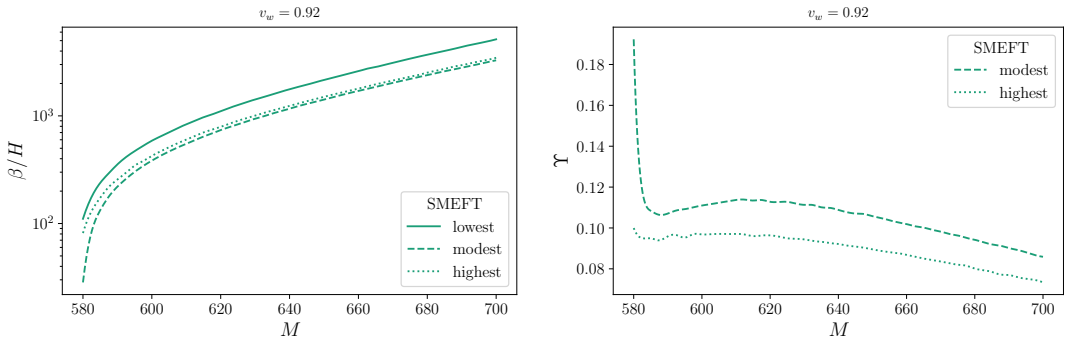

Figure 5.5: **SMEFT**: The left panel shows the inverse time duration of the phase transition at the different levels of diligence using Eq. (5.6, 5.13, 4.77). The lowest and modest diligences are estimated using the first derivative of the action dS/dT and the highest diligence is computed directly from the mean bubble separation, Eq. 4.62. The right panel shows the suppression factor due to the lifetime of the source using Eq. 5.14 and Eq. 5.36 for modest and highest diligence respectively. The lowest diligence corresponds to $\Upsilon \to 1$. The temperatures are set to T_n (5.4), T_p (5.11), and T_f (4.70) for the lowest, modest, and highest diligence respectively.

in SMEFT, the dark renormalizable model, and xSM. The error in the peak gravitational wave energy density,

$$\frac{\Delta\Omega}{\Omega} = \frac{|\Omega^j h^2 - \Omega^{\rm high} h^2|}{\min\left[\Omega^j h^2, \Omega^{\rm high} h^2\right]}, \tag{5.62}$$

where $j = (\text{low}, \text{mod})$ refers to lowest, modest, and highest diligence respectively, will be used to compare the different levels of diligence.

5.4.1 SMEFT

The SMEFT model we consider has the scale of the zero-temperature one loop potential set to $\mu = T$ as well as temperature dependence in the running of the couplings. This will contribute additional temperature dependence to the speed of sound calculations in the broken phase. We note that Ref. [374] also considered the beyond the bag model in SMEFT using a high temperature expansion of the effective potential. The speed of sound will never reach the bag model with $c_s^2 = 1/3$ as seen in the top figure left of Fig. 5.4. The green curves show the different levels of diligence for the speed of sound in the broken phase and the dashed gray curve represents $c_s^2 = 1/3$. The magenta curve is the speed of sound calculated in symmetric phase which is approximately the same in each level and does not deviate far from the bag model. We do not consider any additional relativistic degrees of freedom and thus expect little deviations between the speed of sound in the symmetric phase. As the scale M grows large, the speed of sound in the broken phase approaches a constant value of $c_s^2 \sim 0.32$. There is noticeable disagreement between the different levels below $M = 600$ where there is mild supercooling. For a given M, the speed of sound is only a function of temperature. The differences in c_s^2 in the broken phase is the result of these different temperatures at which the speed of sound is set to when calculating the strength of the phase transition $\alpha_{\bar{\theta}}(c_s^2)$. The large difference in T_p and T_f is due to the approximations of T_p in Eq. 5.11 which is less accurate when S_3/T acquires a minimum for smaller M.

On the top right panel of Fig. 5.4 we show the strength of the phase transition computed at the different levels of diligence. Both the lowest and modest diligence curves have $c_s^2 = 1/3$ whereas the highest diligence curve corresponds to the beyond the bag calculation with c_s^2 shown in the top left panel. Although each level is computed at different temperatures, the lowest diligence is a better approximation of the strength of the phase transition compared to level 2 which over approximates α. This is a result of T_p computed in the modest diligence placing far below T_f which results in a higher estimated α. The difference between the different levels on the strength of the phase transition is negligible for large M as a result of the asymptotic behavior observed in c_s^2 and the better approximation of T_p when there is no barrier present. There is also a dependence on the bubble wall velocity in both c_s^2 and α for the modest and highest diligence curves in computing T_p and T_f but we only show detonation with $v_w = 0.92$ because the difference is minor. The kinetic energy fraction is shown in the bottom panel of Fig. 5.4 and should depend on the speed of sound and phase transition strength. Similar to what was seen in α, the lowest and highest diligence curves are closer together for large M while the modest diligence curve is the least accurate. For each of the levels, the largest error in both α and K occurs for smaller M where the speed of sound is significantly lower than $c_s^2 = 1/3$ and T_p is far from T_f.

In the left panel of Fig. 5.5, we show the inverse time duration β/H of the phase transition for detonation. The largest difference between modest diligence and highest diligence occurs for small M and is due to the following reason: the minimum formed in the action where T_p calculated in Eq. 5.11 along with β/H

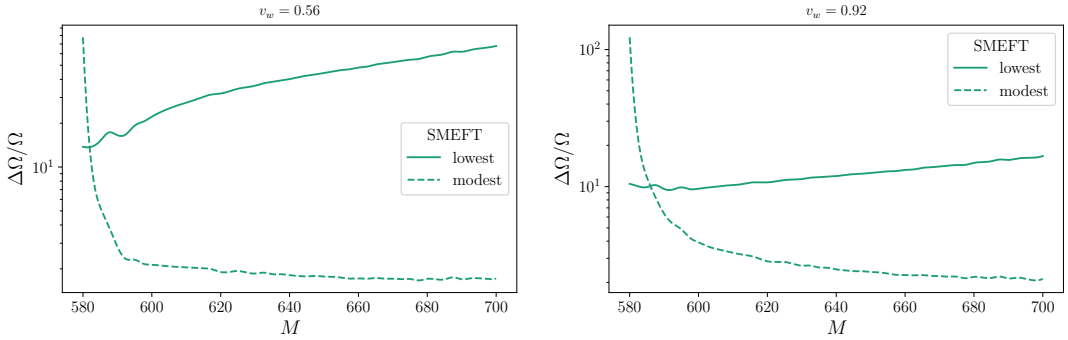

Figure 5.6: **SMEFT**: The relative error when using the lowest and modest levels of diligence, compared to the highest level of diligence (for which $\Delta\Omega/\Omega = 0$). The vertical axis shows the peak (frequency-independent) gravitational wave energy density for detonation. The precise definition of $\Delta\Omega/\Omega$ is given in Eq. 5.62. The horizontal axis corresponds to the cutoff scale M. $\Delta\Omega/\Omega$ is displayed for deflagration and detonation at different levels of diligence using Eq. (5.7, 5.15, 5.37) and Eq. 5.62. The temperatures are set to T_n (5.4), T_p (5.11), and T_f (4.70) for the lowest, modest, and highest diligence respectively. Both the modest and highest diligence contains suppression factors due to the lifetime of the source. The highest diligence contains the suppression factor due to vorticity effects in the plasma.

in Eq. 5.13 are inaccurate when there is a minimum present. The lowest diligence is a better approximation than the modest diligence in this regime. The modest and the highest diligence become indistinguishable for large M when there is no minimum in the action. For small M, the lowest diligence curve appears to be a good approximation for modest diligence. Although β/H estimated from the action is not accurate when there is a minimum, the error using T_n appears to do better than using the approximation of T_p. Contrary to the α and K, β in the lowest diligence never approaches the highest diligence for large M where the error appears to get worse. This is due to the inaccuracy in using the approximate T_n. In this regime, T_p is a better approximation of the inverse time duration as there is no minimum present in the action. The right panel of Fig. 5.5 shows the suppression factor due to the lifetime of the source in the modest and highest diligence. The error between the two levels gets worse for small M which is the result of the error in T_p. The error approaches a constant as M gets large.

In Fig. 5.6 we show the relative error in the peak gravitational wave spectrum for both deflagration and detonation. The error with respect to the highest diligence is estimated using Eq. 5.62. For both deflagration and detonation, the modest diligence spikes to an error of $\Delta\Omega/\Omega \sim 10^2$ for small M. This is correlated with the large error observed in α, K, β, and Υ seen in Fig. 5.4 and Fig. 5.5. The modest diligence error for both profile types slowly approach a constant value as M grows large which is the result of the minimal error in α, β/H, K. The error in Υ appears to become a constant for large M. The suppression factors due to the lifetime of the source grow to zero as M grows large which results in the increasing

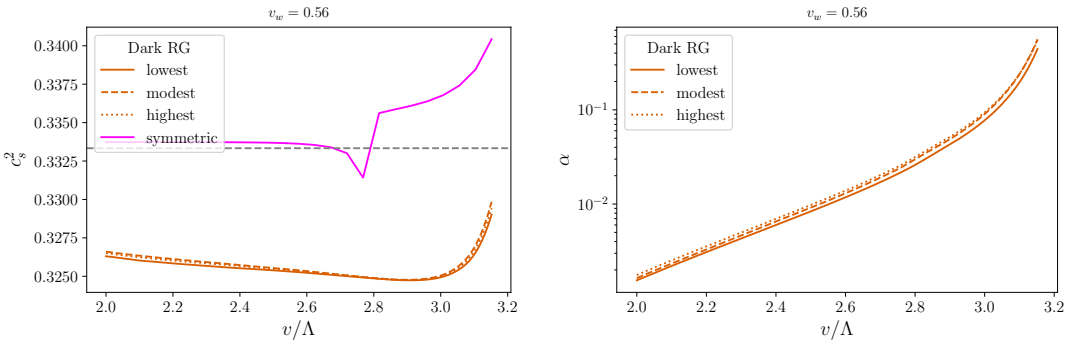

Figure 5.7: **Dark RG**: The left panel shows the speed of sound calculated in the symmetric and broken phase using Eq. 5.23 at the different levels of diligence. The gray dashed line corresponds to the bag model with $c_s^2 = 1/3$. The symmetric phase (solid magenta) is only shown at highest diligence. The right panel shows the strength of the phase transition at the different levels of diligence using Eq. (5.5, 5.12, 5.25). The temperatures are set to T_n (5.4), T_p (5.11), and T_f (4.70) for the lowest, modest, and highest diligence respectively. The numerical calculation of the speed of sound only enters in the highest diligence of α.

behavior of the peak error in the lowest diligence which does not include any suppression factors. Overall we notice an error in the peak gravitational wave energy density of $10^1 - 10^2$ for lowest diligence and $10^0 - 10^2$ for modest diligence.

5.4.2 Dark Renormalizable Models

The dark renormalizable model considered in the analysis does not couple to the Standard Model and will consist of a $N = 10$ group, and $2N - 1$ gauge bosons with charge $g_D = 0.8$. The scale of the one-loop potential is also T independent.

These will result in a speed of sound in the symmetric phase that differs from the one seen in SMEFT.

We show the speed of sound calculated using Eq. 5.23 on the left panel of Fig. 5.7 for the different levels of diligence. The differences between the levels of diligence in the speed of sound are only minor. We show only the highest diligence curve for the speed of sound in the symmetric phase. For small v/Λ, the speed of sound in the symmetric phase remains constant with a value slightly above the one given in the bag model. This is attributed to the additional degrees of freedom arising from the dark sector. The speed of sound above $v/\Lambda = 2.6$ begins to decrease until it reaches a discontinuity near $v/\Lambda = 2.8$. It then jumps to $c_s^2 = 0.336$ where it begins to monotonically increase. This discontinuity is a result of the daisy terms in the effective potential. With out the daisy terms, the speed of sound in the symmetric phase would be smoothly connected and monotonically increasing.

The strength of the phase transition is plotted on the right panel Fig. 5.7. The different levels appear to agree very well with each other with the lowest diligence becoming slightly worse at high v/Λ. For most of the parameter space, the highest diligence has the greatest α because it is computed at the numerically calculated values for c_s^2 in the broken phase which results in a amplification compared to the other two levels. This is due to the factor $(1 + c_s^{-2})$ in $\alpha_{\bar{\theta}}$. The error between the modest and highest diligence begins to decrease as v/Λ increases which is related to the speed of sound approaching $c_s^2 = 1/3$. Despite the differences between the different levels, the speed of sound in the broken phase lies between

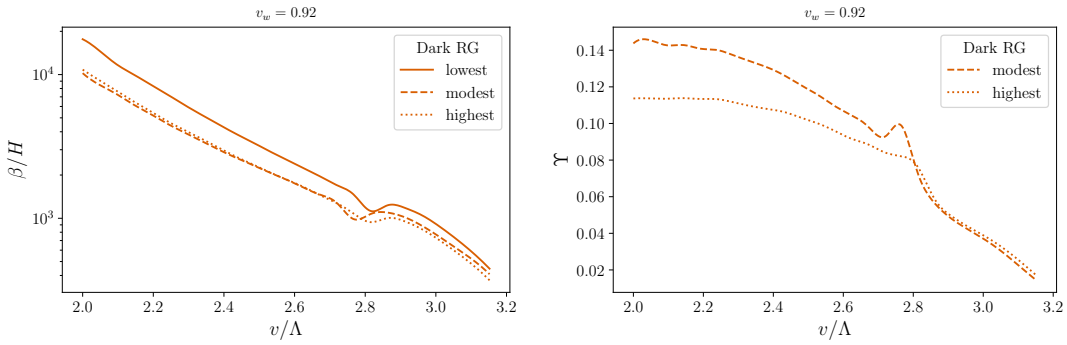

Figure 5.8: **Dark RG**: The inverse time duration of the phase transition at the different levels of diligence using Eq. (5.6, 5.13, 4.77). The lowest and modest diligences are estimated using the first derivative of the action dS/dT and the highest diligence is computed directly from the mean bubble separation. The right panel shows the suppression factor due to the lifetime of the source using Eq. 5.14 and Eq. 5.36 for modest and highest diligence respectively. The lowest diligence corresponds to $\Upsilon \to 1$. The temperatures are set to T_n (5.4), T_p (5.11), and T_f (4.70) for the lowest, modest, and highest diligence respectively.

$c_s^2 \sim 0.325 - 0.330$ and does not contribute a significant source of error to the strength of the phase transition.

The inverse duration of the phase transition is plotted in the left panel of Fig. 5.8 for detonation. The lowest diligence calculated using Eq. 5.6 consistently over approximates β/H while modest diligence calculated using Eq. 5.13 agrees well with the highest diligence found from the mean bubble separation. There were no minima found in the action for any of the parameters in consideration so the difference between T_p calculated using Eq. 5.11 in the modest diligence

and T_f calculated using Eq. 4.70 in the highest diligence is only minor. The dips near $v/\Lambda > 2.8$ in β/H are the result of the shape of $S(T)/T$ which causes the highest error between the modest and highest diligence. This dip also effects the suppression factor due to the lifetime of the source as seen in the right panel of Fig. 5.8. The modest diligence over-approximates the suppression factor up until $v/\Lambda \sim 2.8$ where they eventually become approximately equal in magnitude. The large v/Λ regime has a small β/H and large α which results in a small lifetime of the source $\tau_{\rm sw}$. The modest diligence suppression factor is then an appropriate approximation in this regime.

The error in the gravitational wave spectrum is shown in Fig. 5.9 for deflagration and detonation. For both the lowest and modest diligence, the error remains roughly constant until $v/\Lambda \sim 2.8$ where it exhibits some oscillations. This behavior is related to the dips in Fig. 5.8. Past $v/\Lambda \sim 2.8$, both the lowest and modest diligence begin to increase. The error in the lowest diligence past this point is dominated by the lack of suppression factor due to the lifetime of the source. The suppression factor remains roughly constant until $v/\Lambda \sim 2.8$ where it begins to approach zero and as a result increases the error. The increasing behavior in the modest diligence is likely due to the separation in β/H between the modest and highest diligence in Fig. 5.8 and the suppression factor from vorticity and reheating effects in the plasma which are stronger for larger α. The values of the speed of sound in the symmetric and broken phase calculated at T_f are not far from the bag model of $c_s^2 = 1/3$ and we do not consider it a strong source of error in the peak gravitational wave energy density spectrum. Overall

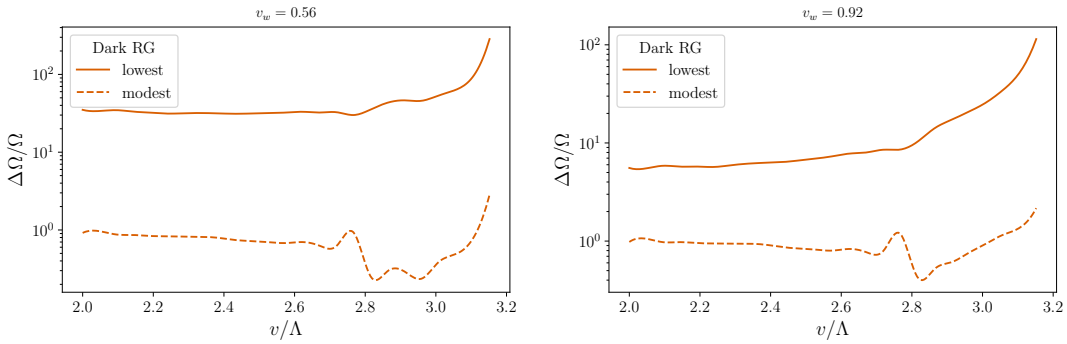

Figure 5.9: **Dark RG**: The relative error when using the lowest and modest levels of diligence, compared to the highest level of diligence (for which $\Delta\Omega/\Omega = 0$). The vertical axis shows the peak (frequency-independent) gravitational wave energy density for detonation. The precise definition of $\Delta\Omega/\Omega$ is given in Eq. 5.62. The horizontal axis corresponds to the ratio of the tree level v.e.v to the cut off scale v/Λ. $\Delta\Omega/\Omega$ is displayed for deflagration and detonation at different levels of diligence using Eq. (5.7, 5.15, 5.37) and Eq. 5.62. The temperatures are set to T_n (5.4), T_p (5.11), and T_f (4.70) for the lowest, modest, and highest diligence respectively. Both the modest and highest diligence contains suppression factors due to the lifetime of the source. The highest diligence contains the suppression factor due to vorticity effects in the plasma.

we notice an error in the peak gravitational wave energy density of $10^1 - 10^3$ for lowest diligence and $10^{-1} - 10^1$ for modest diligence.

5.4.3 xSM

We show in the top left panel of Fig. 5.10 the speed of sound in the symmetric and broken phase for a scan over the heavy singlet mass in the xSM model while holding all other parameters constant. The speed of sound in the symmetric phase is approximately $c_s^2 = 1/3$ as in the bag model. The speed of sound in broken phase deviates far from the bag model where it approaches zero as $m_{h_2} \to 0$. The speed of is strongly correlated with the cubic term that arises from the extra scalar who also acquires a tree level vacuum expectation value. The speed of sound can then be suppressed by increasing the b_3 parameter. This strong suppression in the broken phase speed of sound will lead to an amplification in the strength of the phase transition as seen in the top right panel of Fig. 5.10. The strength of the phase transition in the highest diligence grows larger compared to the other levels as the singlet gets heavier. This is directly related to the suppression in the speed of sound in the broken phase. There is a minor difference in the lower singlet mass range. The kinetic energy fraction is shown in the bottom panel of Fig. 5.10. The lowest and modest diligence both overestimate K for the entire range of the parameter space which is not observed in α. This can be attributed to the approximations used in the kinetic energy fraction pre-factor $\alpha/(1+\alpha)$ used in the peak gravitational wave energy density in Eq. 5.7 and the speed of sound dependence in solving the beyond the bag model hydrodynamic equations.

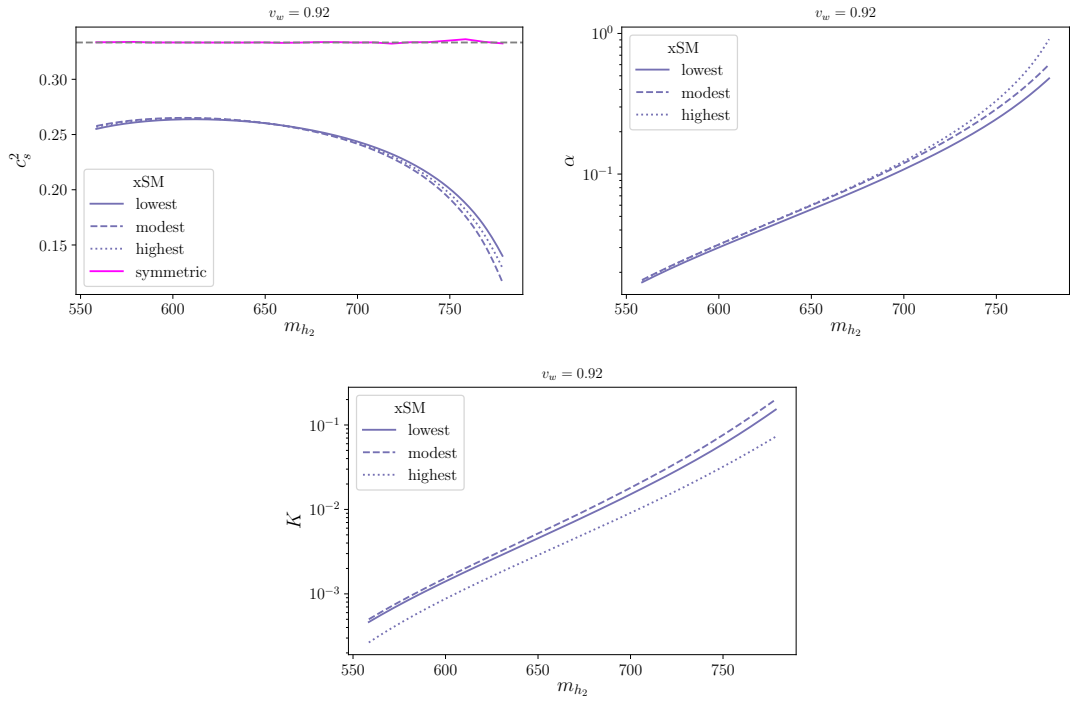

Figure 5.10: **xSM**: The top left panel shows the speed of sound calculated in the symmetric and broken phase using Eq. 5.23 at the different levels of diligence. The gray dashed line corresponds to the bag model with $c_s^2 = 1/3$. The symmetric phase (solid magenta) is only shown at highest diligence. The top right panel shows the strength of the phase transition at the different levels of diligence using Eq. (5.5, 5.12, 5.25). The bottom panel shows the kinetic energy fraction at the different levels of diligence where the lowest and modest diligence use fits for κ to get K and the highest diligence uses Eq. 5.31. The temperatures are set to T_n (5.4), T_p (5.11), and T_f (4.70) for the lowest, modest, and highest diligence respectively. The numerical calculation of the speed of sound only enters in the highest diligence of α.

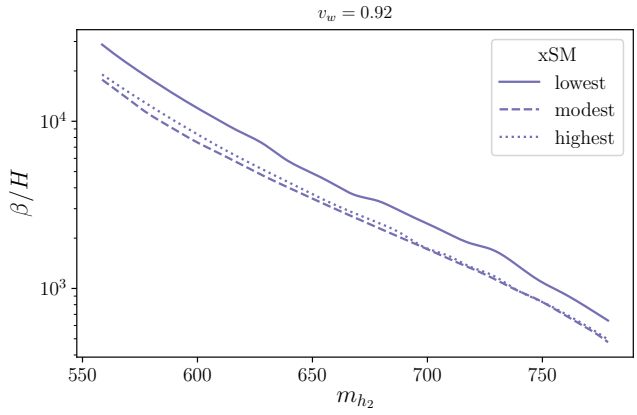

Figure 5.11: **xSM**: The inverse time duration of the phase transition at the different levels of diligence using Eq. (5.6, 5.13, 4.77). The lowest and modest diligences are estimated using the first derivative of the action dS/dT and the highest diligence is computed directly from the mean bubble separation. The temperatures are set to T_n (5.4), T_p (5.11), and T_f (4.70) for the lowest, modest, and highest diligence respectively.

The inverse time duration of the phase transition is plotted in Fig. 5.11 for the different levels of diligence. The modest diligence is a better approximation than that of the first level for β/H but slightly under-approximates the spectrum for lower mass ranges. The lowest diligence is a poor approximation for β/H for the entire parameter space.

The error in the gravitational wave spectrum compared to the highest diligence for deflagration and detonation is given in Fig. 5.12. The largest error in the spectrum occurs for the lowest diligence and this is due to the lack of suppression factor for the finite lifetime of the source and the larger uncertainty in β/H. The suppression factor for the modest diligence case is an under-approximation to the finite lifetime of the source particularly in the higher singlet mass regions. Both the lowest and modest diligence receive significant errors from neglecting the beyond the bag contributions to the kinetic energy which over estimates the peak spectrum which also gets worse for higher singlet masses. Overall the range of error in the peak gravitational wave energy density is between $[10^2 \sim 10^3]$ and $[10^0 \sim 10^2]$ for the different levels of diligence. All of the points above the range in m_{h_2} shown are certainly viable points and may even reach higher levels of error. However, this range in m_{h_2} is chosen such that all the points remain in either deflagration or detonation for both consistency and the lack of numerical simulations for hybrids.

5.4.4 Mean Bubble Separation vs Inverse Time Duration

The gravitational wave energy density is dependent on determining the mean bubble separation when the phase transition ends at temperature T_f. An approximation to the mean bubble separation can be determined by calculating the inverse time duration, β/H, from the first derivative of the action. This calculation is typically only valid when there is a negligible barrier at zero temperature. However, if there is a barrier at tree level, a minimum in the action will develop near T_f and the second derivative, β_2 will become relevant while the first derivative will vanish. The bubble nucleation rate can then take on the form

$$p = p_0 \exp\left[-S_* - \frac{1}{2}\beta_2^2(t - t_*)^2\right], \tag{5.63}$$

where t_* is the time when the temperature is near T_f and $S_* = S_3(T_*)/T_*$. The above result will ultimately lead to a new relation between the mean bubble separation R_* and the inverse time duration of the phase transition β.

This subtlety is not usually taken into account and the relation between R_* and β that is useful for gravitational wave calculations is simply given by the approximate formula

$$HR_* = (8\pi)^{1/3} v_w \left(\frac{H_*}{\beta}\right), \text{ with } \quad \beta = HTdS/dT, \tag{5.64}$$

where β is related to the first derivative of the action regardless of the presence of a barrier. Out of the models we consider, SMEFT and xSM can acquire tree level barriers that result in a minimum in the action. The lowest and modest diligence results presented here assume Eq. 5.64 always hold which can result in significant

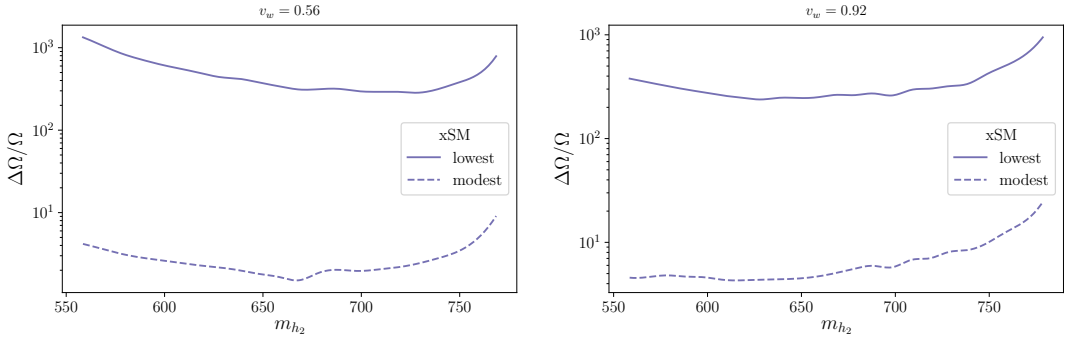

Figure 5.12: **Dark RG**: The relative error when using the lowest and modest levels of diligence, compared to the highest level of diligence (for which $\Delta\Omega/\Omega = 0$). The vertical axis shows the peak (frequency-independent) gravitational wave energy density for detonation. The precise definition of $\Delta\Omega/\Omega$ is given in Eq. 5.62. The horizontal axis corresponds to the heavy singlet mass m_{h_2}. $\Delta\Omega/\Omega$ is displayed for deflagration and detonation at different levels of diligence using Eq. (5.7, 5.15, 5.37) and Eq. 5.62. The temperatures are set to T_n (5.4), T_p (5.11), and T_f (4.70) for the lowest, modest, and highest diligence respectively. Both the modest and highest diligence contains suppression factors due to the lifetime of the source. The highest diligence contains the suppression factor due to vorticity effects in the plasma.

errors for these two models. Furthermore, the percolation temperature at which β/H is estimated is a function of β/H, Eq. 5.13, which can also acquire error if the barrier is not sufficiently taken care of. The highest diligence results can side-step these issues by numerically calculating the mean bubble separation from the number bubble density which is independent of any assumptions about the curvature of the action, i.e

$$HR_* = \left(\frac{n_b}{H^3}\right)^{-1/3}, \tag{5.65}$$

evaluated at the final temperature T_f. The final temperature as well does not depend on any underlying assumptions about the curvature of the action because it is numerically calculated from the false vacuum fraction. For comparisons between the inverse time durations with respect to the highest diligence, we first calculate HR_* and use Eq. 5.64 to determine an effective β/H.

The comparison between HR_* using Eq. 5.64 and Eq. 5.65 is shown in Fig. 5.13 where the left figure corresponds to SMEFT and right figure corresponds to xSM. The solid lines represent the proper mean bubble separation calculated at T_f. The dotted and dashed lines correspond to the mean bubble separation calculated first from β at T_f and T_p respectively. We denote T_p to refer to the estimation given in Eq. 5.11. Below $M = 600$ GeV in SMEFT, the action acquires a minimum as a result of the tree level barrier at zero temperature which causes $\beta(T_p)$ to significantly over-approximate HR_*. As mentioned previously, this is a result of the underlying assumptions in approximating both T_p and β which ignore the barrier. The mean bubble separation calculated from $\beta(T_f)$ performs better than

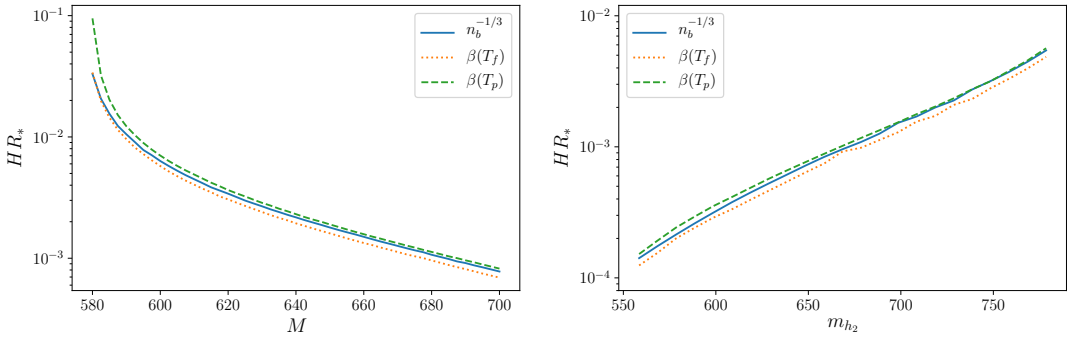

Figure 5.13: The mean bubble separation times the Hubble parameter for SMEFT (**left**) and xSM (**right**). The solid line corresponds to the numerically calculated value defined in Eq. 5.65 evaluated at T_f (4.70). The dashed and dotted lines correspond to the estimated value using Eq. 5.64 evaluated at T_f (4.70) and T_p(5.11) respectively.

$\beta(T_p)$ in this regime with nearly identical HR_* predictions compared to $n_b^{-1/3}$. This is largely due to T_f being independent of any assumptions on the action.

The xSM model consists of a second scalar and several parameters which when varied may induce either first step or second step phase transitions. The bench marks chosen involve scanning of the heavy singlet mass while holding the other model parameters fixed. All of the points resulted in a one step phase transition along with no minimum in the action. On the right of Fig. 5.13, we see that all three methods resulted in a roughly consistent approximation of HR_* with slightly better performance from $\beta(T_p)$ for large m_{h_2}. This can be attributed to the lack of minimum in the action observed in the parameter space. We reserve a further analysis of the mean bubble separation in xSM for future work.

Effect	Range of error (medium)	Range of error (low)	Type of error
Transition temperature	$\mathcal{O}(10^{-4} - 10^{1})$	$\mathcal{O}(10^{-1} - 10^{0})$	Random
Mean bubble separation	$\mathcal{O}(0 - 10^{-1})$	$\mathcal{O}(10^{-1} - 10^{0})$	Suppression
Fluid velocity	$\mathcal{O}(10^{-2} - 10^{0})$	$\mathcal{O}(10^{-2} - 10^{0})$	Random
Finite lifetime	$\mathcal{O}(10^{-3} - 10^{-1})$	$\mathcal{O}(10^{1} - 10^{3})$	Enhancement
Vorticity effects	$\mathcal{O}(10^{-1} - 10^{0})$	–	Random

Table 5.1: Full range of error of $\Delta\Omega/\Omega$ for each individual effect comparing the medium diligence and low diligence approaches to the high diligence approach.

5.5 Summary of Results

The previous results involved fixing certain characteristics associated with each of the outlined levels of diligence. In this section, we will fix all of the quantities as high diligence while varying the level of a single quantity to determine its impact on the error of $\Delta\Omega/\Omega$. Table 5.1 shows the range of error we observe associated with varying the level of diligence in the calculation of the transition temperature, mean bubble separation, fluid velocity, finite lifetime of the source, and vorticity effects. The base level of comparison will use Ω_{GW} calculated using Eq. 5.37 which assumes the transition temperature is at T_f and includes beyond the bag effects and the suppression factors due to the finite lifetime of the source and reheating effects in the plasma. We will now proceed to describe how the range of errors are calculated.

The transition temperatures used for the different levels were T_n (5.4) and

T_p (5.11. The frequency independent $\Omega_{\rm GW}$ is now calculated at high diligence using Eq. 5.37 for both the lowest and modest diligence. This is to show how $\Omega_{\rm GW}$ can change purely by the temperature at which the transition is assumed to take place. The lowest diligence will use T_n to calculate $\Delta\Omega/\Omega$ while the modest diligence will use T_p. The base level comparison is $\Omega_{\rm GW}$ at T_f which corresponds to the previously defined high diligence. Varying the transition temperature leads to an error of $(10^{-1} - 10^{0})$ and $(10^{-4} - 10^{1})$ for lowest and modest diligence respectively. The modest diligence can experience a larger error than the lowest diligence and this is due to the result of the strong super-cooling observed in SMEFT when $M \simeq 600$. The approximations used in calculating T_p break down when a minimum develops in the action and results in the 10^1 peak in the error for modest diligence. The error in the lowest diligence results in an enhancement in the spectrum which is attributed to $T_n > T_f$. The modest diligence experienced both enhancement and suppression which is due to T_p being much closer to T_f. The lowest diligence primarily had $\Omega_{\rm GW}^{\rm low} < \Omega_{\rm GW}^{\rm high}$ and modest diligence had $\Omega_{\rm GW}^{\rm med} > \Omega_{\rm GW}^{\rm high}$. For these reasons, we conclude that the type of error due to the transition temperature is random and dependent on the underlying model.

The estimation of the error due to the mean bubble separation will involve calculating R_*H from the β/H at T_n for the lowest diligence and R_*H from n_b at T_f for modest diligence. We use T_f for the modest diligence in determining the relevant quantities in $\Omega_{\rm GW}$ in this case to minimize error which may arise from using the T_p approximation. All quantities in $\Omega_{\rm GW}$ are calculated in high diligence at T_n and T_f for lowest and modest diligence respectively. The lowest

diligence exhibits the largest error with a range of $(10^{-1} - 10^{0})$ while modest diligence has the range $(10^{-3} - 10^{-1})$. The error in modest diligence observed in the table is only due to the approximation of the mean bubble separation from the inverse time duration but it is expected to be higher if T_p is used as opposed to T_f which helps to correct the error. Both the lowest and modest diligence had mostly $\Omega_{\rm GW}^{\rm low,med} < \Omega_{\rm GW}^{\rm high}$ with modest diligence having a couple benchmarks with $\Omega_{\rm GW}^{\rm med} > \Omega_{\rm GW}^{\rm high}$. We denote this type of error as predominately suppression.

The error estimate from the fluid velocity involves comparing the fits for kappa given in Appendix C to solving the hydrodynamic profiles numerically. The fluid velocity is related to the kappa through the kinetic energy fraction K in Eq. (5.10,5.31,5.33). The lowest diligence calculates $\Omega_{\rm GW}$ at T_f in the highest diligence with the replacement that K and U_f are now calculated using the fits to κ and the bag calculation for α. The modest diligence is the same as the lowest diligence except that κ is calculated using the hydrodynamic profiles with $c_s^2 = 1/3$ in the bag model. The error associated with the different treatments of the fluid velocity is $(10^{-2} - 10^{0})$ for lowest diligence and $(10^{-3} - 10^{0})$ for modest diligence. This represents the amount of error that one might expect in these models when performing precise calculations of $\Omega_{\rm GW}$ but without taking into consideration the beyond the bag treatment of the speed of sound in the plasma. The type of error we observe for the fluid velocity is random.

To determine the impact of the suppression factor due to the finite lifetime of the source has on the error, we compare $\Omega_{\rm GW}$ calculated in Eq. 5.37 with out Υ for the lowest diligence and with the replacement $\Upsilon \to \tau_{\rm SW} H$ corresponding

to Eq. 5.14 for the modest diligence. All quantities are evaluated at T_f. Modest diligence will also contain the suppression to U_f due to vorticity and reheating effects in the plasma. Note that this suppression is less dramatic than what one might naively expect from ref [5], as the suppression in the fluid velocity results in a longer lifetime for the soundwaves. For the range of models we consider, the error for modest diligence is in the range $(10^{-3} - 10^{-1})$ and represents the validity of the approximation used in Υ. The error in the lowest diligence experiences the highest error with a range of $(10^{1} - 10^{3})$. For all of the models, $\Omega_{\rm GW}^{\rm low,med} > \Omega_{\rm GW}^{\rm high}$. This type of error is an enhancement.

The last row in Table 5.1 corresponds to the error in $\Omega_{\rm GW}$ calculated using Eq. 5.37 without suppression factors arising from vorticity and reheating effects in the plasma. This is compared to the full suppression in highest diligence which uses $U_{f,\rm max}$ in the lifetime of the source as well. The range of error we observe is in the range of $10^{-1} - 10^{1}$. Neglecting $U_{f,\rm max}$ in the suppression factor will contribute at most an error of 0.62. The lowest diligence experienced $\Omega_{\rm GW}^{\rm low} < \Omega_{\rm GW}^{\rm high}$ for the all of the models. The modest diligence experienced mostly random error. The primary focus should be on modest diligence so we denote this type of error as random.

5.6 Conclusion

In this work we have examined the cost of various short-cuts and approximations used in the literature when predicting the gravitational wave spectrum generated

by a cosmological first order phase transition. Even in the case where some modest diligence has been used in the calculation, we found the cost to often be comparable to problems in finite temperature QFT such as the scale dependence that arises from the break down of perturbation theory as well as the gauge dependence. Assuming detonations, the dominant cost in cases where there is a fair amount of super-cooling is from poor estimates of the percolation temperature in Eq. 5.11. The poor estimate of the percolation temperature has a knock on effect in enhancing the errors that arise from using the bag model and an estimate for the suppression factor. In the case where there is no tree-level barrier delaying the nucleation of the phase transition, the dominant error is due to the bag model approximation.

Although the errors are often as large as finite temperature QFT errors, they are arguably easier to reduce. At present, all of these errors can be handled except for the reheating and vorticity effects where we had to rely on interpolations. High diligence calculations for multiple models were considerably more tractable than the two loop calculations required to bring scale dependence at finite temperature under control [354]. We recommend future phenomenological calculations of gravitational wave signals from primordial phase transitions at the very least take the level of theoretical uncertainties into consideration.

Chapter 6

Bose-Einstein Conensate

Many studies have been dedicated to understanding the map between properties at the Lagrangian level and the behavior of the BEC system such as its mass and density profile [156, 6, 161, 162, 163, 164, 167, 140, 375, 165, 376, 157, 158, 377]. In [378], hydrodynamic approach is used and confirms the results from field space analysis. In [379], formation of boson stars inside DM halo is simulated. On the other hand, the effect of extra scalars in a BEC system with both gravitational and possibly non-gravitational interactions among the scalars remains largely under-explored. In particular, due to numerical challenges, most previous studies have focused on single scalar BEC systems, with a few exceptions: multiple scalar BEC systems with negligible non-gravitational interactions were explored in [380]; analytical approximations for multi-scalar BEC systems with self-interactions were explored in [381]; a Newtonian analysis on multi-scalar BEC in the limit of large quartic coupling [382]. Existence of solutions in the presence of a few types of interactions are studied in [383, 384, 385]. In contrast, we undertake a full General Relativity (GR) numerical study of the properties of BECs made of two interacting scalars, including both non-gravitational self-interactions and interactions between the scalars, followed by simple analytical understanding, and its phenomenological implications. Given that feeble repulsive self-interactions can lead to drastic changes in the mass profile at the macroscopic level [141, 167], it can be expected that interactions between different scalars will have an important

impact and leave unique imprints on the BEC system mass profile. The purpose of our paper is to carefully investigate such imprints, and ask whether they can be utilized to predict unique observational signatures or help address long-standing puzzles.

Our study proceeds along two directions. At the stellar scale, a light scalar of mass $m \sim 10^{-10}$ eV allows the formation of solar mass stellar structures. The formation and compactness can be greatly enhanced due to the presence of a repulsive self-interaction in the scalar potential, or compromised by an attractive self-interaction [153, 156, 167]. The strength and form of the non-gravitational interactions leave imprints on the GW signal. With the presence of extra scalars and interactions between multiple scalars, the features in GW are richer, with the maximal compactness of a stable BEC system being $\sim \mathcal{O}(0.2)$. In particular, we show the important role the interaction between the species ($\pm\phi_1^2\phi_2^2$) plays in either stabilizing or destabilizing the self-gravitating two scalar BEC system. It could also have implications for the recent GW190521 event. With this perspective in mind, we explore the mass versus compactness parameter space of a stellar BEC consisting of two ultralight scalars.

The second major focus of our paper is the behavior of the BEC at galactic scales. In the case of BEC DM composed of a single scalar field, the mass profile has a unique scaling behavior controlled by a single parameter: the central value of the wave function ($\propto$ (central density)$^{1/2}$ of the BEC.) As shown in [151, 6], this scaling behavior is in tension with observational data [7]. This can be understood from the scaling behavior of the scalar's equation of motion, either from the

Schrödinger-Newton equation, or from the relativistic EKG equation: in the single scalar case, the scaling is parametrized as $M[\phi(0)], R[\phi(0)]$, with $\phi(0)$ being the central value of the classical wave function. This means that dynamics does not play any role in determining the mass-radius relation, $M(R)$, which is fixed once a scalar potential is chosen. With the presence of a second scalar, the theory space is enlarged from one dimensional $\{\phi(0)\}$ to two dimensional $\{\phi_1(0), \phi_2(0)\}$. As we will show in subsequent sections, the ratio of the two BEC structures plays a role in the mass-radius relation of the total BEC structure, meanwhile the system is stable against radial perturbation even the fraction of each component varies. This holds out the possibility of accommodating observational data with BEC DM composed of multiple scalars while maintaining stability against radial perturbation; we show that this is indeed the case. We stress that, we are not claiming to provide a mass-radius relation of the BEC, as that requires accounting for the dynamics of the scalars that determines the mass ratio of the two components, which is beyond the scope of this work. Instead, we study the stability of the BEC against radial perturbations, when a ratio of the two components is given. Under this assumption, we show that there is parameter space to accommodate the galactic data [7] and address the problem raised by [6]. As the first part of a study series, we lay out the ground work and justifies the necessities of studying multi-scalar ultralight dark matter dynamics.

Our results rely on numerically integrating the complete relativistic Einstein-Klein-Gordon (EKG) equations. We do so by implementing an efficient algorithm not common in boson star studies to solve the set of equation of motion for

arbitrary parameters. Our algorithm employs the Relaxation Method described in [386] which can solve a system of differential equations subjected to their boundary conditions as opposed to the initial value shooting method typically used in these type of equations. This approach can be easily extended to N-scalar systems.[1] The results are verified by comparing against the usual shooting method in the single scalar case [167, 178]. Besides the exact numerical solutions, we also provide analysis adopting a simple ansatz and write out the non-relativistic Hamiltonian. The scaling behavior in the linear regime is affected mainly by the mass ratio (m_1/m_2) of the two scalars, while that in the nonlinear regime is affected more by the non-gravitational interactions between the two scalars. In particular, we demonstrate that with mild repulsive interactions between the two scalars $\lambda_{12}\phi_1^2\phi_2^2$, the system can be stabilized up to very large denstiy, a behavior that was only known to exist in the case of repulsive self-interaction $\lambda\phi^4$ [141, 165, 156, 167]. We show that such a repulsive interaction can be realized in a realistic particle model with collective symmetry breaking [387].

To summarize, we highlight the following points in this work:

- At the galactic scale, we show that the presence of a second scalar renders the theory capable of accommodating the mass profile indicated by observational data while maintaining its radial stability, which cannot be done in a system of a single scalar [6].

- At the stellar scale, we show that a repulsive interaction between two

[1] We note that the relaxation method avoids the problem of multi-dimension shooting, yet it still suffers from the stiffness issue if the separation of scales is large. That means, in the case of N-scalars, the separation between the lightest one and the heaviest one cannot be too large.

scalars, $\lambda\phi_1^2\phi_2^2$, can stabilize the system up to high density, which was only known to exist in a single scalar system with repulsive self-interactions [141, 165, 167, 178]. We provide a particle model realization as a proof of concept.

- We have developed complete and fast code that utilizes the Relaxation Method to solve the BEC system with two scalars, and is easy to generalize to multiple scalars. The code has been made public.[2]

This paper is organized as follows. We will begin by defining the phenomenological model of two scalars in Section 6.1. We set up the stage for numerical computations of the Einstein-Klein-Gordon system. We then take the non-relativistic limit to simplify the system and perform analytical investigations of the behavior, including both the transition from one scalar dominating to the other, and the effect of the non-gravitational interactions between the two scalars. We then verify the static solutions numerically, as well as perform time evolution of the system to ensure that the solution is indeed stable against radial perturbations. In Section 6.2 we apply our analysis toolkit to the galactic scale BEC system and show that this can address the scaling problem of ultralight dark matter while maintaining radial stability. In Section 6.3 we focus on the stellar scale and show the effect of non-gravitational interactions in the context of two scalar system. In Section 6.4 we discuss a possible particle model construction. We then conclude in Section 6.5. We provide details for computing the equation of motion

[2]The code can be downloaded at https://github.com/vagiedd/BosonStars .

in Appendix G, outline the numerical recipe we use for the code in Appendix H, and verify that it can reproduce the single scalar limit in Appendix I.

6.1 Bose-Einstein Condensate with Multiple Scalars

6.1.1 Phenomenological Model

The Lagrangian for a complex scalar system consisting of N particles reads

$$\mathcal{L} = \sum_{n}^{N} -\frac{1}{2} g^{\mu\nu} \partial_\mu \phi_i^* \partial_\nu \phi_i - V(|\phi_1|^2, |\phi_2|^2, ...) \tag{6.1}$$

where $g^{\mu\nu}$ is the space-time metric inverse with the signature $(-,+,+,+)$, and ϕ_n is the n-th scalar field. The potential V characterizes the interactions between the scalar fields and is a function of the coupling strengths and the modulus squared of ϕ. In this work we only consider the case of two complex scalars in the ground state, which can be easily generalized to compute BEC of more scalar fields in our numerical framework. The Lagrangian for 2 complex scalars with generic interactions reads

$$\begin{aligned} \mathcal{L} = &-\frac{1}{2} g^{\mu\nu} \partial_\mu \phi_1^* \partial_\nu \phi_1 - \frac{1}{2} m_1^2 |\phi_1|^2 - \frac{1}{4} c_1 |\phi_1|^4 \\ &- \frac{1}{2} g^{\mu\nu} \partial_\mu \phi_2^* \partial_\nu \phi_2 - \frac{1}{2} m_2^2 |\phi_2|^2 - \frac{1}{4} c_2 |\phi_2|^4 - \frac{1}{4} c_{12} |\phi_1|^2 |\phi_2|^2, \end{aligned} \tag{6.2}$$

where $c's$ are the coupling constants that can be either positive or negative. We note that stability of the potential is ensured by some higher order operators and this is taken as a truncation of the full potential. The scalar fields interact with

gravity through the the minimal gravitational coupling

$$S = \int \left(\frac{1}{16\pi G} R + \mathcal{L} \right) \sqrt{-g} d^4x, \tag{6.3}$$

where R is the Ricci scalar determined by the metric g and $\mathcal{L}$ is given in Eq. 6.2. Variation of the action with respect to the metric gives rise to Einstein equations

$$R_{\mu\nu} - \frac{1}{2} R = 8\pi G T_{\mu\nu}, \tag{6.4}$$

where $R_{\mu\nu}$ is the Ricci tensor, and $T_{\mu\nu}$ the energy-momentum tensor given by

$$\begin{aligned} T^\nu_\mu =& \sum_i \left(\frac{\delta \mathcal{L}}{\delta(\partial_\nu \phi_i)} \partial_\mu \phi_i + \frac{\delta \mathcal{L}}{\delta(\partial_\nu \phi_i^*)} \partial_\mu \phi_i^* \right) - \delta^\nu_\mu \mathcal{L} \\ =& -\frac{1}{2} g^{\nu\nu'} \partial_{\nu'} \phi_1^* \partial_\mu \phi - \frac{1}{2} g^{\nu\nu'} \partial_{\nu'} \phi_1 \partial_\mu \phi_1^* - \frac{1}{2} g^{\nu\nu'} \partial_{\nu'} \phi_2^* \partial_\mu \phi_2 \\ & - \frac{1}{2} g^{\nu\nu'} \partial_{\nu'} \phi_2 \partial_\mu \phi_2^* + \delta^\nu_\mu \left(\frac{1}{2} g^{\mu\nu} \partial_\mu \phi_1^* \partial_\nu \phi_1 + \frac{1}{2} m_1^2 |\phi_1|^2 + \frac{1}{4} c_1 |\phi_1|^4 \right. \\ & \left. + \frac{1}{2} g^{\mu\nu} \partial_\mu \phi_2^* \partial_\nu \phi_2 + \frac{1}{2} m_2^2 |\phi_2|^2 + \frac{1}{4} c_2 |\phi_2|^4 + \frac{1}{4} c_{12} |\phi_1|^2 |\phi_2|^2 \right). \end{aligned} \tag{6.5}$$

Note that since gauge fields are not the focus here, the simpler definition of T^ν_μ is equivalent to the one using variation with respect to the metric. If we vary the action with respect to the scalar field we get the Klein-Gordon equation

$$g^{\mu\nu} \nabla_\mu \nabla_\nu \phi_i = \frac{dV}{d\phi_i^*}, \tag{6.6}$$

where ∇ is the covariant derivative that contains the Christoffel symbols.

6.1.2 Metric parametrization

Assuming spherical symmetry of the metric, we parametrize the metric as

$$ds^2 = -B(r) dt^2 + A(r) dr^2 + r^2 d\theta^2 + r^2 \sin^2\theta d\phi^2. \tag{6.7}$$

Solving the ^t_t and ^r_r components of the Einstein equation, we have

$$\begin{aligned}
&\frac{4\pi G_N}{B(r)}\partial_t\phi_1\partial_t\phi_1^* + \frac{4\pi G_N}{A(r)}\partial_r\phi\partial_r\phi_1^* + \frac{4\pi G_N}{B(r)}\partial_t\phi_2\partial_t\phi_2^* + \frac{4\pi G_N}{A(r)}\partial_r\phi_2\partial_r\phi_2^* \\
&\quad + 4\pi G_N m_1^2|\phi_1|^2 + 4\pi G_N m_2^2|\phi_2|^2 + 2\pi G_N c_1|\phi_1|^4 + 2\pi G_N c_2|\phi_2|^4 + 2\pi G_N c_{12}\phi_1|^2|\phi_2|^2 \\
&\quad - \frac{A'(r)}{rA(r)^2} + \frac{1}{r^2A(r)} - \frac{1}{r^2} = 0, \\
&\frac{4\pi G_N}{B(r)}\partial_t\phi_1\partial_t\phi_1^* + \frac{4\pi G_N}{A(r)}\partial_r\phi_1\partial_r\phi_1^* + \frac{4\pi G_N}{B(r)}\partial_t\phi_2\partial_t\phi_2^* + \frac{4\pi G_N}{A(r)}\partial_r\phi_2\partial_r\phi_2^* \\
&\quad - 4\pi G_N m_1^2|\phi_1|^2 - 4\pi G_N m_2^2|\phi_2|^2 - 2\pi G_N c_1|\phi_1|^4 - 2\pi G_N c_2|\phi_2|^4 - 2\pi G_N c_{12}|\phi_1|^2|\phi_2|^2 \\
&\quad - \frac{B'(r)}{rA(r)B(r)} - \frac{1}{r^2A(r)} + \frac{1}{r^2} = 0.
\end{aligned} \tag{6.8}$$

Two extra constraints come from the Klein-Gordon equations of motion. Plugging in the covariant derivative, we get

$$\begin{aligned}
&\frac{1}{A}\partial_r^2\phi_1 - \frac{1}{B}\partial_t^2\phi_1 + \partial_r\phi_1\left(\frac{B'(r)}{2A(r)B(r)} - \frac{A'(r)}{2A(r)^2} + \frac{2}{A(r)r}\right) \\
&\quad - m_1^2\phi_1 - c_1|\phi_1|^2\phi_1 - \frac{1}{2}c_{12}|\phi_2|^2\phi_1 = 0, \\
&\frac{1}{A}\partial_r^2\phi_2 - \frac{1}{B}\partial_t^2\phi_2 + \partial_r\phi_2\left(\frac{B'(r)}{2A(r)B(r)} - \frac{A'(r)}{2A(r)^2} + \frac{2}{A(r)r}\right) \\
&\quad - m_2^2\phi_2 - c_2|\phi_2|^2\phi_2 - \frac{1}{2}c_{12}|\phi_1|^2\phi_2 = 0.
\end{aligned} \tag{6.9}$$

6.1.3 Rescaling to Dimensionless Variables

We take the harmonic ansatz with energy eigenstates $\phi_i(t,r) = \Phi_i(r)\mathrm{e}^{-i\mu_i t}$. Plugging it into the equation of motion we can separate the time evolution part of ϕ_i.

In order to solve it numerically, we perform the following rescaling of variables:

$$\begin{aligned}
\Phi_1 &= \widetilde{\Phi}_1\ (4\pi G_N)^{-1/2}, & \Phi_2 &= \widetilde{\Phi}_2\ (4\pi G_N)^{-1/2}, \\
\mu_1 &= \widetilde{\mu}_1\ m_1, & \mu_2 &= \widetilde{\mu}_2\ m_1, \\
c_1 &= \widetilde{\lambda}_1\ 4\pi G_N m_1^2, & c_2 &= \widetilde{\lambda}_2\ 4\pi G_N m_1^2, \\
c_{12} &= \widetilde{\lambda}_{12}\ 4\pi G_N m_1^2, & m_2 &= \widetilde{m}_r m_1, \\
r &= \widetilde{r}/m_1, & &
\end{aligned} \tag{6.10}$$

where the variable with a tilde is dimensionless.[3] If one parametrizes c_i in the notation usually adapted in the axion literature using the Peccei-Quinn symmetry breaking scale, $c_i = m_i^2/f_i^2$, it reads

$$\begin{aligned}
\widetilde{\lambda}_1 &= \frac{1}{4\pi}\left(\frac{M_{Pl}}{f_1}\right)^2, \\
\widetilde{\lambda}_2 &= \frac{1}{4\pi}\left(\frac{M_{Pl}}{f_2}\right)^2 \widetilde{m}_r^2.
\end{aligned} \tag{6.11}$$

The strength of the interaction terms can be parameterized by the size of f_i. In other words, $\widetilde{\lambda} \sim 1$ parametrizes a self-interaction whose strength is comparable to gravity with $f \sim M_{Pl}$. The dimensionless variables will be used for numerically solving the system. In what follows, we assume m_1, m_2 close to each other, so are f_1 and f_2. Therefore, we parametrize the coupling strength c's in the unit of m_1^2/f^2 with f chosen at 10^{17} GeV. In other words, we have

$$\begin{aligned}
c_1 &= \lambda_1 \frac{m_1^2}{f^2}, \\
c_2 &= \lambda_2 \frac{m_1^2}{f^2}, \\
c_{12} &= \lambda_{12} \frac{m_1^2}{f^2}.
\end{aligned} \tag{6.12}$$

[3]For comparison, in Ref. [141], $\widetilde{r}, \widetilde{\Phi}, \widetilde{\mu}, \widetilde{\lambda}$ are denoted as $x, \sigma, \Omega, \Lambda$ respectively.

We will parametrize the three physical couplings with order one numbers in a tuple, $(\lambda_1, \lambda_2, \lambda_{12})$ in the rest of the paper. In terms of the dimensionless variables, we can write the equations of motion as

$$\begin{aligned}
&\left(\frac{\widetilde{\mu}_1^2}{B}+1\right)\widetilde{\Phi}_1^2+\frac{1}{A}\widetilde{\Phi}_1'^2+\frac{1}{2}\widetilde{\lambda}_1\widetilde{\Phi}_1^4+\left(\frac{\widetilde{\mu}_2^2}{B}+\widetilde{m}_r^2\right)\widetilde{\Phi}_2^2+\frac{1}{A}\widetilde{\Phi}_2'^2+\frac{1}{2}\widetilde{\lambda}_2\widetilde{\Phi}_2^4+\frac{1}{2}\widetilde{\lambda}_{12}\widetilde{\Phi}_1^2\Phi_2^2\\
&\quad-\frac{A'}{\widetilde{r}A^2}+\frac{1}{\widetilde{r}^2A}-\frac{1}{\widetilde{r}^2}=0,\\
&\left(\frac{\widetilde{\mu}_1^2}{B}-1\right)\widetilde{\Phi}_1^2+\frac{1}{A}\widetilde{\Phi}_1'^2-\frac{1}{2}\widetilde{\lambda}_1\widetilde{\Phi}_1^4+\left(\frac{\widetilde{\mu}_2^2}{B}-\widetilde{m}_r^2\right)\widetilde{\Phi}_2^2+\frac{1}{A}\widetilde{\Phi}_2'^2-\frac{1}{2}\widetilde{\lambda}_2\widetilde{\Phi}_2^4-\frac{1}{2}\widetilde{\lambda}_{12}\widetilde{\Phi}_1^2\Phi_2^2\\
&\quad-\frac{B'}{\widetilde{r}AB}-\frac{1}{\widetilde{r}^2A}+\frac{1}{\widetilde{r}^2}=0,\\
&\frac{1}{A}\widetilde{\Phi}_1''+\left(\frac{\widetilde{\mu}_1^2}{B}-1\right)\widetilde{\Phi}_1+\widetilde{\Phi}_1'\left(\frac{B'}{2AB}-\frac{A'}{2A^2}+\frac{2}{A\widetilde{r}}\right)-\widetilde{\lambda}_1\widetilde{\Phi}_1^3-\frac{1}{2}\widetilde{\lambda}_{12}\widetilde{\Phi}_2^2\Phi_1=0,\\
&\frac{1}{A}\widetilde{\Phi}_2''+\left(\frac{\widetilde{\mu}_2^2}{B}-\widetilde{m}_r^2\right)\widetilde{\Phi}_2+\widetilde{\Phi}_2'\left(\frac{B'}{2AB}-\frac{A'}{2A^2}+\frac{2}{A\widetilde{r}}\right)-\widetilde{\lambda}_2\widetilde{\Phi}_2^3-\frac{1}{2}\widetilde{\lambda}_{12}\widetilde{\Phi}_1^2\Phi_2=0.
\end{aligned} \tag{6.13}$$

This concludes our setup of the problem, and we can solve Eq. (6.13) numerically. For details of the numerical algorithm, one can refer to Appendix H. Before we proceed to discuss the results and physical implications, we take a small detour to discuss the stability of solutions to Eq. (6.13).

6.1.4 Time Evolution

To verify that the solution is indeed stable against radial perturbations, we perform the time evolution using a finite difference method. This way, we can verify the temporal harmonic ansatz $\Phi_i(r,t)=\Phi_i(r)e^{-i\mu_i t}$. The detailed procedure can be found in Appendix H.3. We outline this procedure here briefly.

First, one solves the static equations (6.13). This will serve as the initial condition for the numerical time evolution. To check if it is a stable system,

we perform a radial perturbation by $\Phi \to \Phi(1+\epsilon)$, and use $\Phi(1+\epsilon)$ as the initial condition instead. Here ϵ represents how far we perturb away from the static solution. In the stable case, the system can evolve for a long time with small oscillations, while in the unstable case the wave function quickly collapses or blows up depending on the sign of ϵ. We show a sample stable solution in Fig. 6.1 for $\lambda_1 = \lambda_2 = \lambda_{12} = -1$ and initial central densities of $\widetilde{\Phi}_1(0) = 10^{-4}$ and $\widetilde{\Phi}_2(0) = 5 \times 10^{-5}$, together with an unstable solution of $\widetilde{\Phi}_1(0) = 10^{-4}$ and $\widetilde{\Phi}_2(0) = 10^{-2}$. On top of the quasi-normal mode, there is no sign of decay after $\sim 100 m^{-1}$ in the stable scenario while the field with the unstable configuration decays considerably.

6.1.5 Mass Profile of the BEC Structure

With the solution to Eq. (6.13) in hand, one can derive the physical properties of the BEC system. The total mass of the BEC system is found by integrating the T_0^0 component of the energy momentum tensor

$$\begin{aligned} M_{BS} &\equiv 4\pi \int_0^\infty dr r^2 T_0^0 \\ &= 4\pi \int_0^\infty dr r^2 \Bigg(\frac{\mu_1^2}{2B}\Phi_1^2 + \frac{1}{2}m_1^2\Phi_1^2 + \frac{1}{2A}\partial_r\Phi_1^2 + \frac{1}{4}\lambda_1\Phi_1^4 + \\ &\qquad \frac{\mu_2^2}{2B}\Phi_2^2 + \frac{1}{2}m_2^2\Phi_2^2 + \frac{1}{2A}\partial_r\Phi_2^2 + \frac{1}{4}\lambda_2\Phi_2^4 + \frac{1}{4}\lambda_{12}\Phi_1^2\Phi_2^2 \Bigg) \end{aligned} \tag{6.14}$$

In the linear regime, *i.e.* non-relativistic limit, this reduces to the sum of the rest mass from the two scalars: $M_{BS} \approx M_1 + M_2 = m_1 N_1 + m_2 N_2 + \mathcal{O}(B-1) + \mathcal{O}(1-A)$, with the subscript BS standing for BEC system. The compactness of the BEC

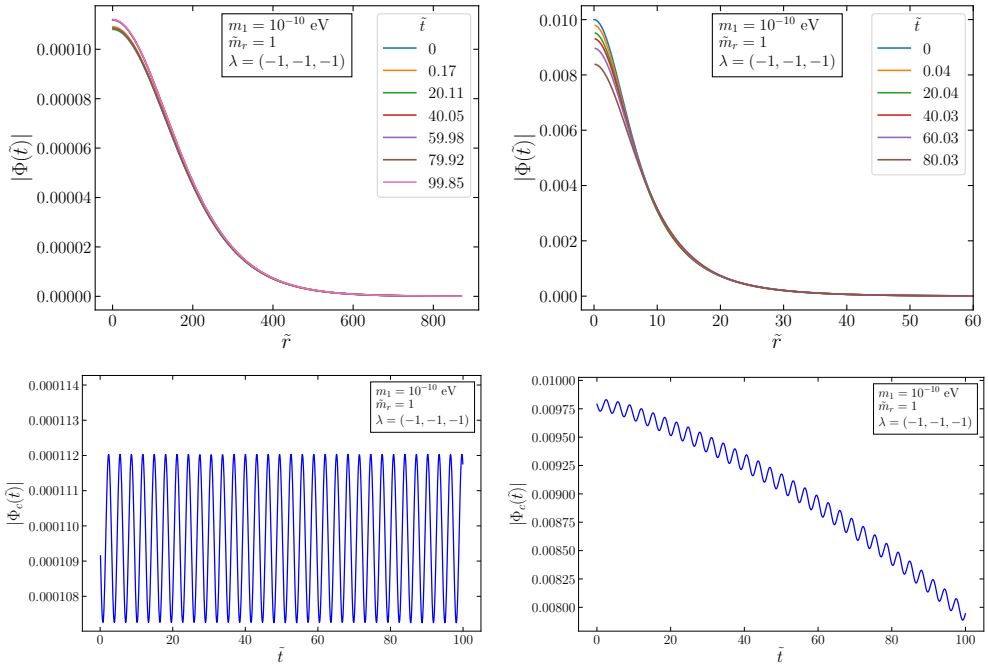

Figure 6.1: From top left clockwise: 1) time snapshots of the wave function of a stable configuration being radially perturbed $\psi \to \psi(1+\epsilon)$, with the vertical axis showing the sum of the modulus squared of the wave functions for Φ_1 and Φ_2 for $\lambda_1 = \lambda_2 = \lambda_{12} = -1$. 2) Same plot for an unstable configuration by increasing the central density controlled by $\Phi_1(0)$ and $\Phi_2(0)$. The wave function diverges quickly after a short time. 3) Unstable configuration in time domain shows the BEC collapsing within a short time period. 4) Stable configuration in time domain shows the system having small oscillation but maintaining a stable configuration. All the radial perturbations are done with $\epsilon \sim 2\%$. The stable configuration is chosen as $\widetilde{\Phi}_1(0) = 10^{-4}$ and $\widetilde{\Phi}_2(0) = 5 \times 10^{-5}$; the unstable configuration $\widetilde{\Phi}_1(0) = 10^{-4}$ and $\widetilde{\Phi}_2(0) = 10^{-2}$.

system is defined as the mass-radius ratio in natural units

$$C_{BS} = \frac{G_N M_{BS}}{R_{90}} \tag{6.15}$$

where R_{90} is the radius that contains 90% of the total mass. Similar to the mass components, in the limit of small interaction between Φ_1 and Φ_2, we can also define C_1 and C_2 as the compactness of the BEC component corresponding to Φ_1 and Φ_2, respectively. For a given set of model parameters, (λ, m), in the single scalar scenario, the mass and compactness are solely determined by a single variable, $\Phi(r = 0)$, which is related to the central density of the BEC system. As a result, the compactness is a function of mass. In the case of two scalar BEC, this is no longer true. One can find solutions with different combinations of $\Phi_1(0), \Phi_2(0)$, which essentially enlarges the parameter space to being 2-dimensional. The mass profile in the $C_{BS} - M_{BS}$ plane is no longer a curve, but a 2D region. A detailed analysis for various BEC mass profiles will be given in the results section of Section 6.2 and 6.3 respectively.

6.1.6 Non-Relativistic Limit

Although we solve the system in the full relativistic regime, expanding in the weak gravity limit can bring insights to various properties of the system. The waveforms of Φ_1 and Φ_2 should decay to zero as $r \to \infty$. We also expect that the

metric becomes non-relativistic for large r such that

$$\begin{aligned} A(r) &= 1 - 2V(r) \\ B(r) &= 1 + 2V(r) \\ V(r) &= -\frac{GM(r)}{r} = -\frac{G(M_1(r) + M_2(r))}{r}. \end{aligned} \tag{6.16}$$

We adopt the following ansatz for the wave function, which is verified by the numerical computation to hold well enough at sufficiently large radius.

$$\Phi_i = \sqrt{\frac{N_i}{\pi m_i R_i^3}} e^{-r/R_i} \tag{6.17}$$

where N_i is the total number of particles for either Φ_1 or Φ_2 and R_i is characteristic size of each BEC clump. Using this non-relativistic ansatz, we may integrate each term individually in Eq. 6.14 and combine terms to give the non-relativistic Hamiltonian. In the weak gravity limit, one can parametrize the eigenvalues as

$$\mu_i = m_i \left(1 - \alpha V(r)\right). \tag{6.18}$$

Matching to the non-relativistic results in the leading terms, we found $\alpha = 5/4$ reproduces the self-gravity term as in the single scalar case [167]. We can then write out the Hamiltonian as

$$\begin{aligned} H_{kin} &= + \frac{N_1}{2m_1 R_1^2} + \frac{N_2}{2m_2 R_2^2} \\ H_{int} &= + \frac{\lambda_1 N_1^2}{32\pi f^2 R_1^3} + \frac{\lambda_2 N_2^2}{32\pi f^2 R_2^3} + \frac{\lambda_{12} N_1 N_2}{4\pi f^2 \left(R_1 + R_2\right)^3} \\ H_{grav} &= - \frac{5G m_1^2 N_1^2}{16 R_1} - \frac{5G m_2^2 N_2^2}{16 R_2} - \frac{G m_1 m_2 N_1 N_2}{R_{\text{eff}}} \\ H_{metric} &= - \frac{5G N_1^2}{16 R_1^3} - \frac{5G N_2^2}{16 R_2^3} - \frac{G N_1 N_2}{\widetilde{R}_{\text{eff}}^3} \end{aligned} \tag{6.19}$$

with

$$\frac{1}{R_{\rm eff}} = \frac{5}{8R_1} + \frac{5}{8R_2} - \frac{1}{R_1+R_2} - \frac{R_1R_2}{(R_1+R_2)^3},$$
$$\frac{1}{\widetilde{R}^3_{\rm eff}} = \frac{m_1(4R_1+R_2)}{m_2(R_1+R_2)^4} + \frac{m_2(R_1+4R_2)}{m_1(R_1+R_2)^4}.$$

We can immediately recognize the familiar form of kinetic terms, self-interaction terms, self-gravity terms, and the first two terms in H_{metric}, which are due to the kinetic term in the curved space-time consistent with the result in [167, 178]. However, the Hamiltonian also contains a term proportional to $\lambda_{12}N_1N_2$ that is due to the non-gravitational interaction between the two scalars. In addition, there are terms proportional to $G_NM_1M_2$ due to the gravitational interaction between the two scalars which are not present in the single scalar case. One recovers the one scalar result if either N_1 or N_2 is set to zero. In the limit of $\lambda_{12} \to 0$ and $R_1, R_2 \sim R$, $1/R_{\rm eff}$ reduces to $(5/8R)$, which is consistent with the result of [381] up to the H_{grav} term.

A discussion based on the Hamiltonian is in order. In the linear regime, one can safely neglect the terms in H_{int} and H_{metric}. Without loss of generality, when $N_1 \gg N_2$, the gradient term will balance the gravity term Eq. 6.19 to give

$$N \approx N_1 \propto \frac{M_{Pl}^2}{m_1^3 R_1}. \tag{6.20}$$

Whether Φ_1 or Φ_2 dominates is solely determined by the central value, $\Phi_1(0)$ and $\Phi_2(0)$. Therefore, we have

$$M_{BS} \sim \begin{cases} \frac{M_{Pl}^2}{m_1}\sqrt{C}, & N_1 \gg N_2 \\ \frac{M_{Pl}^2}{m_2}\sqrt{C}, & N_2 \gg N_1 \end{cases} \tag{6.21}$$

It is expected that when one goes from the Φ_1-dominating regime to Φ_2-dominating regime, the $M-C$ relation will smoothly transition from one to the other. This is verified by the numerical computation and shown in Fig. 6.2. This has interesting implications for the solitonic core, in the context of galactic scale BEC. We will discuss this feature in more detail in Section 6.2. Note that we only show the result with $m_2/m_1 = 1/2$ due to the numerical complexity, but in principle the result should hold for much larger scalar ratios. This means that by adjusting the central densities of the two BEC components, $\Phi_1(0)$ and $\Phi_2(0)$, one can have non-trivial mass profiles that cannot be mimicked by a single scalar BEC system.

In the nonlinear regime, the non-gravitational interactions are important. In contrast to the single scalar case, we have three non-gravitational interaction terms proportional to λ_1, λ_2, and λ_{12} respectively. It is known that a repulsive self-interaction $+\Phi^4$ stabilizes the system [141, 165, 156, 167, 178], while the attractive $-\Phi^4$ renders the system unstable once it goes to the nonlinear regime [164, 156, 167]. In the two scalar system, we observe that a repulsive non-gravitational interaction $+\Phi_1^2\Phi_2^2$ also stabilizes the system. This can be understood by looking into the Hamiltonian of the system. In the nonlinear regime, the important terms are the gravity potential and the nonlinear terms. We assume Φ_2 dominates the system, $N_2 > N_1$:

$$\widetilde{H}(R_2) \approx \frac{\widetilde{\lambda}_2\widetilde{N}_2^2}{8\widetilde{R}_2^3} + \frac{\widetilde{\lambda}_{12}\widetilde{N}_2\widetilde{N}_1}{8\widetilde{R}_2^3} - \frac{5\widetilde{N}_2^2}{16\widetilde{R}_2}, \tag{6.22}$$

where $H = \widetilde{H}m\Delta^2$, $N = \widetilde{N}(m/M_{Pl})^2\Delta$, with Δ being some large number for normalization. If we start with $\widetilde{\lambda}_1 < 0, \widetilde{\lambda}_2 < 0, \widetilde{\lambda}_{12} > 0$ ($\widetilde{\lambda}_1 > 0, \widetilde{\lambda}_2 > 0, \widetilde{\lambda}_{12} < 0$),

we observe that the BEC system can be stabilized (destabilized), respectively, when the following condition is met:

$$\frac{\widetilde{N}_1}{\widetilde{N}_2} > \left|\frac{\widetilde{\lambda}_2}{\widetilde{\lambda}_{12}}\right|. \tag{6.23}$$

We demonstrate this both analytically and numerically in Fig. 6.3. This has some interesting implications for boson stars. Contrary to the common understanding that BECs resulting from $-\phi^4$ or $\Lambda^4(1-\cos(\phi))$ potentials (*e.g.* axion stars) are dilute, they can be stabilized up to high density if there are multiple of them and different species interact with each other through a repulsive interaction.

In other combinations of λ's, the presence of the coupling between the two scalars can also offer unique features in the $C_{BS} - M_{BS}$ curves in the non-linear regime that are not possible in the single scalar limit. This has interesting implications for the stellar scale BEC structure. We will discuss this application in more detail in Section 6.3 and show the results for how the nonlinear regime is changed by varying the model parameters, λ_1, λ_2, λ_{12}, and m_1,m_2.

6.2 Galactic Scale BEC Structure

Having discussed the behavior of the two scalar BEC system, we now turn to applications: the first being the implications at galactic scales. We first briefly review the problem of using single scalar BEC to fit galaxy data. For details one can refer to e.g. [6]. We then show that with the second scalar and the transitioning behavior demonstrated in Section 6.1.6, both the best fit and the data points themselves can be accommodated in the two scalar scenario.

6.2.1 The Problem with a Single Scalar BEC

While the NFW profile describes dark matter halo density to good precision at radii larger than $\sim$ kpc, it is known that at sub-kpc distances the densities of typical galaxies approach constant values. Measurements of galaxy rotation curves yield the profile of the core density and core size across galaxies of different sizes [388, 389, 7, 6]. One can parametrize the density by

$$\rho(r) = \frac{\rho_c}{1 + r^2/R_c^2}, \tag{6.24}$$

where R_c is the radius where the density drops to half of the central density. By comparing with the measurement in [7], one can see the core size and core density can be fitted by $\rho_c \propto 1/R_c^\beta$, with $\beta \approx 1.3$ [6]. On the other hand, in a single scalar system, the scaling behavior is completely fixed by the scalar potential and dynamics can not change the mass-radius relation. For example, in the linear regime, it is H_{kin} balancing with H_{grav}, which gives the scaling shown in Eq. (6.20). This translates to $\rho \sim 1/R^4$. Similarly, one can try different polynomial potentials, and they result in different β's, but none of them falls into $1 \lesssim \beta \lesssim 1.3$ even if one takes into account the scattering of the data. The values of the scaling index β are summarized in Table 6.1. This poses a challenge to using ultralight dark matter to address the core-cusp problem [6], which was one of the main motivations of ultralight dark matter [390, 142]. As we have briefly discussed, this problem can be understood as follows. When the system is composed of one

	H_{kin}	ϕ^4	ϕ^6
H_{grav}	$\beta = 4$	$\beta = \infty$	$\beta = -2$
$-\phi^4$	$(\beta = 2)$	n/a	$\beta = 0$

Table 6.1: The scaling index β for one scalar BEC with different scalar potentials. In any given regime, the system is balanced by two dominating terms, one in the top row and one from the left column. Note that $-\phi^4$ balancing H_{kin} is not stable.

scalar, the Hamiltonian can be written as

$$H \approx \frac{N_1}{2m_1 R_1^2} + \frac{\lambda_1 N_1^2}{32\pi f^2 R_1^3} - \frac{5Gm_1^2 N_1^2}{16R_1} - \frac{5GN_1^2}{16R_1^3}, \tag{6.25}$$

which leads to a fixed $M(R)$ relation. There is no room for the scalar dynamics to alter this relation, as both mass and radius are parametrized by the $\phi(0)$.

6.2.2 Two-Scalar BEC to the Rescue

In this section, we first allow $\Phi_1(0)$ and $\Phi_2(0)$ to vary freely, and show that, while maintaining radial stability, there is parameter space that can accommodate the galactic data. We then comment on the implication for the dynamics of the two scalars.

We note that in the case of a two scalar system with $m_1 \neq m_2$, the curve in the $C - M$ plane is a smooth interpolation of the mass profile of each scalar as shown in Fig. 6.2. Scanning over the $\Phi_1(0) - \Phi_2(0)$ space gives us a region in the $C - M$ plane, with one-to-one correspondence of each $(\Phi_1(0), \Phi_2(0))$ point to a

(C, M) point. On the other hand, galactic data points can be fit with a curve of $M \sim C^{2.4}$, *i.e.* $\rho \sim 1/R^{1.3}$. Therefore, by looking at the $(\Phi_1(0), \Phi_2(0))$ to (C, M) correspondence, one can find the one-dimensional curve that reproduces the best fit of the data. We show this explicitly in Fig. 6.4. We observe that a curve in $\Phi_1(0), \Phi_2(0)$ space can accommodate the best fit. In particular, we observe the mass profile of the total BEC is mostly dominated by one component if the component weighs more than 75% percent of the total mass. This indeed is a useful criteria in determining the dominant BEC component, as starting from this point the compactness is mainly determined by the dominant species. We show this in the right plot of Fig. 6.4.

As we discussed in Section 6.2.1, with two scalars one can accommodate the galactic data points even after taking into account the scattering of the data set, instead of just the $\rho \sim 1/R^{1.3}$ curve that best fits the data points. This can be done with the following procedure: we overlay the galactic data points with the numerical scan in the $C - M$ space (or equivalently in the $\rho - R$ space.) Then for each data point we can find a numerical point that is identical up to the scan resolution. We can then go back to the $\Phi_1(0), \Phi_2(0)$ space and identify the value for the $\Phi_1(0), \Phi_2(0)$ pair needed to reproduce this data point. The result is shown in Fig. 6.5.

We emphasize that, however, this does not mean the two scalar BEC can accommodate any galactic data, or lacks predictability. While our approach only considers radial stability and existence of solutions of the BEC system, this exercise translates the galactic data to a requirement of the field value in the

classical field configuration space. This requirement, shown in the right panels of Figs. (6.4-6.5), can be further constrained after the two scalar dynamics is taken into account. In addition, because of the extra scalar, there could be new constraints specific to the two scalar system, such as that related to the relaxation time scale. Since in this work we focus on the radial stability of the BEC system, we leave the study dedicated for constraining the two scalar BEC with galactic data for the future.

Lastly, we can extrapolate the numerical scan to the scenario where two scalars have a larger mass ratio. Given that we know the BEC system behaves like a single scalar when $\Phi_1(0) \gg \Phi_2(0)$ or vice versa, we can estimate how big a mass ratio is needed to accommodate all the data points. The extrapolation result is shown in Fig. 6.6 with $m_1 = 2 \times 10^{-24}$ eV and $m_2 = 2 \times 10^{-21}$ eV. This can be further used to constrain the two scalar model. At its face value, it seems that Lyman-alpha [391, 392] and subhalo mass function[150] might heavily constrain the lighter of the two scalar. However, it is known that the nonlinear interaction terms could play an important role in the evolution of cosmic perturbation and structure formation [132, 393, 140]. The extrapolation shown in Fig. 6.6 is in $m_1/m_2 \sim \mathcal{O}(10^{-3})$. If one fixes the radius, the BEC ratio M_1/M_2 needs to change three orders of magnitudes to go from ϕ_1 dominating the system to ϕ_2 dominating the system. More specifically, one needs that at $R_c \sim 10\,\mathrm{kpc}$, scalar one dominates, and at $R_c \sim 0.5\,\mathrm{kpc}$ scalar two dominates.

To summarize, we stress three points that distinguish two scalar BEC from the single scalar BEC at the galactic scale: 1) With a single scalar, the mass and

radius of the BEC is fixed by the scalar potential instead of scalar dynamics. As a result, it is highly nontrivial to find a potential that reproduces $\beta \approx 1.3$. This is verified by checking different combinations of potentials. This is no longer the case with two scalar BEC as we have a two-dimensional parameter space. In this case, both the scalar potential and the ratio of the two components (hence scalar dynamics) affect the BEC's mass-radius relation. 2) In the single scalar BEC, it is even harder to accommodate the scattering of the points, even if one manages to find a potential that reproduces $\rho \sim 1/R^{1.3}$, other than attributing it to observational errors. In the two scalar scenario, it is natural to have a scattering due to dynamics that leads to a fluctuation of $\Phi_1(0)/\Phi_2(0)$ from the best fit curve.

6.3 Stellar Scale BEC Structure

Having discussed galactic scale BEC, we now turn to the properties of two-scalar stellar scale BECs.

Whether it is possible to stabilize a BEC system determines how dense the system can become before it is destroyed by self-gravity. In the single scalar scenario, there is only one way to support gravity to form $C \sim \mathcal{O}(0.1)$ dense objects: by using repulsive $+\phi^{2n}$ potentials, whose model realizations have been shown to be non-trivial but possible [140]. Because of the presence of a second scalar, and non-gravitational interactions for both scalars and between them, we show that there are two new ways to support such systems to become dense

enough. This could be relevant for gravitational wave signals from their binary mergers at LIGO-Virgo and LISA.

6.3.1 Non-gravitational Interaction between Two Scalars

In Section 6.1.6, we have already seen that the BEC structure can be drastically affected by the interaction $+\phi_1^2\phi_2^2$ term. This has significance for exotic compact searches at stellar scale, such as binary mergers at LIGO and LISA. In this section, we show more details on the effect of non-gravitational interactions in the nonlinear regime, with different combinations of $\lambda_1, \lambda_2, \lambda_{12}$. Among them, the most interesting case is $\lambda_1 < 0, \lambda_2 < 0, \lambda_{12} > 0$. Without the non-gravitational interaction proportional to λ_{12}, neither ϕ_1 or ϕ_2 can form a BEC system that is compact enough to be detectable say at LIGO through gravitational wave radiated by the binary mergers. However, $+\phi_1^2\phi_2^2$ provides pressure to support the gravitational collapse such that the system can be much denser as demonstrated in Fig. 6.7. This is consistent with the analysis in Eq. (6.22).

In the case of $-\phi_1^2\phi_2^2$, we note that just as the non-gravitational self-interaction counterpart$-\phi^4$, it renders the system unstable once this term becomes important. This can also be understood using Eq. (6.22). The effect is observed in the numerical solutions shown in Fig. 6.8.

We now comment on the difference between $\phi_1^2\phi_2^2$ and ϕ^4 types of interactions, and their impact on the resulted boson stars. One might think that if $\phi_1 \propto \phi_2$ everywhere, this two types of interactions are quite similar. However, this is rarely the case. At stellar scale, the formation history of BEC is highly nontrivial.

In lack of a simulation, there is no reason to believe ϕ_1, ϕ_2 populate in every place proportionally. In the case of $V \sim -\phi_1^4 - \phi_2^4 + \phi_1^2\phi_2^2$, for example, there could exist boson stars consisting mainly ϕ_1 and those consisting mostly ϕ_2 due to their separate fragmentation history [379]. Neither of the two types would be detectable because of the $-\phi^4$ potential. However, when the two stars merge, the interaction between the species now can support the self-gravity and allow the star to acquire more material to become denser, up to a point that it is detectable at LIGO/Virgo. In the case of $V \sim +\phi_1^4 + \phi_2^4 - \phi_1^2\phi_2^2$, on the other hand, the stars consisting mostly ϕ_1 or ϕ_2 could be very dense. However, unlike the single scalar BEC, the maximal compactness of either type is not capped by the metric fluctuation, but the term $-\phi_1^2\phi_2^2$. When two boson stars of kinds merge, it is more likely to result in an unstable BEC due to the $-\phi_1^2\phi_2^2$ term. In this case, one would not expect there remains a final boson star, but instead a phenomena dubbed Bosenova [132] could happen. Even before the two finishes merging, the resulted BEC system goes beyond the critical maximal mass, due to $-\phi_1^2\phi_2^2$. This could lead to gravitational wave different from those from single scalar ϕ^4 BEC mergers [167, 173]. As described in [379], attractive self-interaction leads to fragmentation, it is only natural to expect an attractive interaction between the two scalars could also lead to fragmentation, but only when BEC's of different types encounter. This could lead to novel nonlinear behaviors in boson star formations. In both scenarios above, we see the difference between $\phi_1^2\phi_2^2$ and ϕ^4 boson stars related to their formation history.

On the aspect of observation, $\phi_1^2\phi_2^2$ boson stars are also quite distinct from ϕ^4

boson stars. From Eq. (6.22), one can see that when ϕ_2^4 term balances self-gravity, it leads to the usual mass curve, $M \propto C$. However, when $\phi_2^2\phi_1^2$ balances self-gravity with ϕ_1 being a sub-component, the mass curve is

$$M \propto M_1^{1/3} C^{2/3}. \tag{6.26}$$

When the sub-component M_1 is fixed, the mass curve is different from a $+\phi^4$ BEC system. On the other hand, due to the non-linear effect of gravity at small scales, one naturally expect the ϕ_1 component, M_1 to vary from star to star. As a result, we expect some scattering around this mass curve, which is another feature that ϕ^4 mass curve does not have.

On the aspect of model building, as we will show in the following sections, ultralight scalars with interaction between multiple species can be achieved naturally. It is shown in [140] that it is nontrivial to build a $+\phi^4$ theory. Given that axions/ALPs all have a $-\phi^4$ interaction, we show that they can indeed lead to compact BEC structures if there are extra interactions - such as $+\phi_1^2\phi_2^2$ - that arises naturally from collective symmetry breaking and stabilizes the system, it could lead to dense axion stars. This hints for a different class of models compared to those that lead to a $+\phi^4$ theory.

6.3.2 Implication for Gravitational Wave Detection

In the past, LIGO-Virgo have observed numerous binary black hole mergers and a few neutron star mergers. Besides the tests of GR, there have been studies on probing new physics by detecting binary mergers consisting of exotic compact

objects [153, 167, 375, 178, 195] to name a few. While axions are well studied and motivated in particle physics, the compactness of axion stars is far below LIGO sensitivity, which renders a direct detection of axion star binary mergers impossible[4]. This changes when one takes into account extra scalars with non-gravitational interactions between them. As we have shown in Section 6.3.1, a repulsive $+\phi_1^2\phi_2^2$ can support the system made of two axions up to $\mathcal{O}(0.2)$ compactness, a behavior that was only known to exist in repulsive self-interaction system [167].

For a generic binary system, the gravitational wave during its inspiral phase is

$$f_{GW} = \sqrt{\frac{M_1 + M_2}{\pi^2 \ell^3}}, \tag{6.27}$$

where M_1, M_2 are the masses of each inspiral object, ℓ the major semi-axis. Assuming equal mass system, the innermost stable circular orbit (ISCO) happens at $\ell = 6R$, with R being the radius of the star. The gravitational wave frequency at ISCO can be expressed as

$$f_{ISCO} = \sqrt{\frac{2M}{\pi^2(6R)^3}} = \frac{C^{3/2} M_{Pl}^2}{2\pi \cdot 3^{3/2} M} \approx 50 \text{ Hz} \left(\frac{M_\odot}{M}\right) \left(\frac{C}{0.04}\right)^{3/2}. \tag{6.28}$$

From the ISCO frequency one can extract the size of each object. The signal strength in frequency space is given as [395]

$$\begin{aligned} \widetilde{h}(f) &= \left(\frac{\sqrt{5/24} G_N^{5/6}}{\pi^{2/3} c^{3/2}}\right) \frac{M_c^{5/6}}{f_{GW}^{7/6} D_L} \\ &\overset{ISCO}{\approx} 7.2 \times 10^{-24} \text{Hz}^{-1} \left(\frac{M}{M_\odot}\right)^2 \left(\frac{C}{0.04}\right)^{-7/4} \left(\frac{D_L}{100 \text{ Mpc}}\right)^{-1}, \end{aligned} \tag{6.29}$$

[4]It is noted that [394] argues that there exist a dense branch for axion stars, yet [159] shows the lifetime of the dense branch is too short.

where the second line is estimated at $f_{GW} = f_{ISCO}$. The signal-to-noise ratio (SNR) is computed as

$$\rho^2 = 4 \int_0^{f_{ISCO}} \frac{|\widetilde{h}(f)|^2}{S_n(f)} df, \tag{6.30}$$

where $S_n(f)$ is the detecor noise power spectral density [396]. We require $\rho > 8$ for a possible detection. The LIGO sensitivity band is shown in Fig. 6.9, together with the mass-compactness profile of the BEC objects. It is observed that with a single axion-like particle ($-\phi^4$ self-interaction) the BEC structure is far from LIGO sensitivity band, while a repulsive interaction between the two scalars supports the system to $\mathcal{O}(0.2)$ region that is relevant at LIGO.

With gravitational wave detectors LIGO-Virgo finishing O3 and being upgraded for higher sensitivity, KAGRA [397] started the observation run, and LIGO-India planned to join the network in the near future, we emphasize that this serves as an example that the interferometry facilities have potential to probe fundamental particles and interesting interactions beyond gravity.

Intriguingly, LIGO-Virgo have recently detected a compact binary merger event (GW190521) with a total mass of 150 $M_\odot$ [398, 399], with the primary mass 85^{+21}_{-14} $M_\odot$ falling in the mass gap predicted by pair-instability supernova theory, $65 - 120$ $M_\odot$. In Fig. 6.9, we show that a BEC system made of two scalars of mass $\sim 10^{-11}$ eV can produce compact structures in the range of 100 $M_\odot$. While a dedicated analysis is needed to investigate its GW signals in our model, it is shown that certain types of boson stars could potentially reproduce the event [400].

6.3.3 Comparison with previous work

Before we move on to the particle model, we briefly discuss the relation and differences with previous studies on multiple species BEC [381] and [380]. In [381] the scenario of multiple axions are discussed in details. We list the main differences between this work and [381] and comment on them in more details.

- the analysis of [381] is performed in the non-relativistic limit, while we solve the full EKG system;
- between different species [381] assume they only interact gravitationally, while we allow interactions $\propto |\phi_1|^2|\phi_2|^2$;
- analytical approximation to the solution of Schödinger-Newton equation is carefully studied by [381] while we solve the EKG system both numerically and analytically.

We note that the first two points are relevant when the field value is large. In particular, the first point captures the GR effect so that it allows us to apply the method to both the galactic scale BEC and the stellar scale. We also observe that in Eq. (6.19) our Hamiltonian precisely reproduces the result of [381] (Eq. 2.15 therein) in the limit $R_1 \approx R_2$. When $R_1 \neq R_2$, we have $\mathcal{O}(1)$ difference due to the choice of our anzats. We stress that we contain higher order terms $H_{metric} \propto G/R^3$, which have the origin of metric perturbation beyond Newtonian gravity, hence only shows up when one solves the EKG system. This is discussed in [167] with a single species.

Astrophysical implications of multiple axions are discussed in [380]. We note a few differences compared to this work.

- The work of [380] uses the so-called independent approximation, which treats solitons of different sizes separately. This allows them to go in to a regime where the mass of the heaviest one is four orders of magnitude larger than the lightest one.
- Similar to [381], [380] uses the Newtonian limit.
- [380] assumes the scalars only interact gravitationally.
- The observational data include the Fornax Galaxy, central Milky Way; Ultra Faint Galaxies; and globular cluster 47 Tuc. In this work our fit at galaxy scale is motivated by [7].
- [380] also performs a Bayesian analysis to fit with the scalar mass, with the presence of extra nuisance parameters from the astrophysical environment.

6.4 Model Realization

In this section we discuss how multiple light scalars with repulsive interactions between them can be realized from the point of view of particle physics model building. It is well known that light scalars can be generated by identifying them as pseudo-Nambu-Goldstone bosons (pNGB) after the spontaneous breaking of some approximate global symmetry. Applications of this idea related to addressing the electroweak hierarchy include leveraging breaking patterns such as $SU(5) \to SO(5)$

[401], $SU(3) \times SU(3) \to SU(3)$ [402], $SU(6) \to Sp(6)$ [387], and $SO(6) \to SO(5)$ [403], to name a few. It was shown in [140] that similar collective symmetry breaking mechanisms can be used to generate repulsive self-interaction in the context of ultra-light dark matter, and potentially a large separation between the scalar mass and the symmetry breaking scale, which is needed to ensure the interaction between the scalars remains weak. We show that this can be extended to the two scalar scenario, which leads to a repulsive interaction between the two light scalars while being technically natural.

After spontaneous symmetry breaking of a global symmetry, such as $SU(6)$ to $Sp(6)$ in [387], one could end up with the following effective potential

$$c_1 f^2 \left| s + \frac{i}{2f}[\phi_2^\dagger \phi_1] \right|^2 + c_2 f^2 \left| s - \frac{i}{2f}[\phi_2^\dagger \phi_1] \right|^2 , \tag{6.31}$$

where s, ϕ_1, ϕ_2 are pNGB living in the quotient group, $SU(6)/Sp(6)$ in this example, and $c_{1,2}$ dimensionless coefficients that can be naturally small yet positive. s is a singlet under gauge transformations, while both ϕ_1 and ϕ_2 are gauge multiplets, doublets of two $SU(2)$'s in the specific case. $[\phi\phi]$ indicates a proper contraction with the gauge indices. One can see that each of the two terms in Eq. (6.31) preserves a direction of the infinitesimal global transformation:

$$\begin{aligned} \phi_1 &\to \phi_1 + \epsilon_1, \\ \phi_2 &\to \phi_2 + \epsilon_2, \\ s &\to s - \frac{i}{2f}([\epsilon_2^\dagger \phi_1] + [\phi_2^\dagger \epsilon_1]) \end{aligned} \tag{6.32}$$

for the first term, and

$$\begin{aligned}\phi_1 &\to \phi_1 + \epsilon_1,\\ \phi_2 &\to \phi_2 + \epsilon_2,\\ s &\to s + \frac{i}{2f}([\epsilon_2^\dagger \phi_1] + [\phi_2^\dagger \epsilon_1])\end{aligned} \tag{6.33}$$

for the second term. Equation (6.31) generates a mass for the singlet s to be $m_s^2 \sim f^2(c_1 + c_2)$. Integrating out the scalar s, we have a interaction between ϕ_1 and ϕ_2 at tree level

$$V_{int}(\phi_1, \phi_2) \sim \frac{c_1 c_2}{c_1 + c_2} |[\phi_2^\dagger \phi_1]|^2. \tag{6.34}$$

Mass terms for ϕ_1 and ϕ_2 are generated at one loop level,

$$V_m(\phi_1, \phi_2) \sim m_1^2 |\phi_1|^2 + m_2^2 |\phi_2|^2 + m_{12}^2([\phi_1^\dagger \phi_2] + h.c.), \tag{6.35}$$

where

$$m_1^2 \sim m_2^2 \sim \frac{c_1 c_2}{16\pi^2} f^2, \tag{6.36}$$

where we neglect the logarithmic part that is $\sim \mathcal{O}(1)$. Choosing a small $c_{1,2}$ leads to a large separation between the symmetry breaking scale and the scalar mass. The low energy potential is $V = V_m + V_{int}$. When $m_{12} \to 0$, the system has a total of four complex scalars that enjoy two separate $U(1)$'s, with generator θ_1 and θ_2:

$$\begin{aligned}\phi_1 &\to \mathrm{e}^{+i\theta_1}\, \phi_1,\\ \phi_2 &\to \mathrm{e}^{+i\theta_2}\, \phi_2.\end{aligned} \tag{6.37}$$

We hasten to add that the model we have proposed, which falls under the genre of "Little Dark Matter" models introduced in [140], is a proof-of-principle model construct of two-scalar ultralight scalar system with a repulsive interaction.

6.5 Conclusion

In this paper, we have demonstrated interesting features in a two scalar BEC system with spherical symmetry. We have developed numerical code to solve the system exactly. We first verified its stability against radial perturbations by performing numerical time evolution. We then went on to show two main features of the system:

1) **Galactic Scale:** The difference of the mass of the two scalars allows us to extend the BEC mass profile in the $C - M$ plane from a curve to a region, hence open up new parameter space. This is due to the fact that, with a fixed set of theory parameters, $[M_{BS}(\Phi_1(0)), C_{BS}(\Phi_1(0))]$ is extended to $[M_{BS}(\Phi_1(0), \Phi_2(0))$, $C_{BS}(\Phi_1(0), \Phi_2(0))]$. We show that this has interesting indications to the problem [6] that one scalar BEC cannot fit the dark matter core profile at the galactic scale.

2) **Stellar Scale:** At the stellar scale with $m \sim 10^{-10}$ eV, we show that the non-gravitational interactions between the two scalars $\Phi_1^2\Phi_2^2$ can play an important role in stabilizing the system up to high compactness. This is similar to the fact that $+\phi^4$ self-interaction stabilizes the system and achieves compactness $C \sim \mathcal{O}(0.2)$. This has important implications for possible detections at LIGO-

Virgo. In addition, with $m_1 \neq m_2$, we show that the transitioning from Φ_1 dominating to Φ_2 dominating holds for different choices of $\lambda' s$. In particular, in the case of $\lambda_1 \cdot \lambda_2 < 0$, the stability is determined by the dominating scalar with highest occupation number. This also hints at interesting phenomenology at gravitational detectors such as LIGO-Virgo and LISA.

Based on our results, there are several interesting future directions. For example: how does the presence of extra scalar(s) affect the cosmological evolution compared to the single scalar scenario? Given that it is known non-gravitational self-interaction can lead to an altered structure formation history as demonstrated in [140, 393], the non-gravitational interaction between the two scalars will likely also change the structure formation process. This might change the bounds on ultra-light dark matter bounds derived from Lyman-alpha [391, 392] and subhalo mass function [150].

In addition, with two scalars the BEC spans a region in the mass-compactness plane instead of forming a curve. One could ask if all points in that region are equally possible to form. The answer is likely negative as galactic scale dynamics might affect the relation among the central density of each scalar. However, addressing this issue is beyond the scope of this work, where our focus is on the mass profile of stable BEC systems. Indeed, the two questions described above may be related, and addressing them requires dedicated simulations. We leave this for future work.

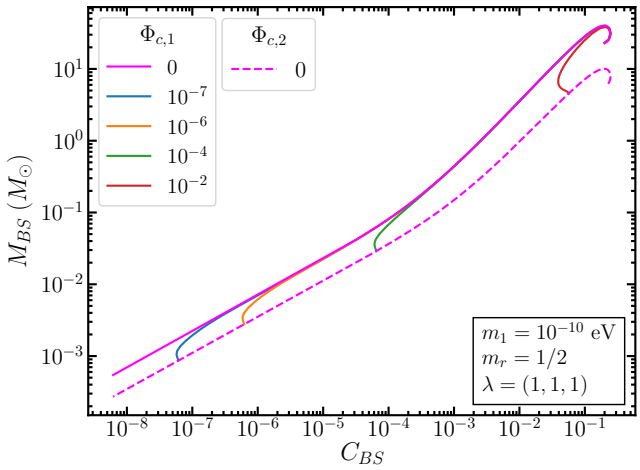

Figure 6.2: The total mass vs compactness for various values of $\Phi_1(0)$ and $\Phi_2(0)$ with $\lambda_1 = 1$, $\lambda_2 = 1$, and $\lambda_{12} = 1$. We scan $\Phi_1(0)$ and $\Phi_2(0)$ to show the existence of stable solutions. The solid magenta line corresponds to the single scalar limit with $m = 5 \times 10^{-11}$ eV and the dashed magenta line is the single scalar limit with $m = 10^{-10}$ eV. The solid lines in between corresponds to $m_1 = 10^{-10}$ eV and $m_2 = 5 \times 10^{-11}$ with each curve corresponding to a different fixed $\Phi_1(0)$ and scanning over $\Phi_2(0)$. We let Φ_1 dominate first, and Φ_2 starts to dominate the system at different places due to $\Phi_1(0)$ fixed at different values in blue, orange, green, and red curves. One can see that the moment Φ_2 starts to dominate, the curve transition from the dashed to solid magenta as expected.

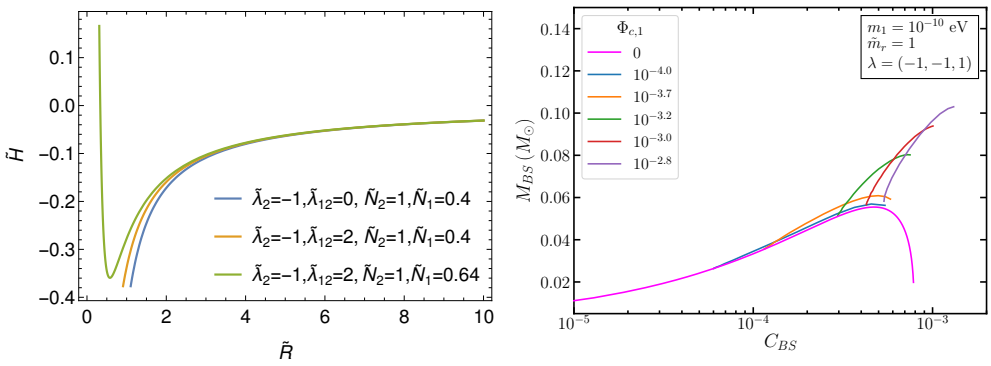

Figure 6.3: Left: the rescaled Hamiltonian as a function of the BEC radius $\widetilde{R}$ in the nonlinear regime, and $N_2 > N_1$. In particular, we observe that when there is no interaction between Φ_1 and Φ_2, it behaves the same as the single scalar case where $-\Phi_2^4$ destroys the local minimum so the system is not stable (blue curve). When (a) there is a repulsive interaction $\lambda_{12} > 0$, and (b) the sub-dominant scalar number, N_1, is large enough, one can see the local minimum is restored (green curve). This happens only when both conditions are fulfilled. With only (a), the system still lacks local minimum (orange curve). Right: The numerical solutions verifies the previous analysis. As an example, we choose $\widetilde{\lambda}_1 = 1, \widetilde{\lambda}_2 = -1, \widetilde{\lambda}_{12} = 1$. All curves are generated by scanning over $\Phi_2(0)$. The magenta curve is with only Φ_2 field. One can see the there are no more solutions beyond $C_{BS} \gtrsim 8 \times 10^{-4}$ due to $-\Phi_2^4$ self-interaction. In the colored curves we add a sub-component Φ_1 with $\Phi_1(0)$ fixed to the labeled value, and again scan over $\Phi_2(0)$. When the subdominant scalar Φ_1 number is large enough (green, red, purple), the system can becomes stable again and one can find solutions at $C_{BS} > 10^{-3}$, consistent with our analytical approximation. We scan $\Phi_2(0)$ to show the existence of stable solutions.

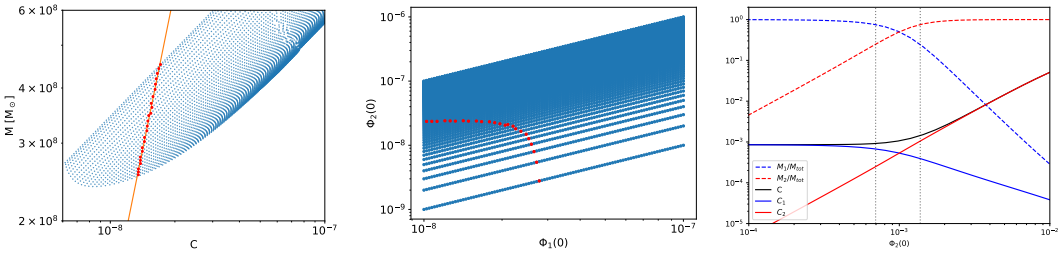

Figure 6.4: Left and middle: this is one example numerical scan over $\Phi_1(0)$, $\Phi_2(0)$ (blue points). Each blue point in the middle plot gives a unique mass profile, *i.e.* a blue point in the left panel in the $C - M$ space. The orange line is the best fit taken from [6]. From the numerical data cloud we pick the points to reconstruct the orange curve. These are shown as the red points in both panels. This particular scan is conducted with $m_1 = 10^{-22}$ eV, $m_2 = 2 \times 10^{-22}$ eV, and $\lambda_1 = \lambda_2 = \lambda_{12} = 0$. We scan $\Phi_1(0)$ and $\Phi_2(0)$ to show the existence of stable solutions. Right: we show the transition region from Φ_1 dominating to Φ_2 dominating by taking one slice of the scan with fixed $\Phi_1(0)$. One can see that indeed when one component mass is more than 75% the total mass, the compactness of the system is mostly determined by this mass component. We define the region between the grey dotted region to be the transition region.

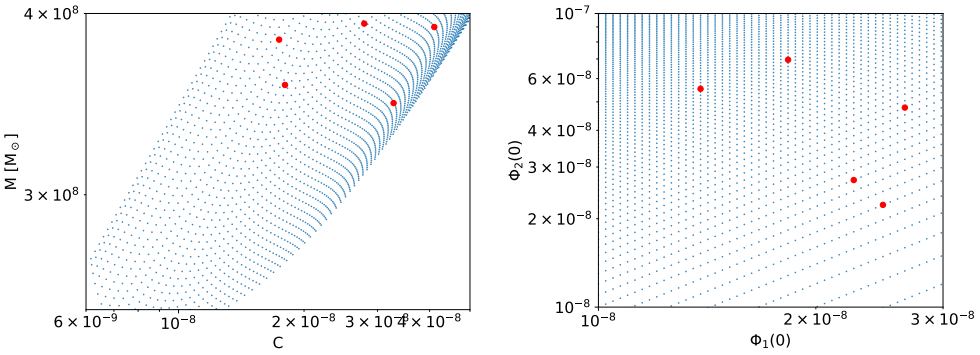

Figure 6.5: We show the numerical scan (blue) in both $C - M$ space (left) and $\Phi_1(0), \Phi_2(0)$ space (right). The red points are a few data points taken from [7]. This particular scan is conducted with $m_1 = 10^{-22}$ eV, $m_2 = 2 \times 10^{-22}$ eV, and $\lambda_1 = \lambda_2 = \lambda_{12} = 0$. See the main text for more details. We scan $\Phi_1(0)$ and $\Phi_2(0)$ to show solutions exist while the system maintains radial stability.

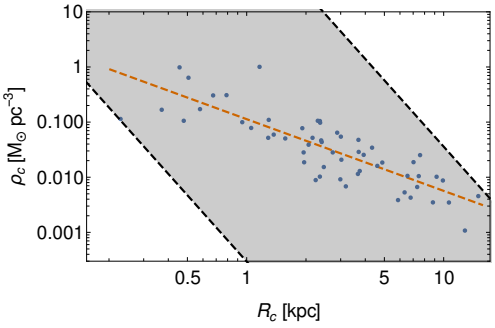

Figure 6.6: We extrapolate the numerical results to a larger mass separation, $m_1 = 2 \times 10^{-24}$ eV and $m_2 = 2 \times 10^{-21}$ eV. The grey region is what the two scalar BEC system covers with varying central density determined by $\Phi_1(0)$, $\Phi_2(0)$. One can see that it not only contains the best fit curve (orange) that represents $\rho_c \approx 1/R_c^{1.3}$, it also incorporates the scattering of the data. The data points are from [7], and fit adopted from [6]. We extrapolate the scalar mass gap m_1/m_2, while use a range in the BEC fraction, M_1/M_2, comparable to our numerical computations with smaller m_1/m_2 to show the existence of stable solutions.

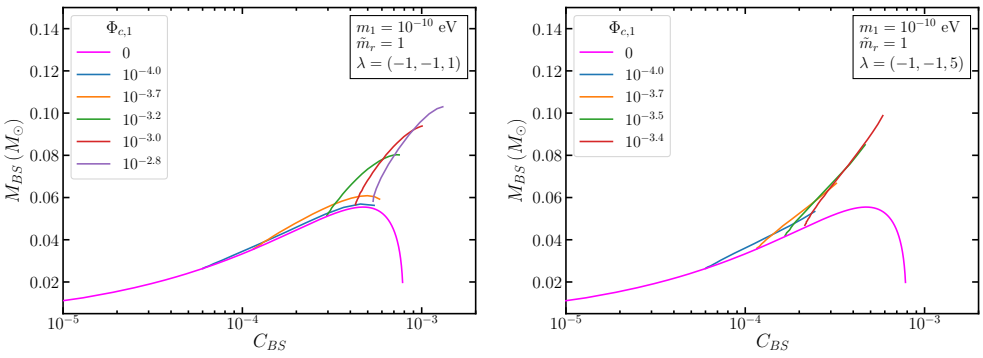

Figure 6.7: The mass vs compactness for a scan over $\Phi_2(0)$ for various fixed $\Phi_1(0)$. $\widetilde{\lambda}_{12} = 1$ (left) is the same as right panel of Fig. 6.3, for comparison with $\widetilde{\lambda}_{12} = 5$ (right). The magenta curve corresponds to the single scalar limit. All curves are generated by scanning over $\Phi_2(0)$. Different colors correspond to fixing $\Phi_1(0)$ to different values.

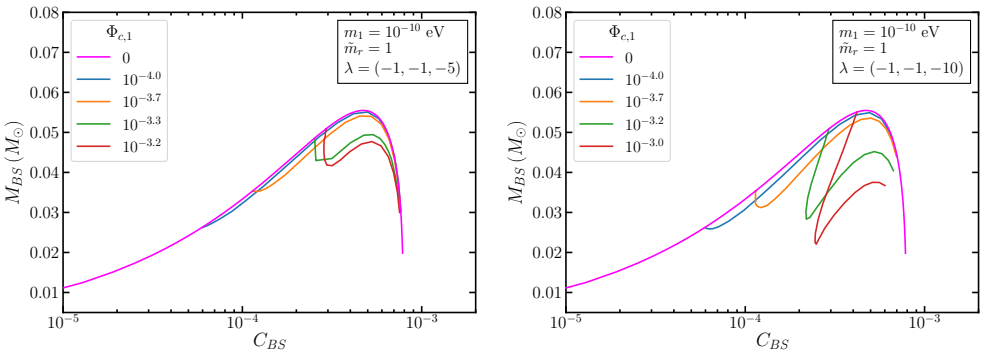

Figure 6.8: When $\widetilde{\lambda}_{12} = -5$ (left) and $\widetilde{\lambda}_{12} = -10$ (right). One can see the extra interaction term can dominate over the kinetic term earlier. Once it happens, the Hamiltonian loses its local minimum and the system becomes unstable. All curves are generated by scanning over $\Phi_2(0)$. Different colors correspond to fixing $\Phi_1(0)$ to different values.

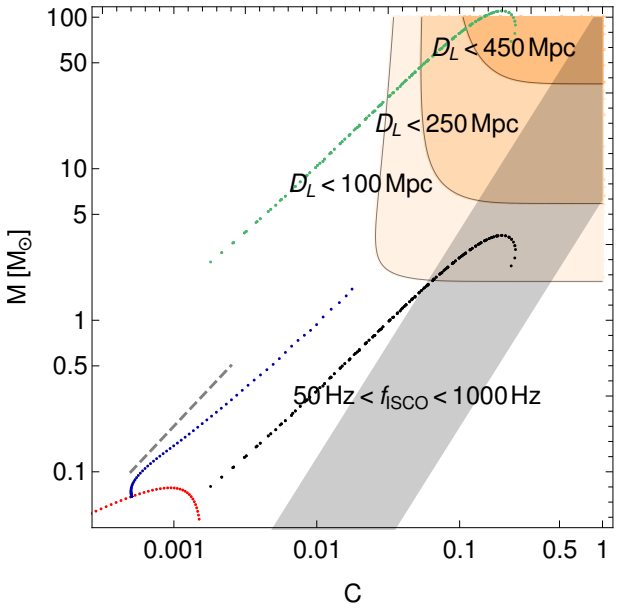

Figure 6.9: The orange bands correspond to the required $C - M$ region that can give SNR $\rho > 8$ needed for detection, given different luminosity distances. The grey band corresponds to the region that f_{ISCO} is in the LIGO sensitivity band, 50 Hz $\sim$ 1000 Hz. The red curve is the mass-compactness profile of a single axion with attractive ϕ_1^4 with $\lambda_1 = -0.5$. The blue curve is achieved by adding a second axion to the red curve while fixing $\phi_1(0)$ and varying $\phi_2(0)$. The interactions are $\lambda_1 = \lambda_2 = -0.5, \lambda_{12} = +5$. We only show part of the curve due to computational complexity related to the stiffness in the equations. The black and green curves are achieved by varying both $\phi_1(0)$ and $\phi_2(0)$, with the same interactions as the blue curve. The red and blue have mass set to 10^{-10} eV, the black 3×10^{-10} eV, and green 10^{-11} eV. The grey dashed line is a guide for the eye, to show $M \propto C$, the mass relation one expects from a single scalar $+\phi^4$ BEC. One can see that indeed, when $\phi_1(0)$ is fixed, the mass curve has a slow smaller than one, as discussed in Eq. (214).

Chapter 7

Testing Affleck Dine Baryogensis

7.1 Introduction

Generically, the Q-balls produced through the fragmentation of the Affleck-Dine condensate are large and long-lived. Consequently, they may evolve as non-relativistic matter, and eventually come to dominate the energy density of the Universe. If the Q-balls decay rapidly, there is a sudden change in the equation of state for the Universe. This results in rapidly oscillating scalar perturbations, which enhances the primordial gravitational wave spectrum from inflation. This is analogous to the so-called poltergeist mechanism, in which the sudden decay of black holes also enhances the gravitational wave spectrum [404]. This is in contrast to the case where gravitational waves are produced during the fragmentation of the condensate, as it is typical that the condensate is a small fraction of the initial total energy [405, 406]. Our proposed test is also potentially complimentary to tests that consider predictions on the ratio of scalar to isocurvature perturbations in D-term inflation [407] and the backreaction of the Affleck-Dine potential onto the inflaton potential which can conflict with cosmic microwave background constraints [408].

In this letter, we first argue that Affleck-Dine scenarios generically have this epoch of early matter domination, and secondly, the Q-ball decay rate is sufficiently fast to enhance the gravitational wave spectrum. In particular, the

sudden transition avoids the suppression that occurs in a gradual transition like Moduli decay [409]. The conditions for a fast transition are easily satisfied. Analytical arguments and simulations show that the Q-ball mass distribution is sharply peaked [187, 410, 411, 412]. Secondly, the charge quanta inside the Q-balls decay to fermions. Q-balls decay when the decay rate per unit charge is larger than the Hubble parameter. We show below that this is suppressed by a surface area to volume factor, and therefore the decay rate per unit charge accelerates as the Q-ball decays, similar to black hole decay.

Furthermore, avoiding an overabundance of gravitinos results in a gravitational wave spectrum that is at sufficiently low frequencies to be observed. Finally, although in this work we make no statistical claims, we present a variety of points in parameter space where the Q-balls are sufficiently long lived to dominate the energy density and produce a detectable gravitational wave signal. Thus, if such a signal is observed, we can narrow the cause down to two known scenarios - an early period of Q-ball domination, which is likely a consequence of Affleck-Dine baryogenesis, or an early period of light primordial black hole domination [404].

7.2 Q-ball Induced Early Matter Domination

During inflation, the field Φ acquires a vacuum expectation value when averaged over super-horizon scales [413, 414, 183, 415, 416]. At the end of inflation, it relaxes towards its equilibrium value as the field fragments to form Q-balls [187, 182]. During the relaxation process, a charge excess is produced as the field VEV follows

a curving path in field space, which is biased either clockwise or counter-clockwise by the small CP-violating operator. However, as a higher dimensional operator, it will also be sensitive to the initial post-inflationary VEV, which is subject to random fluctuations during inflation. Consequently, some Hubble patches will have an excess of Q charge while other have an excess of $\bar{Q}$ charge. Therefore, there are symmetric and asymmetric components to the initial Q-ball density.

After fragmentation, most of the condensate's initial energy is contained in Q-balls rather than individual particles, particularly if the couplings between the scalar field and fermions is small [187, 410]. If the asymmetric component is small (as is expected due to the smallness of the observed baryon asymmetry), the symmetric component must then be large. We parameterize the asymmetric component of the Q-ball energy density

$$r = \frac{n_{\bar{Q}} - n_Q}{n_{\bar{Q}} + n_Q} \,, \tag{7.1}$$

and we expect r to be within an order of magnitude of the baryon asymmetry. (This can also be understood as a consequence of a highly elliptical orbit during relaxation, which simulations connect to a large symmetric component [412].)

In the thin wall regime, the vacuum expectation value inside the Q-ball can be found by minimizing $V(\Phi^2)/\Phi^2$ where Φ parameterizes the flat direction in the Affleck-Dine potential. The energy per unit charge of a single Q-ball is given by

$$\omega = \sqrt{\frac{2V(v)}{v^2}}, \tag{7.2}$$

where v is the VEV inside the Q-ball. (We discuss specific potentials in Ap-

pendix K.) The total initial energy in Q-balls after fragmentation is then

$$\rho_Q = Q_0 \omega n_0 \tag{7.3}$$

where $n_0 \sim N_Q H_0^3$ is the initial number density of the Q-balls and Q_0 is their initial charge. Simulations suggest $N_Q \sim 1000$ for gravity-mediated SUSY scenarios and $N_Q \sim \mathcal{O}(1)$ for most gauge-mediated scenarios, if higher dimensional operators are negligible. However, in this scenario the resulting Q-balls are in the thick wall (as opposed to thin wall) regime [411]. Although we focus on thin wall Q-balls in this work, we note that scaling arguments suggest thick wall Q-balls are longer lived and thus also can induce early matter dominated epochs (see Appendix K).

It is straightforward to derive a condition for the initial charge of the Q-balls in terms of the initial baryon asymmetry Y_{B0}, r, and the reheating temperature T_0,

$$Q_0 = \frac{3 Y_{B0} M_{\rm Pl}^3}{800\sqrt{5}\pi^{5/2} g_* r T_0^3}. \tag{7.4}$$

The initial Q-balls produced after fragmentation are typically quite large; in our benchmark scenarios, the initial charges are above 10^{29}. Consequently, they will travel at non-relativistic speeds in the post-inflationary plasma. Then, if the Q-balls live long enough, they dominate the energy density of the universe. We can approximate the temperature of matter-radiation equality in the limit where Q-ball decay is negligible as

$$T_{\rm eq} \sim \frac{4 Y_{B0} \omega}{3r} \ . \tag{7.5}$$

Although long-lived, the Q-balls produced by the fragmentation of the Affleck-Dine condensate are not absolutely stable; indeed, they cannot be since their

conserved charge must be transferred to Standard Model particles. The sfermions carrying the charge can decay to a quark (or lepton) and neutralino or chargino. Expressions for the relevant coupling can be found in Ref. [417], although we will parameterize the vertex in terms of an effective Yukawa coupling $y_{\rm eff}$.

This decay happens only at the surface of the Q-ball, for one of two reasons. First, if the VEV of the squark or slepton fields inside the Q-ball (which carry the charge) is significantly larger then the energy per unit charge ω, then the large induced fermion masses can forbid the decay inside the Q-ball. The induced masses of the Standard Model fermions have magnitude gv, where $g = g_3$ for quarks if the Q-ball is made of squarks and $g = g_2$ for leptons if the Q-balls is made of sleptons [418]. Therefore, if $gv \gtrsim \omega$, then the decay occurs only at the surface of the Q-ball, where the VEV drops to zero.

Alternatively, if the decay is not forbidden, then decays in the interior of the Q-ball rapidly fill up the Fermi sea. Thereafter, the Q-ball quanta decay only at the surface as long as the diffusion time, $t_D \sim 3R^2/\lambda$, is sufficiently long. The mean free path is $\lambda \sim 1/\sigma_{\psi\phi} n$, where number density $n = 3Q_0/(4\pi R^3)$ refers to the density of scalar quanta inside the Q-ball. The diffusion time is shortest for the highest momentum, which is $\sim \omega/2$ when the decay is energetically forbidden. The diffusion time can then be approximated using the scattering cross section $\sigma_{\psi\phi} \sim g_i^4/(\omega/2)^2$, where $g_i \in (g_Y, g_2, g_3)$ depending on the Standard Model fermion and sfermion involved.

For the benchmark points presented below, decays inside the Q-ball are suppressed for the first reason. Regardless of the reason, the Q-ball evaporation

rate is suppressed by the ratio of the surface area to the volume. Specifically, the radius scales as $Q^{1/3}$, so when the decay occurs only at the surface the decay rate scales as $Q^{2/3}$ instead of as Q. A Q-ball decays once the decay per unit charge is larger than the Hubble parameter. We see that when decays occur only on the surface, $\Gamma_{\rm Q-ball}/Q \propto Q^{-1/3}$, which means that it accelerates as the Q-ball shrinks. Therefore, Q-ball decay is an effectively instantaneous decay, similar to black holes [419, 404].

The charge depletion per unit time per unit area of a Q ball obeys the equation [420]

$$\frac{dQ}{dt\,dA} = \frac{y_{\rm eff} v \omega^2}{64\pi} \tag{7.6}$$

where v is the field value of the condensate and $y_{\rm eff}$ is the effective Yukawa coupling, accounting for mixing angles. In the thin wall limit,

$$R = \left(\frac{3Q}{4\pi\omega v^2}\right)^{1/3}, \tag{7.7}$$

which gives

$$\frac{\Gamma_{\rm Q-ball}}{Q} = \frac{y_{\rm eff} v \omega^2 Q^{-1/3}}{16} \left(\frac{3}{4\pi\omega v^2}\right)^{2/3}. \tag{7.8}$$

For the Q-balls to decay after dominating the energy density, we must therefore require $\Gamma_{\rm Q-ball}/HQ\big|_{T=T_{\rm eq}} \ll 1$. Approximating the left side at $Q = Q_0$, we find the condition

$$\frac{0.178 y_{\rm eff} r^{7/3} T_0}{Y_{B0}^{7/3} \omega^{2/3} (g_* v)^{1/3}} \left(\frac{1000}{N_Q}\right)^{1/3} \ll 1\ . \tag{7.9}$$

The large symmetric component $r \sim Y_{B0}$ is vital due to the $Y_{B0}^{-7/3}$ factor, which would otherwise make this condition difficult to satisfy. As expected, this prefers small Yukawa couplings, which result in long-lived Q-balls.

We emphasize that for our numerical analysis, we solved the differential equation $dQ/dt = -\Gamma_{\mathrm{Q-Ball}}(Q,T)$. We also note that the initial baryon asymmetry will be larger than it is today because the decay of the Q-ball dilutes the charge asymmetry. The final asymmetry is given by

$$Y_B = Y_{B0}\left(1 + \frac{4Y_{B0}}{3r}T_{\mathrm{dec}}\right)^{-3/4}, \tag{7.10}$$

where T_{dec} is the temperature at which the Q-balls decay and $Y_B = 8.59 \times 10^{-11}$ as given by Planck [421].

Because the Q-ball mass fraction is sharply peaked at a single value and the decay is effectively instantaneous, the scale factor and Hubble approximately obey step function solutions

$$\frac{a(\eta)}{a(\eta_R)} = \begin{cases} \left(\frac{\eta}{\eta_R}\right)^2 \\ 2\frac{\eta}{\eta_R} - 1 \end{cases}, \quad H(\eta) = \begin{cases} \frac{2}{\eta} & (\eta \leq \eta_R) \\ \frac{1}{\eta - \eta_R/2} & (\eta > \eta_R) \end{cases} \tag{7.11}$$

where η is the conformal time; η_R is specifically the conformal time at which radiation domination recommences.

7.3 Gravitational waves

We assume inflation generates a primordial scalar power spectrum of the form

$$\mathcal{P}_\zeta(k) = \Theta(k_{\mathrm{inf}} - k) A_s \left(\frac{k}{k_*}\right)^{n_s - 1} \tag{7.12}$$

for some cutoff scale k_{inf} with n_s being the spectral tilt, k_* being the pivot scale and A_s being the amplitude at the pivot scale. We take typical values of $A_s = 2.1 \times 10^{-9}$, $n_s = 0.97$, $k_* = 0.05$ Mpc^{-1} [421].

Scalar perturbations grow with the scale factor during any matter domination epoch, including the Q-ball dominated epoch mentioned above, which can in turn induce gravitational waves [419, 409]. Our analysis of the induced gravitational wave signal follows [409] and therefore we similarly work within the conformal Newtonian gauge and assume Gaussian curvature perturbations.

If matter domination is sufficiently long, then perturbations at small scales can enter the non-linear regime where a linear analysis is insufficient. Such non-linearities become important at scales $k_{\rm NL} \sim 470/\eta_R$, where η_R is the conformal time at which the Q-ball-caused matter domination era abruptly ended. In this work, we neglect the non-linear regime and therefore we restrict ourselves to points in parameter space at which the maximum comoving mode enhanced by early matter domination satisfies $k_{\rm max} \lesssim 470/\eta_R$. We note that there may still be detectable gravitational wave signals in the parameter space where this is not satisfied, although we leave the analysis of the non-linear regime to future work.

Using the step function approximations given above, the power spectrum of gravitational waves at conformal time η is [422]

$$\Omega_{\rm GW}(\eta, k) = \frac{1}{24}\left(\frac{k}{a(\eta)H(\eta)}\right)^2 \overline{\mathcal{P}_h(\eta, k)} \tag{7.13}$$

where the time averaged power spectrum of the induced gravitational waves is related to the scalar (curvature) power spectrum as

$$\overline{\mathcal{P}_h(\eta, k)} = 4\int_0^\infty dv \quad \int_{|1-v|}^{1+v} du \left(\frac{4v^2 - (1+v^2-u^2)^2}{4vu}\right)^2 \times \overline{I^2(u, v, k, \eta, \eta_R}\mathcal{P}_\zeta(uk)\mathcal{P}_\zeta(vk) \ . \tag{7.14}$$

In the above the time dependence of the gravitational waves is

$$I(u,v,k,\eta,\eta_R) = \int_0^{k\eta} d(\overline{k\eta})\frac{a(\bar{\eta})}{a(\eta)}kG_k(\eta,\bar{\eta})f(u,v,\overline{k\eta},k\eta_R) \tag{7.15}$$

where the Greens function is the solution of the equation

$$\frac{\partial^2 G(\eta,\bar{\eta})}{\partial\eta^2} + \left(k^2 - \frac{1}{a}\frac{\partial^2 a}{\partial\eta^2}\right)G(\eta,\bar{\eta}) = \delta(\eta-\bar{\eta}) \tag{7.16}$$

and the source function has the form

$$\begin{aligned} f(u,v,\overline{k\eta},k\eta_R) \;=\; & \frac{3}{25(1+w)}\left(2(5+3w)\Phi(u\overline{k\eta})\Phi(v\overline{k\eta})\right. \\ & +4H^{-1}\frac{\partial}{\partial\eta}\left(\Phi(u\overline{k\eta})\Phi(v\overline{k\eta})\right) \\ & \left.+4H^{-2}\frac{\partial}{\partial\eta}\Phi(u\overline{k\eta})\frac{\partial}{\partial\eta}\Phi(v\overline{k\eta})\right)\ . \end{aligned} \tag{7.17}$$

In these equations w is the equation of state parameter and Φ is the transfer function of the gravitational potential, which obeys the evolution equation [423]

$$\frac{\partial^2\Phi}{\partial\eta^2} + 3(1+w)H\frac{\partial\Phi}{\partial\eta} + wk^2\Phi = 0\ . \tag{7.18}$$

For a sufficiently quick transition from matter to radiation domination, we can use the analytic formulae for the gravitational wave power spectrum in Ref. [419] which we give in the supplementary material.

This rapid transition is necessary to produce the sharp peak through the "poltergeist" mechanism [404]. During the early matter domination epoch, density perturbations in non-relativistic Q-ball modes grow and form overdensities. The Q-ball decay, which is rapid as compared to the Hubble time, converts these overdensities into relativistically moving sound waves, which serve as sources of gravitational waves. Gravitational waves exhibit a rapidly growing resonance

mode which is amplified by interactions with a sound wave comoving at a certain angle [424, 419, 404]. This resonance results in a dramatic enhancement at a certain frequency, as can be seen in our Fig. 7.1. It is important that the transition to radiation domination is rapid, because otherwise the overdensities dissolve gradually and do not result in any relativistically moving modes.

7.4 Results

We present the gravitational wave signal for three sample points in parameter space in Fig. 7.1. These were chosen to have Yukawa couplings similar in size to those in the Standard Model; the precise values of the parameters are given in Table 7.1. To retain generality, we specify the VEV v and energy density per charge ω of the Q-balls, instead of specializing to a particular potential. Gravity and gauge-mediation models which produce Q-balls with these properties are discussed in Appendix K.

Calculated quantities, such as the equality and decay temperatures, for these benchmark points are given in Table 7.2. We note that since ω is within one order of magnitude of T_0, the temperature at which Q-balls are produced, it is self-consistent to neglect finite temperature corrections to ω, which are induced via loop corrections.

The observable range is controlled by the proposed frequency sensitivity of future gravitational wave detectors with high temperature probed by higher frequencies. At present the highest frequency gravitational wave detectors with

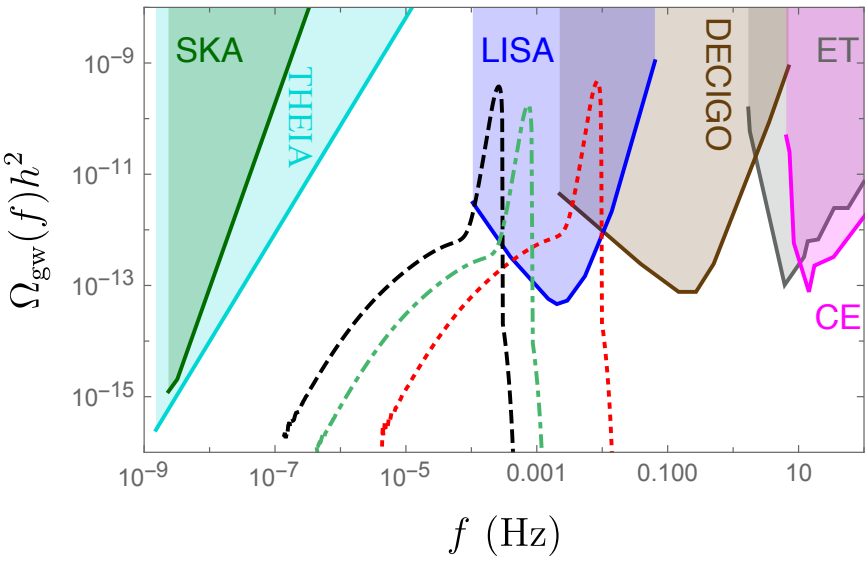

Figure 7.1: The gravitational wave signal for three benchmark scenarios, which have effective Yukawa couplings similar to the Standard Model bottom quark (red, dotted), up quark (olive, dot-dashed), and electron (black, dashed). These clearly produce signals within the reach of future experiments, which were taken from Ref. [8, 9] for DECIGO with 3 units and an observation time of 1 year, Ref. [10] for LISA with an observation time of 4 years, ref. [11, 12] for THEIA with an observation time of 20 years, Ref. [13, 8, 14] for Einstein Telescope with an observation time of one year, Ref. [15] for the Cosmic Explorer and ref. [16] for SKA.

ω (GeV)	v (GeV)	$Y_{\bar{B}}$	r	T_0 (GeV)	N_Q	y_{eff}
6.66×10^5	3.80×10^{10}	1.11×10^{-8}	1.56×10^{-8}	4.59×10^6	1000	0.024
8.45×10^5	1.92×10^9	1.36×10^{-8}	2.76×10^{-7}	8.04×10^6	1000	1.4×10^{-5}
9.95×10^5	7.21×10^9	2.10×10^{-8}	1.38×10^{-6}	3.56×10^6	1000	2.9×10^{-6}

Table 7.1: Parameters used in our three benchmark points in Fig. 7.1. In addition to the Q-ball parameters ω and v, Y_B is the initial charge asymmetry after fragmentation which occurs at temperature T_0, N_Q is the average initial number of Q-balls per Hubble volume after fragmentation, and $r \sim Y_B$ is the ratio of the asymmetric component. Note that the Yukawa couplings are equal to that of the Standard Model bottom quark, up quark, and electron in the top, middle, and bottom rows. Additionally, we have taken $g_* = 106$ in our analysis.

enough sensitivity are the Cosmic Explorer [15] and the Einstein Telescope [425] although higher frequency proposals are a promising work in progress [127]. We see that DECIGO has particularly good coverage of our expected signal.

There is a modest trend for points with smaller Yukawa couplings to decay later and therefore to have lower frequency peaks. For the signal to be observable, the Q-balls must decay when the temperature falls in the range 20 GeV $< T_{\text{dec}} < 2 \times 10^7$ GeV. The upper bound is frequently satisfied even for large reheating temperatures, although a low reheating temperature is often preferred to avoid overproduction of gravitinos, though the exact bound on the reheating temperature depends on the mass of the gravitino [426, 427, 428, 429]. We have imposed $T_R < 10^7$ GeV for all benchmarks.

Q_0	$T_{\rm eq}$ (GeV)	$T_{\rm dec}$ (GeV)
1.14×10^{31}	6.34×10^5	1368
1.47×10^{29}	55520	138
5.18×10^{29}	20050	458

Table 7.2: Calculated quantities for the three benchmark points in 7.1. $T_{\rm eq}$ is the temperature of Q-ball-radiation equality and $T_{\rm dec}$ is the temperature of Q-ball decay.

7.5 Conclusions

As a high-scale phenomenon, it is difficult to observationally confirm Affleck-Dine baryogenesis. We have shown here that broad class of Affleck-Dine models produce a detectable gravitational wave signal within the range of the Einstein Telescope and/or Decigo. Such signals are a consequence of the sudden end of an early matter-domination epoch, which occurs if the Q-balls from the fragmentation of the Affleck-Dine condensate are sufficiently long-lived. A low reheating temperature, motivated by the gravitino problem, ensures a signal within the observable frequency range, but we find that this is not a requirement. Thus, if a signal is indeed observed, we can narrow the cause down to two known scenarios- an early period of Q-ball domination, which is a natural outcome of Affleck-Dine baryogenesis, or an early period of light primordial black hole domination [404].

Appendix A

The Example Effective Potential

Here we provide details of the example effective potential used in Sec. 4.3, so that those results can be reproduced more easily. The effective potential was originally used as a high temperature approximation for the standard model (see, e.g., Ref. [17]), given by

$$V(\phi, T) = D(T^2 - T_0^2)\phi^2 - ET\phi^3 + \frac{\lambda}{4}\phi^4. \tag{A.1}$$

Here $D > 0$, $E > 0$, $\lambda > 0$ and λ has a weak dependence on T. The first term has a positive coefficient when $T > T_0$ to restore the symmetry. The third, the cubic term, when is sufficiently smaller, helps create a barrier together with the first term, and creates another minimum. Since this example is only used to provide a simple benchmark effective potential to show the effects of the expansion of the universe, we will take these parameters to be T independent. It should be noted that an effective potential of this form can characterize features of a wide class of beyond the standard model scenarios in the high temperature approximation. We will use this effective potential to calculate bounce solutions and corresponding parameters relevant for the phase transition.

Though there are four free parameters for this simple effective potential, a rescaling of both the coordinates and the scalar fields allows to reduce to only one dynamical parameter [17]. The rescaled fields and coordinates are defined as

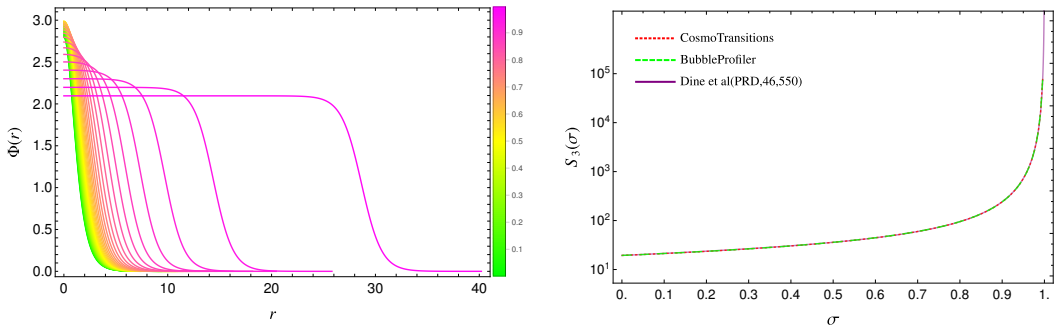

Figure A.1: Left panel: the bounce solutions for the example effective potential with rescaled fields and coordinates used in this work for different choices of σ, with the color-map denoting values of σ. Right panel: comparison of the corresponding $S_3(T)/T$ obtained with different packages and the analytical fit provided in Ref. [17].

$\Phi = 2ET\phi/M^2$ and $X = Mx$. The Lagrangian then becomes

$$\mathcal{L} = \frac{M^6}{4E^2T^2}\left[\frac{1}{2}(\partial_X\Phi)^2 - \frac{1}{2}\Phi^2 + \frac{1}{2}\Phi^3 - \frac{1}{8}\sigma\Phi^4\right], \tag{A.2}$$

where $\sigma \equiv \lambda M^2/(2E^2T^2)$ [1]. The behavior of the effective potential for the rescaled fields during the phase transition is solely controlled by σ. When $\sigma < 9/8$, a second minimum develops at the temperature

$$T = \sqrt{\frac{T_0^2}{1 - \frac{9E^2}{8\lambda D}}}. \tag{A.3}$$

When $\sigma = 1$, this minimum is degenerate with the one at the origin, which corresponds to a critical temperature of

$$T_c = \sqrt{\frac{T_0^2}{1 - \frac{E^2}{\lambda D}}}. \tag{A.4}$$

Therefore for the rescaled field Φ and coordinate X, there is essentially one parameter σ that determines the shape of the potential. Calculating the bounce

[1] This is of course different from the σ defined in Eq. 4.102

solution and S_3 for all choices of σ is sufficient to cover the full parameter space of the original four parameters. Define the S_3 action for the rescaled fields and coordinates as $\widetilde{S}_3(\sigma)$, then the action $S_3(T)$ for the original four parameter theory can be obtained directly as

$$\frac{S_3(T)}{T} = \frac{M^3}{4E^2T^3}\widetilde{S}_3(\sigma). \tag{A.5}$$

The bounce solutions for various choices of σ are shown in the left panel of Fig. A.1 and the corresponding $S_3(\sigma)$ shown as red dotted and green dashed lines for solutions solved from CosmoTransitions [281] and BubbleProfiler [373] respectively. In this plot, there is also a purple curve, corresponding to the analytical fit in Ref. [17]:

$$\widetilde{S}_3(\sigma) = 4 \times 4.85 \times \left\{1 + \frac{\sigma}{4}\left[1 + \frac{2.4}{1-\sigma} + \frac{0.26}{(1-\sigma)^2}\right]\right\}. \tag{A.6}$$

We can see in the whole region plotted, the three results agree very well with each other. So our results in previous sections can be followed by simply choosing above analytical fit. For the example used in Sec. 4.3, $T_0 = 75\text{GeV}$, $E = D = 0.1$ and $\lambda = 0.2$, which gives $T_c = 106.066\text{GeV}$.

Appendix B

The Previously Derived Effective Lifetime of the Source

Here we revisit the deviation that led to the conclusion that the effective lifetime of the source is one Hubble time in a radiation dominated universe, as was originally obtained in Ref. [68]. We will follow closely their notations, using the conformal time η as variable instead of y, and using a_* rather than a_s. Also we study both RD and MD, though only RD is studied in Ref. [68].

We start with Eq. 4.17 and do the integrals over $\widetilde{\eta}_1$ and $\widetilde{\eta}_2$. We can keep only the leading contribution by neglecting the highly oscillatory part in the Green's functions. This means for the trigonometric function, we keep only the parts with argument $(\widetilde{\eta}_1 - \widetilde{\eta}_2)$ and find

$$\begin{aligned}
&\frac{\partial G(\widetilde{\eta}, \widetilde{\eta}_1)}{\partial \widetilde{\eta}} \frac{\partial G(\widetilde{\eta}, \widetilde{\eta}_2)}{\partial \widetilde{\eta}} \\
&= \frac{\widetilde{\eta}_1 \widetilde{\eta}_2}{2} \times \begin{cases} \widetilde{\eta}^{-2}(1 + \widetilde{\eta}^{-2}) \cos(\widetilde{\eta}_1 - \widetilde{\eta}_2), \\ \widetilde{\eta}^{-4}(1 + 3\widetilde{\eta}^{-2} + 9\widetilde{\eta}^{-4})[(\widetilde{\eta}_1 - \widetilde{\eta}_2) \sin(\widetilde{\eta}_1 - \widetilde{\eta}_2) + (1 + \widetilde{\eta}_1 \widetilde{\eta}_2) \cos(\widetilde{\eta}_1 - \widetilde{\eta}_2)], \end{cases}
\end{aligned} \tag{B.1}$$

where the upper and lower row applies to radiation and matter dominated universe respectively. Now switch integration variables from $\widetilde{\eta}_1$ and $\widetilde{\eta}_2$ to $x \equiv (\widetilde{\eta}_1 + \widetilde{\eta}_2)/2$ and $z = \widetilde{\eta}_1 - \widetilde{\eta}_2$. This results in the relation $\widetilde{\eta}_1 \widetilde{\eta}_2 = x^2 - \frac{z^2}{4}$. Under these

manipulations, the power spectral density of h' becomes:

$$P_{h'} = [16\pi G\left(\widetilde{\bar{\epsilon}}+\widetilde{\bar{p}}\right)\bar{U}_f^2]^2 L_f^3 \left\{ \begin{array}{l} \widetilde{\eta}^{-2}(1+\widetilde{\eta}^{-2}) \\ \\ \widetilde{\eta}^{-4}(1+3\widetilde{\eta}^{-2}+9\widetilde{\eta}^{-4}) \end{array} \right\} \int dx \int dz \frac{1}{k^2} \frac{\widetilde{\eta}_1 \widetilde{\eta}_2 a_*^8}{a^2(\eta_1)a^2(\eta_2)}$$
$$\times \frac{1}{2} \left\{ \begin{array}{l} \cos z \\ \\ z\sin z + (1+x^2-\frac{z^2}{4})\cos z \end{array} \right\} \widetilde{\Pi}^2(\widetilde{L}_f, \widetilde{\eta}_1, \widetilde{\eta}_2). \tag{B.2}$$

Here $\widetilde{L}_f \equiv kL_f$. The expression can be reorganized to show the correct dependence on $a(\eta)$ and we have for the correlator of $\dot{h}$:

$$P_{\dot{h}} = \frac{a_*^6}{a^4(\eta)} \frac{1}{k^2} [16\pi G\left(\widetilde{\bar{\epsilon}}+\widetilde{\bar{p}}\right)\bar{U}_f^2]^2 L_f^3 \left\{ \begin{array}{l} 1+\widetilde{\eta}^{-2} \\ \\ 1+3\widetilde{\eta}^{-2}+9\widetilde{\eta}^{-4} \end{array} \right\} \int_{\widetilde{\eta}_*}^{\widetilde{\eta}} dx \int dz$$
$$\times \frac{1}{2} \left\{ \begin{array}{l} \frac{\widetilde{\eta}_*^2}{x^2-z^2/4} \\ \\ \frac{\widetilde{\eta}_*^4}{(x^2-z^2/4)^3} \end{array} \right\} \left\{ \begin{array}{l} \cos z \\ \\ z\sin z + (1+x^2-\frac{z^2}{4})\cos z \end{array} \right\} \widetilde{\Pi}^2(\widetilde{L}_f, \widetilde{\eta}_1, \widetilde{\eta}_2) \tag{B.3}$$

As we have seen the source is largely stationary, that is, the correlator $\widetilde{\Pi}^2(\widetilde{L}_f, \widetilde{\eta}_1, \widetilde{\eta}_2)$ depends only on z but not on x. Then it can be written as $\widetilde{\Pi}^2(\widetilde{L}_f, z)$. Also the autocorrelation time z is very small compared with the Hubble time, so we can neglect the z dependence on the denominators in the first curly bracket and keep only the x^2 term for MD in the second curly bracket, which then allows the integration over x, giving

$$\int_{\widetilde{\eta}_*}^{\widetilde{\eta}} dx \frac{1}{x^2} = \frac{1}{\widetilde{\eta}_*} - \frac{1}{\widetilde{\eta}}, \qquad \int_{\widetilde{\eta}_*}^{\widetilde{\eta}} dx \frac{1}{x^4} = \frac{1}{3}(\frac{1}{\widetilde{\eta}_*^3} - \frac{1}{\widetilde{\eta}^3}). \tag{B.4}$$

Here is where things become subtle. The second term for RD is neglected in Ref. [68]. This leads to a result that corresponds to the asymptotic value $\Upsilon = 1$ for RD, and as we have seen the short duration of the source does not allow to

neglect this term. Lets continue to reproduce the result of Ref. [68] by keeping only the first term. This gives

$$
\begin{aligned}
P_h &= \frac{a_*^6}{a^4(\eta)}\frac{1}{k^2}[16\pi G\left(\bar{\widetilde{\epsilon}}+\bar{\widetilde{p}}\right)\bar{U}_f^2]^2 L_f^3 \left\{ \begin{array}{l} 1+\widetilde{\eta}^{-2} \\ \\ (1+3\widetilde{\eta}^{-2}+9\widetilde{\eta}^{-4})/3 \end{array} \right\} \widetilde{\eta}_* \\
&\qquad \times \int dz \frac{\cos(z)}{2}\widetilde{\Pi}^2(\widetilde{L}_f, z) \\
&= \frac{a_*^4}{a^4(\eta)}[16\pi G\left(\bar{\widetilde{\epsilon}}+\bar{\widetilde{p}}\right)\bar{U}_f^2]^2 L_f^3 \left\{ \begin{array}{l} 1+\widetilde{\eta}^{-2} \\ \\ (1+3\widetilde{\eta}^{-2}+9\widetilde{\eta}^{-4})/3 \end{array} \right\} (a_*\eta_*)(a_* L_f)\widetilde{P}_{\rm GW}(kL_f).
\end{aligned}
\tag{B.5}
$$

In the second line, the following definition is used:

$$
\widetilde{P}_{\rm GW}(kL_f) = \frac{1}{kL_f}\int dz \frac{\cos z}{2}\widetilde{\Pi}^2(\widetilde{L}_f, z). \tag{B.6}
$$

The variables appearing in above equations can further be reorganized so that we have a result similar to Eq.(A10) in Ref. [68]:

$$
\begin{aligned}
\mathcal{P}_{\rm GW}(t,k) = 3\Gamma^2\bar{U}_f^4 \left(\frac{a_*^4}{a^4}\frac{H_{*R}^4}{H^2 H_*^2}\right) &\left\{ \begin{array}{l} 1+\widetilde{\eta}^{-2} \\ \\ (1+3\widetilde{\eta}^{-2}+9\widetilde{\eta}^{-4})/3 \end{array} \right\} \\
&\times (H_* a_* \eta_*)(H_* a_* L_f)\frac{(kL_f)^3}{2\pi^2}\widetilde{\mathcal{P}}_{\rm GW}(kL_f).
\end{aligned}
\tag{B.7}
$$

For RD, $H_* a_* \eta_* = 1$ and $a_* L_f$ is the physical length scale (L_f^* in Ref. [68]). If we also neglect the variation of the Hubble rate from H_* to H, and since in this case $H_{*R} = H_*$, and also neglect the terms suppressed by $1/\widetilde{\eta}$ in the curly bracket due to the assumed relation $\widetilde{\eta} \gg \widetilde{\eta}_*$, then the result for RD reduces to Eq.(A11) in Ref. [68]. Because $H_* a_* \eta_* = 1$ and also because the power spectrum in Minkowski spacetime is proportional to $H_* \tau_{\rm sw}$, it is concluded in Ref. [68] that the effective

lifetime is a Hubble time. This is true if indeed $\widetilde{\eta} \gg \widetilde{\eta}_*$, but as we have seen it requires many Hubble times for the asymptotic value to be reached. The sound wave, however, is likely to be disrupted by the onset of shocks or turbulence or damped by other dissipative processes, which certainly do not allow the sound wave to remain active that long for the asymptotic value to be reached. So the main point is we can not assume $\widetilde{\eta} \gg \widetilde{\eta}_*$ and neglect the second term in the first equation of Eq. B.4.

While non-relevant here for MD, we can still compare its asymptotic value with what we already find in previous sections. From above equation we can see the quantity in the curly bracket is 1/3 for MD and 1 for RD. But for MD, $H_* a_* \eta * = 2$, then the asymptotic value of Υ is 2/3 for MD, which is consistent with our previous result.

Appendix C

Kinetic Energy Efficiency Coefficient

The kinetic energy efficiency coefficient may be solved by integrating over the enthalpy and velocity profiles around a single bubble,

$$\kappa = \frac{3}{\epsilon v_w^3} \int_0^{\xi_{max}} d\xi \xi^2 \omega \gamma^2 v^2, \tag{C.1}$$

where ϵ is the bag constant and $\xi = r/t$ is a self similar coordinate in terms of the distance form the bubble center r and the time since nucleation t. The fits to κ are provided in [70] and are valid in the range $10^{-3} < \alpha < 10$ to a precision of 10%. The fits are found by splitting the parameter space of v_w into three regions and four boundary conditions. The boundary conditions are

$$\kappa_A \simeq v_w^{6/5} \frac{6.9\alpha}{1.36 - 0.037\sqrt{\alpha} + \alpha}, \text{ for } v_w \ll c_s, \tag{C.2}$$

$$\kappa_B \simeq \frac{\alpha^{2/5}}{0.017 + (0.997 + \alpha)^{2/5}}, \text{ for } v_w = c_s, \tag{C.3}$$

$$\kappa_C \simeq \frac{\sqrt{\alpha}}{0.135 + \sqrt{0.98} + \alpha}, \text{ for } v_w = v_J = \frac{\sqrt{\frac{2}{3}\alpha + \alpha^2} + \sqrt{1/3}}{1 + \alpha}, \tag{C.4}$$

$$\kappa_D \simeq \frac{\alpha}{0.73 + 0.083\sqrt{\alpha} + \alpha}, \text{ for } v_w \to 1, \tag{C.5}$$

where v_J is the Jouguet velocity and c_s is the speed of sound. Subsonic deflagrations in the region $v_w \lesssim c_s$ have a kinetic energy cofficient approximated by

$$\kappa \simeq \frac{c_s^{11/5} \kappa_A \kappa_B}{\left(c_s^{11/5} - v_w^{11/5}\right) \kappa_B + v_w c_s^{6/5} \kappa_A}, \tag{C.6}$$

and detonations in the region $v_w > v_J$ by

$$\kappa \simeq \frac{(v_J - 1)^3 v_J^{5/2} v_w^{-5/2} \kappa_C \kappa_D}{\left[(v_J - 1)^3 - (v_w - 1)^3\right] v_J^{5/2} \kappa_C + (v_w - 1)^3 \kappa_D}, \tag{C.7}$$

Supersonic deflagrations, hybrid, in the region $c_s \lesssim v_w \lesssim v_J$ can be approximated by

$$\kappa \simeq \kappa_B + (v_w - c_s)\,\delta\kappa + \frac{(v_w - c_s)^3}{(v_J - c_s)}\left[\kappa_C - \kappa_B - (v_J - c_s)\,\delta\kappa\right], \tag{C.8}$$

where

$$\delta\kappa \simeq -0.9 \log \frac{\sqrt{\alpha}}{1+\sqrt{\alpha}}. \tag{C.9}$$

Appendix D

Toy Model

D.1 Toy Effective Potential

A general free energy density of a single scalar field, ϕ, under a high temperature expansion can be written in the form

$$f(\phi, T) = D(T^2 - T_0^2)\phi^2 - ET\phi^3 + \frac{1}{4}\lambda\phi^4 + \Delta V - \frac{1}{3}aT^4, \tag{D.1}$$

where ΔV is added to the potential to cancel out the zero temperature minimum such that $f(\phi_{\min}, 0) = 0$. The Standard Model effective potential was considered in Ref. [17]. We require $D > 0$, $E > 0$, $\lambda > 0$ to ensure symmetry is broken at low temperature and generate a barrier between the symmetric and broken phase. The vacuum terms are not necessary for determining the phase transition structure of the model, however, they are necessary for determining the temperature dependence of the speed of sound.

The structure of the potential along with the constraints on the parameters allows for simple analytical forms for the minima as a function of temperature. The minimum is found by minimizing Eq. D.1 with respect to the scalar field which results in

$$\phi_{\min} = \frac{3ET \pm \sqrt{9E^2T^2 - 8D\lambda(T_0^2 - T^2)}}{2\lambda}, \tag{D.2}$$

where the '+' sign gives the local minimum. When T is large, the global minimum will sit at the origin with $\phi_{\min} = 0$. As T decreases, a second minimum will

develop at

$$T = \sqrt{\frac{T_0^2}{1 - \frac{9}{8}\frac{E^2}{\lambda D}}}. \tag{D.3}$$

This minimum will eventually become degenerate with minimum at the origin at the critical temperature when

$$T_C = \sqrt{\frac{T_0^2}{1 - \frac{E^2}{\lambda D}}}. \tag{D.4}$$

The Euclidean action of a bounce configuration, S_3, will start from infinity at $T = T_c$ and decrease with temperature. There is an analytical form for the action given by

$$\frac{S_3(T)}{T} = \frac{M^3}{4E^2T^3}\widetilde{S}_3(\sigma), \tag{D.5}$$

$$\widetilde{S}_3(\sigma) = 4 \times 4.85 \times \left[1 + \frac{\sigma}{4}\left(1 + \frac{2.4}{1-\sigma} + \frac{0.26}{(1-\sigma)^2}\right)\right], \tag{D.6}$$

where $\sigma = \lambda M^2/(2E^2T^2)$ controls the overall shape of the potential [17]. The critical temperature and the action are necessary to determine the dynamics of the phase transition and calculate the relevant transition temperatures such as T_n,T_p, and T_f and the mean bubble separation $R_*(v_w, \beta)$.

The hydrodynamics of the phase transition are determined by the pressure and energy density in the symmetric and broken phase where $p_s = -f(0, T)$ and $p_b = -f(\phi_{\min}, T)$. The energy density can be computed from the transformation of pressure

$$e = T\frac{\partial p}{\partial T} - p, \tag{D.7}$$

which can be evaluated in both the symmetric and the broken phase. From

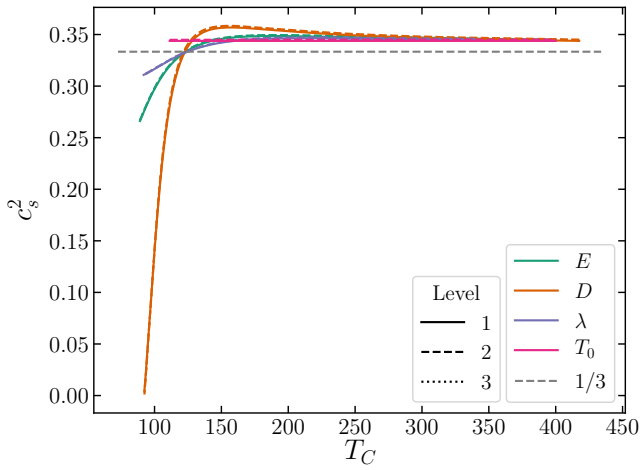

Figure D.1: Speed of sound computed in the different levels of diligence.

Eq. D.1, the pressure in the symmetric and broken phases are

$$p_s = -f(0,T) = \frac{1}{3}aT^4 - \Delta V, \tag{D.8}$$

$$p_b = -f(\Phi_{\min},T), \tag{D.9}$$

where the pressure in the broken phase has additional dependence on temperature arising from $\phi_{\min}$. The speed of sound may be found from the pressure using Eq. 5.23 in both the symmetric and broken phase. The temperature dependence from the minimum of the scalar field will result in a speed sound that is function of the model parameters and its form will depend on the overall shape of the potential.

D.2 Results for toy model

Here we show the different levels of diligence in calculating the thermal parameters and the gravitation wave spectrum in the toy model. The analysis involves

individual scans over the different model parameters (E, D, λ, T_0) while holding the others fixed. A full analysis of the toy model should involve a randomized scan over all of the parameters but we perform the scan this way in hopes to see any trends in varying the different model parameters. In Eq. D.4, the critical temperature is a function of all four model parameters. For this reason, T_C will be used as a basis for each scan. The first step in the beyond the bag calculations is to compute the speed of sound in the symmetric and broken phase. For the toy model, we only consider detonation, $v_w = 0.92$, where the speed of sound in the symmetric phase is set to $c_s^2 = 1/3$ and the degrees of freedom consist of only the standard model sector. The speed of sound in the broken phase may be found through Eq. 5.23. The transition temperatures for the different levels of diligence are T_n (5.4), T_p (5.11), and T_f (4.70). Example calculations for various phase transition quantities used in the high diligence calculations such as the false vacuum fraction, mean bubble separation, lifetime of the source, and T_f in the toy model may be found in Ref. [361].

In Fig. D.1, we calculate the speed of sound in the broken phase for each level of diligence. The gray dashed line corresponds to $c_s^2 = 1/3$. This involves first calculating the speed of sound as a function temperature using Eq. 5.23 and then evaluating it at (T_n, T_p, T_f) computed in the different levels of diligence. We note that in computing the strength of the phase transition only the highest diligence level will involve this calculation. This is merely to show the level of variance in computing the speed of sound at different temperature stages. For specific values and range chosen, there is only minor change to the speed of sound

computed in the different levels however how much variance is present is strongly model dependent. We do notice that the speed of sound can have a significant deviation away from $c_s^2 = 1/3$ in the bag model. The strongest deviation is caused by varying the barrier term, E, and the quadratic multiplicity term, D as seen in the green and purple curves. The speed of sound can go as low as $c_s^2 \sim 0.22$ and as high as $c_s^2 \sim 0.36$. Varying the zero temperature mass term, T_0, did not have any noticeable impact on the speed of sound while the quartic coupling term, λ, had a mild impact on the speed of sound. This is likely due to the temperature independence of the terms that involve T_0 and λ. The parameters D and E on the other hand, multiply T^2 and T respectively and will result in a change in the temperature dependence. The speed of sound in the broken phase is related to the temperature derivatives of the pressure which is evaluated at $p_b(T) = V_{\text{eff}}(\phi_{\min}(T), T)$ and hence D and E will impact the minimum at finite temperature. The smallest speed of sound in the broken phase corresponds to small E and large D.

We show in Fig. D.2 the phase transition strength computed in the different level of diligence (left) and the comparison between α_θ computed in the bag model versus $\alpha_{\bar{\theta}}$ computed in the beyond the bag model at T_f for both quantities (right). We see in the left figure that going higher in the level of diligence results in an increase in the phase transition strength compared to lowest diligence. This can be attributed to more vacuum energy being released at T_p compared to T_n. On the right, to better compare the difference between the bag model and the beyond the bag model, we compute the ratio of α_θ and $\alpha_{\bar{\theta}}$ computed at the same temperature,

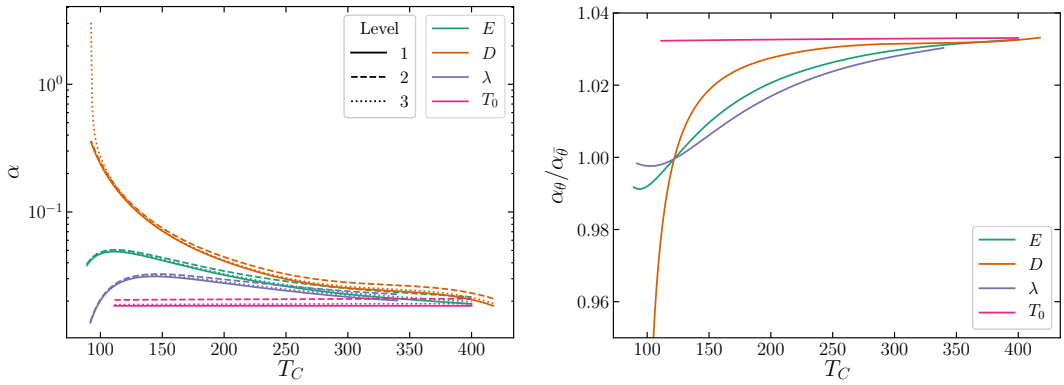

Figure D.2: Left: The strength of phase transition computed at the different levels of diligence. Right: The ratio of strength of the phase transition computed at T_f for the bag model α_θ and the beyond the bag model $\alpha_{\bar{\theta}}$.

T_f. For $T_c < 100$, α_θ is less than $\alpha_{\bar{\theta}}$ which is the result of $c_s^2 < 1/3$ as seen in Fig. D.1. This has to do with the $(1 + c_s^{-2})$ factor in $\alpha_{\bar{\theta}}$. When $T_c > 100$, we see that the opposite is true when $c_s^2 > 1/3$. Similarly, the largest deviations are due to the parameters D and E.

The error in the gravitational wave spectrum of the toy model for different scans in the model parameters is shown in the left of Fig. D.3. The lowest and modest diligence peak gravitational wave energy density Ω_{GW} is calculated using Eq. 5.7 and Eq. 5.15 respectively. The comparison in error is computed with respect to the highest diligence in Eq. 5.37. The lowest diligence level has error in the range $\Delta\Omega/\Omega \sim [10^1, 10^3]$ for all parameter scans. The modest diligence level is closest to the highest diligence with error in the range $\Delta\Omega/\Omega \sim [10^0, 10^1]$ for the different scans. The highest error occurs for $T_C \sim 100$. This is related to beyond the bag effects which exhibited suppression for the scans in (E, D).

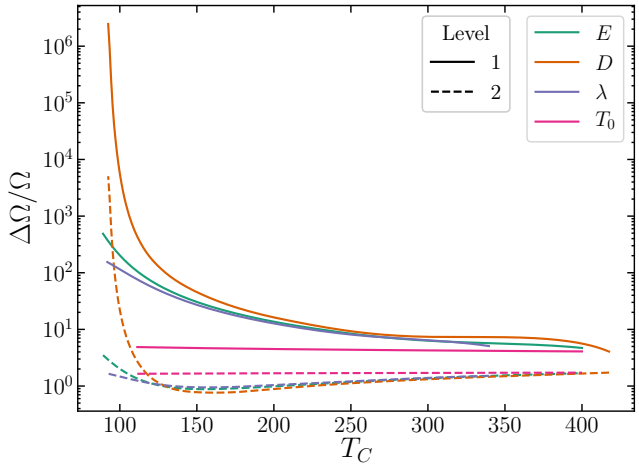

Figure D.3: Error of the gravitational spectrum computed at the different levels of diligence.

Appendix E

Perturbative Unitarity S Matrix

We consider a total of eleven $2 \to 2$ channels of scalars and longitudinal gauge bosons scatterings. These are grouped into seven charge neutral channels ($h_1h_1, h_2h_2, h_1h_2, h_1Z, h_2Z,$ three charge-1 channels (h_1W^+, h_2W^+, ZW^+) and one charge-2 channel (W^+W^-). The leading partial wave amplitudes of these scatterings are given collectively by a symmetric matrix, which itself is a direct sum of the matrices from these three groups: $\mathcal{S} = \mathcal{S}_0 \bigoplus \mathcal{S}_1 \bigoplus \mathcal{S}_2$. The tree level perturbative unitarity requires that the absolute value of each eigenvalue of this matrix is less than $(1/2 \times 16\pi)$. The non-zero elements of the 7×7 matrix $\mathcal{S}_0$ is listed as follows(see e.g., Ref. [430] for

a detailed calculation):

$$
\begin{aligned}
\mathcal{S}_{11} &= -3\left(a_2 c_\theta^2 s_\theta^2 + b_4 s_\theta^4 + \lambda c_\theta^4\right), \\
\mathcal{S}_{12} &= \frac{1}{8}\left(3\cos(4\theta)\left(-a_2 + b_4 + \lambda\right) - a_2 - 3b_4 - 3\lambda\right), \\
\mathcal{S}_{13} &= \frac{3\sin(2\theta)\left(\cos(2\theta)\left(-a_2 + b_4 + \lambda\right) - b_4 + \lambda\right)}{2\sqrt{2}}, \\
\mathcal{S}_{16} &= -\frac{1}{2}a_2 s_\theta^2 - \lambda c_\theta^2, \\
\mathcal{S}_{17} &= -\frac{a_2 s_\theta^2 + 2\lambda c_\theta^2}{\sqrt{2}}, \\
\mathcal{S}_{22} &= -3\left(a_2 c_\theta^2 s_\theta^2 + b_4 c_\theta^4 + \lambda s_\theta^4\right), \\
\mathcal{S}_{23} &= -\frac{3\sin(2\theta)\left(\cos(2\theta)\left(-a_2 + b_4 + \lambda\right) + b_4 - \lambda\right)}{2\sqrt{2}}, \\
\mathcal{S}_{26} &= -\frac{1}{2}a_2 c_\theta^2 - \lambda s_\theta^2, \\
\mathcal{S}_{27} &= -\frac{a_2 c_\theta^2 + 2\lambda s_\theta^2}{\sqrt{2}}, \\
\mathcal{S}_{33} &= \frac{1}{4}\left(3\cos(4\theta)\left(-a_2 + b_4 + \lambda\right) - a_2 - 3b_4 - 3\lambda\right), \\
\mathcal{S}_{36} &= \frac{\left(2\lambda - a_2\right) c_\theta s_\theta}{\sqrt{2}}, \\
\mathcal{S}_{37} &= \left(2\lambda - a_2\right) c_\theta s_\theta, \\
\mathcal{S}_{44} &= -a_2 s_\theta^2 - 2\lambda c_\theta^2, \\
\mathcal{S}_{45} &= \left(2\lambda - a_2\right) c_\theta s_\theta, \\
\mathcal{S}_{55} &= -a_2 c_\theta^2 - 2\lambda s_\theta^2, \\
\mathcal{S}_{66} &= -3\lambda, \\
\mathcal{S}_{67} &= -\sqrt{2}\lambda, \\
\mathcal{S}_{77} &= -4\lambda.
\end{aligned}
\tag{E.1}
$$

For charge-1 channels, we have:

$$\mathcal{S}_1 = \begin{bmatrix} -2\lambda c_\theta^2 - a_2 s_\theta^2 & (2\lambda - a_2)\, c_\theta s_\theta & 0 \\ (2\lambda - a_2)\, c_\theta s_\theta & -a_2 c_\theta^2 - 2\lambda s_\theta^2 & 0 \\ 0 & 0 & -2\lambda \end{bmatrix}.$$

For the charge-2 channel with only one process, the matrix is simply given by $\mathcal{S}_2 = (-2\lambda)$.

Appendix F

Connection with Potential where $v_s = 0$

The potential in Eq. 3.1 can be written into a different form by translating the coordinate system of (H, S) such that the EW vacuum has $\langle S \rangle = 0$ (see e.g., [225]). In this basis, there will generally be an additional tadpole term $(b_1 S)$. Making this translation of field variables leads to the same potential being represented with different potential parameters, without changing the physics [223]. So the scalar couplings as well as their masses and mixing angles wont be affected by this translation. For easy comparison between these two representations, we show here the transformation rules between these two bases. Given potential parameters in the non-tadpole basis in Eq. 3.1, the parameters in the basis where $b_1 \neq 0$(denoted with a prime) can be obtained:

$$
\begin{aligned}
b_1' &= v_s(b_2 + v_s(b_3 + b_4 v_s)), \\
b_2' &= b_2 + v_s(2b_3 + 3b_4 v_s), \\
b_3' &= b_3 + 3b_4 v_s, \\
\mu^{2\prime} &= \mu^2 - \frac{1}{2} v_s(a_1 + a_2 v_s), \\
a_1' &= a_1 + 2a_2 v_s,
\end{aligned}
\tag{F.1}
$$

while a_2, λ, b_4 remains unchanged. On the other hand, given parameters in the tadpole basis where $v_s = 0$ and $b_1 \neq 0$, the parameter set in the basis used in this

work can be found:

$$
\begin{aligned}
v_s &= x, \\
b_2 &= b_2' - x(2b_3' - 3b_4' x), \\
b_3 &= b_3' - 3b_4' x, \\
\mu^2 &= \mu^{2\prime} + \frac{1}{2} x(a_1' - a_2' x), \\
a_1 &= a_1' - 2a_2' x,
\end{aligned}
\tag{F.2}
$$

where x is to be solved from the cubic equation

$$
b_1' - b_2' x + b_3' x^2 - b_4' x^3 = 0, \tag{F.3}
$$

which might give more than one solutions. In the basis $v_s = 0$, the degree of freedom carried by v_s in the basis $v_s \neq 0$ is transformed to a different parameter. For example, one can choose it to be a_2 and then the full set of independent parameters can be chosen as

$$
a_2, \qquad m_{h_2}, \qquad \theta, \qquad b_3, \qquad b_4. \tag{F.4}
$$

We note further there are also studies of this model where a Z_2 symmetry in the S fields are imposed and are spontaneously broken [234, 221, 236]. This specific model correspond to a special limit of the potential here.

Appendix G

Einstein Tensor

We start with the metric as follows,

$$g_{\mu\nu} = \begin{bmatrix} -B(r) & 0 & 0 & 0 \\ 0 & A(r) & 0 & 0 \\ 0 & 0 & r^2 & 0 \\ 0 & 0 & 0 & r^2\sin^2\theta \end{bmatrix}. \tag{G.1}$$

We can then write out the non-zero Christoffel symbol components as

$$\begin{aligned} \Gamma^t_{tr} &= \frac{B'(r)}{2B(r)}, & \Gamma^r_{tt} &= \frac{B'(r)}{2A(r)}, \\ \Gamma^r_{rr} &= \frac{A'(r)}{2A(r)}, & \Gamma^r_{\theta\theta} &= -\frac{r}{A(r)}, & \Gamma^r_{\phi\phi} &= -\frac{r\sin^2(\theta)}{A(r)}, \\ \Gamma^\theta_{r\theta} &= \frac{1}{r}, & \Gamma^\theta_{\phi\phi} &= -\cos(\theta)\sin(\theta), \\ \Gamma^\phi_{r\phi} &= \frac{1}{r}, & \Gamma^\phi_{\theta\phi} &= \cot(\theta), \end{aligned} \tag{G.2}$$

from which the Einstein tensor G^ν_μ can be calculated

$$\begin{aligned} G^t_t &= -\frac{A'(r)}{rA(r)^2} + \frac{1}{r^2A(r)} - \frac{1}{r^2}, \\ G^r_r &= \frac{B'(r)}{rA(r)B(r)} + \frac{1}{r^2A(r)} - \frac{1}{r^2}, \\ G^\theta_\theta &= -\frac{A'(r)B'(r)}{4A(r)^2B(r)} - \frac{A'(r)}{2rA(r)^2} + \frac{B''(r)}{2A(r)B(r)} - \frac{B'(r)^2}{4A(r)B(r)^2} + \frac{B'(r)}{2rA(r)B(r)}, \\ G^\phi_\phi &= -\frac{A'(r)B'(r)}{4A(r)^2B(r)} - \frac{A'(r)}{2rA(r)^2} + \frac{B''(r)}{2A(r)B(r)} - \frac{B'(r)^2}{4A(r)B(r)^2} + \frac{B'(r)}{2rA(r)B(r)} \end{aligned} \tag{G.3}$$

Appendix H

Numerical Procedure

Typically the equations of motion are solved using the shooting method which is successful in the one scalar case where the solution can easily converge to the ground state configuration. The equations get numerically difficult to solve when extra scalars are introduced, particularly in the nonlinear regime where λ can have significant contribution to the total mass. A workaround was found by implementing a relaxation algorithm into our personal code which proved successful in solving the differential equations.

H.1 Relaxation Method

To find numerical solutions, we use the relaxation algorithm described in chapter 18 of *Numerical Recipes* [386]. We first write the system in the standard form

$$\mathbf{y}'(t) = \mathbf{g}(t, \mathbf{y}). \tag{H.1}$$

. We want to solve this system over the interval $[a, b]$. We start with a trial solution $\bar{\mathbf{y}}$ that satisfies all boundary conditions. Then we choose a set of evenly spaced points $\{t_k\}_{k=0}^{M-1}$ spanning the interval. At each point except for t_0, we form the difference equations

$$\mathbf{E}_k = \bar{\mathbf{y}}(t_k) - \bar{\mathbf{y}}(t_{k-1}) - (t_k - t_{k-1})\mathbf{g}(t_{\text{av}}, \bar{\mathbf{y}}_{\text{av}}), \tag{H.2}$$

where t_{av} and $\bar{\mathbf{y}}_{\text{av}}$ are the averages of t_k and t_{k-1}, and $\bar{\mathbf{y}}(t_k)$ and $\bar{\mathbf{y}}(t_{k-1})$ respectively. We want to adjust our trial solution so that each $\mathbf{E}_k$ vanishes. Let $\Delta\bar{\mathbf{y}}(t)$ represent the adjustments we need to make to the trial solutions at each of the grid points so that

$$\mathbf{E}_k\big(\bar{\mathbf{y}}(t_{k-1}) + \Delta\bar{\mathbf{y}}(t_{k-1}), \bar{\mathbf{y}}(t_k) + \Delta\bar{\mathbf{y}}(t_k)\big) = 0. \tag{H.3}$$

We can approximate $\Delta\bar{\mathbf{y}}(t)$ at each of the grid points by expanding $\mathbf{E}_k$ as a first-order Taylor series in $\Delta\bar{\mathbf{y}}$. Then we have

$$\begin{aligned}\mathbf{0} &= \mathbf{E}_k\big(\bar{\mathbf{y}}(t_{k-1}) + \Delta\bar{\mathbf{y}}(t_{k-1}), \bar{\mathbf{y}}(t_k) + \Delta\bar{\mathbf{y}}(t_k)\big) \\ &\approx \mathbf{E}_k\big(\bar{\mathbf{y}}(t_{k-1}), \bar{\mathbf{y}}(t_k)\big) + \sum_{n=0}^{N-1} \frac{\partial \mathbf{E}_k}{\partial \bar{y}_n(t_{k-1})} \Delta\bar{y}_n(t_{k-1}) + \sum_{n=0}^{N-1} \frac{\partial \mathbf{E}_k}{\partial \bar{y}_n(t_k)} \Delta\bar{y}_n(t_k),\end{aligned} \tag{H.4}$$

where N is the dimension of $\mathbf{y}$ and $\bar{y}_n(t_k)$ is the nth component of $\bar{\mathbf{y}}(t_k)$. Since we already know $\mathbf{E}_k\big(\bar{\mathbf{y}}(t_{k-1}), \bar{\mathbf{y}}(t_k)\big)$, this gives us $N \cdot (M-1)$ equations for $N \cdot M$ unknowns. The remaining N equations come from the boundary conditions.

These equations, together with the boundary conditions, allow us to solve for the first-order corrections $\Delta\bar{\mathbf{y}}(t_k)$. By adding these corrections to $\bar{\mathbf{y}}(t)$, we obtain a new trial solution. We then iteratively repeat this process with the new trial solution until the trial solutions converge. We determine convergence by measuring the average size of the components of the correction vectors $\Delta\bar{\mathbf{y}}(t_k)$. Once the average size of the corrections becomes small enough, we assume that the trial solutions have converged to the correct solution.

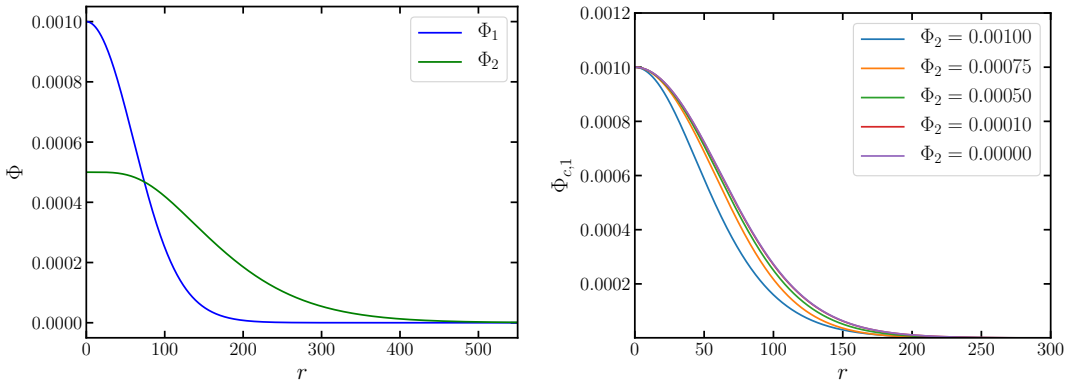

Figure H.1: The left figure includes the wave forms for Φ_1 and Φ_2. The right figure fixes $\Phi_1(0) = 0.001$ and shows the effect of changing $\Phi_2(0)$. For $\Phi_2(0) \ll \Phi_1(0)$ the profiles behave like the one scalar case with $\Phi_c = 0.001$. When $\Phi_1(0) < \Phi_{2,1}$ we see a difference compared to the single boson case. Calculations were performed with $\lambda_1 = \lambda_2 = \lambda_{12} = 1$, $m_1 = 10^{-10}$ GeV, and $\widetilde{m}_r = 0.5$.

H.2 Static Case

The profiles for $A, B, \Phi_1, \Phi_2, \Phi_1'$,and Φ_2' are found by solving the equations of motion using the relaxation method. The boundary conditions at the origin and

at infinity are given by

$$\Phi_n(0) = \Phi_{\mathrm{c,n}} \tag{H.5}$$

$$\Phi_n'(0) = 0 \tag{H.6}$$

$$A(0) = 0 \tag{H.7}$$

$$B(0) = B_0 \tag{H.8}$$

$$\lim_{r\to\infty} \Phi_n(r) = 0 \tag{H.9}$$

$$\lim_{r\to\infty} \Phi_n'(r) = 0 \tag{H.10}$$

$$\lim_{r\to\infty} B(r) = \frac{1}{A(r)}. \tag{H.11}$$

For appropriate choices of the eigenvalues $\mu_{1,2}$ we can find the ground state configurations for $\Phi_{1,2}$. Although $\Phi_{1,2}$ must satisfy all of the boundaries conditions above, we can introduce constant differential equations to the equation of motion for the parameters of the problem without changing the physics of the system. This allows us to exploit the iterative process of the relaxation method to guess the values for $\mu_{1,2}$ until they converge to correct values as $r \to \infty$. We do this by including the following differential equations for $\mu_{1,2}$ into the relaxation method

$$\frac{d\mu_n}{dr} = 0, \text{ n =1,2} \tag{H.12}$$

which allows in total 6 differential equations and 13 boundary conditions to be met. The numerical procedure to solve the equations of motion is as follows:

1. Choose an initial guess for $A, B, \Phi_{1,2}, \Phi_{1,2}'$ that satisfies the boundary conditions.

2. Run relaxation method on an interval $[0, r_{\mathrm{out}}]$

3. If the error begins to diverge, recursively try a smaller interval and use that as an initial guess until it finds a solution.

4. If $\Phi_{1,2} < 0$ or $\Phi'_{1,2} > 0$, try again on a smaller interval with more grid points because an excited state was found.

5. Check if $\Phi_{1,2}(r_{\rm out}) < \epsilon$ where ϵ is a percentage of the initial central density. If true, $\Phi_{1,2}$ has decayed to its asymptotic value at $r_{\rm out} = \infty$ and the ground state has been found.

6. If condition 5 is not met increase $r_{\rm out}$ and start from 2.

Once the ground state solutions are found for Φ_1 and Φ_2, the initial value of B_0 and the eigenvalues, μ_1 and μ_2 will be found to guarantee the boundary values are met. A sample plot of $\Phi_{1,2}$ is included in Fig. H.1. The left figure is a representative plot of the wave profiles for Φ_1 and Φ_2. The equations of motion couple both scalars together. We can see from the right figure the impact the second scalar has on Φ_1 by varying its central density. For $m_1 = 10^{-10}$ eV and $\widetilde{m}_r = 0.5$, the equation of motions look like the single scalar case when $\Phi_2(0) \ll \Phi_1(0)$. However, when $\Phi_2(0) \sim \Phi_1(0)$, the wave profile of Φ_1 deviates from the single scalar case as expected.

H.3 Time Evolution

To ensure the stability of the equations of motion, we must first check how the equations of motion evolve under small radial perturbations. We first approximate

the partial derivatives in the equations motion as central finite differences :

$$\frac{\partial f}{\partial r} = \frac{f^i_{j+1}(r,t) - f^i_{j-1}(r,t)}{2\Delta r}, \tag{H.13}$$

$$\frac{\partial f}{\partial t} = \frac{f^{i+1}_{j}(r,t) - f^i_{j}(r,t)}{\Delta t}, \tag{H.14}$$

$$\frac{\partial^2 f}{\partial r^2} = \frac{f^i_{j+1}(r,t) - 2f^i_{j}(r,t) + f^i_{j-1}(r,t)}{\Delta r^2}, \tag{H.15}$$

$$\frac{\partial^2 f}{\partial t^2} = \frac{f^{i+1}_{j}(r,t) - 2f^i_{j}(r,t) + f^{i-1}_{j}(r,t)}{\Delta t^2}, \tag{H.16}$$

where i and j correspond to steps in space and time respectively. The step sizes are given by Δr and Δt. We note that these expressions are only valid for $i \in [1, N_t - 1]$ and $j \in [1, N_r - 1]$ where $i = 0, ..., N_t$ and $j = 0, ..., N_r$. For the endpoints we use either backwards or forward difference. Using finite differences we see that the two Klein-Gordon equations of motion give

$$\Phi^{i+1}_{j,(1,2)} = 2\Phi^{i}_{j,(1,2)} - \Phi^{i-1}_{j,(1,2)} + \Delta t^2 F\left(r, A, B, \Phi_1, \Phi_2, , A', B', \Phi_1', \Phi_2'\right). \tag{H.17}$$

To find the time evolution of the system we perform the following steps:

1. Solve the static equations of motion.

2. Perturb $\Phi_{1,2}$ by a factor of $(1 + \epsilon)$.

3. Perform the first time step in the Klein-Gordon equations for $\Phi_{1,2}$ using Eq H.17 where the static solution is $\Phi^{i-1}_{j,(1,2)}$ and the perturbed solution is $\Phi^{i}_{j,(1,2)}$.

4. Perturb $\Phi_{1,2}$ by a factor of $(1 + \epsilon)$.

5. Solve the remaining two differential equations using the Relaxation Method to get A_j^{i+1} and B_j^{i+1}.

6. Repeat.

Sufficient time steps were performed following the above procedure to ensure the stability of the time evolution equations for sample benchmark points.

The physical time, t, used in the equations of motion is in units of m^{-1} with the corresponding dimensionless time, $\widetilde{t}$, given by

$$t = \frac{1}{m}\widetilde{t}. \tag{H.18}$$

The time evolution of the single scalar case was previously studied in [156] for both the stable and unstable branch with different re-scaled quantities. To match with the notation there, we compare our dimensionless variable with the ones used in [156]. The potential used in the analysis considers the non-relativistic interaction term

$$V_{nr} = \frac{\psi^{*2}\psi^2}{16f^2} \tag{H.19}$$

with the following ansatz for the scalar field

$$\Phi = \frac{1}{\sqrt{m}}\Psi(r) = \sqrt{\frac{N}{\pi m R^3}}e^{-r/R} \tag{H.20}$$

where R is the decay length scale and N is the total number of particles. The re-scaled quantities are

$$\begin{aligned} R &= \frac{M_{Pl}}{mf}\hat{R} \\ N &= \frac{M_{Pl}f}{m^2}\hat{N} \\ \Psi &= \frac{\sqrt{m}f^2}{M_{Pl}}\hat{\Psi}, \end{aligned}$$

where $\hat{X}$ is the dimensionless counterpart of variable X used in [156]. The corresponding time evolution equation of the scalar field in dimensionless units is

$$i\frac{\partial\hat{\Psi}}{\partial\hat{t}} = -\frac{1}{2\hat{r}}\frac{\partial^2}{\partial\hat{r}^2}\left(\hat{r}\hat{\Psi}\right) + \hat{\phi}_N\hat{\Psi} - \frac{1}{8}|\hat{\Psi}|^2\hat{\Psi} \tag{H.21}$$

where $\hat{\phi}_N$ is the newtonian potential. If we restore the physical parameters in the above equation, the physical time will become

$$t = \frac{M_{Pl}^2}{mf^2}\,\hat{t}. \tag{H.22}$$

This allows for simple comparison by setting the physical times equal to each other. The scalar field is related by

$$\widetilde{\Phi} = \frac{\sqrt{4\pi}f^2}{M_{Pl}^2}\hat{\Psi}. \tag{H.23}$$

Appendix I

Single Scalar Limit

In this section we verify that in the limit of $m_1 = m_2$, and $\lambda_1 \sim \lambda_2$, one recovers the single scalar limit as expected. In the non-relativistic section it was stated that the scalar limit occurs when one of the number densities dominates over the other. The number density in the non-relativistic limit is given by

$$N_i = 4\pi \int dr r^2 m_i |\Phi_i(r)|^2 \tag{I.1}$$

where the index $i = 1, 2$ corresponds to each scalar, and the integral is over the scalars central density. This is related to the mass of the star for the two scalar system as

$$M = m_1 N_1 + m_2 N_2. \tag{I.2}$$

The single scalar limit is taken for when $\Phi_2(0) \gg \Phi_1(0)$ and vice versa. In Fig. I.1 we show that the single scalar limit can be recovered when $\Phi_1(0)$ is chosen to be small. In Fig. I.2, we show C_2 versus M_2 for the second scalar's contribution to the BEC system mass and compactness where we scan over $\Phi_2(0)$ for different values of fixed $\Phi_1(0)$. The curves represent scans over the two central densities. Each curve for the two scalar scans begin with $\Phi_2(0) \ll \Phi_1(0)$ on the far left points. The curves all begin with masses much below the single scalar limit which means that the second scalar contribuion to the total mass of the star is subdominate and we can safely assume $N_2 \ll N_1$. Each one of the curves eventually lead towards the single scalar limit when $\Phi_2(0)$ grows larger. This behavior confirms the analytical

approximationa of the single scalar limits to determine the nonlinear and linear regimes done in section 6.1.6.

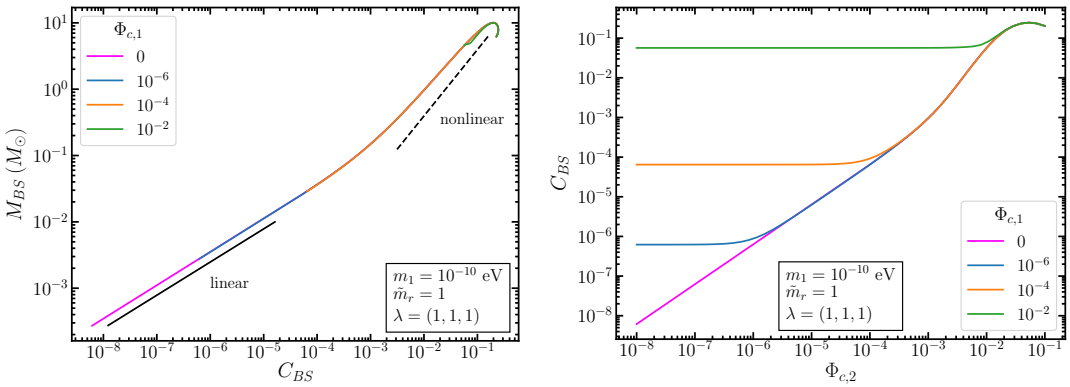

Figure I.1: BEC structure obtained with equal mass for the two scalars and different fixed central density of one scalar, $\Phi_{1,c}$, and different coupling choices. Left: the total mass vs compactness for various $\Phi_1(0)$ and $\Phi_2(0)$ for $\lambda_1 = 1$, $\lambda_2 = 1$, and $\lambda_{12} = 1$. The solid lines correspond to fixed $\Phi_1(0)$ while scanning over $\Phi_2(0)$. The solid magenta curve corresponds to the single scalar limit by setting $\Phi_1(0) = 0$ and scanning over $\Phi_2(0)$. The solid and dashed black lines represent the linear and nonlinear scaling cases when M_{BS} is derived from Eq. 6.19. Right: the compactness versus $\Phi_2(0)$ for different values of $\Phi_1(0)$. It plateaus to a fixed value of C_{BS} when $\Phi_2(0)$ is small and the star is dominated by Φ_1.The turning point occurs when $\Phi_2(0) \approx \Phi_1(0)$

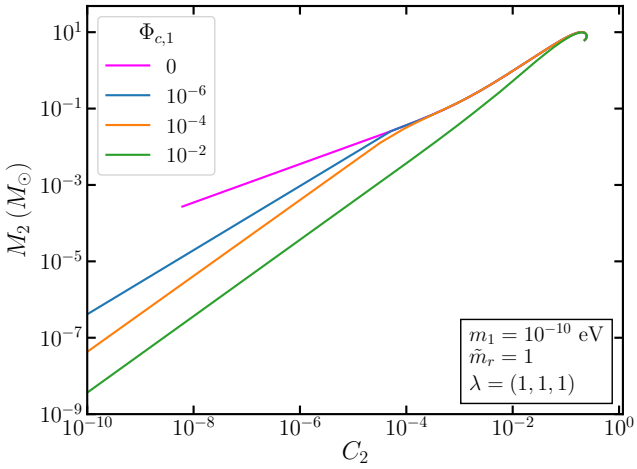

Figure I.2: The changes to a single scalar BEC profile due to the existence of another scalar with varying central density. The mass versus compactness only taking into consideration the contribution from Φ_2. The single scalar limit is given by the blue curve. The other curves at scanning over $\Phi_2(0)$ at different fixed values of $\Phi_1(0)$.

Appendix J

Transitioning from Φ_1 to Φ_2 in the Nonlinear Regime

We numerically verify that in the nonlinear regime, the transition between ϕ_1 dominating to ϕ_2 dominating still happens as expected. As seen in Section 6.1.6, a two scalar hierarchy $m_1 < m_2$ interpolates two scenarios where Φ_1 dominates the system ($N_1 \gg N_2$,) and that where Φ_2 dominates ($N_2 \gg N_1$.) We verify that this transitioning behavior still persists in the nonlinear regime.

One observes that when one scalar has a stable nonlinear self-interaction (e.g. $+\phi^4$,) and the other unstable self-interaction (e.g. $-\phi^4$,) once the system transitions from the unstable scalar dominating to the stable scalar dominating, it is then stabilized, and vice versa. This can be see in Fig. J.1. Another way of seeing this transitioning effect is through a less drastic setup, with $\lambda_1, \lambda_2 > 0$ but have different values. The $C - M$ curve has different shape if Φ_1 or Φ_2 forms BEC alone. In the two scalar system, by arranging $\Phi_1(0)$ and $\Phi_2(0)$ carefully, one can get any point in between the two curves shown as the shaded region in Fig. J.2.

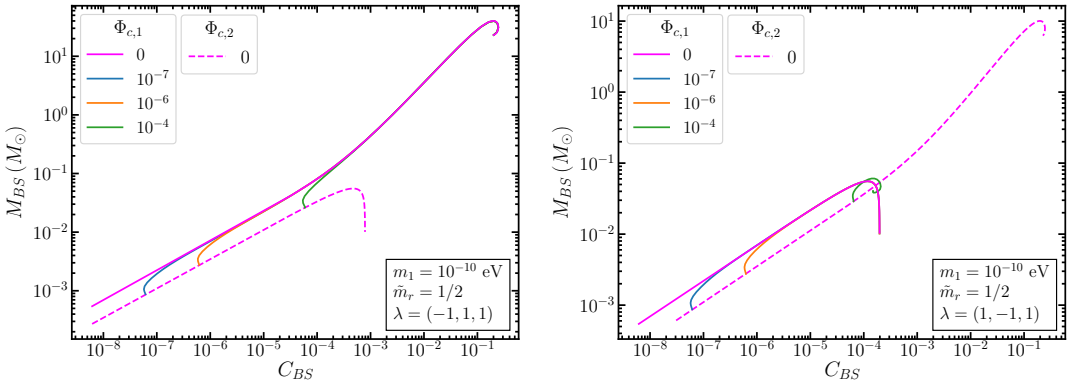

Figure J.1: The total mass vs compactness for various values of $\Phi_1(0)$ and $\Phi_2(0)$, with $\lambda_1 = -1$, $\lambda_2 = 1$ (left) and $\lambda_1 = 1$, $\lambda_2 = -1$ (right). All solid curves are generated by scanning over $\Phi_2(0)$ and fixing $\Phi_1(0)$ at labeled values, while the dashed curve is setting $\Phi_2(0)$ to zero and scanning over $\Phi_1(0)$.

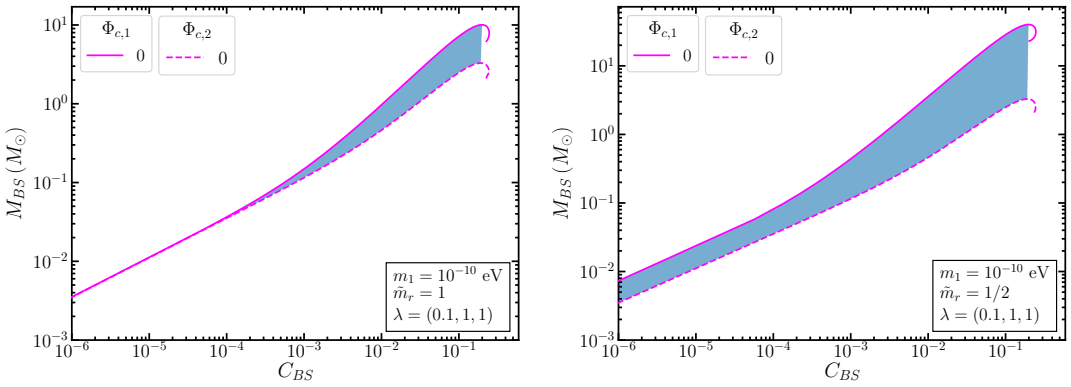

Figure J.2: The mass profile of the BEC with $\lambda_1 = 0.1$, $\lambda_2 = 1$, and $\lambda_{12} = 1$. The mass ratio between the two scalars is $\widetilde{m}_r = 1$ in the left figure and $\widetilde{m}_r = 1/2$ in the right figure. The shaded region is the region a stable BEC system can form.

Appendix K

Explicit Potentials

To keep the discussion as general as possible, we have avoided specifying a potential. In this appendix, we discuss Q-balls in both gauge-mediated and gravity-mediated scenarios.

In the gauge-mediated supersymmetric scenario the potential is

$$V(\Phi) = m^4 \log\left(1 + \frac{|\Phi|^2}{m^2}\right) + \frac{1}{\Lambda^2}|\Phi|^6, \tag{K.1}$$

plus a small CP-violating term. When the second term is negligible, the resulting Q-balls are thick wall Q-ball [411], for which the analysis presented here is inapplicable. However, scaling arguments favor a Q-ball domination epoch. Fragmentation tends to produce one large Q-ball in each Hubble volume [410], resulting in a sharply peaked mass distribution at large masses, which tend to be long-lived. Furthermore, the radius now scales as $Q^{1/4}$, and after accounting to the scalings of the VEV and energy per unit charge with Q, we expect the Q-ball decay rate to scale as $Q^{1/4}$. This is suppressed compared to the thin-wall rate, and therefore, the Q-balls will tend to be longer-lived. $\Gamma_{\mathrm{Q-ball}}/HQ$ then scales as $Q^{-3/4}$, which increases as the charge decreases, leading to the rapid matter-to-radiation transition. We plan to address this scenario more fully in future work.

When the second term in (K.1) is not negligible, then the resulting Q-balls are in the thin wall regime, although since the energy per charge ω is independent of the charge Q, the equilibrium state is not one Q-ball per Hubble volume.

Alternatively, one can consider gravity-mediated SUSY breaking, in which case the Affleck-Dine condensate has the potential

$$V(\Phi) = m^2|\Phi|^2\left(1 + K\log\left(\frac{|\Phi|^2}{m^2}\right)\right) + \frac{1}{\Lambda^2}|\Phi|^6, \tag{K.2}$$

where Λ is an effective scale for the higher-dimensional operator, m is the mass of the scalar field, and $K \approx -0.01$ to -0.1 is a one-loop correction. Since $K < 0$, Q-balls can be formed, and in the thin wall limit, the VEV inside the Q-ball is given by [190]

$$v \approx \left(\Lambda M_{\rm Pl}\sqrt{\frac{|K|}{2}}\right)^{1/2}, \tag{K.3}$$

from which an expression for ω can be found.

In Table K.1 we show one choice of parameters for the gauge-mediated potential (left) and gravity-mediated potential (right) for each benchmark set of parameters discussed in the text. That is, in each row the Q-balls produced have the same VEV v and energy-per-unit-charge ω as in corresponding row in Table 7.1. For the gauge-mediated scenario, we have ensured that the sixth order term is relevant so that we are in the thin-wall regime. We see that in all cases the scale of the effective operator, Λ, is well above the reheating temperature.

Gauge-Mediated		Gravity-Mediated	
m (GeV)	Λ (GeV)	m (GeV)	Λ (GeV)
6.07×10^7	4.54×10^{15}	2.16×10^6	4.23×10^{15}
1.76×10^7	1.10×10^{13}	1.13×10^6	2.07×10^{13}
3.61×10^7	1.35×10^{14}	1.63×10^6	2.01×10^{14}

Table K.1: Parameters for the potentials (K.1) and (K.2) which produce Q-balls corresponding to our three benchmark points. The first row corresponds to our first benchmark in Table 7.1, the second row corresponds the second benchmark, and the third corresponds to the third. For the gravity-mediated scenario, we have fixed $k = -0.05$.

Appendix L

Supplementary material

We here outline the gravitational wave spectrum from an instantaneous transition from matter to radiation domination, following Ref [419]. We define the following functions:

$$s_0(x, x_{\rm max}) = \left(\Theta\left[\frac{2x_{\rm max}}{1+\sqrt{3}} - x\right] + \left(2\frac{x_{\rm max}}{x} - \sqrt{3}\right)\right.$$
$$\left.\Theta\left[x - 2\frac{x_{\rm max}}{1+\sqrt{3}}\right]\Theta\left[2\frac{x_{\rm max}}{\sqrt{3}} - x\right]\right) \times \Theta\left[2\frac{x_{\rm max}}{\sqrt{3}} - x\right], \tag{L.1}$$

along with

$$S_i(x) = \int_0^x dz \frac{\sin z}{z}, \qquad C_i(x) = -\int_x^\infty dz \frac{\cos z}{z}\ . \tag{L.2}$$

The gravitational wave spectrum involves a resonant contribution, $\Omega_{\rm res}$, an infrared contribution, $\Omega_{\rm IR}$, and a non-resonant UV contribution, $\Omega_{\rm UV}$, such that the total spectrum is given by

$$\Omega_{\rm GW}(x, x_{\rm max}) = \Omega_{\rm res} +$$
$$3A_s^2 x_{\rm max}^8 \frac{4C_i[\frac{x}{2}]^2 + (\pi - 2S_i[\frac{x}{2}])^2}{2^{17+2n_s}625(3+2n_s)} \left(\frac{2x_{\rm max}}{x} - 1\right)^{2n_s}$$
$$\times \left(\frac{x}{x_*}\right)^{2(n_s-1)} \left(\Omega_{\rm IR}\Theta[x_{\rm max} - x] + \Omega_{\rm UV}\Theta\left[x - x_{\rm max}\right]\right), \tag{L.3}$$

where we define $X \equiv x/x_{\rm max}$ to write

$$\begin{aligned}
\Omega_{\rm IR} &= \frac{1}{(2+n_s)(3+n_s)(4+n_s)(5+2n_s)(7+2n_s)} \\
&\times \big(1536 - 6144X + (7168 - 1920n_s - 256n_s^2)X^2 \\
&+(5760n_s + 768n_s^2)X^3 \\
&+(1328n_s + 3056n_s^2 + 832n_s^3 + 64n_s^4)X^4 \\
&- (7168 + 12256n_s + 7392n_s^2 + 1664n_s^3 + 128n_s^4)X^5 \\
&+ (7392 + 10992n_s + 5784n_s^2 + 1248n_s^3 + 96n_s^4)X^6 \\
&- (2784 + 3904n_s + 1960n_s^2 + 416n_s^3 + 32n_s^4)X^7 \\
&+ (370 + 503n_s + 247n_s^2 + 52n_s^3 + 4n_s^4)X^8 \\
&- 256\,(1-X)^6\,[(6 + 6(2+n_s)X \\
&+(2+n_s)(5+2n_s)X^2]\left(1 - \frac{X}{2-X}\right)^{2n_s}\Bigg),
\end{aligned} \tag{L.4}$$

and

$$\begin{aligned}
\Omega_{\rm UV} &= 2\,(2-X)^4\,\Gamma[4+2n_s] \\
&\times \left(\frac{X^4}{\Gamma[5+2n_s]} - \frac{4X^2\,(2-X)^2}{\Gamma[7+2n_s]} + \frac{24\,(2-X)^4}{\Gamma[9+2n_s]}\right), \\
\Omega_{\rm res} &= \frac{2.3\sqrt{3}3^{n_s}}{625\times 2^{13+2n_s}} x^7 X^{2(n_s-1)} A_s^2 s_0(x, x_{\rm max}) \\
&\times \Bigg(4{}_2F_1[\frac{1}{2}, 1-n_s, \frac{3}{2}, \frac{s_0(x,x_{\rm max})^2}{3}] \\
&- 3{}_2F_1[\frac{1}{2}, -n_s, \frac{3}{2}, \frac{s_0(x,x_{\rm max})^2}{3}] \\
&- s_0(x,x_{\rm max})^2{}_2F_1[\frac{3}{2}, -n_s, \frac{5}{2}, \frac{s_0(x,x_{\rm max})^2}{3}]\Bigg)
\end{aligned} \tag{L.5}$$

where ${}_2F_1$ is the hypergeometric function. To convert to a frequency spectrum, simply take $x_* = 1/k_*\eta_r$ and

$$\begin{aligned}\Omega_{\rm GW}(f)h^2 &= 0.39h^2\Omega_r \\ &\times \Omega_{\rm GW}\left[4.1\times10^{-24}\left(\frac{\eta_r}{\rm GeV^{-1}}\right)f, \frac{T_{\rm eq}}{T_{\rm dec}}\right].\end{aligned} \tag{L.6}$$

References

[1] S. Di Vita, G. Durieux, C. Grojean, J. Gu, Z. Liu, G. Panico, M. Riembau, and T. Vantalon, JHEP **02**, 178 (2018).

[2] T. Liu, K.-F. Lyu, J. Ren, and H. X. Zhu, Phys. Rev. **D98**, 093004 (2018).

[3] M. Hindmarsh and M. Hijazi, JCAP **1912**, 062 (2019).

[4] P. M. Schicho, T. V. I. Tenkanen, and J. Österman, (2021).

[5] D. Cutting, M. Hindmarsh, and D. J. Weir, (2019).

[6] H. Deng, M. P. Hertzberg, M. H. Namjoo, and A. Masoumi, Phys. Rev. D **98**, 023513 (2018).

[7] D. C. Rodrigues, A. del Popolo, V. Marra, and P. L. C. de Oliveira, Mon. Not. Roy. Astron. Soc. **470**, 2410 (2017).

[8] C. J. Moore, R. H. Cole, and C. P. L. Berry, Class. Quant. Grav. **32**, 015014 (2015).

[9] S. Kawamura *et al.*, (2020).

[10] C. Caprini *et al.*, JCAP **03**, 024 (2020).

[11] C. Boehm *et al.*, (2017).

[12] J. Garcia-Bellido, H. Murayama, and G. White, (2021).

[13] M. Maggiore *et al.*, JCAP **03**, 050 (2020).

[14] K. Inomata and T. Nakama, Phys. Rev. D **99**, 043511 (2019).

[15] D. Reitze *et al.*, Bull. Am. Astron. Soc. **51**, 035 (2019).

[16] G. Janssen *et al.*, PoS **AASKA14**, 037 (2015).

[17] M. Dine, R. G. Leigh, P. Y. Huet, A. D. Linde, and D. A. Linde, Phys. Rev. D **46**, 550 (1992).

[18] B. P. Abbott *et al.*, Phys. Rev. Lett. **116**, 061102 (2016).

[19] H. Audley *et al.*, (2017).

[20] K. Yagi and N. Seto, Phys. Rev. **D83**, 044011 (2011), [Erratum: Phys. Rev.D95,no.10,109901(2017)].

[21] X. Gong *et al.*, J. Phys. Conf. Ser. **610**, 012011 (2015).

[22] J. Luo *et al.*, Class. Quant. Grav. **33**, 035010 (2016).

[23] A. Klein *et al.*, Phys. Rev. **D93**, 024003 (2016).

[24] S. Babak, J. Gair, A. Sesana, E. Barausse, C. F. Sopuerta, C. P. L. Berry, E. Berti, P. Amaro-Seoane, A. Petiteau, and A. Klein, Phys. Rev. **D95**, 103012 (2017).

[25] C. Caprini *et al.*, JCAP **1604**, 001 (2016).

[26] D. J. Weir, Phil. Trans. Roy. Soc. Lond. **A376**, 20170126 (2018).

[27] A. Mazumdar and G. White, (2018).

[28] G. Bertone *et al.*, (2019).

[29] E. Barausse *et al.*, (2020).

[30] B. P. Abbott *et al.*, Phys. Rev. Lett. **118**, 121101 (2017), [Erratum: Phys.Rev.Lett. 119, 029901 (2017)].

[31] B. Abbott *et al.*, Phys. Rev. D **100**, 061101 (2019).

[32] C. Grojean and G. Servant, Phys. Rev. **D75**, 043507 (2007).

[33] V. Vaskonen, Phys. Rev. **D95**, 123515 (2017).

[34] G. Dorsch, S. Huber, T. Konstandin, and J. No, JCAP **05**, 052 (2017).

[35] A. Beniwal, M. Lewicki, M. White, and A. G. Williams, (2018).

[36] Z. Kang, P. Ko, and T. Matsui, JHEP **02**, 115 (2018).

[37] C. Delaunay, C. Grojean, and J. D. Wells, JHEP **04**, 029 (2008).

[38] M. Chala, C. Krause, and G. Nardini, JHEP **07**, 062 (2018).

[39] S. A. Ellis, S. Ipek, and G. White, JHEP **08**, 002 (2019).

[40] A. Alves, D. Gonçalves, T. Ghosh, H.-K. Guo, and K. Sinha, JHEP **03**, 053 (2020).

[41] A. Alves, T. Ghosh, H.-K. Guo, K. Sinha, and D. Vagie, JHEP **04**, 052 (2019).

[42] J. Ellis, M. Lewicki, J. M. No, and V. Vaskonen, JCAP **06**, 024 (2019).

[43] A. P. Morais and R. Pasechnik, JCAP **04**, 036 (2020).

[44] A. Addazi, A. Marcianò, and R. Pasechnik, MDPI Physics **1**, 92 (2019).

[45] C. Wainwright, S. Profumo, and M. J. Ramsey-Musolf, Phys. Rev. D **84**, 023521 (2011).

[46] R. Zhou, L. Bian, and H.-K. Guo, Phys. Rev. D **101**, 091903 (2020).

[47] J. Bernon, L. Bian, and Y. Jiang, JHEP **05**, 151 (2018).

[48] P. Schwaller, Phys. Rev. Lett. **115**, 181101 (2015).

[49] J. Jaeckel, V. V. Khoze, and M. Spannowsky, Phys. Rev. D **94**, 103519 (2016).

[50] M. Chala, G. Nardini, and I. Sobolev, Phys. Rev. D **94**, 055006 (2016).

[51] A. Addazi, Mod. Phys. Lett. A **32**, 1750049 (2017).

[52] W. Chao, H.-K. Guo, and J. Shu, JCAP **1709**, 009 (2017).

[53] I. Baldes, JCAP **05**, 028 (2017).

[54] A. Addazi and A. Marciano, Chin. Phys. **C42**, 023107 (2018).

[55] D. Croon, V. Sanz, and G. White, JHEP **08**, 203 (2018).

[56] I. Baldes and C. Garcia-Cely, JHEP **05**, 190 (2019).

[57] M. Fairbairn, E. Hardy, and A. Wickens, JHEP **07**, 044 (2019).

[58] D. Dunsky, L. J. Hall, and K. Harigaya, JHEP **02**, 078 (2020).

[59] P. Archer-Smith, D. Linthorne, and D. Stolarski, Phys. Rev. D **101**, 095016 (2020).

[60] E. Hall, T. Konstandin, R. McGehee, and H. Murayama, (2019).

[61] L. Bian, W. Cheng, H.-K. Guo, and Y. Zhang, (2019).

[62] X. Wang, F. P. Huang, and X. Zhang, JCAP **05**, 045 (2020).

[63] D. Croon, T. E. Gonzalo, and G. White, (2018).

[64] A. Greljo, T. Opferkuch, and B. A. Stefanek, Phys. Rev. Lett. **124**, 171802 (2020).

[65] W.-C. Huang, F. Sannino, and Z.-W. Wang, (2020).

[66] V. Brdar, L. Graf, A. J. Helmboldt, and X.-J. Xu, JCAP **12**, 027 (2019).

[67] M. Hindmarsh, S. J. Huber, K. Rummukainen, and D. J. Weir, Phys. Rev. Lett. **112**, 041301 (2014).

[68] M. Hindmarsh, S. J. Huber, K. Rummukainen, and D. J. Weir, Phys. Rev. **D92**, 123009 (2015).

[69] M. Hindmarsh, S. J. Huber, K. Rummukainen, and D. J. Weir, Phys. Rev. **D96**, 103520 (2017).

[70] J. R. Espinosa, T. Konstandin, J. M. No, and G. Servant, JCAP **1006**, 028 (2010).

[71] M. Hindmarsh, Phys. Rev. Lett. **120**, 071301 (2018).

[72] K. Kajantie, M. Laine, K. Rummukainen, and M. E. Shaposhnikov, Nucl. Phys. B **466**, 189 (1996).

[73] K. Kajantie, M. Laine, K. Rummukainen, and M. E. Shaposhnikov, Phys. Rev. Lett. **77**, 2887 (1996).

[74] K. Kajantie, M. Laine, K. Rummukainen, and M. E. Shaposhnikov, Nucl. Phys. B **493**, 413 (1997).

[75] F. Csikor, Z. Fodor, and J. Heitger, Phys. Rev. Lett. **82**, 21 (1999).

[76] A. Bazavov *et al.*, Phys. Rev. D **85**, 054503 (2012).

[77] S. Gupta, X. Luo, B. Mohanty, H. G. Ritter, and N. Xu, Science **332**, 1525 (2011).

[78] C. Grojean, G. Servant, and J. D. Wells, Phys. Rev. **D71**, 036001 (2005).

[79] J. M. Cline, G. Laporte, H. Yamashita, and S. Kraml, JHEP **07**, 040 (2009).

[80] M. Carena, N. R. Shah, and C. E. M. Wagner, Phys. Rev. D **85**, 036003 (2012).

[81] G. Gil, P. Chankowski, and M. Krawczyk, Phys. Lett. B **717**, 396 (2012).

[82] M. Carena, G. Nardini, M. Quiros, and C. E. Wagner, JHEP **02**, 001 (2013).

[83] M. Fairbairn and R. Hogan, JHEP **09**, 022 (2013).

[84] S. Profumo, M. J. Ramsey-Musolf, C. L. Wainwright, and P. Winslow, Phys. Rev. **D91**, 035018 (2015).

[85] J. Kozaczuk, S. Profumo, L. S. Haskins, and C. L. Wainwright, JHEP **01**, 144 (2015).

[86] I. Baldes, T. Konstandin, and G. Servant, Phys. Lett. B **786**, 373 (2018).

[87] C.-W. Chiang, M. J. Ramsey-Musolf, and E. Senaha, Phys. Rev. D **97**, 015005 (2018).

[88] Q.-H. Cao, F. P. Huang, K.-P. Xie, and X. Zhang, Chin. Phys. C **42**, 023103 (2018).

[89] B. von Harling and G. Servant, JHEP **01**, 159 (2018).

[90] L. Bian, H.-K. Guo, and J. Shu, Chin. Phys. **C42**, 093106 (2018).

[91] A. Angelescu and P. Huang, (2018).

[92] S. Bruggisser, B. Von Harling, O. Matsedonskyi, and G. Servant, JHEP **12**, 099 (2018).

[93] P. Athron, C. Balazs, A. Fowlie, G. Pozzo, G. White, and Y. Zhang, JHEP **11**, 151 (2019).

[94] K. Kainulainen, V. Keus, L. Niemi, K. Rummukainen, T. V. Tenkanen, and V. Vaskonen, JHEP **06**, 075 (2019).

[95] J. Ellis, M. Fairbairn, M. Lewicki, V. Vaskonen, and A. Wickens, JCAP **09**, 019 (2019).

[96] A. Papaefstathiou and G. White, (2020).

[97] M. Postma and G. White, (2020).

[98] A. Alves, D. Gonçalves, T. Ghosh, H.-K. Guo, and K. Sinha, (2020).

[99] S. Baum, M. Carena, N. R. Shah, C. E. M. Wagner, and Y. Wang, (2020).

[100] A. Paul, U. Mukhopadhyay, and D. Majumdar, (2020).

[101] L. Bian, H.-K. Guo, Y. Wu, and R. Zhou, Phys. Rev. D **101**, 035011 (2020).

[102] Z. Zhang, C. Cai, X.-M. Jiang, Y.-L. Tang, Z.-H. Yu, and H.-H. Zhang, (2021).

[103] J. M. Cline, A. Friedlander, D.-M. He, K. Kainulainen, B. Laurent, and D. Tucker-Smith, (2021).

[104] H. Davoudiasl, Phys. Rev. Lett. **123**, 101102 (2019).

[105] D. J. Schwarz and M. Stuke, JCAP **11**, 025 (2009), [Erratum: JCAP 10, E01 (2010)].

[106] C. Caprini, R. Durrer, and X. Siemens, Phys. Rev. D **82**, 063511 (2010).

[107] G. Barenboim and W.-I. Park, JCAP **04**, 048 (2017).

[108] M. Pandey and A. Paul, (2020).

[109] A. Mohamadnejad, Eur. Phys. J. C **80**, 197 (2020).

[110] A. J. Helmboldt, J. Kubo, and S. van der Woude, Phys. Rev. D **100**, 055025 (2019).

[111] D. Croon, R. Houtz, and V. Sanz, JHEP **07**, 146 (2019).

[112] M. Breitbach, J. Kopp, E. Madge, T. Opferkuch, and P. Schwaller, (2018).

[113] A. Bhoonah, J. Bramante, S. Nerval, and N. Song, (2020).

[114] M. Li, Q.-S. Yan, Y. Zhang, and Z. Zhao, (2020).

[115] T. Ghosh, H.-K. Guo, T. Han, and H. Liu, (2020).

[116] F. Huang, V. Sanz, J. Shu, and X. Xue, (2021).

[117] W.-C. Huang, M. Reichert, F. Sannino, and Z.-W. Wang, (2020).

[118] F. Bigazzi, A. Caddeo, A. L. Cotrone, and A. Paredes, (2020).

[119] A. Azatov, M. Vanvlasselaer, and W. Yin, (2021).

[120] W. Chao, W.-F. Cui, H.-K. Guo, and J. Shu, (2017).

[121] N. Haba and T. Yamada, Phys. Rev. D **101**, 075027 (2020).

[122] N. Okada, O. Seto, and H. Uchida, (2020).

[123] L. Marzola, A. Racioppi, and V. Vaskonen, Eur. Phys. J. **C77**, 484 (2017).

[124] N. Okada and O. Seto, Phys. Rev. D **98**, 063532 (2018).

[125] T. Hasegawa, N. Okada, and O. Seto, Phys. Rev. D **99**, 095039 (2019).

[126] P. S. B. Dev and A. Mazumdar, Phys. Rev. **D93**, 104001 (2016).

[127] N. Aggarwal *et al.*, (2020).

[128] K. Ackley *et al.*, Publ. Astron. Soc. Austral. **37**, e047 (2020).

[129] S. Weinberg, Phys. Rev. Lett. **40**, 223 (1978).

[130] F. Wilczek, Phys. Rev. Lett. **40**, 279 (1978).

[131] P. Svrcek and E. Witten, JHEP **06**, 051 (2006).

[132] A. Arvanitaki, S. Dimopoulos, S. Dubovsky, N. Kaloper, and J. March-Russell, Phys. Rev. D **81**, 123530 (2010).

[133] M. Cicoli, M. Goodsell, and A. Ringwald, JHEP **10**, 146 (2012).

[134] B. S. Acharya, K. Bobkov, and P. Kumar, JHEP **11**, 105 (2010).

[135] D. Jackson Kimball *et al.*, Springer Proc. Phys. **245**, 105 (2020).

[136] A. Garcon *et al.*, (2019).

[137] J. L. Ouellet *et al.*, Phys. Rev. Lett. **122**, 121802 (2019).

[138] I. M. Bloch, Y. Hochberg, E. Kuflik, and T. Volansky, JHEP **01**, 167 (2020).

[139] P. W. Graham, S. Haciomeroglu, D. E. Kaplan, Z. Omarov, S. Rajendran, and Y. K. Semertzidis, (2020).

[140] J. Fan, Phys. Dark Univ. **14**, 84 (2016).

[141] M. Colpi, S. L. Shapiro, and I. Wasserman, Phys. Rev. Lett. **57**, 2485 (1986).

[142] L. Hui, J. P. Ostriker, S. Tremaine, and E. Witten, Phys. Rev. D **95**, 043541 (2017).

[143] H.-Y. Schive, T. Chiueh, and T. Broadhurst, Nature Phys. **10**, 496 (2014).

[144] H.-Y. Schive, M.-H. Liao, T.-P. Woo, S.-K. Wong, T. Chiueh, T. Broadhurst, and W.-Y. P. Hwang, Phys. Rev. Lett. **113**, 261302 (2014).

[145] B. Schwabe, J. C. Niemeyer, and J. F. Engels, Phys. Rev. D **94**, 043513 (2016).

[146] J. Veltmaat and J. C. Niemeyer, Phys. Rev. D **94**, 123523 (2016).

[147] P. Mocz, M. Vogelsberger, V. H. Robles, J. Zavala, M. Boylan-Kolchin, A. Fialkov, and L. Hernquist, Mon. Not. Roy. Astron. Soc. **471**, 4559 (2017).

[148] N. C. Amorisco and A. Loeb, (2018).

[149] E. Armengaud, N. Palanque-Delabrouille, C. Yèche, D. J. E. Marsh, and J. Baur, Monthly Notices of the Royal Astronomical Society **471**, 4606 (2017).

[150] K. Schutz, Phys. Rev. D **101**, 123026 (2020).

[151] N. Bar, D. Blas, K. Blum, and S. Sibiryakov, Phys. Rev. D **98**, 083027 (2018).

[152] K. Blum, E. Castorina, and M. Simonović, Astrophys. J. Lett. **892**, L27 (2020).

[153] G. F. Giudice, M. McCullough, and A. Urbano, JCAP **1610**, 001 (2016).

[154] S. L. Liebling and C. Palenzuela, Living Rev. Rel. **20**, 5 (2017).

[155] R. L. Guenther, Ph.D. thesis, THE UNIVERSITY OF TEXAS AT AUSTIN., 1995.

[156] E. D. Schiappacasse and M. P. Hertzberg, JCAP **01**, 037 (2018), [Erratum: JCAP 03, E01 (2018)].

[157] P.-H. Chavanis, Phys. Rev. D **84**, 043531 (2011).

[158] P. Chavanis and L. Delfini, Phys. Rev. D **84**, 043532 (2011).

[159] L. Visinelli, S. Baum, J. Redondo, K. Freese, and F. Wilczek, Phys. Lett. **B777**, 64 (2018).

[160] J. Eby, K. Mukaida, M. Takimoto, L. Wijewardhana, and M. Yamada, Phys. Rev. D **99**, 123503 (2019).

[161] J. Eby, P. Suranyi, and L. Wijewardhana, JCAP **04**, 038 (2018).

[162] J. Eby, M. Leembruggen, L. Street, P. Suranyi, and L. Wijewardhana, Phys. Rev. D **98**, 123013 (2018).

[163] J. Eby, P. Suranyi, and L. Wijewardhana, Mod. Phys. Lett. A **31**, 1650090 (2016).

[164] J. Eby, M. Leembruggen, P. Suranyi, and L. Wijewardhana, JHEP **12**, 066 (2016).

[165] M. Gleiser, Phys. Rev. D **38**, 2376 (1988).

[166] M. P. Hertzberg, F. Rompineve, and J. Yang, (2020).

[167] D. Croon, J. Fan, and C. Sun, JCAP **1904**, 008 (2019).

[168] A. Bernal, J. Barranco, D. Alic, and C. Palenzuela, Physical Review D **81**, (2010).

[169] F. Kling, A. Rajaraman, and F. L. Rivera, (2020).

[170] K. Blum, R. T. D'Agnolo, M. Lisanti, and B. R. Safdi, Phys. Lett. B **737**, 30 (2014).

[171] N. Bar, K. Blum, J. Eby, and R. Sato, Phys. Rev. D **99**, 103020 (2019).

[172] M. Bezares and C. Palenzuela, Class. Quant. Grav. **35**, 234002 (2018).

[173] T. Helfer, E. A. Lim, M. A. G. Garcia, and M. A. Amin, Phys. Rev. D **99**, 044046 (2019).

[174] P. S. B. Dev, M. Lindner, and S. Ohmer, Phys. Lett. B **773**, 219 (2017).

[175] M. P. Hertzberg and E. D. Schiappacasse, JCAP **11**, 004 (2018).

[176] M. P. Hertzberg, Y. Li, and E. D. Schiappacasse, JCAP **07**, 067 (2020).

[177] M. A. Amin and Z.-G. Mou, (2020).

[178] H.-K. Guo, K. Sinha, and C. Sun, JCAP **09**, 032 (2019).

[179] A. Prabhu, (2020).

[180] A. D. Sakharov, Pisma Zh. Eksp. Teor. Fiz. **5**, 32 (1967), [Usp. Fiz. Nauk161,no.5,61(1991)].

[181] M. E. Shaposhnikov, Nucl. Phys. B **287**, 757 (1987).

[182] M. Dine and A. Kusenko, Rev. Mod. Phys. **76**, 1 (2003).

[183] I. Affleck and M. Dine, Nucl. Phys. B **249**, 361 (1985).

[184] M. Dine, L. Randall, and S. D. Thomas, Nucl. Phys. B **458**, 291 (1996).

[185] R. Allahverdi and A. Mazumdar, New J. Phys. **14**, 125013 (2012).

[186] T. Gherghetta, C. F. Kolda, and S. P. Martin, Nucl. Phys. B **468**, 37 (1996).

[187] A. Kusenko and M. E. Shaposhnikov, Phys. Lett. B **418**, 46 (1998).

[188] G. Rosen, J. Math. Phys. **9**, 996 (1968).

[189] R. Friedberg, T. D. Lee, and A. Sirlin, Phys. Rev. D **13**, 2739 (1976).

[190] S. R. Coleman, Nucl. Phys. **B262**, 263 (1985), [Erratum: Nucl. Phys.B269,744(1986)].

[191] A. Kusenko, Phys. Lett. B **404**, 285 (1997).

[192] A. Kusenko, Phys. Lett. B **405**, 108 (1997).

[193] T. Alanne, K. Tuominen, and V. Vaskonen, Nucl. Phys. **B889**, 692 (2014).

[194] M. Aoki, H. Goto, and J. Kubo, Phys. Rev. **D96**, 075045 (2017).

[195] Y. Bai, A. J. Long, and S. Lu, (2018).

[196] R.-G. Cai, Z. Cao, Z.-K. Guo, S.-J. Wang, and T. Yang, Natl. Sci. Rev. **4**, 687 (2017).

[197] C. Caprini and D. G. Figueroa, Class. Quant. Grav. **35**, 163001 (2018).

[198] D. J. H. Chung, A. J. Long, and L.-T. Wang, Phys. Rev. **D87**, 023509 (2013).

[199] A. Beniwal, Ph.D. thesis, Adelaide U., 2018-07.

[200] K. Hashino, R. Jinno, M. Kakizaki, S. Kanemura, T. Takahashi, and M. Takimoto, (2018).

[201] C. Marzo, L. Marzola, and V. Vaskonen, (2018).

[202] A. Beniwal, M. Lewicki, J. D. Wells, M. White, and A. G. Williams, JHEP **08**, 108 (2017).

[203] K. Hashino, M. Kakizaki, S. Kanemura, P. Ko, and T. Matsui, JHEP **06**, 088 (2018).

[204] A. Addazi, Y.-F. Cai, and A. Marciano, Phys. Lett. **B782**, 732 (2018).

[205] C.-W. Chiang and E. Senaha, Phys. Lett. **B774**, 489 (2017).

[206] Y. Wan, B. Imtiaz, and Y.-F. Cai, (2018).

[207] Y. Chen, M. Huang, and Q.-S. Yan, JHEP **05**, 178 (2018).

[208] T. Vieu, A. P. Morais, and R. Pasechnik, JCAP **1807**, 014 (2018).

[209] P. Basler, M. Mühlleitner, and J. Wittbrodt, JHEP **03**, 061 (2018).

[210] R. Jinno, S. Lee, H. Seong, and M. Takimoto, JCAP **1711**, 050 (2017).

[211] K. Tsumura, M. Yamada, and Y. Yamaguchi, JCAP **1707**, 044 (2017).

[212] A. Hektor, K. Kannike, and V. Vaskonen, Phys. Rev. **D98**, 015032 (2018).

[213] F. P. Huang and J.-H. Yu, Phys. Rev. **D98**, 095022 (2018).

[214] P. H. Ghorbani, Phys. Rev. **D98**, 115016 (2018).

[215] A. Addazi and A. Marciano, Chin. Phys. **C42**, 023105 (2018).

[216] C.-Y. Chen, J. Kozaczuk, and I. M. Lewis, JHEP **08**, 096 (2017).

[217] A. Kobakhidze, C. Lagger, A. Manning, and J. Yue, Eur. Phys. J. **C77**, 570 (2017).

[218] R. Zhou, W. Cheng, X. Deng, L. Bian, and Y. Wu, (2018).

[219] S. Profumo, M. J. Ramsey-Musolf, and G. Shaughnessy, JHEP **08**, 010 (2007).

[220] T. Huang, J. M. No, L. Pernié, M. Ramsey-Musolf, A. Safonov, M. Spannowsky, and P. Winslow, Phys. Rev. **D96**, 035007 (2017).

[221] T. Robens and T. Stefaniak, Eur. Phys. J. **C75**, 104 (2015).

[222] A. V. Kotwal, M. J. Ramsey-Musolf, J. M. No, and P. Winslow, Phys. Rev. **D94**, 035022 (2016).

[223] J. R. Espinosa, T. Konstandin, and F. Riva, Nucl. Phys. **B854**, 592 (2012).

[224] J. Kozaczuk, JHEP **10**, 135 (2015).

[225] I. M. Lewis and M. Sullivan, Phys. Rev. **D96**, 035037 (2017).

[226] A. Azatov, R. Contino, G. Panico, and M. Son, Phys. Rev. **D92**, 035001 (2015).

[227] A. Alves, T. Ghosh, and K. Sinha, Phys. Rev. **D96**, 035022 (2017).

[228] T. Plehn and M. Rauch, Phys. Rev. **D72**, 053008 (2005).

[229] T. Binoth, S. Karg, N. Kauer, and R. Ruckl, Phys. Rev. **D74**, 113008 (2006).

[230] W. Bizoń, U. Haisch, and L. Rottoli, (2018).

[231] S. Inoue, M. J. Ramsey-Musolf, and Y. Zhang, Phys. Rev. **D89**, 115023 (2014).

[232] C.-Y. Chen, H.-L. Li, and M. Ramsey-Musolf, Phys. Rev. **D97**, 015020 (2018).

[233] H.-K. Guo, Y.-Y. Li, T. Liu, M. Ramsey-Musolf, and J. Shu, Phys. Rev. **D96**, 115034 (2017).

[234] G. M. Pruna and T. Robens, Phys. Rev. **D88**, 115012 (2013).

[235] G. Aad *et al.*, JHEP **08**, 045 (2016).

[236] M. Carena, Z. Liu, and M. Riembau, Phys. Rev. **D97**, 095032 (2018).

[237] D. López-Val and T. Robens, Phys. Rev. **D90**, 114018 (2014).

[238] M. E. Peskin and T. Takeuchi, Phys. Rev. **D46**, 381 (1992).

[239] K. Hagiwara, S. Matsumoto, D. Haidt, and C. S. Kim, Z. Phys. **C64**, 559 (1994), [Erratum: Z. Phys.C68,352(1995)].

[240] J. Alcaraz *et al.*, (2006).

[241] T. Aaltonen *et al.*, Phys. Rev. Lett. **108**, 151803 (2012).

[242] V. M. Abazov *et al.*, Phys. Rev. **D89**, 012005 (2014).

[243] D. E. Morrissey and M. J. Ramsey-Musolf, New J. Phys. **14**, 125003 (2012).

[244] S. R. Coleman and E. J. Weinberg, Phys. Rev. **D7**, 1888 (1973).

[245] M. Quiros, in *Proceedings, Summer School in High-energy physics and cosmology: Trieste, Italy, June 29-July 17, 1998* (PUBLISHER, ADDRESS, 1999), pp. 187–259.

[246] R. R. Parwani, Phys. Rev. **D45**, 4695 (1992), [Erratum: Phys. Rev.D48,5965(1993)].

[247] D. J. Gross, R. D. Pisarski, and L. G. Yaffe, Rev. Mod. Phys. **53**, 43 (1981).

[248] H. H. Patel and M. J. Ramsey-Musolf, JHEP **07**, 029 (2011).

[249] A. Alves, T. Ghosh, H.-K. Guo, and K. Sinha, (2018).

[250] M. S. Turner, E. J. Weinberg, and L. M. Widrow, Phys. Rev. **D46**, 2384 (1992).

[251] G. V. Dunne and H. Min, Phys. Rev. **D72**, 125004 (2005).

[252] A. Andreassen, D. Farhi, W. Frost, and M. D. Schwartz, Phys. Rev. **D95**, 085011 (2017).

[253] S. Weinberg, *The quantum theory of fields. Vol. 2: Modern applications* (Cambridge University Press, ADDRESS, 2013).

[254] R. Apreda, M. Maggiore, A. Nicolis, and A. Riotto, Nucl. Phys. **B631**, 342 (2002).

[255] M. Kamionkowski, A. Kosowsky, and M. S. Turner, Phys. Rev. **D49**, 2837 (1994).

[256] J. M. Cline, in *Les Houches Summer School - Session 86: Particle Physics and Cosmology: The Fabric of Spacetime Les Houches, France, July 31-August 25, 2006* (PUBLISHER, ADDRESS, 2006).

[257] H. H. Patel and M. J. Ramsey-Musolf, Phys. Rev. **D88**, 035013 (2013).

[258] M. J. Ramsey-Musolf, P. Winslow, and G. White, Phys. Rev. **D97**, 123509 (2018).

[259] J. M. No, Phys. Rev. **D84**, 124025 (2011).

[260] H. Kurki-Suonio and M. Laine, Phys. Rev. **D51**, 5431 (1995).

[261] P. J. Steinhardt, Phys. Rev. **D25**, 2074 (1982).

[262] P. John and M. G. Schmidt, Nucl. Phys. **B598**, 291 (2001), [Erratum: Nucl. Phys.B648,449(2003)].

[263] V. Cirigliano, S. Profumo, and M. J. Ramsey-Musolf, JHEP **07**, 002 (2006).

[264] D. J. H. Chung, B. Garbrecht, M. Ramsey-Musolf, and S. Tulin, JHEP **12**, 067 (2009).

[265] W. Chao and M. J. Ramsey-Musolf, JHEP **10**, 180 (2014).

[266] C. Lee, V. Cirigliano, and M. J. Ramsey-Musolf, Phys. Rev. **D71**, 075010 (2005).

[267] D. Bodeker, G. D. Moore, and K. Rummukainen, Phys. Rev. **D61**, 056003 (2000).

[268] J. Engel, M. J. Ramsey-Musolf, and U. van Kolck, Prog. Part. Nucl. Phys. **71**, 21 (2013).

[269] T. Chupp, P. Fierlinger, M. Ramsey-Musolf, and J. Singh, (2017).

[270] A. Kosowsky, M. S. Turner, and R. Watkins, Phys. Rev. **D45**, 4514 (1992).

[271] A. Kosowsky, M. S. Turner, and R. Watkins, Phys. Rev. Lett. **69**, 2026 (1992).

[272] A. Kosowsky and M. S. Turner, Phys. Rev. **D47**, 4372 (1993).

[273] S. J. Huber and T. Konstandin, JCAP **0809**, 022 (2008).

[274] R. Jinno and M. Takimoto, Phys. Rev. **D95**, 024009 (2017).

[275] R. Jinno and M. Takimoto, (2017).

[276] D. Bodeker and G. D. Moore, JCAP **0905**, 009 (2009).

[277] D. Bodeker and G. D. Moore, JCAP **1705**, 025 (2017).

[278] C. Caprini, R. Durrer, and G. Servant, JCAP **0912**, 024 (2009).

[279] P. Binetruy, A. Bohe, C. Caprini, and J.-F. Dufaux, JCAP **1206**, 027 (2012).

[280] E. Thrane and J. D. Romano, Phys. Rev. **D88**, 124032 (2013).

[281] C. L. Wainwright, Comput. Phys. Commun. **183**, 2006 (2012).

[282] J. Ellis, M. Lewicki, and J. M. No, Submitted to: JCAP (2018).

[283] D. Curtin *et al.*, (2018).

[284] O. J. P. Eboli, G. C. Marques, S. F. Novaes, and A. A. Natale, Phys. Lett. **B197**, 269 (1987).

[285] T. Plehn, M. Spira, and P. M. Zerwas, Nucl. Phys. **B479**, 46 (1996), [Erratum: Nucl. Phys.B531,655(1998)].

[286] J. Alwall, R. Frederix, S. Frixione, V. Hirschi, F. Maltoni, O. Mattelaer, H. S. Shao, T. Stelzer, P. Torrielli, and M. Zaro, JHEP **07**, 079 (2014).

[287] A. M. Sirunyan *et al.*, Phys. Lett. **B788**, 7 (2019).

[288] A. M. Sirunyan *et al.*, Phys. Lett. **B778**, 101 (2018).

[289] A. M. Sirunyan *et al.*, Phys. Lett. **B781**, 244 (2018).

[290] A. M. Sirunyan *et al.*, JHEP **08**, 152 (2018).

[291] A. M. Sirunyan *et al.*, (2018).

[292] A. M. Sirunyan *et al.*, Submitted to: JHEP (2018).

[293] A. M. Sirunyan *et al.*, JHEP **01**, 054 (2018).

[294] A. M. Sirunyan *et al.*, Submitted to: Phys. Rev. Lett. (2018).

[295] M. Aaboud *et al.*, JHEP **11**, 040 (2018).

[296] M. Aaboud *et al.*, Phys. Rev. Lett. **121**, 191801 (2018).

[297] M. Aaboud *et al.*, (2018).

[298] M. Aaboud *et al.*, Submitted to: JHEP (2018).

[299] M. Aaboud *et al.*, (2018).

[300] T. A. collaboration, (2018).

[301] D. de Florian *et al.*, (2016).

[302] S. Borowka, C. Duhr, F. Maltoni, D. Pagani, A. Shivaji, and X. Zhao, Submitted to: JHEP (2018).

[303] W. Kilian, S. Sun, Q.-S. Yan, X. Zhao, and Z. Zhao, (2018).

[304] D. Jurčiukonis and L. Lavoura, (2018).

[305] F. Maltoni, D. Pagani, and X. Zhao, JHEP **07**, 087 (2018).

[306] C.-Y. Chen, Q.-S. Yan, X. Zhao, Y.-M. Zhong, and Z. Zhao, Phys. Rev. **D93**, 013007 (2016).

[307] M. Aaboud *et al.*, Phys. Rev. **D98**, 052008 (2018).

[308] J. Ellis, M. Lewicki, and J. M. No, (2020).

[309] G. Kane, K. Sinha, and S. Watson, Int. J. Mod. Phys. D **24**, 1530022 (2015).

[310] R. Allahverdi *et al.*, (2020).

[311] T. Banks, M. Berkooz, S. Shenker, G. W. Moore, and P. Steinhardt, Phys. Rev. D **52**, 3548 (1995).

[312] T. Banks, M. Berkooz, and P. Steinhardt, Phys. Rev. D **52**, 705 (1995).

[313] G. Coughlan, W. Fischler, E. W. Kolb, S. Raby, and G. G. Ross, Phys. Lett. B **131**, 59 (1983).

[314] T. Banks, D. B. Kaplan, and A. E. Nelson, Phys. Rev. D **49**, 779 (1994).

[315] B. Dutta, L. Leblond, and K. Sinha, Phys. Rev. D **80**, 035014 (2009).

[316] R. Allahverdi, B. Dutta, and K. Sinha, Phys. Rev. D **87**, 075024 (2013).

[317] B. S. Acharya, P. Kumar, K. Bobkov, G. Kane, J. Shao, and S. Watson, JHEP **06**, 064 (2008).

[318] B. S. Acharya, G. Kane, S. Watson, and P. Kumar, Phys. Rev. D **80**, 083529 (2009).

[319] A. L. Erickcek, K. Sinha, and S. Watson, Phys. Rev. D **94**, 063502 (2016).

[320] M. Sten Delos, T. Linden, and A. L. Erickcek, Phys. Rev. D **100**, 123546 (2019).

[321] A. L. Erickcek, Phys. Rev. D **92**, 103505 (2015).

[322] M. Drees and F. Hajkarim, JCAP **02**, 057 (2018).

[323] C. Cosme, M. Dutra, T. Ma, Y. Wu, and L. Yang, (2020).

[324] R. Allahverdi, B. Dutta, and K. Sinha, Phys. Rev. D **82**, 035004 (2010).

[325] C. Pallis, Nucl. Phys. B **751**, 129 (2006).

[326] J. Lankinen, O. Kerppo, and I. Vilja, Phys. Rev. D **101**, 063529 (2020).

[327] K. Nakayama and F. Takahashi, JCAP **11**, 009 (2010).

[328] C. Pallis, JCAP **10**, 015 (2005).

[329] D. Grin, T. L. Smith, and M. Kamionkowski, Phys. Rev. D **77**, 085020 (2008).

[330] K. Dimopoulos and T. Markkanen, JCAP **06**, 021 (2018).

[331] K. Redmond and A. L. Erickcek, Phys. Rev. D **96**, 043511 (2017).

[332] D. Bettoni, G. Domènech, and J. Rubio, JCAP **02**, 034 (2019).

[333] D. Bettoni and J. Rubio, JCAP **01**, 002 (2020).

[334] S. Bhattacharya, S. Mohanty, and P. Parashari, Phys. Rev. D **102**, 043522 (2020).

[335] G. Barenboim and W.-I. Park, Phys. Lett. **B759**, 430 (2016).

[336] N. Bernal and F. Hajkarim, Phys. Rev. **D100**, 063502 (2019).

[337] F. D'Eramo and K. Schmitz, Phys. Rev. Research. **1**, 013010 (2019).

[338] M. Geller, A. Hook, R. Sundrum, and Y. Tsai, Phys. Rev. Lett. **121**, 201303 (2018).

[339] Y. Cui, M. Lewicki, D. E. Morrissey, and J. D. Wells, Phys. Rev. D **97**, 123505 (2018).

[340] S. Weinberg, *Cosmology* (PUBLISHER, ADDRESS, 2008).

[341] A. D. Linde, Phys. Lett. **100B**, 37 (1981).

[342] A. D. Linde, Nucl. Phys. **B216**, 421 (1983), [Erratum: Nucl. Phys.B223,544(1983)].

[343] R. J. Scherrer and M. S. Turner, Phys. Rev. **D31**, 681 (1985).

[344] A. H. Guth and E. J. Weinberg, Phys. Rev. **D23**, 876 (1981).

[345] G. D. Moore and T. Prokopec, Phys. Rev. **D52**, 7182 (1995).

[346] R.-G. Cai and S.-J. Wang, Sci. China Phys. Mech. Astron. **61**, 080411 (2018).

[347] J. Ignatius, K. Kajantie, H. Kurki-Suonio, and M. Laine, Phys. Rev. D **49**, 3854 (1994).

[348] H. Kurki-Suonio and M. Laine, Phys. Rev. D **54**, 7163 (1996).

[349] B.-H. Liu, L. D. McLerran, and N. Turok, Phys. Rev. **D46**, 2668 (1992).

[350] T. Konstandin, G. Nardini, and I. Rues, JCAP **1409**, 028 (2014).

[351] A. Brandenburg, K. Enqvist, and P. Olesen, Phys. Rev. **D54**, 1291 (1996).

[352] R. M. Gailis, N. E. Frankel, and C. P. Dettmann, Phys. Rev. **D52**, 6901 (1995).

[353] U.-L. Pen and N. Turok, Phys. Rev. Lett. **117**, 131301 (2016).

[354] D. Croon, O. Gould, P. Schicho, T. V. Tenkanen, and G. White, (2020).

[355] K. Kajantie, M. Laine, K. Rummukainen, and M. E. Shaposhnikov, Nucl. Phys. B **458**, 90 (1996).

[356] D. Curtin, P. Meade, and H. Ramani, Eur. Phys. J. C **78**, 787 (2018).

[357] O. Gould, (2021).

[358] B. Garbrecht and P. Millington, Phys. Rev. D **92**, 125022 (2015).

[359] W.-Y. Ai, J. S. Cruz, B. Garbrecht, and C. Tamarit, Phys. Rev. D **102**, 085001 (2020).

[360] L. Niemi, M. Ramsey-Musolf, T. V. Tenkanen, and D. J. Weir, (2020).

[361] H.-K. Guo, K. Sinha, D. Vagie, and G. White, (2020).

[362] F. Giese, T. Konstandin, and J. van de Vis, (2020).

[363] F. Giese, T. Konstandin, K. Schmitz, and J. Van De Vis, (2020).

[364] M. J. Ramsey-Musolf, JHEP **09**, 179 (2020).

[365] M. Hindmarsh, S. J. Huber, K. Rummukainen, and D. J. Weir, Phys. Rev. D **92**, 123009 (2015).

[366] D. Cutting, M. Hindmarsh, and D. J. Weir, Phys. Rev. D **97**, 123513 (2018).

[367] D. O'Connell, M. J. Ramsey-Musolf, and M. B. Wise, Phys. Rev. D **75**, 037701 (2007).

[368] J. Elias-Miró, J. R. Espinosa, and T. Konstandin, Journal of High Energy Physics **2014**, (2014).

[369] V. Barger, P. Langacker, M. McCaskey, M. J. Ramsey-Musolf, and G. Shaughnessy, Phys. Rev. D **77**, 035005 (2008).

[370] W. Liu and K.-P. Xie, (2021).

[371] C.-W. Chiang, Y.-T. Li, and E. Senaha, Phys. Lett. **B789**, 154 (2019).

[372] K. Fuyuto and E. Senaha, Phys. Rev. D **90**, 015015 (2014).

[373] P. Athron, C. Balázs, M. Bardsley, A. Fowlie, D. Harries, and G. White, (2019).

[374] X. Wang, F. P. Huang, and X. Zhang, (2020).

[375] D. Croon, M. Gleiser, S. Mohapatra, and C. Sun, Phys. Lett. B **783**, 158 (2018).

[376] L. Berezhiani and J. Khoury, Phys. Rev. **D92**, 103510 (2015).

[377] E. G. Ferreira, G. Franzmann, J. Khoury, and R. Brandenberger, JCAP **08**, 027 (2019).

[378] P.-H. Chavanis and T. Harko, Phys. Rev. D **86**, 064011 (2012).

[379] J. Chen, X. Du, E. W. Lentz, D. J. E. Marsh, and J. C. Niemeyer, (2020).

[380] H. N. Luu, S.-H. H. Tye, and T. Broadhurst, Phys. Dark Univ. **30**, 100636 (2020).

[381] J. Eby, L. Street, P. Suranyi, L. R. Wijewardhana, and M. Leembruggen, (2020).

[382] N. Kan and K. Shiraishi, Phys. Rev. D **96**, 103009 (2017).

[383] Y. Brihaye and B. Hartmann, Nonlinearity **21**, 1937 (2008).

[384] Y. Brihaye and B. Hartmann, Phys. Rev. D **79**, 064013 (2009).

[385] Y. Brihaye, T. Caebergs, B. Hartmann, and M. Minkov, Phys. Rev. D **80**, 064014 (2009).

[386] W. H. Press, S. A. Teukolsky, W. T. Vetterling, and B. P. Flannery, *Numerical Recipes 3rd Edition: The Art of Scientific Computing*, 3 ed. (Cambridge University Press, New York, NY, USA, 2007).

[387] I. Low, W. Skiba, and D. Tucker-Smith, Phys. Rev. D **66**, 072001 (2002).

[388] F. Donato, G. Gentile, P. Salucci, C. F. Martins, M. I. Wilkinson, G. Gilmore, E. K. Grebel, A. Koch, and R. Wyse, Mon. Not. Roy. Astron. Soc. **397**, 1169 (2009).

[389] P. Salucci, Astron. Astrophys. Rev. **27**, 2 (2019).

[390] W. Hu, R. Barkana, and A. Gruzinov, Phys. Rev. Lett. **85**, 1158 (2000).

[391] V. Irˇ sič, M. Viel, M. G. Haehnelt, J. S. Bolton, and G. D. Becker, Phys. Rev. Lett. **119**, 031302 (2017).

[392] M. Nori, R. Murgia, V. Irˇ sič, M. Baldi, and M. Viel, Mon. Not. Roy. Astron. Soc. **482**, 3227 (2019).

[393] A. Arvanitaki, S. Dimopoulos, M. Galanis, L. Lehner, J. O. Thompson, and K. Van Tilburg, Phys. Rev. D **101**, 083014 (2020).

[394] E. Braaten, A. Mohapatra, and H. Zhang, Phys. Rev. Lett. **117**, 121801 (2016).

[395] S. Khan, S. Husa, M. Hannam, F. Ohme, M. Pürrer, X. Jiménez Forteza, and A. Bohé, Phys. Rev. D **93**, 044007 (2016).

[396] L. Barsotti, P. Fritschel, M. Evans, and S. Gras, , lIGO Document T1800044-v5, https://dcc.ligo.org/LIGO-T1800044/public.

[397] T. Akutsu *et al.*, (2020).

[398] R. Abbott *et al.*, Phys. Rev. Lett. **125**, 101102 (2020).

[399] R. Abbott *et al.*, Astrophys. J. **900**, L13 (2020).

[400] J. Calderón Bustillo, N. Sanchis-Gual, A. Torres-Forné, J. A. Font, A. Vajpeyi, R. Smith, C. Herdeiro, E. Radu, and S. H. Leong, (2020).

[401] N. Arkani-Hamed, A. Cohen, E. Katz, and A. Nelson, JHEP **07**, 034 (2002).

[402] N. Arkani-Hamed, A. Cohen, E. Katz, A. Nelson, T. Gregoire, and J. G. Wacker, JHEP **08**, 021 (2002).

[403] M. Schmaltz and J. Thaler, JHEP **03**, 137 (2009).

[404] K. Inomata, M. Kawasaki, K. Mukaida, T. Terada, and T. T. Yanagida, Phys. Rev. D **101**, 123533 (2020).

[405] A. Kusenko and A. Mazumdar, Phys. Rev. Lett. **101**, 211301 (2008).

[406] A. Kusenko, A. Mazumdar, and T. Multamaki, Phys. Rev. D **79**, 124034 (2009).

[407] K. Enqvist and J. McDonald, Phys. Rev. D **62**, 043502 (2000).

[408] D. Marsh, JHEP **05**, 041 (2012).

[409] K. Inomata, K. Kohri, T. Nakama, and T. Terada, JCAP **1910**, 071 (2019).

[410] S. Kasuya and M. Kawasaki, Phys. Rev. D **61**, 041301 (2000).

[411] T. Multamaki and I. Vilja, Nucl. Phys. B **574**, 130 (2000).

[412] T. Hiramatsu, M. Kawasaki, and F. Takahashi, JCAP **06**, 008 (2010).

[413] T. S. Bunch and P. C. W. Davies, Proc. Roy. Soc. Lond. A **360**, 117 (1978).

[414] A. D. Linde, Phys. Lett. B **116**, 335 (1982).

[415] K.-M. Lee and E. J. Weinberg, Phys. Rev. D **36**, 1088 (1987).

[416] A. A. Starobinsky and J. Yokoyama, Phys. Rev. D **50**, 6357 (1994).

[417] J. Rosiek, (1995).

[418] A. Kusenko, L. Loveridge, and M. Shaposhnikov, Phys. Rev. D **72**, 025015 (2005).

[419] K. Inomata, K. Kohri, T. Nakama, and T. Terada, Phys. Rev. D **100**, 043532 (2019).

[420] A. G. Cohen, S. R. Coleman, H. Georgi, and A. Manohar, Nucl. Phys. B **272**, 301 (1986).

[421] N. Aghanim *et al.*, Astron. Astrophys. **641**, A6 (2020).

[422] K. Kohri and T. Terada, Phys. Rev. D **97**, 123532 (2018).

[423] V. Mukhanov, *Physical Foundations of Cosmology* (Cambridge University Press, Oxford, 2005).

[424] K. N. Ananda, C. Clarkson, and D. Wands, Phys. Rev. D **75**, 123518 (2007).

[425] M. Punturo *et al.*, Class. Quant. Grav. **27**, 194002 (2010).

[426] M. Y. Khlopov and A. D. Linde, Phys. Lett. B **138**, 265 (1984).

[427] J. Pradler and F. D. Steffen, Phys. Lett. B **648**, 224 (2007).

[428] H. Eberl, I. D. Gialamas, and V. C. Spanos, Phys. Rev. D **103**, 075025 (2021).

[429] R. Arya, N. Mahajan, and R. Rangarajan, Phys. Lett. B **772**, 258 (2017).

[430] S. Kanemura and K. Yagyu, Phys. Lett. **B751**, 289 (2015).